

**On the fatigue behaviour and modelling of fatigue life
for laser-welded Ti-6Al-4V**

Vom Promotionsausschuss der
Technischen Universität Hamburg
zur Erlangung des akademischen Grades
Doktor-Ingenieur (Dr.-Ing.)

genehmigte Dissertation

von

Fedor Fomin

aus

Bender

2019

1. Gutachter: Herr Prof. Dr.-Ing. habil. Norbert Huber

2. Gutachter: Herr Prof. Dr.-Ing. Thomas Niendorf

Tag der mündlichen Prüfung: 11.11.2019.

Acknowledgements

This PhD thesis is based on the research work carried out in the Department of Laser Processing and Structural Assessment at the Institute of Materials Research, Materials Mechanics of Helmholtz Zentrum Geesthacht (HZG).

I owe a huge debt of gratitude to my first supervisor Prof. Norbert Huber for his expert guidance, support and insightful suggestions. I am also thankful to Prof. Thomas Niendorf for careful reading and review of the thesis.

I am extremely grateful to my second supervisor - the head of the Department of Laser Processing and Structural Assessment at HZG, Dr. Nikolai Kashaev, for his encouragement, constant support and valuable feedback throughout the duration of this research. In particular, I am thankful to him for helping me establish the framework of this thesis and numerous valuable comments that improved the manuscript considerably.

I would like to thank all my research fellows with whom I have had great pleasure to work during this PhD work. My special thanks go to all the team members at HZG for their friendship, fruitful scientific discussions and a warm working atmosphere. I wish to express my deep gratitude to Dr. Volker Ventzke and Falk Dorn for their valuable contributions and practical suggestions regarding the microstructure-related part of this work. I wish to thank Kay Erdmann, Rene Dinse, Stefan Riekehr, Peter Haack, Manfred Horstmann, Jürgen Knaack and Hamdi Tek for giving me a professional technical support and assistance in the experimental program. I am thankful to Dr. Vasyil Haramus for his assistance with the laboratory X-ray inspection equipment. Many thanks to Gleb Dovzhenko for his support with the evaluation of the X-ray diffraction measurements of residual stresses.

I would like to thank all the members of the TUHH/HZG Graduate School of Materials Science and especially its former coordinator Dr. Alette Winter for the diversified workshops, interesting symposia and great time together.

Finally, I would like to express my infinite gratitude to my family for their love, continuous encouragement and always believing in me.

Hamburg, 26.11.2019

Fedor Fomin

Abstract

Structural strength may degrade during the service life of an aircraft due to undetected material defects or accidental damages. Since the introduction of damage-tolerance regulations for the certification of aircraft structures in the late 1970's, fatigue resistance is a design criterion for airframe structural elements and engine components. Design and fabrication processes must ensure that manufacturing flaws or fatigue damages do not lead to any catastrophic failure up to the next scheduled inspection. In recent years, the increased demand and more stringent requirements relating to the structural weight and fuel consumption have driven the need for advanced materials and novel fabrication techniques. The superior fatigue- and damage-tolerance characteristics of newly developed structures pose a major challenge to their real application in the aerospace industry.

Welded structures are particularly susceptible to fatigue cracking due to stress concentration and material degradation after the weld thermal cycles. Despite significant benefits provided by welding as a manufacturing step, there is still a lack of understanding when it comes to the explanation of how the welded joints fail under cyclic loading and what are the ways to extend the weld lifetime beyond the designed value. This study aims to investigate the fatigue behaviour of the laser-welded high-strength Ti-6Al-4V alloy in the region of high cycle fatigue (HCF) by focusing on the three following aspects: First, the crack initiation mechanism and the influence of weld defects on fatigue performance are comprehensively studied. Second, a set of post-weld treatments that can tolerate the inherent weld imperfections and thereby extend the fatigue life are analysed. Finally, a lifetime assessment model for predicting the joint durability in the HCF regime is developed.

Detailed microstructural characterization and mechanical testing of the Ti-6Al-4V weldments demonstrated a strong mismatch between the weld zone and the base metal. The enhanced notch sensitivity of the weld and the inherent welding-induced defects result in relatively poor fatigue performance. Surface weld imperfections, such as underfills and weld toes, act as stress raisers and initiate fatigue cracks early in the fatigue life. Five methods, including thermal and mechanical treatments for the weld lifetime prolongation, have been quantitatively characterized. It was shown that local surface modification techniques that enable smoothening of the weld notches lead to significant improvement of the fatigue properties. A novel methodology to apply laser remelting as a local post-weld surface treatment has been proposed. Application of a suitable surface smoothening technique can increase the weld fatigue limit almost by a factor of three, thereby approaching the base material level. Under these circumstances, fatigue cracks initiate at the welding-induced porosity underneath the surface and result in a fish-eye type of fracture.

Conditions responsible for the fatigue origin transition from the surface to the interior were studied. The effect of near-surface residual stresses generated via laser shock peening (LSP) on the growth of the surface and internal cracks was evaluated. The results highlight that if sufficient surface quality is ensured, internal pores or microstructural inhomogeneities control the fatigue behaviour. The present work provides a necessary experimental background and deeper insights into the mechanisms of interior-initiated fatigue fracture.

A robust and efficient analytical assessment model for internally flawed materials has been developed on the basis of a fracture mechanics approach. An extensive experimental programme at the coupon test level has been undertaken to obtain the fundamental material-specific constants and to validate the semi-empirical model. It has been shown that the effect of short cracks, the environment at the crack tip, and the crack origin position should be considered for accurate predictions. The statistical distribution of internal welding-induced defects has been quantitatively characterized and subsequently incorporated into the modelling framework to predict the fatigue scatter range. The probabilistic methodology of fatigue life assessment, developed in this work, can be potentially used for the reliability assessment of components with various types of defects, thus enabling a prospective adoption of the defect-tolerant design for welded structures.

Zusammenfassung

Unentdeckte Materialdefekte oder zufällige Unfallschäden können zu einer Degradation der strukturellen Festigkeit von Flugzeugstrukturen während der Betriebslebensdauer führen. Seit Einführung der Schadenstoleranz ist die Ermüdungsbeständigkeit das maßgebliche Auslegungskriterium für Rumpfstrukturelemente sowie Triebwerkskomponenten und deren Zertifizierung. Die aktuellen Auslegungs- und Fertigungsmethoden müssen sicherstellen, dass Herstellungsfehler oder Ermüdungsschäden kein katastrophales Versagen bis zur nächsten Wartung verursachen können. In den letzten Jahren haben zunehmender Bedarf und steigende Anforderungen an Strukturgewicht und Treibstoffverbrauch die ständige Entwicklung von neuartigen Hochleistungsmaterialien und Fertigungsverfahren vorangetrieben. Vor diesem Hintergrund stellt die Verbesserung von Ermüdungs- und Schadenstoleranzeigenschaften neu entwickelter Strukturen die größte Herausforderung hinsichtlich ihrer Anwendung in der Luftfahrtindustrie dar.

Schweißverbindungen sind besonders anfällig für Ermüdungsrisssbildung aufgrund von Spannungskonzentrationen an Schweißfehlern und der unerwünschten Umwandlungen des Werkstoffgefüges, welche während eines thermischen Schweißzyklus aktiviert werden. Trotz signifikanter Vorteile des Schweißens mangelt es noch am Verständnis zu Versagensmechanismen von geschweißten Strukturen sowie zu Nachbehandlungsverfahren zur Lebensdauersteigerung. Das Ziel der vorliegenden Arbeit ist die experimentelle und theoretische Untersuchung des Ermüdungsverhaltens der laserstrahlgeschweißten Titan-Legierung Ti-6Al-4V im Bereich von hohen Lastzyklen (HCF) unter besonderer Berücksichtigung der folgenden drei Aspekte: 1.) die werkstoffmechanischen Vorgänge der Rissinitiierung in der Schweißnaht und Einfluss von Schweißfehlern auf die Ermüdungseigenschaften werden ausführlich erforscht; 2.) verschiedene Arten von Behandlungsverfahren nach dem Schweißen mit dem Ziel, die Lebensdauer der geschweißten Strukturen zu erhöhen, werden analysiert und 3.) im Rahmen einer theoretischen Studie wird abschließend ein bruchmechanisches Berechnungsmodell entwickelt, welche die Abschätzung der Dauerfestigkeit von Schweißverbindungen und deren Streuung mit hinreichender Genauigkeit ermöglicht. Der Modellansatz wird anhand von experimentellen Untersuchungsergebnissen überprüft.

Eine detaillierte Charakterisierung der Mikrostruktur und mechanischen Eigenschaften zeigt, dass wesentliche Unterschiede zwischen Grundwerkstoff und Schweißnaht bestehen. Die höhere Kerbempfindlichkeit der Schmelzzone gepaart mit unvermeidlich erzeugten Schweißnahtfehlern führt zu verminderter Schwingfestigkeit der Schweißnaht im HCF-Bereich. Zahlreiche Oberflächenfehler von Schweißnähten u.a. Einbrandkerben fungieren als lokale Spannungskonzentratoren und initiieren Mikrorisse bereits in einer früheren Lebensdauerphase. Zur Erhöhung der Ermüdungsfestigkeit und damit der Lebensdauer werden thermische und mechanische Ansätze zur Nachbehandlung optimiert und quantitativ charakterisiert. In diesen Untersuchungen wird nachgewiesen, dass lokale Methoden der Oberflächenmodifikation, die ein Glätten der Oberfläche ermöglichen, zur deutlichen Verbesserung der Dauerfestigkeit von Schweißverbindungen führen. Eine innovative laserstrahlgestützte Methode wie das Laserumschmelzverfahren wird als eine lokale Oberflächenbehandlung nach dem Schweißprozess vorgeschlagen. Im Rahmen dieser Arbeit gelang es, durch eine sorgfältige und systematische Optimierung der geeigneten

Nachbehandlungsverfahren, die Dauerfestigkeit von laserstrahlgeschweißten Verbindungen um den Faktor 3 zu erhöhen. Dabei nähert sich die Schwingfestigkeit der Schweißverbindungen dem Niveau des Grundwerkstoffes. Es wird gezeigt, dass Rissinitiierung an schweißbedingten Mikrodefekten wie Poren dicht unterhalb der Oberfläche erfolgt und zum sogenannten „Fish-Eye“-Bruch führt. Die Bedingungen für den Übergang von Rissen ausgehend von Oberflächenkerben zu inneren Mikroporen werden untersucht. Der Einfluss von oberflächennahen Druckeigenstressungen, erzeugt mittels Laser Shock Peening (LSP), auf die Fortschrittsraten von Oberflächenrissen sowie Innenrissen wird ausgewertet. Die Ergebnisse deuten darauf hin, dass die inneren schweißbedingten Defekte und mikrostrukturellen Inhomogenitäten die Rissinitiierung verursachen und für die Betriebslebensdauer einer Ti-6Al-4V-Laserstrahlschweißverbindung bestimmend sind. Die vorliegende Arbeit beinhaltet die umfassende experimentelle Basis zum Verständnis werkstoffmechanischer Zusammenhänge und tiefgehende Einsichten in die Versagensmechanismen Ti-6Al-4V-Laserstrahlschweißverbindungen mit inneren rissinitierenden Defekten.

Ein robustes und effizientes analytisches Modell zur Abschätzung der Lebensdauer von Materialien mit inneren Mikrokerben und -defekten wird auf der Basis erweiterter kontinuumsmechanischer Konzepte entwickelt. Ein umfangreiches Versuchsprogramm zur Ermittlung der materialspezifischen bruchmechanischen Kennwerte und Validierung des analytischen Modells wird umgesetzt. Der hier vorgeschlagene Modellansatz zeigt, dass das Kurzrisssverhalten, die Umgebungsbedingungen an der Rissfront und der Rissausgangspunkt eine entscheidende Rolle bei der genauen Vorhersage des Schadensgeschehens spielen. Darüber hinaus erlaubt der Modellansatz, eine experimentell ermittelte Porenverteilung in das Modell zu integrieren und damit die große Streuung der Versuchsergebnisse zu bewerten. Die entwickelte Methodik zur Lebensdauervorhersage kann zur Zuverlässigkeitsbeurteilung von mangelbehafteten Bauteilen angewandt werden und dadurch zur Weiterentwicklung von zukünftigen defekttoleranten Auslegungsmethoden von geschweißten Strukturen beitragen.

Contents

1	Introduction	1
1.1	Motivation and research objectives.....	1
1.2	General approach	4
1.3	Thesis layout	5
2	State of the art	7
2.1	Titanium and its alloys	7
2.1.1	Applications	7
2.1.2	Basic properties	7
2.1.3	Ti-6Al-4V alloy.....	9
2.2	Fusion welding techniques.....	11
2.2.1	Keyhole mode vs. conduction mode	12
2.2.2	Tungsten inert gas (TIG) welding	13
2.2.3	Electron beam welding (EBW)	14
2.2.4	Laser beam welding (LBW).....	15
2.3	Fatigue behaviour of Ti-6Al-4V	17
2.3.1	Basic concepts of fatigue.....	17
2.3.2	Fatigue behaviour of Ti-6Al-4V base metal.....	19
2.3.3	Fatigue of Ti-6Al-4V welds	21
2.3.4	Internal crack initiation	22
2.4	Lifetime extension methods	24
2.5	Fatigue life assessment.....	26
3	Methodology	31
3.1	Experimental procedures.....	31
3.1.1	Material	31
3.1.2	Laser processing.....	31
3.1.3	Microstructure analysis	34
3.1.4	Microhardness	35
3.1.5	Residual stresses.....	35
3.1.6	Mechanical properties	37
3.1.7	Radiographic inspection.....	38
3.1.8	Heat treatment	39

3.2	Adopted fracture mechanics concepts	40
3.2.1	Stages of fatigue life	40
3.2.2	Stress intensity factor (SIF)	41
3.2.3	Short cracks	43
3.3	Statistical tools.....	44
3.3.1	Basic concepts of fatigue statistics	44
3.3.2	Weibull plot.....	46
3.3.3	Multivariate random variables.....	47
4	Weld characterization.....	49
4.1	Laser beam welding (LBW)	49
4.2	Macroscopic appearance of the weld.....	51
4.3	Microstructural analysis	53
4.3.1	Base material (BM)	53
4.3.2	Fusion zone (FZ)	55
4.3.3	Heat-affected zone (HAZ)	56
4.3.4	Effect of heat treatment on the weld microstructure	57
4.3.5	Thermally simulated material of the weld zone	60
4.4	Hardness	61
4.4.1	Microhardness in the as-welded condition	61
4.4.2	Effect of heat treatment	62
4.5	Residual stresses.....	65
4.5.1	As-welded condition.....	65
4.5.2	Effect of heat-treatment	67
4.6	Tensile tests	67
4.7	Fatigue tests	69
4.8	Fatigue crack propagation (FCP) tests.....	72
4.9	Porosity characterization	74
4.9.1	Spatial and size distributions	74
4.9.2	Effect of process parameters.....	76
5	Methods for improvement of fatigue properties.....	79
5.1	Machining.....	79
5.2	Post-weld heat treatment (PWHT)	82
5.3	Laser surface remelting (LSR)	85

5.4	Laser shock peening (LSP)	86
5.5	Process parameter variation	89
5.6	Conclusions	90
6	Mechanism of internal fatigue failure	93
6.1	Fish-eye fracture of welds	93
6.2	Fish-eye fracture of base material	98
6.3	Generalized scheme of the fish-eye fracture	100
7	Lifetime prediction	103
7.1	Model development	103
7.1.1	Model assumptions	103
7.1.2	Modified fracture-mechanics framework	104
7.1.3	Short cracks model	108
7.1.4	FCP properties derived from S-N data	111
7.2	Application of the model	113
7.2.1	Prediction of fatigue scatter	113
7.2.2	Probabilistic modelling of the initiating pore size distribution	117
7.3	Conclusions	118
8	Summary and outlook	121
8.1	Summary and conclusions	121
8.2	Recommendations for future work	123
	Bibliography	125

List of abbreviations

BCC	Body-Centred Cubic crystal lattice
BM	Base Material
BPP	Beam Parameter Product
CD-function	Cumulative Distribution Function
CFRP	Carbon Fibre Reinforced Polymer
COD	Crack Opening Displacement
DA	Duplex Annealing
DoE	Design of Experiments
EBSD	Electron Back Scatter Diffraction
EBW	Electron Beam Welding
EDX	Energy Dispersive X-ray analysis
ESPI	Electronic Speckle Pattern Interferometry
FA	Full Annealing
FCP	Fatigue Crack Propagation
FOD	Foreign Object Damage
FZ	Fusion Zone
HAZ	Heat-Affected Zone
HCF	High Cycle Fatigue
HCP	Hexagonal Close-Packed crystal lattice
HDM	Hole Drilling Method
HV	Vickers Hardness
IPF	Inverse Pole Figure
LBW	Laser Beam Welding
LEFM	Linear Elastic Fracture Mechanics
LSR	Laser Surface Remelting
mrd	multiple of a random density
ODA	Optically Dark Area
ODF	Orientation Distribution Function
OM	Optical Microscope

PAW	Plasma Arc Welding
PF	Pole Figure
PD-function	Probability Density Function
PWHT	Post-Weld Heat Treatment
RA	Recrystallization Annealing
RD	Rolling Direction of the metal sheet
SEM	Scanning Electron Microscope
SIF	Stress Intensity Factor
SP	Shot Peening
SRA	Stress Relief Annealing
TIG	Tungsten Inert Gas welding
TD	Transverse Direction of the metal sheet
UTS	Ultimate Tensile Strength
WQ	Water Quenching

List of symbols

a	crack length (for internal crack – its radius)
\sqrt{area}	projection area of the internal defect in the Murakami equation
a_i	initial crack length
a_f	final crack length
a_0	El Haddad parameter
a_1, a_2	fit parameters in the extended El Haddad equation
d	pore diameter
da/dN	crack propagation rate
f	Newman's crack-closure function
f_{OD}	probability density of the orientation distribution function
h	pore depth
$p_D(d)$	probability density function of the pore diameter
$p_H(h)$	probability density functions of the pore depth under the surface
$p_N(N)$	probability density function of the fatigue life
$p_{H D}(h d)$	conditional probability density function of H given D
q	notch sensitivity factor
w_0	laser beam waist radius
C, n, p	fit parameters in the crack-growth equation
D	pore diameter as a random variable
E	the Young's modulus
F_{min}, F_{max}	minimum and maximum applied loads, respectively
H	pore depth as a random variable
K_c	fracture toughness
K_f	fatigue notch factor
K_t	elastic stress concentration factor
M^2	beam quality factor
N	fatigue life
N_i	crack initiation phase
N_α	characteristic life of the Weibull distribution

$N_{ODA}, N_{FY}, N_{surf}$	stages of fatigue life: crack growth within ODA, in the fish-eye zone and outside the fish-eye, respectively
R	applied load ratio ($R = F_{min}/F_{max}$), where F_{min} – minimum applied force, F_{max} – maximum applied force.
R_{pl}	reversed plastic zone size at the crack tip
SS_{res}	residual sum of squares
SS_{tot}	total sum of squares
T_S	solidus temperature
$U_{LC}, U_{SC}(a)$	crack-closure ratio for long cracks and short cracks, respectively
Y	boundary correction factor for ΔK calculation
Z_R	Rayleigh length
β	shape parameter of the Weibull distribution function
ε	fracture strain
θ	divergence half-angle of the focused laser beam
λ	laser wavelength
μ, s	mean value and standard deviation of the log-normal distribution
σ	remote applied stress
σ_{max}	maximum stress of the fatigue loading cycle
$\sigma_{0.2}$	the yield strength of the material
σ_w	fatigue limit for $R = -1$ in the Murakami equation
$\Delta\sigma$	applied stress range
$\Delta\sigma_e$	fatigue limit at 10^7 cycles
ΔK	stress intensity factor range
ΔK_{th}	threshold stress intensity factor range
$\Delta K_{th,LC}$	threshold stress intensity factor range for long cracks
ΔK_{eff}	effective stress intensity factor range
$\Delta K_{th,eff}$	intrinsic fatigue-crack propagation threshold
$\Delta K_{th,op}$	extrinsic part of the crack propagation threshold

1 Introduction

1.1 Motivation and research objectives

Commercial aviation has come a long way since the beginning of the jet engine era and its growth is expected to continue. Future traffic volumes and passenger numbers are expected to grow by 4% to 5% per year in the next decades [1]. A steadily increasing demand for air travel expands market opportunities and requires further developments in safety and security. Research and innovation in air transportation systems are the key drivers for tomorrow's mobility as well as the answer to environmental and energy challenges. In view of a greater number of aircraft movements, it is important that travel remains safe, fast, affordable, and environmentally friendly. Aeronautics is recognized as one of the top advanced technology sectors that generates innovative solutions to meet these new challenges.

A renewed Strategic Research and Innovation Agenda (SRIA) has been developed by ACARE (Advisory Council for Aeronautics Research in Europe) to meet the ambitious goals for a sustainable and competitive aviation sector defined by Flightpath 2050 [2]. They include a 75% reduction in CO₂ emission, a 90% reduction in NO_x and 65% in perceived noise by 2050 compared to the 2000 levels. These substantial emission reductions and mobility goals require radically new groundbreaking technologies to be incorporated into novel aircraft configurations. Conventional design and manufacturing concepts currently in use are gradually approaching their intrinsic performance limits. By 2050, around 75% of the world's present fleet will be replaced by aircraft that adopt new technologies [3]. In this context, major developments can be potentially realized in different aircraft systems such as energy efficient engine architectures, new fuselage construction concepts, optimized wing designs, and new flight guidance systems. Therefore, the need today is even greater for industry and research to develop new advanced materials and effective fabrication techniques for more environmentally friendly aircraft to meet market needs.

Advanced fusion and solid-state welding technologies help reduce fabrication costs and minimize the structural weight, thus contributing to overall aircraft efficiency improvement. Laser beam welding (LBW) has become increasingly competitive over the last several decades due to its high productivity, single-step process, and significant practical advantages over the electron beam welding (EBW) because LBW does not need a vacuum environment. Fibre optic delivery systems integrated with modern multi-axial robots enable the welding of complex 3D configurations even on a large scale. Owing to superior technical characteristics compared to conventional fabrication methods, incorporation of automated LBW into the manufacturing chain offers substantial economic benefits without significant losses in structural integrity, as was first demonstrated by the LBW of skin/stringer joints in aluminium fuselage panels of the Airbus A318 aircraft in the early 2000's. Since that time, the new concept of integral laser-welded fuselage shell has become a well-established process for lower fuselage panels in several Airbus aircraft [4]. At the same time, the LBW technique is finding wide and diversified applications in the gas turbine engine sector [5], automotive, and bio-medical industries [6].

A majority of metallic materials can be successfully welded by LBW in different configurations. Most titanium alloys, being highly weldable, are considered as promising candidates for joining by means of laser beam. With its low density (60% that of steel), high strength, and excellent corrosion

resistance, titanium is the material of choice for many key aerospace structural applications including airframes and engines. Initially, the development of titanium processing techniques in the mid 1950's was driven by the extensive use of this material for jet engine applications. The use of titanium as a percentage of engine weight has steadily increased since then, thus contributing to improved engine performance. In airframe structural applications, titanium is utilized to a much lesser extent than aluminium due to the relatively high cost of the raw material and fabrication of parts. However, aluminium cannot be used as a structural material for components subjected to elevated temperatures, if corrosion or weight limitations are primary considerations. Hence, the added cost must be adjusted against the advantage of titanium's superior structural efficiency.

Ti-6Al-4V (ASTM Grade 5) is the most commonly used titanium alloy in the aerospace industry, accounting for about 60% of the total titanium production [7]. This alloy is used almost in all sections of airframes, nacelles, pylons, landing gears etc. In gas turbine engines, Ti-6Al-4V is used for both static and rotating components [5]. Large titanium parts are traditionally manufactured from castings or forgings that are subsequently machined into the final shape [8]. By this, a significant amount of material is milled away, having a negative impact on the overall buy-to-fly ratio. Fabricating these parts by welding, instead of machining, offers several benefits regarding cost and weight reductions. Welding, being a near net-shape technology, can be considered as an alternative to machining or casting. Moreover, a combination of welding and subsequent hot deep drawing enables the manufacturing of parts with complex geometries that cannot be realized by other fabrication techniques [9].

The LBW of the Ti-6Al-4V alloy in butt- and T-joint configurations has been extensively studied over the last few decades and reported by a number of researchers [10, 11]. The industrial application of LBW as a joining technique for titanium components of jet engines has started only recently [12]. It is well known that the weld zones of Ti-6Al-4V exhibit higher tensile strength and lower ductility due to the hardening phenomenon upon fast cooling. This effect provides a shielding effect and protects the weld from fracture under static loading [13]. However, inferior fatigue behaviour of laser-welded titanium joints, considerably lower than that of the base metal, is commonly observed [13]. Since the Ti-6Al-4V alloy is primarily used in fatigue-critical components subjected to cyclic loads, poor fatigue behaviour of laser-welded joints is considered a serious problem limiting their wide industrial application. Inferior fatigue and damage tolerance characteristics of welded Ti-6Al-4V are related to inherent welding-induced defects in the weld zone [9]. This problem is even exacerbated by an increased brittleness of the material after solidification. Thus, several life-limiting factors contribute to fatigue property degradation. In this regard, a greater understanding of the reasons and mechanisms for fatigue failure of the laser-welded Ti-6Al-4V joints is of great importance.

After several catastrophic accidents, fatigue and damage tolerance regulations were introduced in the aircraft industry in the late 1970's [14]. Considering the primary applications of Ti-6Al-4V, high cycle fatigue (HCF) is a major factor that negatively impacts safety and, at the same time, increases maintenance costs [15]. HCF results from vibratory stress cycles induced by various aeromechanical sources. It is a widespread phenomenon in aircraft gas turbine engines that has historically led to numerous premature failures of engine components [16]. Overall, HCF accounts for almost a half of engine-related failures [17]. Thus, design of laser-welded titanium joints in engines as well as airframes requires a thorough quantitative analysis of their HCF properties. Crack initiation and propagation in a weld may, eventually, lead to component failure and result in catastrophic consequences. The present HCF design methodology is highly empirical and relies heavily on the

service experience to establish material allowable safety factors for each type of damage [17, 18]. Designing a component based on such over-conservative empirical guidelines is highly impractical and does not fit with the modern tendency of weight reduction and fuel efficiency. A defect-tolerant approach that considers the physical mechanisms of fatigue failure such as crack initiation and growth in a less empirical manner is needed. Accurate durability and life prediction assessments of welded titanium components in the presence of weld defects subjected to HCF loads are critical.

In addition, mitigation of the fatigue failure risk is crucial to ensure in-service safety and reduce the costs associated with maintenance and replacement. In this regard, potential methods to prolong the service life of laser-welded titanium joints beyond their originally designed lifetime are of paramount significance. Since the traditional procedures to increase the fatigue strength of components are associated with high costs [19], some alternative solutions to effectively extend the fatigue lifetime should be found. For a welded structure, a post-weld treatment technology aiming at fatigue life extension should be applied locally without affecting the overall mechanical properties. Moreover, the effects of fatigue strength improvement should be accounted for in the predictive schemes for lifetime assessment.

It is well known that the surface quality has a primary influence on the crack initiation in the region of high cycles [14]. Fatigue cracks normally start from the surface roughness or other types of stress concentrators. With increasing demands for greater safety, better performance characteristics, and lower production costs, surface finishing technologies to eliminate surface flaws have evolved significantly. Under these circumstances, internal material flaws and inhomogeneities are prone to initiate cracks underneath the surface [20, 21]. Current HCF assessment procedures and design rules pay no attention to internal material defects. Hence, interior-initiated cracks should also be considered in the lifetime prediction models in order to reduce the risk of catastrophic HCF failure of welds.

The present PhD work aims to address the role of various types of welding-induced defects on the HCF performance of laser-welded Ti-6Al-4V butt joints. The main objectives of this study can be summarized as follows:

1. The mechanism of fatigue crack initiation and growth in laser-welded Ti-6Al-4V alloy shall be comprehensively studied with respect to the effects of weld microstructure, surface and internal defects, residual stresses, and loading conditions.
2. The effectiveness of various post-weld processing techniques for fatigue life extension in the HCF regime shall be analysed and quantified. Special focus shall be placed on the laser-based techniques for local surface modification.
3. The model for fatigue life assessment of laser-welded Ti-6Al-4V butt joints shall be developed and validated based on the experimental fatigue data. The model shall consider the physical mechanism of crack initiation from weld defects, account for several types of defects, and reasonably address the fatigue scatter.

The assigned objectives of the work can be regarded as consistent milestones on the way towards the development of a laser-based technology to produce the Ti-6Al-4V joints showing a fatigue strength comparable to that of the base metal. This ambitious and still unsolved problem of any joining procedure will facilitate future applications of advanced laser-assisted manufacturing technologies. This, in turn, will contribute to the fulfilment of the global aims of achieving a sustainable and more environmentally friendly aviation sector.

1.2 General approach

In accordance with the defined objectives of this work, a combination of experimental and theoretical approaches has been adopted. An extensive experimental programme comprising a large number of employed techniques provides the necessary background for a deeper understanding of fatigue failure mechanisms. On the other hand, it results in a set of fundamental material-specific properties required for the development of a fatigue life assessment model. Special attention is paid to guarantee a close symbiotic interrelation between the theoretical and experimental results. A schematic diagram of the main philosophy underlying the entire work is shown in Figure 1.1. The link between the laser beam welding process and the final HCF properties of welds is broken down into three dominant factors – weld defects, microstructure, and residual stresses. Laser welding experiments, followed by fatigue testing and comprehensive analysis of the weld regions, have been carried out to identify the influence of LBW process parameters on the final weld characteristics. At this stage, various types of surface and internal defects as well as conditions responsible for their occurrence were considered with a special caution. Then, five different types of post-weld mechanical and thermal treatments were analysed to determine the optimum technology suitable for fatigue life prolongation in the HCF regime. The underlying reasons contributing to the increase of fatigue strength were carefully characterized by microstructural and fractographic observations. Ultimately, a fatigue life assessment methodology was developed on the basis of fracture mechanics framework. Experimental data obtained prior to the model development have been used to identify the most pragmatic theoretical approach accounting for the physical mechanisms of fatigue crack initiation and growth in a less empirical manner.

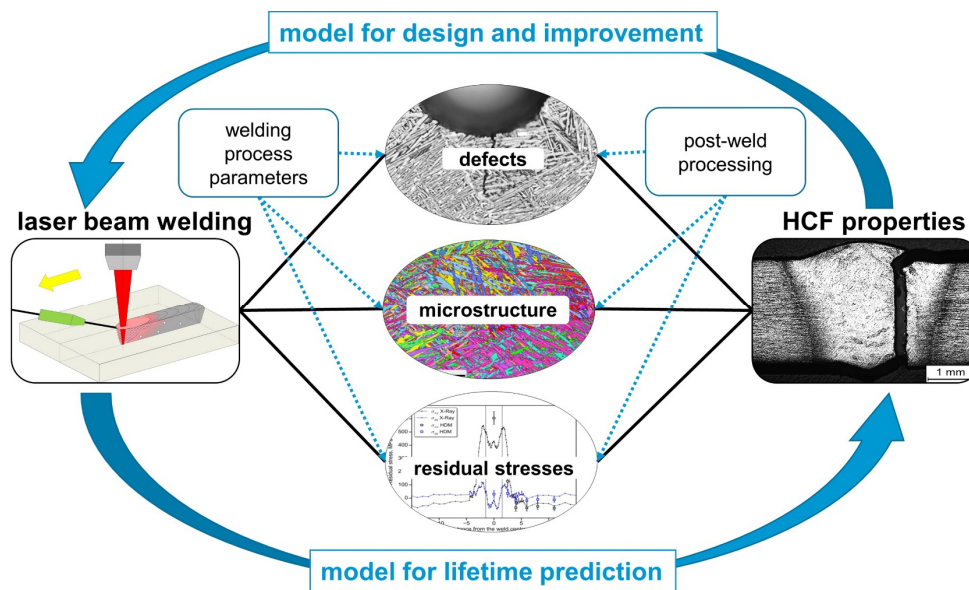


Figure 1.1. General scheme of the approach followed in the PhD work.

Through the realization of the scheduled experimental procedures, the overall approach of this work was slightly modified in accordance with the actual experimental results. At the beginning of the work, internal defects such as porosity were considered unimportant for the weld HCF performance. However, fatigue testing of the joints subjected to post-weld mechanical treatment by means of laser processing revealed a pronounced deteriorative effect of internal pores on fatigue life. Subsequently, a key role of internal defects in the HCF failure was realized and incorporated into the assessment

model being developed. These findings helped reduce the number of input factors and concentrate the model predictions on internal defects, thus making the assessment procedure less complicated and easier to implement in engineering applications.

1.3 Thesis layout

To present the experimental and modelling results in a consistent way conforming to the global scientific approach, this thesis is organized in the following chapters:

Chapter 2: State of the Art. This chapter presents an extensive literature review on several relevant topics related to the subject of the thesis. In the first part, Ti-6Al-4V alloy and its basic physical and mechanical properties are summarized. Then, the most common types of fusion welding suitable for titanium alloys are described and compared with laser welding. Fatigue properties of Ti-6Al-4V are analysed with respect to microstructure and surface conditions. Particular attention is paid to the existing methods for fatigue life extension and their efficiency. Finally, the modern approaches used for lifetime prediction in the HCF regime are presented.

Chapter 3: Methodology. This chapter gives a brief overview of the experimental procedures as well as the theoretical concepts applied in the present work. The first part describes the experimental details of laser processing techniques and procedures for weld examination. This is followed by the types of mechanical testing strategies, specimen geometry, and loading conditions. The second part of this chapter introduces some important concepts of fracture mechanics and models used in common practice and adopted in this study. The last part presents some statistical tools required for the characterization of fatigue scatter.

Chapter 4: Weld characterization. The experimental results are structured to give a complete picture of the weld quality and the most important characteristics. First, the weld microstructure and microhardness distribution are correlated to show the effect of microstructural transformations on the local strength in the weld zone. Besides the fatigue testing, tensile and crack propagation tests have been carried out to identify a full spectrum of weld mechanical properties. The distribution of residual stresses in the proximity to the weld is measured by two different techniques. The number and severity of surface and internal weld defects are analysed and correlated with the LBW process parameters. Particular focus has been put on the experimental determination of the pore distribution by the X-ray analysis of the welding seam.

Chapter 5: Methods for fatigue properties improvement. This chapter presents five different post-weld treatment procedures aiming at the fatigue life extension. The improvement potential of conventional machining and post-weld heat treatment is compared with laser-based processing techniques. A novel procedure of laser remelting is proposed to reduce the stress concentration of surface defects. The effect of near-surface residual stresses induced by laser shock peening (LSP) on fatigue crack initiation and growth is studied. Finally, it is shown how the adjustment of welding parameters can minimize the internal defects in laser-welded Ti-6Al-4V butt joints. The conclusions on the most effective and promising techniques enabling the maximum fatigue strength are drawn.

Chapter 6: Mechanism of internal fatigue failure. This chapter acts as a gradual transition from the experimental part to the modelling chapter. A thorough fractographic analysis of the fatigued specimens after HCF failure is used to quantitatively describe the stages of fatigue

crack growth. It is demonstrated that porosity governs the fatigue behaviour of surface-treated weldments. Moreover, fatigue testing and subsequent fracture surface examination of the unwelded base material show that interior crack initiation is a common attribute of HCF failure even in the absence of internal weld defects. Microstructural features are correlated with the crack initiation sites and a generalized scheme of interior-initiated fatigue failure is developed.

Chapter 7: Lifetime prediction. This chapter presents an adopted fracture mechanics framework applied to develop a fatigue life estimation model for laser-welded Ti-6Al-4V accounting for internal crack initiation. The first part describes the modifications of existing approaches employed to describe the behaviour of internal short cracks in the weld zone of Ti-6Al-4V. Then, the model is validated with the experimental fatigue data and applied to predict the fatigue scatter range. The distribution of pores is statistically analysed and integrated into the model to evaluate the HCF failure probability.

Chapter 8. Summary and outlook. The last chapter summarizes the most prominent results and conclusions of this work in relation to the initial research objectives. An agreement between the modelling and experiments is evaluated and discussed. Recommendations for future research are finally given.

2 State of the art

2.1 Titanium and its alloys

2.1.1 Applications

Outstanding basic characteristics and superior structural efficiency of titanium alloys make them attractive for a variety of applications in airframes (due to high strength, low density), gas turbine engines (due to high strength, good creep resistance), biomedical and chemical industry (due to corrosion resistance). The high costs associated with titanium usage still restrict the wider use of its alloys in other industrial sectors. Approximately 10% of the Boeing 777 airframe weight is titanium, whereas the total use of titanium in the Airbus aircraft family is between 4–5% [22]. The weight share of titanium in modern gas turbine engines is about 25–30% [8, 23], being applied mainly for disks and airfoils in the fan and compressor sections [5, 22]. The usage of titanium in offshore structures and shipbuilding has become more common in recent years due to its high corrosion and fatigue resistance in the seawater.

The demand for titanium usage has boomed in the past few decades. It has been driven mainly by its current largest consumer: the aerospace sector. Considering the wider use of carbon fibre reinforced polymers (CFRP) in the aircraft industry, metallic/composite interfaces are becoming increasingly common [7]. From this perspective, the use of titanium alloys helps minimize the risk of galvanic corrosion with carbon fibres that is a common problem for aluminium alloys. So, the amount of titanium used in the A350XWB aircraft manufactured by Airbus, where a large amount of CFRP is used, has grown by more than a factor of two compared to the conventional aircraft with aluminium fuselage [24]. Similarly, titanium usage in the Boeing 787 aircraft, which is roughly 50% composite by weight, has reached the highest percentage (about 20%) of any commercial aircraft in history [22].

The high price of titanium primarily stems from the high reactivity of this metal with atmospheric gases. Thus, the use of inert atmosphere or vacuum is required during the production of titanium ingots. Additional major cost drivers are high energy needs and the initial high cost of the raw materials [25]. On the other hand, high reactivity with oxygen leads to the formation of a stable oxide layer when exposed to air, thus resulting in superior corrosion resistance. Owing to enhanced oxidation and creep processes, the maximum service temperature for titanium alloys is limited to approximately 600°C. Above this temperature, activated diffusion processes generate a brittle oxygen-rich surface layer or a so-called α case, which negatively affects the mechanical properties.

2.1.2 Basic properties

Pure titanium undergoes an allotropic phase transformation at 882°C changing from a body-centred cubic (BCC) β phase at higher temperatures to a hexagonal close-packed (HCP) crystal structure or α phase at lower temperatures. The transformation temperature and kinetics are strongly dependent on the alloying elements and the purity of the metal. The unit crystal cells of the α and β phases with corresponding lattice parameters are shown in Figure 2.1(a, b). The three most densely packed lattice planes of the α phase are basal planes (0002), one of the three prismatic planes $\{10\bar{1}0\}$ and one of the six pyramidal planes $\{10\bar{1}1\}$. Figure 2.1(b) also indicates the family of the most densely packed $\{110\}$ lattice planes in the BCC β phase. The α phase content in Ti-6Al-4V at room temperature is normally around 90–95% [26]. Therefore, the α phase properties govern the overall characteristics of

the Ti-6Al-4V alloy. The inherent anisotropic nature of the HCP crystal structure of the α phase has important consequences for the elastic mechanical properties of titanium alloys. It was reported that, depending on the stress direction, the modulus of elasticity E of pure α titanium crystal varies between 145 GPa (stress is parallel to the c -axis in Figure 2.1(a)) and 100 GPa (stress is perpendicular to the c -axis in Figure 2.1(a)) [27]. Elastic properties of the polycrystalline α titanium rely on the nature and intensity of crystallographic texture. Therefore, a strong texture after the rolling process results in a pronounced anisotropy of mechanical properties in different sheet directions.

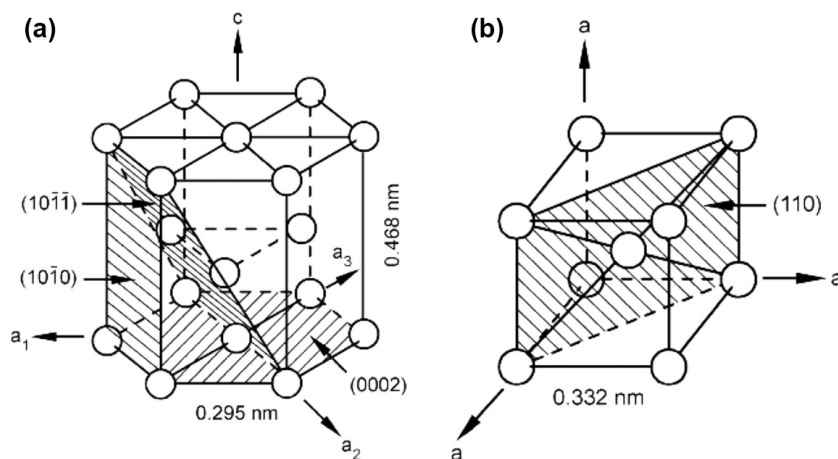


Figure 2.1. Unit cells with corresponding densely packed lattice planes: (a) HCP α phase; (b) BCC β phase (reprinted from [22] by permission of Springer Nature).

Alloying elements in titanium are usually classified into α - or β -stabilizing additions, depending on whether they increase or decrease the $\alpha \rightarrow \beta$ transition temperature. Aluminium, oxygen, and nitrogen are all strong α stabilizers and increase the β transition temperature. It is important to note that, with an increasing aluminium content, a brittle intermetallic Ti_3Al (α_2) phase can be formed in titanium alloys. According to the binary Ti-Al phase diagram, coherent Ti_3Al precipitates start to form in the α phase at about 5–7% aluminium content [22]. The β -stabilizing elements can be divided into β isomorphous and β eutectoid forming elements, depending on the resulting binary phase diagram. The most widely used β isomorphous alloying elements are vanadium (V), molybdenum (Mo) and niobium (Nb). Certain concentrations of these elements make it possible to stabilize the β phase even at room temperature.

Commercial titanium alloys are classified into three categories – α , $\alpha+\beta$ and β alloys – according to their position in the β isomorphous pseudo-binary diagram and the phase content at room temperature (see Figure 2.2(a)). The group of α alloys consists of various grades of commercially pure titanium containing only small amounts of β phase (less than 5%). These alloys do not show any response on the application of heat treatment and are, therefore, highly weldable. The group of $\alpha+\beta$ alloys has a range from the $\alpha/\alpha+\beta$ phase boundary up to the intersection of the martensitic line M_s with a horizontal axis representing the room temperature. Thus, $\alpha+\beta$ alloys transform martensitically upon fast cooling rates from the β phase field. This group of titanium alloys is dominated by the most widely used Ti-6Al-4V titanium alloy, which is in the focus of this work. Microstructures of $\alpha+\beta$ alloys are generally described by the size and arrangement of the constituent α and β phases. Metastable β alloys are located in the equilibrium $\alpha+\beta$ phase region of the phase diagram shown in Figure 2.2(a) beyond the M_s line. Stable β alloys do not exist as commercial materials. One of the important features of the β alloys is that they do not undergo martensitic transformation at high cooling rates. In general,

commercial β titanium alloys have lower modulus of elasticity E than α and $\alpha+\beta$ alloys. Typical values are in the range 70–100 GPa [28].

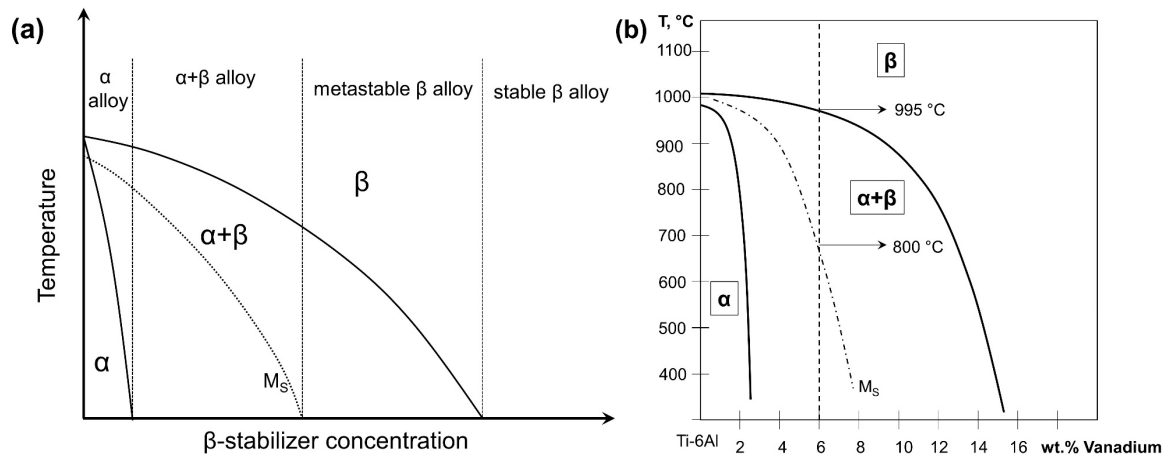


Figure 2.2. (a) Classification of titanium alloys according to the pseudo-binary section of a β isomorphous phase diagram (depicted and adopted according to [25]); (b) position of Ti-6Al-4V on the phase diagram of the Ti-6Al – V system (depicted and adopted according to [28]).

2.1.3 Ti-6Al-4V alloy

Ti-6Al-4V (Grade 5 by the ASTM classification) alloy was initially developed in the 1950's and first used for compressor blades in gas turbine engines [28]. Today, the wrought Ti-6Al-4V is a 'workhorse' $\alpha+\beta$ alloy and is used extensively in manufacturing gas turbine engines and airframes. The aerospace industry accounts for more than 80% of the entire Ti-6Al-4V alloy usage [28]. In addition, it is a useful material for surgical implants because of its relatively low modulus of elasticity, and good tensile and fatigue strength. Mechanical properties of Ti-6Al-4V are very sensitive to the microstructure and, in many cases, also to the crystallographic texture of the hexagonal α phase. The correlation between the microstructure and mechanical properties is, therefore, decisive for its effective application.

Being an $\alpha+\beta$ alloy, Ti-6Al-4V may have different volume fractions of the α and β phases, depending on the heat treatment and precise interstitial content. Figure 2.2(b) illustrates the Ti-6Al – V phase diagram with the corresponding phase regions and transformations. In the Ti-6Al-4V titanium alloy, the $\beta \rightarrow \alpha$ transition temperature might be slightly altered by the presence of alloying elements and impurities [29]. Moreover, the temperature range for the transformation depends on the cooling rate and gradually moves towards a lower temperature with an increasing cooling rate. It was reported that Ti-6Al-4V could be treated as an alloy with a $\beta \rightarrow \beta+\alpha$ equilibrium transus temperature of around $995 \pm 20^\circ\text{C}$, as schematically shown in Figure 2.2(b). However, martensitic transformation upon fast cooling starts at temperatures below 800°C (see M_s line in Figure 2.2(b)). Ti-6Al-4V can acquire a large variety of microstructures, depending on the thermomechanical treatment and processing history. This variety of morphologies can be roughly classified into three distinct categories: lamellar, equiaxed, and a mixture of both (bi-modal microstructure). Typical micrographs of the most common microstructural types are shown in Figure 2.3(a–e).

Lamellar microstructures can be obtained by the recrystallization heat treatment in the β phase field, i.e. the heat treatment temperature should be higher than 1000°C . The most important parameter in the processing route is the cooling rate, which determines the α colony size and the thickness of

individual α plates. In this regard, the $\beta \rightarrow \alpha$ transition can be categorized by three basic mechanisms, depending on the cooling rate from the β -phase field and the alloy composition: diffusional transformation [30], displacive (martensitic) transformation [29, 31], and massive transformation [32]. Slow cooling into the two-phase $\alpha + \beta$ region from above the β transus leads to diffusion-controlled nucleation and growth of the α phase in the plate form, starting from the β grain boundaries (see Figure 2.3(a)). The resulting lamellar microstructure is characterized by a coarse and plate-like appearance.

If the cooling rate is sufficiently high, the $\beta \rightarrow \alpha$ transformation occurs through a displacive or martensitic mechanism without activating the diffusion processes. Martensitic reaction takes place at cooling rates above some critical cooling rate that can be achieved by quenching. Water quenching of the Ti-6Al-4V alloy from the β phase field results in a very fine needle-like HCP α' martensite (see Figure 2.3(b)). Martensitic transformation is diffusionless in nature and involves a cooperative movement of atoms through a shear type process. At intermediate cooling rates, massive transformation can occur by nucleation and short-range diffusion jumps across the massive/matrix interface. Martensitic and massive transformations are both initiated and completed without any change in the composition between the parent and the product phases. Very often, a careful consideration of the constituent morphology and crystallography is needed to differentiate the martensite from the massive products.

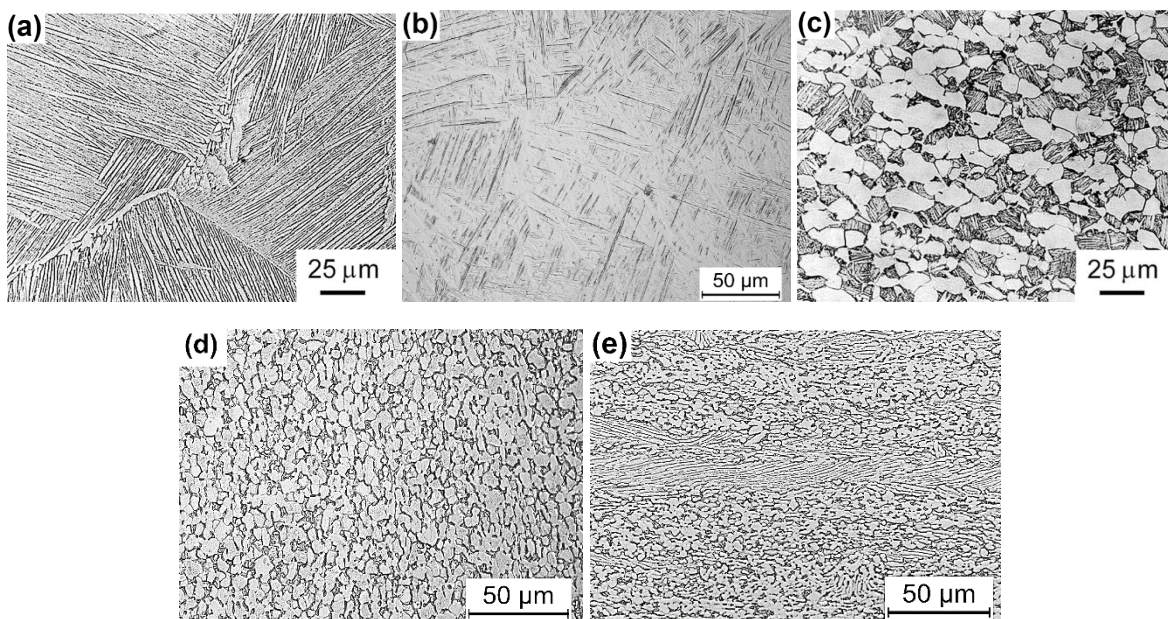


Figure 2.3. Microstructure types of Ti-6Al-4V alloy: (a) coarse lamellar (β -annealed) microstructure (reprinted from [33] by permission of Elsevier); (b) fully martensitic microstructure (reprinted from [34] under CC BY 4.0); (c) bi-modal (duplex) microstructure (reprinted from [33] by permission of Elsevier); (d) equiaxed microstructure (reprinted from [34] under CC BY 4.0); (e) mill-annealed microstructure.

In the Ti-6Al-4V alloy, the products of diffusionless martensitic transformation have a unique acicular morphology. The acicular martensite comprises an intimate mixture of individual α' plates, each having a different variant of the Burgers relationship. Generally, martensitic plates contain a high dislocation density and sometimes twins [22]. Ahmed and Rack investigated the effect of different cooling rates on microstructural transformations in the Ti-6Al-4V alloy [35]. They reported that cooling rates above 410 K/s were required to achieve a fully martensitic microstructure. A massive transformation was observed in their work at cooling rates between 410 and 20 K/s. The massive

mechanism was gradually replaced by the diffusion-controlled Widmanstätten α formation at cooling rates lower than 20 K/s. In their investigation, Ahmed and Rack found that, at cooling rates lower than 410 K/s, a grain boundary α morphology was formed upon cooling. Thus, some remnant α phases between the β grain boundaries acts as an indicator of fully martensitic transformation.

A bi-modal (duplex) type of microstructure consists of isolated primary α grains in a transformed β matrix, as demonstrated in Figure 2.3(c). The processing route to obtain this microstructure includes a hot working in the $\alpha+\beta$ phase field, recrystallization, and the final aging [26]. By controlling the cooling rates, the volume fraction and size of equiaxed α grains can be altered. If the cooling rate from recrystallization annealing is sufficiently low, only the globular α grains will grow, resulting in a fully equiaxed structure, as shown in Figure 2.3(d). A relatively straightforward, but less defined, processing route leads to a mill-annealed type of microstructure, which is very common nowadays. In this case, the recrystallization step is completely omitted and the cooling after hot deformation determines the resulting morphology, which normally has some remnants of deformed lamellar zones in the globular matrix. An example of a typical mill-annealed microstructure for the as-received Ti-6Al-4V sheet is shown in Figure 2.3(e).

2.2 Fusion welding techniques

Fusion welding is the most commonly used joining method for metallic materials and structures. It involves local melting and resolidification of the base metal to form a sound joint. The part of the joint that is melted is known as the fusion zone (FZ). Industrial applications of welding are nowadays of extreme importance. Many large-scale engineering structures such as bridges, ships or airplanes could not have been designed and fabricated without various types of fusion welding. Very often, the application of welding provides numerous structural design options that cannot be realized with other production techniques. Laser welding, which is in the focus of this research, belongs to the fusion welding processes and, therefore, has some inherent characteristics attributed to this type of welding. This section gives a brief overview of some important properties of fusion welding and describes the most widespread welding methods used for joining titanium alloys.

Most α and $\alpha+\beta$ titanium alloys can be welded by a wide variety of conventional fusion and solid-state processes [36]. Fusion welding of titanium is performed principally either by inert-gas-shielded arc or by the high intensity beam welding methods. In general, metal weldability is determined by the capability of the alloy to produce a weld that is free of discontinuities or defects. Owing to a single-phase mode of solidification, the Ti-6Al-4V welds are not susceptible to many of the weld solidification cracking problems that cause troubles with aluminium and ferrous alloys. Nevertheless, owing to some specific requirements with regard to gas shielding, some engineers still believe that titanium is difficult to weld. Indeed, enhanced embrittlement through air contamination is the biggest threat to successful welding; however, if the weld area is thoroughly cleaned and inert gas shielding is provided, titanium welding is relatively easy to implement. Contamination due to inadequate inert gas shielding is the most frequent defect in titanium welds of all types. Visual post-weld inspection based on colour changes correlating with oxide thickness can be used for a qualitative evaluation of the shielding efficiency.

The weldability of an alloy also depends on its ability to produce a joint that exhibits acceptable mechanical properties. On this criterion, the weldability of structural titanium alloys depends primarily on the application of suitable post-weld heat treatment (PWHT). As in the case of any other

metal, subsequent heat treatments for titanium welds are usually performed to reduce the tensile residual stresses formed in the weld zone. PWHT can be performed in a vacuum or argon atmosphere to prevent the above-mentioned formation of the α case layer. Heat treatment in the air is also possible, but the oxidized surface should be removed by grinding or pickling afterwards.

The mechanical properties of welded titanium structures depend on the microstructural characteristics of each weld region, which, in turn, rely on the specific thermal cycles imposed during welding and subsequent heat treatment. As mentioned in the previous section, the characteristics of the $\beta \rightarrow \alpha$ transformed products depend primarily on the cooling rate from above the β transus temperature. According to the published literature, the key microstructural features of the Ti-6Al-4V alloy resulting from the welding process are the prior β grain sizes in the FZ and the products of $\beta \rightarrow \alpha$ transformation during cooling to room temperature [25, 28]. Regardless of the welding type, the FZ in Ti-6Al-4V is normally characterized by coarse columnar prior β grains that epitaxially grow from the fusion line in the direction opposite to the heat flux [22]. The size and morphology of these grains depend on the weld energy input, with higher energies promoting larger grain sizes [28]. Thus, welding creates a microstructural and mechanical mismatch between the weld and base metal. The weld mismatch is of great concern especially with regard to fatigue behaviour.

2.2.1 Keyhole mode vs. conduction mode

All fusion welding processes use any type of heat source to melt a small volume of material that subsequently solidifies to form a weld joint. In this regard, numerous welding procedures are distinguished from each other by the heat generation method. However, regardless of the heat source and the weld type, two fundamental weld modes can be distinguished on the basis of the weld pool shape and the resulting weld seam geometry characteristics. The weld mode classification corresponds to the applied power density magnitude in a heat source at the weld surface. These two basic modes of welding are conduction welding and keyhole or penetration welding, as illustrated schematically in Figure 2.4(a, b). For simplicity, the laser beam is shown as a heat source.

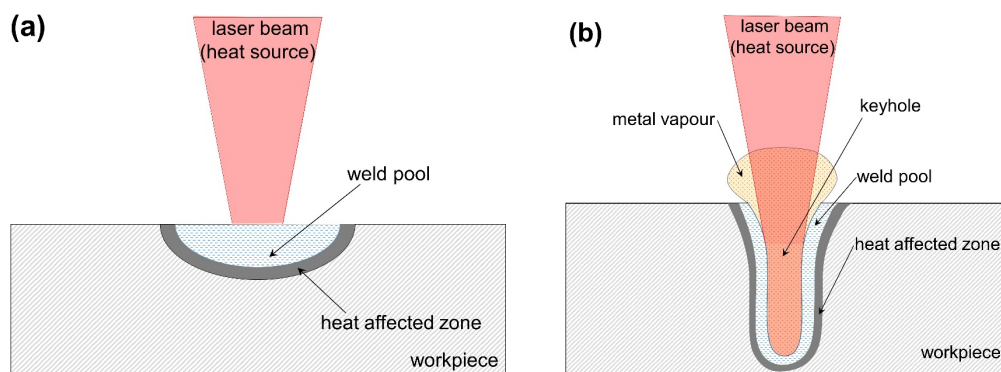


Figure 2.4. Two fundamental welding modes: (a) conduction mode; (b) keyhole mode.

The essential difference between these two welding modes is that the surface of the weld pool remains in its original state during conduction welding and opens up to allow the heat source to enter the melt pool in the keyhole mode. Conduction welding corresponds to relatively low power densities typically below 0.5 MW/cm^2 [6], depending on the processed material. Therefore, the produced weld seam has a wide and shallow shape (see Figure 2.4(a)). The heat is completely absorbed by the workpiece surface and then transferred by the conduction mechanism. The conduction mode offers less perturbation because the heat source (laser or electron beam) does not penetrate the material. The

weld produced in this mode are less susceptible to gas entrapment during welding. The main disadvantage of conduction welding is that the maximum plate thickness that can be welded is limited and depends on the applied power and the heat source. Additionally, high heat input normally attributed to a large heat source results in high residual stresses and distortion.

With an increasing power density of up to 1.0–1.5 MW/cm² [6], a small channel filled with vaporized material or a so-called keyhole is initiated and penetrates the material (Figure 2.4(b)). The vapour pressure from the keyhole walls supported by the heat source ensures keyhole stability and prevents the collapse of the molten material. The keyhole provides a direct delivery of the heat flux into the bulk of the material and maximizes the weld depth. This helps minimize the heat input and the heat-affected zone (HAZ) size. The resulting welds are, therefore, deep and narrow in shape. It should be mentioned that, in this work, welding has been performed primarily in the keyhole mode.

2.2.2 Tungsten inert gas (TIG) welding

Tungsten inert gas (TIG) welding, also known as gas tungsten arc welding (GTAW), is nowadays the most widely applied joining process for titanium alloys including Ti-6Al-4V. An electric arc between the non-consumable tungsten alloy electrode and a workpiece provides the fusion of the joint region, while an inert gas flow protects the electrode and molten pool from atmospheric contamination. A schematic illustration of the TIG process is shown in Figure 2.5(a). Argon or helium normally plays a role of the shielding gas protecting the weld zone. Welds can be made autogenously (without filler material) or with the addition of a compatible filler wire. The TIG welding is the only process that is routinely used at present for circumferential welds of titanium alloys [22]. Its main drawbacks are low productivity, high heat input, and tungsten inclusions in the weld pool. TIG welding is typically performed in conduction mode unless additional measures are undertaken to increase the penetration.

Poor weld metal ductility of TIG welded Ti-6Al-4V is normally observed and attributed to a large prior β grain size stemming from high heat input [36]. Several researchers reported that the FZ microstructure of TIG-welded joints consists of a lamellar α phase with some amounts of the α' martensitic phase [37, 38]. Grain boundary α phase and small amounts of retained β phase might be also present [39]. For arc welding processes such as TIG, cooling rates between 10 to 150 K/s have been usually observed, which can produce a microstructure with a combination of martensitic α' , massive α and diffusional α [40]. According to the results obtained by Ahmed and Rack [35], this cooling rate is not sufficient to achieve a complete martensitic transformation. A typical cross section of the weld FZ performed by TIG welding is shown in Figure 2.5(b). The FZ hardness and tensile strength are typically higher than those of the base material. It was shown that PWHT at 900°C leads to the coarsening of the α phase and can increase the FZ ductility; however, it is accompanied by a commensurate reduction in joint strength [39]. An opportunity to refine the FZ microstructure by changing the weld-pool solidification conditions is offered by the pulsed-current TIG welding. Weld current pulsing results in a slight refinement of prior β grains, leading to a greater hardness, tensile strength, and ductility of Ti-6Al-4V weldments [39].

Plasma arc welding (PAW) can be considered as a type of TIG welding [36]. It retains the high quality associated with TIG welding while having a higher penetration and welding speed. The heat is transferred by an arc generated between a tungsten electrode and either the workpiece or the water-cooled nozzle. A copper tube restricts the arc from expansion to form a collimated arc coming out as a flame. A plasma gas flows through the copper nozzle to produce the characteristic plasma jet. In the conduction-limited mode, a weld pool is similar to that produced by TIG welding, whereas the plasma

jet fully penetrates the joint in the keyhole mode [22]. PAW offers significant productivity gains over TIG welding, especially when operated in the keyhole mode.

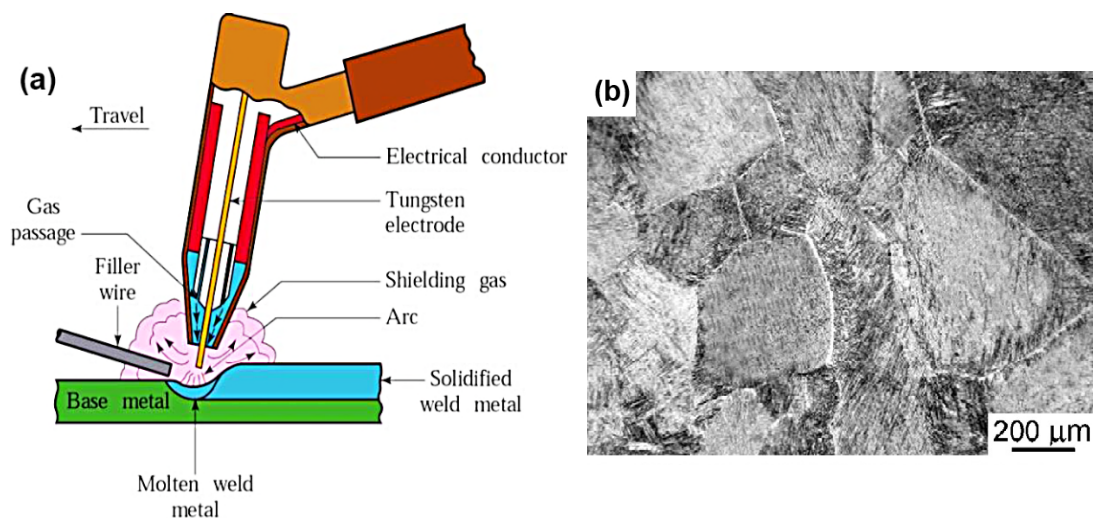


Figure 2.5. (a) Schematic view of the TIG welding (reprinted from [41] under CC BY); (b) lamellar FZ microstructure of the TIG welded Ti-6Al-4V alloy (reprinted from [39] by permission of Elsevier).

2.2.3 Electron beam welding (EBW)

Electron beam welding (EBW) involves the melting of the metals to be joined by the impingement of a focused beam of high-energy electrons. It has traditionally been the preferred process for making critical high-quality welds with low distortion and high reliability in the aerospace industry [36]. Owing to the high intensity of an electron beam, heavy sections can be welded in the keyhole mode in a single pass. The advantages of EBW include high depth of penetration, a narrow heat-affected zone, and low distortion. Conventional EBW is performed in a vacuum of about 10^{-2} Pa [42]. Therefore, a vacuum chamber and a pumping system are required. The latter adds to the significant capital costs of the equipment, especially for large components. A further disadvantage relates to the time needed to achieve a vacuum, thus reducing the overall productivity. In this context, the recently developed electron beam welding facilities operating at atmospheric pressure partly eliminates the inherent costs and productivity problems related to conventional in-vacuum EBW [36].

The basic principle of EBW is illustrated schematically in Figure 2.6(a). The EBW process is performed in a vacuum chamber having a controlled atmosphere. A thermal emission mechanism from a tungsten filament generates free electrons, which are then accelerated by a high voltage between the anode and cathode to achieve a kinetic energy required for welding. At high vacuum, electrons are accelerated by a voltage of about 150 kV and their speed reaches $2 \cdot 10^8$ m/s, which is around two-thirds the speed of light [42]. The electron beam is focused on a small spot by magnetic and electrostatic lenses. When the high-energy electron beam impacts on the metal surface, the kinetic energy of electrons is transformed into heat, leading to a rapid temperature increase. When the beam is focused on a spot size of around 1.0 mm in diameter, a power density is sufficient to activate a keyhole mode that enables deeper and narrower welds. This opens an opportunity to produce a thick weld in a single pass, thus eliminating the need for multi-pass welding needed for conventional TIG or PAW techniques. Numerous works have been devoted to parametric optimization of the EBW process of Ti-6Al-4V for a desired penetration depth, FZ shape, and the weld quality [43, 44, 45]. Since the welding is performed in a vacuum environment, low weld contamination is usually

observed. Nevertheless, internal porosity has been frequently reported to be found in electron beam weldments [46, 47]. Figure 2.6(b) shows a deep penetration single-pass weld of a 50-mm-thick Ti-6Al-4V performed by EBW [48].

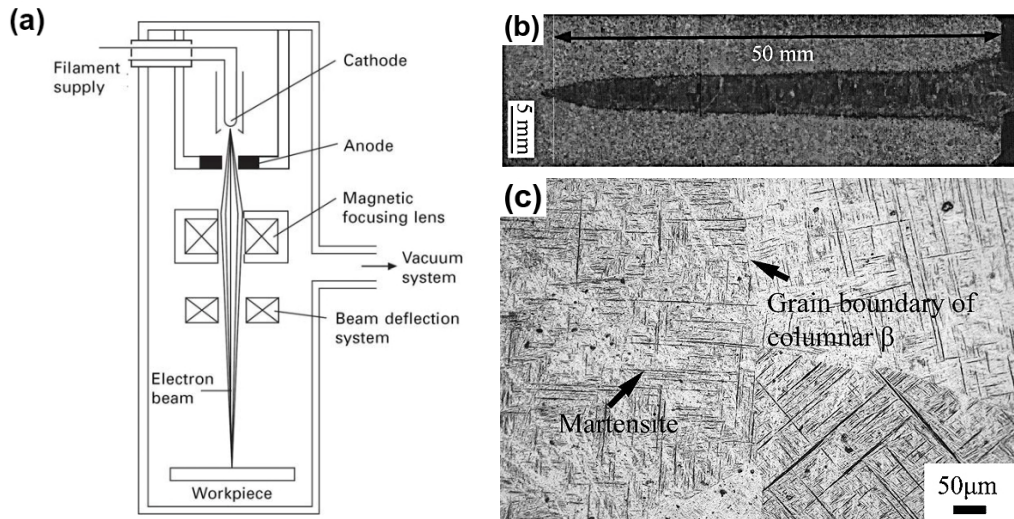


Figure 2.6. (a) Basic principle of EBW in a vacuum chamber (reprinted from [42] by permission of Elsevier); (b) macrograph of a single-pass weld produced by EBW (reprinted from [48] under CC BY-NC-ND); (c) martensitic microstructure of the FZ (reprinted from [49] under CC BY).

EBW is a promising method for joining high strength titanium alloys. The phase transformations and microstructural evolution of the Ti-6Al-4V alloy during EBW are known to be relatively complex, particularly in the FZ. Microstructural analysis of the FZ indicates that the FZ mainly consists of the α' martensitic phase, which greatly contributes to the mechanical properties of welded joints [50]. Figure 2.6(c) shows a fully martensitic morphology of the weld FZ obtained by EBW [49]. Mechanical properties of the EBW joints correlate with microstructural features. The weld tensile strength nearly equals that of the base metal, and fracture under static loading normally occurs outside of the weld [51]. Some authors studied the effect of heat treatment on the mechanical properties of EBW weldments [52, 53]. Tsai et al. pointed out that the subsequent heat treatment at 790°C can provide the weldment a superior combination of tensile properties and elongation [53]. In general, high penetration and low distortion promote the current extensive use of EBW to join thick-section titanium gas turbine engine parts including compressor discs and compressor rotor shafts [42].

2.2.4 Laser beam welding (LBW)

LBW is finding increasing application as a joining process for a titanium sheet and plate. In laser welding, the workpiece is melted by the impingement of a high-intensity coherent beam of light, as shown in Figure 2.7(a). The LBW process offers low distortion, high productivity, and is potentially more flexible for automated welding than TIG welding. The LBW process has some practical advantages over conventional EBW because the LBW application is not restricted by the requirements of high vacuum. Furthermore, the modern high-energy, solid-state lasers offer superior process flexibility due to the possibility of using fibre optic delivery systems. Laser welding is usually done using a local inert gas shielding to prevent weld contamination. From the standpoint of plate thickness to be welded, LBW is generally more limited compared to EBW. However, with the recently developed high-energy, single-mode fibre lasers, the weld depth is comparable to that produced by electron beam. Considering the similarities of the heat sources, metallurgical and

mechanical properties of the welds performed by EBW and LBW are close to each other [36]. Depending on the laser power and the focusing parameters, LBW can be performed either in the conduction mode at relatively low power densities or in the keyhole mode (see Figure 2.4). In welding applications, the most commonly used laser types are CO₂ gas lasers, solid state Nd:YAG lasers, and the recently emerged high-power fibre lasers. Since the availability of high-energy lasers with a good beam quality is relatively new, there have been only few opportunities until now to introduce the LBW process for joining large structures. One of the most prominent examples is the welding of skin/stringer aluminium joints in lower fuselage sections of Airbus A318, A340 and A380 aircraft as a replacement for the mechanically stiffened panels [54].

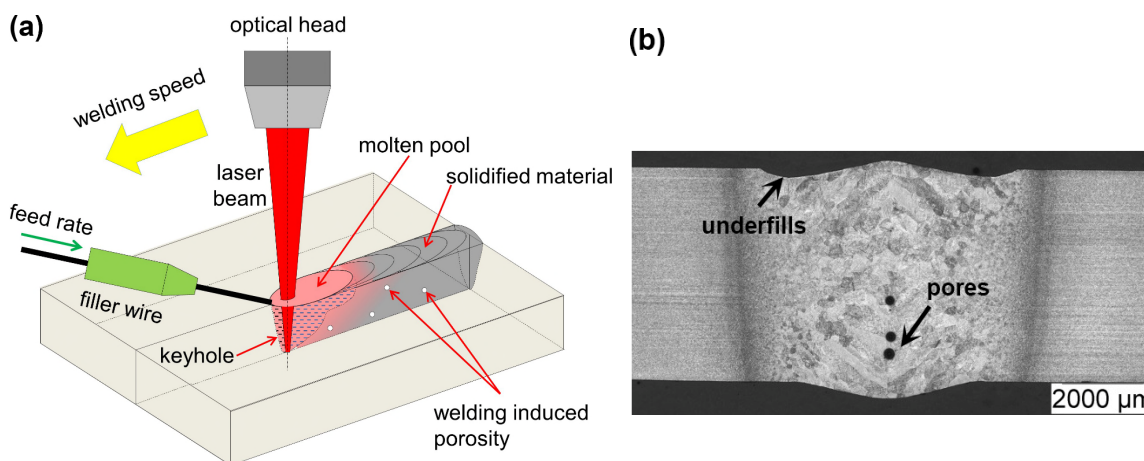


Figure 2.7. (a) General scheme of the LBW technique; (b) cross section of the Ti-6Al-4V weld seam obtained with the Nd:YAG laser (depicted and adopted according to [55]).

Wirdelius et al. reported the industrial application of the LBW-joining technique for thin titanium components of jet engines [12]. Recently, the European project DELASTI (Horizon 2020 Program) has been successfully accomplished, in which the laser welding of dissimilar titanium T-joints for the vertical stabilizer of Airbus A380 has been developed [34, 56]. There have been a number of comparative studies of laser welding in relation to other welding methods suitable for the Ti-6Al-4V alloy [37, 40]. Generally, the LBW method offers a high weld quality and a welding speed comparable to those of EBW [22]. Specific applications may identify the particular strengths and weaknesses of each welding type. Similar to EBW, high cooling rates between 100 to 1000 K/s during the laser welding promote the martensitic $\beta \rightarrow \alpha'$ transformation in the FZ (see Figure 2.7(b)). In contrast, a mixture of the coarser Widmanstätten microstructure with some of the martensitic phase is usually formed at the lower cooling rates associated with TIG or PAW welding. This results in a higher ductility and lower strength of TIG welds compared to the fully martensitic structure after EBW or LBW [57]. Gao et al. compared the effect of the Nd:YAG laser welding and the TIG welding of a thin Ti-6Al-4V plate [37]. They found that the FZ width and the overall residual distortion of the joints welded by TIG were significantly greater than that of the laser-welded joints.

In recent years, there has been a remarkably growing interest in the laser welding of Ti-6Al-4V. Numerous studies have examined how filler materials [11, 58], shielding gas [59, 60], surface preparation [61], and welding parameters [10, 13] are correlated with the weld microstructure and mechanical properties. As discussed in Section 2.1.3, the mechanical properties of the Ti-6Al-4V alloy are significantly affected by the microstructure and the phase content. Previous studies have shown that the LBW process parameters must be carefully optimized to produce a joint with good-

quality [11, 13]. Akman et al. described the microstructure of Ti-6Al-4V welds obtained with the Nd:YAG laser as acicular martensite within large columnar prior β grains [60]. Similar microstructures have been reported for welds obtained with a high-power CO₂ laser [57, 62] and with a fibre laser [10, 63]. This extremely fine acicular morphology exhibits high strength and hardness but relatively low ductility [11, 13]. It has to be noted that most research works focus primarily on the static strength of laser-welded Ti-6Al-4V. Only few researchers addressed the fatigue properties of the laser-welded Ti-6Al-4V [9, 13].

The most frequently observed defects in laser weldments of titanium alloys are underfills and porosity [55, 64]. A typical weld cross section with these defects is shown in Figure 2.7(b). The weld imperfections are particularly undesirable for structures subjected to cyclic loading because they lead to stress concentration and, consequently, premature crack formation. The evaporation and/or expulsion of the molten material from the weld pool and liquid metal flow around the keyhole are dominant processes affecting the formation of underfills [13, 65], which are always present in the case of autogenous laser welding. The inherent spherical shape of most pores observed in laser-welded Ti-6Al-4V indicates a gas-type porosity. A number of researchers have investigated the main causes of porosity formation during laser welding of titanium alloys [59, 65]. Potential sources are related to the keyhole instability leading to the entrapment of shielding gases and the presence of excessive hydrogen in the FZ, which is rejected upon solidification. A parametric study on the influence of welding parameters on the amount of porosity in the laser beam welded Ti-6Al-4V butt joints was qualitatively studied by several researchers [10, 11]. Employing a vacuum environment in the laser-welding process can reduce the problem of porosity in titanium alloys [60].

Post-weld heat treatment is applied to relieve residual stresses, stabilize and homogenize the weld zone microstructure and to improve ductility. Some aspects of the heat treatment effect on the laser welded Ti-6Al-4V have been studied in the work of Cao et al. [66] and Kabir et al. [67]. It has been observed that at temperatures above 700–800°C, the martensitic α' phase decomposes into equilibrium $\alpha+\beta$ with subsequent microstructure coarsening. The weld ductility and fracture toughness were reported to increase with increasing heat treatment temperatures. However, there is still no clear consensus about the influence of PWHT on the weld fatigue performance especially in the HCF regime.

2.3 Fatigue behaviour of Ti-6Al-4V

2.3.1 Basic concepts of fatigue

The term ‘material fatigue’ relates to the progressive deterioration of the material strength during service such that failure can occur at much lower stress and load levels than the original ultimate load level. Since the early studies on metal fatigue conducted by A. Wöhler in the late 19th century, the S-N diagram or a Wöhler curve, which shows a number of cycles to failure N as a function of the applied alternating stress $\Delta\sigma$, has been the basis of design against fatigue failure. A typical shape of the S-N curve in a semi-logarithmic scale ($\Delta\sigma$ vs. $\log(N)$) is illustrated in Figure 2.8. According to the number of endured load cycles, three distinct fatigue regimes can be distinguished, namely the low cycle fatigue (LCF) up to 10^4 – 10^5 cycles, high cycle fatigue (HCF) up to 10^7 cycles and very high cycle fatigue (VHCF) beyond 10^7 cycles. In the majority of cases, the S-N curve is assumed to have a horizontal asymptote or a so-called ‘knee point’ located approximately between 10^6 and 10^7 load cycles. The stress level corresponding to this knee point is generally considered as the ‘fatigue

limit' or 'endurance limit' of a material. Steels, in particular, are considered to possess a well-defined fatigue limit corresponding to a threshold stress amplitude, below which fatigue life is believed to be infinite [68]. Non-ferrous alloys, including titanium alloys, typically do not exhibit any pronounced knee point and the S-N curve usually decreases gradually with an increasing number of load cycles.

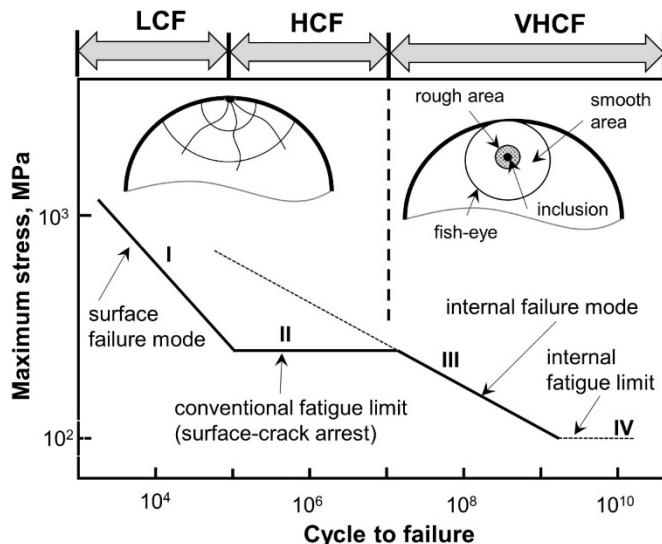


Figure 2.8. Schematic illustration of the basic fatigue regimes and the concept of fatigue limit.

An assumption of the existence of a horizontal asymptote in the range of 10^6 – 10^7 cycles is, in fact, a convenient and economically justified approximation with the aim to reduce the experiment time and is not a rigorous approach. Over the last several decades, numerous fatigue studies on different metallic materials have indicated that fatigue failure can occur in the life regime exceeding 10^7 cycles and at stress amplitudes below the conventional fatigue limit [69, 70]. It implies that there is a further gradual decrease of the S-N curve in the region of very high cycles ($N = 10^7$ – 10^9 cycles), as shown in Figure 2.8. These findings suggest that the endurance limits determined by the conventional fatigue tests cannot provide the safety design data of a component over a very long period. Therefore, fatigue properties in the VHCF regime ($N > 10^7$ cycles) tends to be an important subject in the structural design to ensure long-term safety. In this work, fatigue testing and assessment is conducted up to the conventional fatigue limit at 10^7 cycles. Nevertheless, very important correlations between the present thesis and the topic of VHCF can be found, as identified in the following sections.

The recent studies and available experiment data in the VHCF regime [69, 71] indicate that the well-established current definition of 'fatigue limit', i.e. the critical stress below which the fatigue cracks do not initiate and a component has an infinite fatigue life, should be revised. A correct and reasonable definition of the fatigue limit should consider the recent findings in the field, especially for a further decrease of the S-N curve. Extensive research on the VHCF of high-strength steels carried out by Murakami and co-workers revealed that arrested and non-propagating fatigue cracks are normally present in the specimens tested at the fatigue limit of stress [68]. These findings imply that the condition of crack arrest determines the abrupt change in the slope of the S-N curve. According to Murakami et al., the fatigue limit, in a narrower sense, is the threshold stress for crack propagation and not the critical stress for crack initiation as considered previously [68]. Hereinafter, this particular definition of fatigue limit will be used. In other words, even after testing at the fatigue limit of stress, some micro-cracks might be found in the material; however, the stress level is not sufficient for their further growth and they become arrested [71].

2.3.2 Fatigue behaviour of Ti-6Al-4V base metal

This section provides a brief overview on the effect of fatigue regime, microstructure, stress ratio, and environment on the fatigue behaviour of Ti-6Al-4V base material. The microstructure types have a significant influence on the fatigue strength, in particular on the HCF properties [72]. Wu et al. reported a thorough analysis of these effects on the basis of a systematic analysis of data collected from available sources of the 1972 to 2013 period [72]. However, a special attention must be paid to the specimen preparation conditions and the experimental set-up while comparing the results of fatigue testing from different available sources.

As discussed in Section 2.1.1, Ti-6Al-4V is widely used as a structural material in gas turbine engines. Analysis of published data indicates that fatigue failure of titanium engine components can be correlated with its usage and location in the engine [15, 16]. As shown in Figure 2.9, HCF is the predominant failure mode for titanium parts, with fretting fatigue, LCF, and foreign object damage (FOD) being significant contributors. Nearly 90% of the occurrence has been identified in the fan and compressor (titanium blades, vanes, rotor discs etc.) [16]. These data emphasize the importance of the HCF regime analysis for the Ti-6Al-4V titanium alloy.

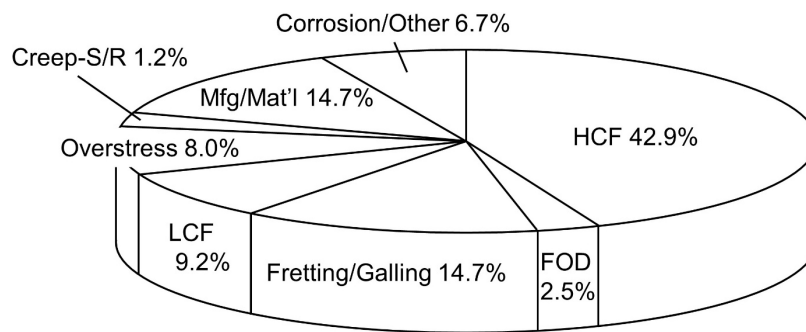


Figure 2.9. Historical distress modes of titanium engine components according to Pratt & Whitney report (depicted and adopted according to [16]).

According to Lütjering, the most influential microstructural parameter on the mechanical properties of lamellar Ti-6Al-4V microstructures is the α colony size, which is controlled by the cooling rate from above the β transus temperature [26]. The α colony size determines the effective slip length in lamellar microstructures because the colony of parallel α plates with almost equal crystallographic orientation (see Figure 2.3(a)) acts as one large grain, and a slip can be easily transferred through the entire colony. As discussed in Section 2.1.3, cooling rates have a big influence on the resulting configuration of the α plates and their colonies. With an increasing cooling rate, the α colony size decreases with a commensurate reduction of effective slip length. This yields a corresponding increase in the yield strength and hardness. A drastic increase in yield strength is observed when the colony structure is changed to a martensitic morphology, in which the colony size is equal to the width of orthogonally oriented individual α plates. The latter is clearly visible in Figure 2.6(c), which shows the martensitic microstructure in the FZ of the EBW joint [53]. With increasing cooling rates, ductility slightly increases at first and then declines. Very high cooling rates, promoting the martensitic transformation, result in relatively low ductility with fracture strain in the range of 4–6% for Ti-6Al-4V [22].

HCF properties are normally attributed to the material resistance against self-initiated microcrack nucleation and growth. It was reported that the dependence of HCF strength dependence on the slip

length and the α colony size is qualitatively similar to that of the yield strength described above [22]. Figure 2.10(a) shows the HCF strength at 10^7 cycles for lamellar microstructure as a function of the cooling rate from the β phase field. The ratio of fatigue limit at $R = -1$ to the yield strength is typically around 0.5 for Ti-6Al-4V. However, it can be as low as 0.45 for very coarse microstructures and as high as 0.6 for very fine-grained microstructures. In lamellar microstructures, fatigue cracks usually nucleate at the longest and widest α plates [72].

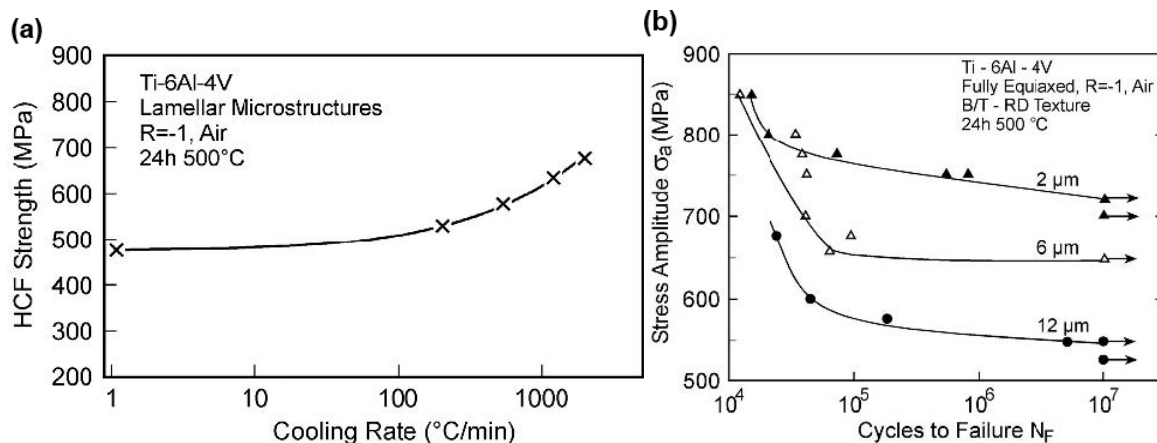


Figure 2.10. (a) Dependence of the HCF strength on cooling rate from the β phase field (reprinted from [22] by permission of Springer Nature); (b) effect of α grain size on the HCF fatigue properties of fully equiaxed microstructures (reprinted from [22] by permission of Springer Nature).

Fatigue behaviour of fully equiaxed microstructures of Ti-6Al-4V alloy is primarily influenced by the α grain size because it determines the effective slip length. As shown in Figure 2.10(b), relatively high fatigue limits can be achieved by the grain refinement. Additionally, very small α grain size results in considerably high magnitudes of ductility. Comparing fully equiaxed and fully lamellar microstructures with equivalent effective slip lengths, the HCF strength values of fully equiaxed microstructures are higher [22].

The effect of crystallographic texture on mechanical properties including fatigue behaviour can be quite pronounced for a fully equiaxed microstructure. A material with a T-type texture, i.e. the basal planes are oriented predominantly in the transverse sheet direction, exhibits a lower fatigue strength than that of a material with a B/T-type of texture (the basal planes are oriented both in the transverse and normal directions of a sheet). Furthermore, anisotropic fatigue properties in different sheet directions have been found for each type of texture [73]. The above-mentioned deviations are enhanced if fatigue testing is performed in a vacuum [22].

The effect of the stress ratio R on the fatigue limit was evaluated by Morrisey et al. [74]. From their work, it can be concluded that the fatigue limit of Ti-6Al-4V (in terms of stress range) decreases with an increase in the stress ratio. The authors have shown that the HCF properties of Ti-6Al-4V alloy exhibit an anomalous mean stress dependency. At high stress ratios, Ti-6Al-4V undergoes a change in the fracture mode to a ductile failure similar to conventional tensile test. Additionally, environmental conditions might have an impact on the fatigue behaviour. Peters et al. [73] have shown large decreases in the fatigue strength of Ti-6Al-4V in air when compared with that in vacuum. In their work, the fatigue life in air was comparable to fatigue life observed in the 3.5% NaCl solution. The fatigue damage and the environmental effect were explained as the result of hydrogen

embrittlement. Finally, it should be noted that surface roughness and near-surface residual stresses can affect the fatigue limit of Ti-6Al-4V considerably [75].

2.3.3 Fatigue of Ti-6Al-4V welds

Welded joints are particularly vulnerable to fatigue damage under cyclic loading. The fatigue strength of welded structures is normally lower than that of unwelded components [76]. In the overall structure, the welds can be therefore considered as the weakest spots regarding the fatigue properties. Nowadays, welded joints are used widely for components under primarily static loading and rarely for fatigue-critical parts. A typical example illustrating this tendency is related to the application of laser welding for 6xxx aluminium alloys in the fuselage panels of several Airbus aircraft. The new concept of welded fuselage panels resulted in a significant manufacturing cost reduction and weight savings compared to conventional riveting techniques [4]. However, the implementation of LBW was restricted to the lower fuselage panels, where the loading conditions are less demanding and only compressive stresses prevail. The welded integral structures have less crack arrest capability than mechanically fastened components and are less reliable from the fatigue perspective. Thus, the introduction of laser welding has thrown up new aspects that have to be taken into account from the damage-tolerance perspective.

Ti-6Al-4V, as a high-strength structural titanium alloy, is often selected as the material for fatigue-critical parts operating in the LCF and HCF. As discussed in the previous section, the Ti-6Al-4V base metal offers superior fatigue and damage tolerance characteristics, if the microstructure and surface conditions are properly designed. However, the application of laser welding or other types of fusion welding has a pronounced detrimental effect on the fatigue performance, thus overriding the characteristic benefits of the base metal [28]. In spite of extensive research carried out in the field of laser welding of Ti-6Al-4V over the past decades, the majority of the works deal with static mechanical properties and only a few researchers analysed a poor HCF behaviour of Ti-6Al-4V after application of laser welding [9, 13]. In this context, better understanding of fatigue failure phenomenon of the LBW Ti-6Al-4V joints is of paramount importance.

In the absence of weld defects and discontinuities, the generally higher yield and tensile strengths of the weld zone versus the mill-annealed base material promote equivalent axial fatigue properties of transverse weld-oriented specimens [28]. In practice, lower axial fatigue properties are commonly observed, particularly in welds made with high energy density [77, 78]. This behaviour is attributed to the presence of undercuts (underfills) or other types of defects that are inevitably generated by fusion welding [28]. Inferior fatigue properties restrict the application of welded titanium joints to many structural components subjected to cyclic loads in operation. The presence of a brittle martensitic structure and residual stresses can further promote the early fatigue crack initiation and a very short fatigue life. The martensitic microstructure, typical for high depth-to-width ratio electron beam and laser welds, is characterized by a toughness values below those of the mill-annealed base metal [36]. This additionally lowers the fatigue strength due to a higher notch sensitivity of the martensitic phase.

Regardless of the welding technique applied, fatigue cracks initiate from the weld defects such as weld toes, underfills etc. All these defects act as stress raisers and degrade the fatigue properties. Squillace et al. have analysed the influence of LBW parameters on the microstructure and mechanical properties of Ti-6Al-4V butt joints [13]. The authors observed that the fatigue life in the as-welded condition was strongly influenced by the value of underfill radius that causes stress concentration at

the weld toe. The magnitude of the stress concentration, in turn, depends on the sharpness of the underfill. The S-N curve tends to move towards a higher number of cycles as the underfill radius increases. This implies that the partial or total elimination of the underfills might improve the weld fatigue strength. In their work, fatigue cracks always started at the lower points of the underfill convexity at the interface between the FZ and HAZ. Kashaev et al. have also reported inferior fatigue properties of the laser-welded Ti-6Al-4V butt joints compared to those of the BM and the similar crack initiation mechanism at the weld toes [9]. A comprehensive literature analysis showed that most of the published works consider only surface defects in the laser-welded titanium joints [13, 79]. There is lack of understanding about how other types of defects, such as internal porosity, affect fatigue performance. Moreover, conditions responsible for the crack origin shift from one type of defect to another are still not clear.

2.3.4 Internal crack initiation

The mechanism of fatigue crack initiation depends on the competition among different defect types. In spite of a general agreement that fatigue failure is a surface phenomenon, numerous researchers have identified internal fatigue origins during the fatigue testing of Ti-6Al-4V and some other titanium alloys [80, 81]. Since titanium is a material characterized by a relatively high level of cleanliness, it is unlikely that non-metallic inclusions or interstitial contamination could be the cause of internal origins as is usually observed in steels. Summarizing the published data on this topic, it can be concluded that interior crack initiation in Ti-6Al-4V can be observed either on pre-existing metallurgical defects [82] induced during manufacturing or microstructural inhomogeneities in the clean material [20].

Early studies on the internal crack initiation sites in titanium alloys have been reported in the mid-1970's. Neal et al. studied the environmental effect on the HCF behaviour of Ti-6Al-4V and found that internal fatigue origins occur below the knee of the S-N curve, i.e. in the region of 10^7 – 10^8 cycles [80]. Analysis of the fatigue crack origins indicated that their incidence was independent of the environment. The cleavage of α grains or groups of grains was responsible for fatigue crack nucleation in their work. Later works demonstrated that fatigue crack initiation in titanium alloys could occur internally in the HCF and VHCF regimes, similar to the so-called “fish-eye” failure of high strength steels in the VHCF region [68]. The initiation area of internally fractured Ti-6Al-4V normally reveals faceted features with a cleavage-like appearance, as shown in Figure 2.11(a–c). The fish-eye fatigue failure of the Ti-6Al-4V alloy in the region of very high cycles ($N > 10^7$ cycles) has been extensively studied in the past few years [20, 21]. VHCF of titanium alloys as well as other structural metallic materials is drawing increased attention because many structural components nowadays operate well beyond 10^7 cycles (car engines, railway axles, gearboxes, etc.). Therefore, the topic of internal crack initiation, even in the absence of internal defects, is of great relevance.

There is still some ambiguity with regard to the formation mechanism of α facets usually found at the internal crack nucleation sites. Pilchak et al. argued that many load cycles contribute to the gradual growth of a facet – i.e. no cleavage mechanism is involved [83]. In contrast, Liu et al. investigated the mechanism of faceted crack initiation in Ti-6Al-4V and concluded that α facets are initiated in the early stages of the lifetime by the cleavage of isolated α grains [20]. In addition, the authors showed that there is a strong relationship between the multi-site faceted crack origins and the microstructure. Despite this disagreement, it is generally accepted that the inherent anisotropic nature of the α phase leads to localized internal stress concentration, which, in turn, depends on the local

misorientation of the neighbouring grains. In other words, depending on the grain crystal orientation that determines the elastic modulus, there are hard and soft grains. As a result, the dislocation slip is facilitated in the soft grains, and the piling up of dislocations at the grain boundaries leads to a cleavage of hard grains [80]. From this perspective, the average α grain size is very important for fatigue properties and increasing the α grain size generally causes a decrease in the fatigue life [84].

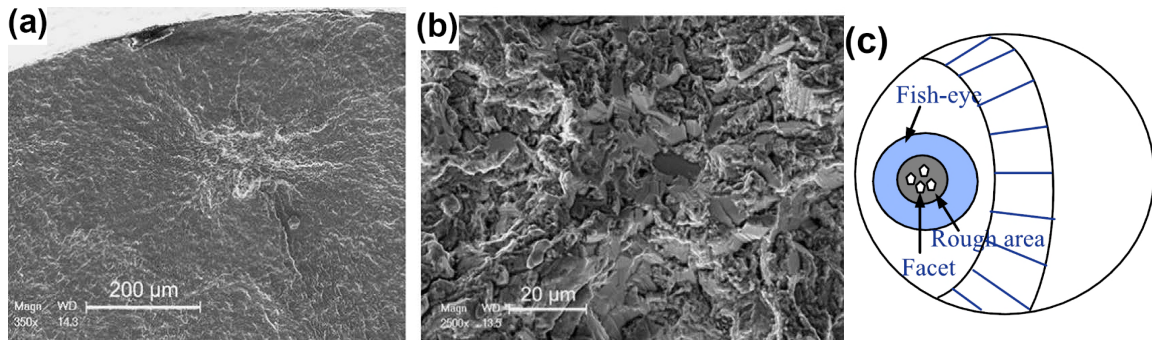


Figure 2.11. Fracture surface appearance after internal crack initiation of Ti-6Al-4V. (a) Low magnification image; (b) crack initiation site with a number of faceted features under higher magnification; (c) schematic presentation of the internal fish-eye fracture. The images are reprinted from [85] by permission of Elsevier.

Interior-initiated fish-eye fatigue failures have also been observed in Ti-6Al-4V alloy fabricated by some advanced powder-based manufacturing processes such as powder metallurgy [86] and additive manufacturing [82]. Voids or cavities are inevitably generated in the components produced by any type of additive manufacturing because of their layered structure. These internal discontinuities were reported to have a strong impact on fatigue properties. Under these circumstances, fatigue cracks are prone to emanate from internal cavities or pores, thus resulting in the fish-eye fatigue failure mode similar to that illustrated in Figure 2.11(a) [82]. The presence of internal defects or voids acting as crack initiators leads to a much earlier transition of the crack origin from surface to interior. In titanium components produced by powder metallurgy, a shift to subsurface occurs after around 10^6 cycles [86], while in wrought titanium alloys it occurs in the VHCF regime, i.e. at approximately 10^7 cycles. The mechanism of crack origin transition is still not well understood, and further research should explain this behaviour. It should be noted that there is almost no published data on the internal fatigue origins in the laser-welded Ti-6Al-4V alloy. Apparently, the as-welded condition is normally tested, and internal weld defects such as pores are less detrimental than surface stress concentrators such as underfills or weld toes. Nevertheless, it is shown in Chapter 5 that, under some circumstances, fatigue cracks in laser-welded Ti-6Al-4V consistently initiate at interior weld defects. Thus, the topic of internal crack nucleation and growth is of great importance in this work.

Transition to the subsurface crack initiation in the case of clean material without any internal defects may happen earlier in the fatigue life if compressive residual stresses are generated in the subsurface layer. It was reported that conventional shot peening treatment could promote the interior-initiated fatigue cracks and fish eye formation starting from around 10^6 load cycles [87], i.e. in the HCF regime. Hence, it is always a combination of several factors including the stress level, material cleanliness, defects as well as surface finishing procedures that determine whether fatigue crack will initiate underneath the surface.

2.4 Lifetime extension methods

As discussed in Section 2.3.3, the application of LBW for joining of Ti-6Al-4V has a strong detrimental effect on fatigue properties. The poor HCF performance of laser-welded butt joints is considered a serious problem that reduces the safety of a welded structure. In this regard, various improvement methods aimed at prolonging the weld lifetime are required. This section briefly summarizes the most widely used techniques for fatigue life extension that can be potentially applied as post-weld processing techniques for the Ti-6Al-4V alloy.

Mechanical surface treatments such as polishing, shot peening (SP), roller-burnishing, and deep-rolling are often applied on high-strength titanium alloys to improve their fatigue performance [19, 88]. These processes induce plastic deformation in the near-surface regions, thus resulting in work-hardening. In addition, compressive residual stresses are generated in the surface layer due to the localized plastic deformation. The effect of different mechanical treatments on the fatigue behaviour of Ti-6Al-4V with lamellar microstructure is shown in Figure 2.12. The fatigue performance of a component after a mechanical surface treatment depends in a complex way on the final surface layer characteristics. Wagner compared the effect of different surface treatments on the fatigue behaviour of Ti-6Al-4V with equiaxed and lamellar microstructures [19]. A combination of three main parameters – surface roughness, dislocation density and residual stresses – determines the influence of mechanical treatment on fatigue properties. SP results in high compressive residual stresses on the surface layer having a depth of about 200 μm ; however, this effect is accompanied by a roughness value much greater than that after roller-burnishing or deep-rolling [19].

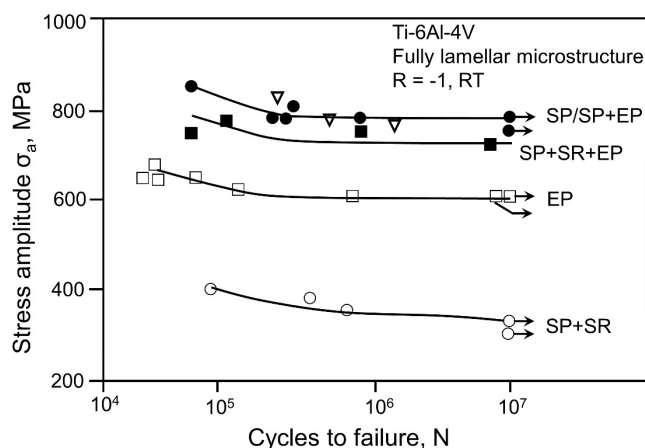


Figure 2.12. Effect of various types of mechanical treatment on the fatigue performance of Ti-6Al-4V (depicted and adopted according to [19]). Abbreviations: SP–shot peening, EP–electro-polishing, SR–stress relief.

Subsequent mechanical polishing or electro-polishing (EP) can mitigate the negative effect of SP on the surface quality. The profiles of dislocation density and residual stress are not affected by this removal of material. Wagner has shown that heat treatment at 600°C for 1 hour is sufficient for complete stress relief, whereas a significant decrease in the shot-peening-induced dislocation density occurs at temperatures only above 650°C [19]. Thus, a suitable heat treatment can separate the effect of residual stresses from that of the high dislocation density (work hardening). The results demonstrated that SP improves the fatigue performance by two mechanisms: retardation of micro-crack growth by residual stresses and an increase of the crack nucleation period in the work-hardened surface layer. Leverant et al. pointed out that fatigue life improvement after SP mainly stems from the prolongation of the crack propagation rather than the nucleation life [88]. It is worth mentioning

that a shift in crack nucleation site from surface to subsurface regions in mechanically surface-treated specimens was frequently observed [19, 87, 88].

The application of SP as a post-weld mechanical treatment of Ti-6Al-4V TIG welds was studied by Berge [89]. Most of the specimens in their work failed in the weld zone. Residual stresses resulting from peening caused the crack initiation at internal defects, generally of a sub-millimetre size. It was shown that internal pores cannot be avoided in TIG welds and are the governing factor for fatigue strength. So, compressive residual stresses can suppress the surface crack initiation in welds and have a positive effect on fatigue properties.

Titanium alloys with shot-peened compressive residual stresses at the surface of components have been extensively used in the aerospace industry since the 1970's [90]. Starting from the early 2000's, an alternative method for generating compressive residual stresses, namely laser shock peening (LSP), has been investigated as a potential substitution for a conventional SP process. Nowadays, LSP is a commercially available process to induce deep residual stresses up to millimetre depths. In this technique, the workpiece surface is treated by a high-energy laser beam with a very short pulse duration to produce compressive residual stresses in the material surface layer. The shock wave is generated via the direct ablation of a coating or ablative tape applied to the surface of the workpiece as shown in Figure 2.13(a). A transparent water layer that suppresses the plasma expansion and ensures momentum transfer considerably enhances the process efficiency. Very high strain rates encountered during the LSP process activate different deformation mechanisms to what is conventionally observed during SP [90]. On comparing with traditional SP, a major advantage of LSP that emerges is its ability to generate residual stresses significantly deeper under the metal surface, while keeping the surface roughness almost unchanged [91]. The latter is demonstrated by the in-depth profiles of residual stresses in Figure 2.13(b).

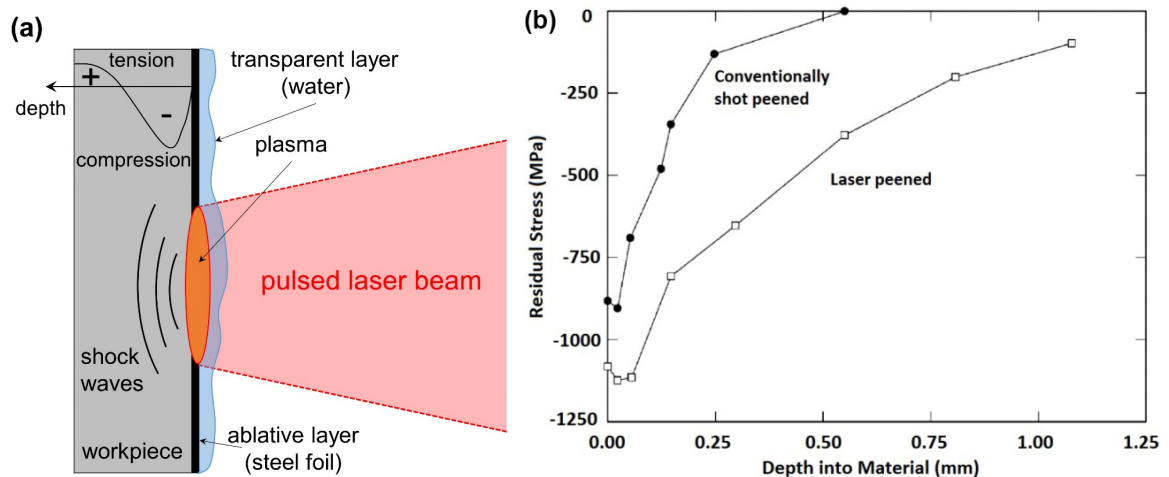


Figure 2.13. (a) Schematic view of the LSP process; (b) comparison of residual stress profiles in Inconel 718 induced by LSP and conventional SP (reprinted from [91] under CC BY).

Extensive research has been done to verify the effect of LSP-induced residual stresses on the fatigue properties of aluminium and titanium alloys. The results of previous studies clearly indicate the beneficial effect of LSP treatment in enhancing the HCF resistance of Ti-6Al-4V [92, 93]. Zhang et al. demonstrated that fatigue strength at $2 \cdot 10^6$ cycles of unnotched Ti-6Al-4V with a bi-modal microstructure can be increased by approximately 40% compared to the as-received condition [93]. According to their results, Figure 2.14 illustrates that the fatigue strength increases with an increasing

number of overlapped spots. The authors pointed out that the specimen is subjected to ablation if the absorbing layer is damaged during LSP, leading to a microstructural degradation and decrement of fatigue life. A few researchers have addressed the influence of LSP on the fatigue properties of fusion welded Ti-6Al-4V. Cao et al. reported that the application of LSP treatment on the laser-welded Ti-6Al-4V has a 50% positive effect on the LCF properties [94]. However, this effect was validated only at one stress level without considering the statistical aspects and fatigue scatter. There is still lack of understanding on how the LSP treatment affects the HCF properties of the laser-welded Ti-6Al-4V alloy. In this regard, the results presented in Chapter 5 fill this gap and provide a comprehensive analysis of various techniques to extend fatigue life in the HCF regime.

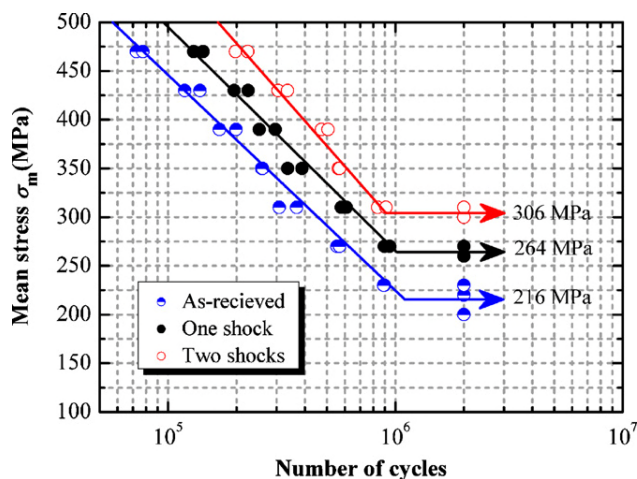


Figure 2.14. Fatigue lives of laser-peened and as-received Ti-6Al-4V specimens at different applied stress levels ($R = 0.3$) (reprinted from [93] by permission of Elsevier).

The LSP process parameters can be thoroughly adjusted and controlled in real time to account for local material properties and component configuration. By this, a tailored structure, with a desired distribution of stiffened regions in the fatigue-critical positions, can be developed. In contrast to traditional shot peening, LSP has a minimal effect on the surface roughness and is an entirely mechanical process. Thus, almost no thermal effect or microstructural changes are observed. The aerospace industry is currently leading the integration of LSP into the manufacturing process (turbine blades, rotor components, disks, gear shafts) [17].

It must be noted that the testing temperature and applied stress level might influence the LSP-induced residual stresses. For instance, Nalla et al. studied a detrimental effect of elevated temperatures on the fatigue response of LSP-treated specimens [92]. A major conclusion from their work is that the beneficial effect is still evident, although reduced, at temperatures as high as 450°C. Cyclic loading at high temperature leads to an almost complete relaxation of the surface compressive residual stresses. It implies that the benefit of surface treatments at higher temperatures is associated primarily with the induced work-hardened near-surface layer suppressing both the crack initiation and initial crack growth.

2.5 Fatigue life assessment

Prediction of a component fatigue life relies on several factors that determine a potentially applicable approach. First, a fatigue failure mode with regard to the number of cycles has to be anticipated. LCF, HCF, and VHCF regimes require considerably different concepts and assumptions for the assessment

of the life span. As mentioned in Section 2.3.2, HCF is the predominant failure mode for titanium alloys used in the aerospace industry, and particularly in the gas turbine engine sector. Therefore, the focus of this thesis is on the HCF fracture of Ti-6Al-4V and the lifetime assessment will be analysed with an emphasis on this particular regime. With extensive use of titanium in fatigue-critical components, accurate durability and life prediction assessment are essential. Development of improved methods for lifetime assessment could reduce the risk of the catastrophic HCF fatigue failure. This appreciably increases the overall service safety and reduces the maintenance costs.

The need for accurate HCF predictions has been felt quite recently. The current assessment approaches are largely empirical and the inherent probabilistic aspects of damage occurrence are overtaken by large safety factors. The latter, in turn, leads to lower allowable stresses and heavier components. A lot of research, primarily stimulated by the engine community, has been conducted over the past few decades. The lack of HCF durability prediction models for titanium was emphasized by Cowles, based on extensive experience with the application of titanium in engine components acquired at Pratt & Whitney [16]. Cowles reported that the most promising future HCF assessment approach is likely to be a hybrid of crack initiation methods combined with fracture mechanics and damage tolerance methods. It was also emphasized that, from a life prediction standpoint, the most threatening defect types for current titanium alloys are internal defects such as hard α grains and porosity [16]. The prediction of HCF failure from internally embedded defects is much more challenging and should include the tools for probabilistic damage tolerance assessment.

Prediction of the fatigue life of a welded joint is even a more problematic task because of the interaction between the numerous factors such as weld defects, microstructural changes, residual stresses, mechanical mismatch etc. A comprehensive description of the fatigue behaviour of welds can be found in the books of Maddox [76] and Schijve [14]. A relatively straightforward and practical approach for the prediction of the fatigue life of welded joints is based on the design codes, where the fatigue life estimate depends on the joint classification [76, 95]. However, these codes have been elaborated for various structural steels and aluminium alloys. In addition, they do not include some recently emerged types of welding, such as laser welding. Thus, the study of durability assessment models of laser-welded titanium alloys is a quite new topic and is of great relevance from the scientific and industrial viewpoints.

Numerous researchers attempted to develop a HCF assessment model for metallic materials and joints. The applied fracture mechanics concepts are usually not material-specific and can be therefore adopted with minor modifications for other materials and configurations. Since the amount of literature is vast, this section reviews only a few existing models for the lifetime assessment in the HCF regime with a particular focus on the influence of internal defects and the fish-eye failure because internal defects play a key role in the HCF fracture of laser-welded Ti-6Al-4V, as shown in Chapter 6. Therefore, conceptual similarities to the current work can be found in the studies dealing not only with welding but also with components in which internal material flaws might initiate fatigue cracks.

In recent years, an increasing amount of research has been done to explain the failure mechanism of high-strength steels in the very high cycle fatigue (VHCF) regime. It was reported that fatigue failures in the VHCF range generally originate from small internal defects and discontinuities, such as non-metallic inclusions [96, 97]. Owing to its typical characteristic appearance, this type of fracture surface is normally called fish-eye. Figure 2.15(a) illustrates a typical fish-eye fracture surface of

high-strength steel. Few models are able to predict the effect of non-metallic inclusions on fatigue strength in the HCF and VHCF regime [98, 99]. This may be because adequate reliable quantitative data on the non-metallic inclusions are hard to obtain. Murakami and co-workers [68] have investigated the effects of defects, inclusions, and inhomogeneities on fatigue behaviour of high strength steels and expressed the fatigue limit as a function of Vickers hardness HV and the inclusion size

$$\sigma_w = \frac{C \cdot (HV + 120)}{(\sqrt{area})^{1/6}}, \quad (2.1)$$

where σ_w is the endurance limit at 10^7 cycles for $R = -1$, HV is Vickers hardness and \sqrt{area} is the square root of the projection area of an inclusion on the loading direction. The parameter C depends on the defect type and for inclusions underneath the surface it equals to 1.56 [68]. The concept of linking the fatigue performance with material hardness has a great practical advantage because the procedure of hardness measurements is relatively straightforward and fast. Within this model, a non-metallic inclusion is assumed to be equivalent to a small crack. The Murakami equation was derived based on the threshold data for crack growth of specimens containing artificial defects ranging from 40 to 500 μm . Thus, for reliable lifetime predictions, the size of inclusion or any other type of defects should be limited to this range. Figure 2.15(b) shows the ratio of the applied cyclic stress to the fatigue limit estimated by the Equation (2.1) for some steel types [68]. It can be seen that the Murakami methodology results in approximately $\pm 10\%$ deviation at 10^7 cycles.

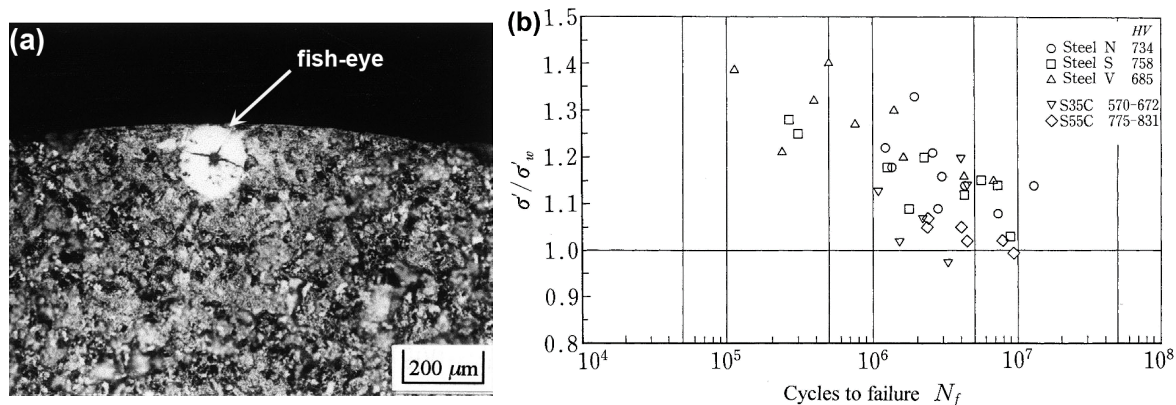


Figure 2.15. (a) Fish eye mark on the fracture surface of SAE 9254 steel (reprinted from [68] by permission of Elsevier); (b) relationship between the ratio of nominal fracture stress σ' to estimated by the Murakami equation fatigue limit σ'_w at inclusion (reprinted from [68] by permission of Elsevier).

A fractographic analysis after interior-initiated fatigue failures in the HCF or VHCF regimes revealed that internal crack initiation inevitably leads to the formation of a ring-like fish-eye pattern at the fracture surface [68, 100]. A non-metallic inclusion or any other type of defects is always located at the centre of the fish-eye mark. A rough circular area in the close vicinity of an inclusion at the fracture origin is normally seen (see Figure 2.11(a) and Figure 2.15(a)) [100]. It is generally accepted that more than 90% of fatigue life is attributed to the formation of a rough area [101]. Therefore, without careful consideration of the crack-growth mechanisms involved in the rough area formation, it is impossible to develop any lifetime prediction model. In addition, since the size of the rough area is typically less than 0.5 mm, special attention should be paid to the short crack effect. There are two opposite viewpoints on distinguishing the crack initiation and propagation stage in the rough area of the fish-eye. Some researchers considered the crack initiation period as a number of cycles to create

a crack length given by the radius of the rough area [102, 103]. However, other researchers consider that fatigue crack initiation from an inclusion or a pore begins early in the fatigue life, and then a fatigue crack grows within the rough area [101, 104]. From this perspective, the size of the rough area can be predicted by an analysis of the short crack growth process using fracture mechanics. The existing theoretical models for a fish-eye formation and the mechanism of crack growth in the rough area can be found elsewhere [100].

Fatigue properties of materials are usually controlled by the presence of defects induced during the manufacturing process. Internally initiated fatigue failures have been also frequently observed in cast parts [105] as well as parts produced by powder metallurgy [86] and additive manufacturing [106]. These findings additionally suggest that appropriate assessment models are needed to account for inherent risks related to interior material flaws. Recently, Cao and Chandran studied the fatigue failure mode and early stage crack growth in the Ti-6Al-4V alloy produced by powder metallurgy [86]. The authors analysed the quantitative relationship between the fatigue life, crack origin size, and the early-stage short crack growth. According to their findings, the transition from surface-initiated to internally initiated failures happens due to domination of crack initiation from larger internal microstructural discontinuities. Based on the fish-eye appearance, the crack growth rates at the early stages of fatigue life were estimated in the magnitude of 10^{-12} – 10^{-10} m/cycle. The effect of a pseudo-vacuum environment at the tip of an internal crack was implicitly taken into account by a correction factor. The authors emphasized the importance of a vacuum environment for accurate predictions.

Beretta and Romano showed that defect-tolerant design and extreme value statistics can be potentially adopted to characterize the correlation between the fatigue strength of additively manufactured Ti-6Al-4V and the number of defects [106]. Based on extensive literature review, they demonstrated that linear elastic fracture mechanics (LEFM) cannot be applied for predicting the fatigue strength of additively manufactured parts with small defects. In addition, the authors used the so-called Kitagawa-Takahashi diagram to correlate the fatigue strength with defects present in the volume. However, it has been assumed that the maximum defect in a given material volume is decisive for crack initiation. As shown in Section 7.2.2, this assumption is not always valid particularly for the Ti-6Al-4V alloy.

Thus, various approaches have been hypothesized to solve the complicated problem of lifetime assessment in the HCF regime. Accounting for internal crack initiation in the predictive schemes makes this issue even more complex and contradictory. Unfortunately, only indirect fractographic measurements are now the single possible tool for model verification. Very little is still known about the growth of short cracks of submillimetre size in the interior of a component subjected to cyclic loading. A significant part of this PhD work is devoted to development of a HCF prediction model, considering the internal welding-induced pores in the laser-welded Ti-6Al-4V. Many existing concepts and approaches have been adopted with slight modifications; however, a few novel and interesting solutions are proposed. A more detailed description of the fracture mechanics tools and models adopted in this work is given as the part of the methodology in the following chapter.

3 Methodology

3.1 Experimental procedures

3.1.1 Material

The material used in this study was a Ti-6Al-4V (ASTM Grade 5, AMS 4911N) [107] alloy in the form of hot-rolled and mill-annealed sheets with a thickness of 2.6 mm supplied by the VSMPO-AVISMA Corporation. The nominal chemical composition of the alloy from the corresponding standard is shown in Table 3.1. For comparison, the contents of alloying-element determined by an energy-dispersive X-ray (EDX) analysis are also shown. Considering the detection limits of the EDX technique used in this work, values lower than approximately 0.5% should be taken as qualitative. Interestingly, an insignificant amount of silicon (Si) has been found in the Ti-6Al-4V alloy in spite of the absence of this alloying element in the standard. Apparently, this addition was deliberately made in order to increase the creep resistance of Ti-6Al-4V. It is widely recognized that a moderate addition of silicon can significantly improve the creep behaviour of titanium alloys [108].

Table 3.1. Chemical composition (wt.%) of Ti-6Al-4V alloy in the original as-received condition.

	Al	V	Fe	Si	N	H	O	Ti
AMS 4911	5.5–6.75	3.5–4.5	< 0.3	-	< 0.05	< 0.015	< 0.20	Bal.
Measured	6.54	3.31	0.21	0.48	-	-	-	89.46

Prior to laser welding experiments, the sheets were cut into the workpieces of required geometry. The first group of coupons for preliminary welding trials had the dimensions of 40 mm × 80 mm. The final large-scale coupons with the size 190 mm × 110 mm were extracted for verification of the effect of specimen size in welding experiments and for subsequent extraction of fatigue samples. These coupon dimensions were sufficient to extract seven fatigue specimens from one weld.

3.1.2 Laser processing

3.1.2.1 Laser beam welding (LBW)

The welding equipment consisted of an 8-kW continuous wave ytterbium fibre laser YLS-8000-S2-Y12 (IPG Photonics Corporation) integrated with an IXION ULM 804 CNC-controlled universal laser machine. A collimation lens with a 120-mm focal length, a focusing lens with a 300-mm focal length, and a process fibre with a diameter of 300 μm were employed to produce a focal spot diameter (beam waist diameter) of approximately $2w_0 = 750 \mu\text{m}$. A schematic illustration of the laser optics is shown in Figure 3.1. The central wavelength of the fibre laser is $\lambda = 1070 \pm 10 \text{ nm}$. The half-angle divergence of the focused laser beam was $\theta = 30.3 \text{ mrad}$. The beam parameter product (BPP) of a laser beam is defined as a product of the beam radius at the beam waist w_0 and the beam divergence half-angle θ :

$$BPP = \theta \cdot w_0. \quad (3.1)$$

The BPP parameter is often used to specify the beam quality, i.e. the higher the BPP, the lower is the beam quality. The smallest possible BPP is achieved for a diffraction-limited Gaussian beam, which

is equal to $\lambda/\pi \approx 0.34 \text{ mm}\cdot\text{mrad}$ for the given wavelength. Real high-power laser beams are normally non-Gaussian, being multimode or mixed-mode. The resulting BPP of the multimode laser beam used in this work is $11.3 \text{ mm}\cdot\text{mrad}$. Another common measure of laser beam quality is the beam quality factor or the M^2 factor. According to the standard [109], it is calculated as the BPP divided by λ/π :

$$M^2 = \frac{\pi\theta w_0}{\lambda}. \quad (3.2)$$

For the beam parameters given above, the M^2 factor equals to 33.3, a typical value for a multimode laser beam. In other words, the laser beam used in the present work can be regarded as around 33 times diffraction-limited.

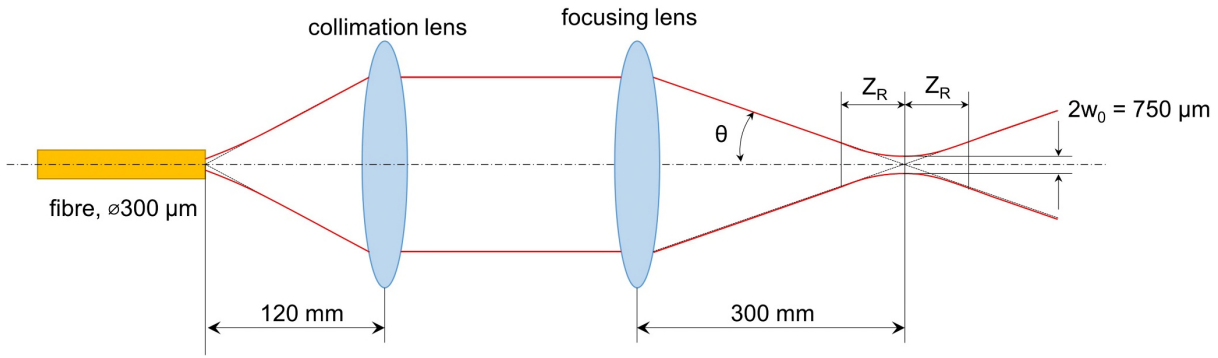


Figure 3.1. Simplified illustration of the laser beam geometry in the optical system including the collimation lens and the focusing optics.

The Rayleigh length Z_R of a laser beam is the distance from the beam waist to the position where the beam radius is increased by a factor of $\sqrt{2}$. This beam quality parameter plays an important role because it essentially reflects the depth of focus for a given laser beam. The Rayleigh length can be estimated as the ratio of the beam waist radius to the divergence half-angle $Z_R = w_0/\theta$ that gives the length of 12.5 mm for the applied laser beam focusing system. According to this result, the current laser beam is not sensitive to the deviations of the focal position, i.e. slight variations of the focal spot relative to the specimen surface in the order of several millimetres do not result in significant changes of the beam diameter. This is one of the major advantages of modern high-power fibre lasers.

Laser welding was performed both autogenously and with the addition of filler material (Ti-6Al-4V wire, diameter of 1.0 mm). Prior to the welding, the faying edges of the specimens were milled, ground, and then thoroughly cleaned with ethanol to remove any surface oxides and contaminants. Owing to the high reactivity of titanium with atmospheric gases at elevated temperatures, adequate measures need to be taken in order to shield the molten pool during the LBW process. The specimens were fixed in an open plastic box filled with argon to protect the weld bead from air during the LBW process. A uniform argon flow around the weld bead was provided by the injection of the shielding gas through the porous aluminium plate at the bottom of the box. Based on the hot gas extraction analysis, Kashaev et al. reported that this technique provides an effective shielding of the weld [11]. The welding direction was perpendicular to the rolling direction (RD) of the material. The optimal combination of welding parameters to obtain a good weld quality and an appropriate weld shape is described in Section 4.1.

3.1.2.2 Laser surface remelting (LSR)

Local remelting of the weld area was selected as a non-contact alternative to traditional machining of the weld surface. LSR was conducted immediately after welding, using the same equipment and laser source as was done for the LBW process. In contrast to the laser-welding process, the interaction of large defocused laser spot with a material surface is characterized by a high back reflection and considerable heat input into the workpiece. Therefore, parameters of the remelting process have been varied with the aim to achieve a desired surface smoothening effect and to minimize the heat input. Otherwise, excessive laser power may lead to overheating of the specimen, resulting in undesired microstructural changes within the base metal. In addition, the high intensity of the back-reflected laser beam may destroy the optical head or other important adjustment devices attached to the optical head. In this context, laser power should be kept at a minimum level. The process parameters finally employed for the LSR treatment were as follows: laser power 3.4 kW, feed rate of 2.0 m/min, focus position of + 80 mm above the workpiece surface and a spot diameter of 5.0 mm. This optimum combination of defocusing and power density in the focal spot provided a sufficient smoothening effect with a minimum laser power for a given welding speed.

The defocusing distance was estimated from the condition that a focal spot should entirely cover the weld zone. The variation of the spot size for a beam with the Rayleigh length Z_R at a distance z along the beam from the beam waist is given by

$$w(z) = w_0 \sqrt{1 + \left(\frac{z}{Z_R}\right)^2}. \quad (3.3)$$

Considering a typical weld width of about 3 mm and inherent deviations from the weld line, the focal spot was assigned to be 5 mm. According to Equation (3.3), defocusing distance should be around 80–85 mm to achieve the selected spot size. Subsequent measurements of the width of the remelted zone showed the correctness of the defocusing strategy and estimations. After the LSR treatment, the welded plates were held in the argon atmosphere for several minutes until they cooled to room temperature.

3.1.2.3 Laser shock peening (LSP)

A general scheme of the LSP process is presented schematically in Figure 2.13(a). The LSP treatment was conducted using an experimental set-up containing a Q-switched high energy flash lamp pumped Nd:YAG laser system integrated with a six-axis KUKA KR30HA industrial robot. The laser, with a wavelength of 1064 nm, was operating at a frequency of 10 Hz and a pulse duration of 20 ns. Pulse energy of 5 J was focused on a square spot of 1 mm × 1 mm on a specimen surface. During the LSP process, a thin steel foil adhesive tape with a thickness of 100 μm was used as an energy absorbing and ablative layer to protect the specimen surface from the thermal influence of plasma. The first trials demonstrated that aluminium foil, traditionally used for this purpose, was not sufficiently strong to withstand very high power densities required for the laser peening of titanium. To maximize the peening effectiveness, the experiments were carried out in a confined plasma configuration. Laminar water flow with a thickness of 2–4 mm was used as a plasma-confining layer. The LSP-treated area covered the welding seam and the neighbouring regions of 10 mm from each side (see Figure 3.2).

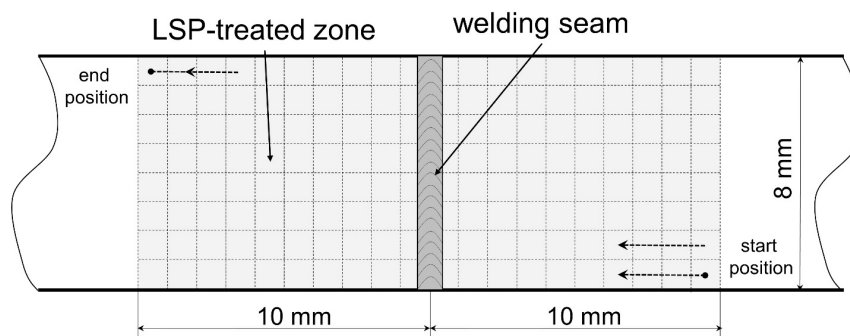


Figure 3.2. Schematic illustration of the LSP-treated region (view from above) in the proximity to the weld and the shot sequence.

Fatigue specimens were subjected to laser peening before extraction from the welded plate. LSP treatment was applied on both sides of the gauge section of fatigue specimens, following the shot pattern shown in Figure 3.2; three shots were applied at the same position (3× overlapping). It is worth mentioning that the opposite sides of the workpiece have been processed sequentially one by one, using a new foil for each treatment. In spite of a longer processing time, this strategy helps to mitigate an inherent bending effect of a treated specimen.

3.1.3 Microstructure analysis

The welded joints as well as the base metal were subjected to thorough microstructural analysis to study the effect of laser processing and the subsequent heat treatment on the local microstructure of the FZ. Transverse cross sections were cut from the stable middle region of the joint for metallographic examination and microhardness testing. After sectioning, the samples were mounted, ground and polished using an oxide polishing suspension compound (OPS). Microstructural observations were performed using both inverted optical microscopy (OM) Leica DMI 5000M and scanning electron microscopy (SEM) JEOL JSM-6490LV. Prior to light microscopy, the specimens were etched by Kroll's reagent (3% HF, 6% HNO₃, 91% distilled water) to unveil the microstructural features. For SEM investigations, a mirror-like OPS polished surface was used. SEM microstructure observations and texture analysis of the joints were conducted using secondary electron images and electron backscatter diffraction (EBSD). The EBSD measurements were normally performed for a specimen area of 135 μm × 135 μm at an acceleration voltage of 30 kV, an emission current of 75 μA, a working distance of 13 mm and a sample tilt angle of 70°. For the orientation calculation, the generalized spherical harmonic series expansion (GSHE) method was applied, based on the triclinic sample symmetry [110]. The average grain size was measured using the OIM software and the results of EBSD measurements. Texture analysis was done by constructing the pole figures and orientation maps of grains in a cross section.

Energy dispersive X-ray spectroscopy (EDX) was used to determine the local chemical composition. In this method, a localized chemical composition was estimated by analysing the X-ray spectrum emitted by a solid when bombarded with a focused electron beam. For EDX analysis, SEM was operated at an acceleration voltage of 15 kV, a working distance of 10 mm and a live time of 150 s. Quantitative analysis of the element concentration was based on the standard ZAF method of correction in which the relative intensity of an X-ray line is proportional to the mass concentration of the element [111]. The acronym 'ZAF' stands for a calculation procedure accounting for the effect

of atomic number (Z), absorption (A), and fluorescence (F) that are estimated separately from suitable physical models.

3.1.4 Microhardness

Since the tensile strength of a metallic material and its hardness are both attributed to the slip within grains, these characteristics are thought to correlate to each other. The empirical relationship between the yield strength, ultimate tensile strength (UTS), and hardness is of great importance for material characterization. It was shown that a well-known linear relationship between the UTS and hardness found and validated for steels holds for titanium alloys as well, though with a bigger scatter [68]. From this perspective, hardness mapping is an effective tool to obtain an additional insight into the distribution of local strength in the areas of interest. Hardness measurements, being significantly easier from the practical point of view, can be considered an indicator of local mechanical properties of the material.

Transverse cross-sections of the samples for microhardness testing were prepared in the same manner as discussed for the microstructural evaluations. The Vickers microindentation hardness test was carried out using a Zwick/ZHU0.2/Z25 universal hardness testing machine and the *testXpert* software. The specimens were tested with a 500-g load applied for 15 s, according to ASTM E384-11 standard [112]. The indentation spacing was 200 μm to provide a minimum recommended distance between the test points. To investigate the thickness gradients, microhardness profiles were measured at three testing positions: radiation exposure side (RES), middle of the weld (M), and the weld root side (RS) (illustrated in Figure 4.10(a)). The distances from the RES and RS lines to the corresponding edges of the specimen were 200 μm each.

3.1.5 Residual stresses

In this work, the measurements of residual stresses were carried out for (1) the quantitative assessment of high tensile welding-induced residual stresses in the proximity to the weld and (2) for characterization of the LSP-induced compressive residual stresses. The spatial distribution of weld residual stresses was measured using the X-ray diffraction at the HZG beamline P07B, located at PETRAIII at DESY (Deutsches Elektronen-Synchrotron, Hamburg). The in-depth profile of compressive residual stresses after LSP was determined by the incremental hole-drilling method (HDM) combined with electronic speckle pattern interferometry (ESPI) using a PRISM system, American Stress Technologies Inc. The HDM is a relatively simple method that is significantly cheaper than the X-ray diffraction technique. It is semi-destructive in nature and can be easily applied to on-site measurements using portable HDM devices. However, the HDM can measure only the in-depth distribution of residual stresses. To obtain any information about the 2D in-plane spatial distribution of residual stresses, multiple points have to be drilled in the region of interest. Thus, the HDM technique has a high in-depth resolution that is compensated by a very low in-plane resolution. The X-ray diffraction method, on the contrary, has a high in-plane resolution, because a high intensity synchrotron beam passes through the entire specimen thickness. This results in the averaging of the residual stresses over the thickness without any detailed information about the in-depth distribution. Hence, in contrast to the HDM, synchrotron measurements provide a high in-plane resolution without any resolution in the thickness direction. The welding-induced residual stresses were measured by both techniques to compare their suitability and effectiveness.

3.1.5.1 Incremental hole drilling method (HDM)

A procedure for residual stress measurement using the HDM is a common technique used today and is standardized in ASTM E837 [113]. More details about the PRISM system and the theoretical aspects can be found elsewhere [114]. The photo of a standard fully integrated PRISM measurement system used in the current work is presented in Figure 3.3(a). In this method, a specific amount of material is removed by drilling a blind hole, and the resulting surface displacements measured by laser interferometry are used to estimate the average stresses in the removed volume. The hole can be drilled in several increments, thereby enabling to obtain some information about the stress as a function of depth. The residual stress distribution can be measured over a depth that normally depends on the drill diameter. To measure the LSP-induced residual stresses in this study, the cutter with a nominal diameter of 2 mm was used. This resulted in a maximum depth of 1 mm that could be used for a reasonable interpretation of the results. The hole was drilled by means of a high-speed turbine mounted on a precise travel stage. All measurements were performed at a rotational speed of 30,000 rpm and 0.04 mm/s feed rate. Finally, the integral method [114] implemented in the PRISM software is used to calculate the residual stresses as a function of depth on the basis of the measured surface strains. The instrument delivers the complete planar stress state defined by three stress components.

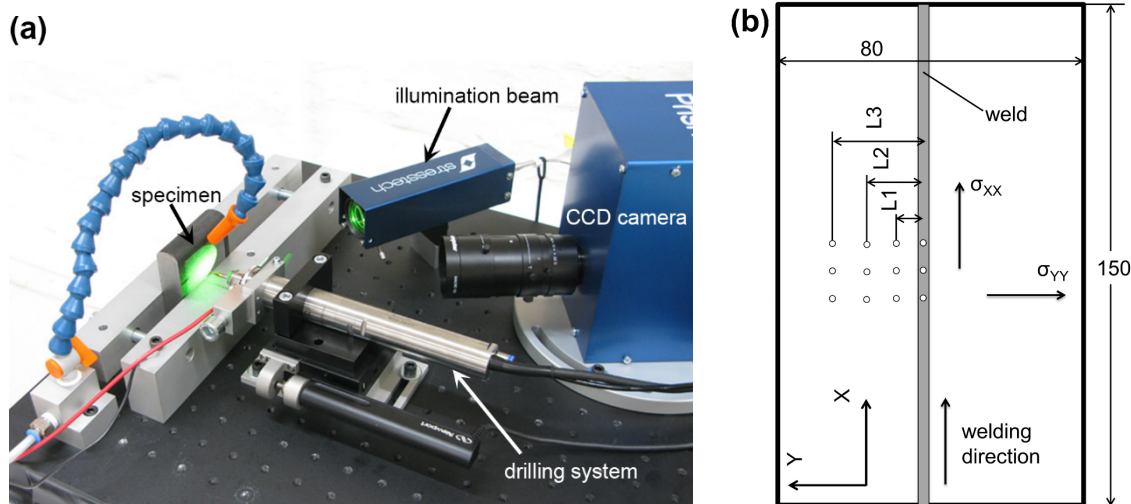


Figure 3.3. (a) A standard PRISM system for measurement of residual stresses by the HDM; (b) the selected geometry of the welded plates with position of drilled holes for residual stress measurements by HDM.

To measure the residual stress distribution in the weld proximity, a drill with a diameter of 0.6 mm was used. The selection of a minimum diameter for this purpose was dictated by the need for higher in-plane resolution because the stresses in the weld area are characterized by steep gradients. The holes were drilled to a depth of 0.3 mm in 10 steps of 0.03 mm. The geometry of welded plates for HDM measurements and locations of the drilled holes are presented schematically in Figure 3.3(b). The distance between neighbouring points was at least 3 mm, in accordance with ASTM E-837. The distribution of residual stresses across the weld region, i.e. along the Y-axis in Figure 3.3(b), was measured by drilling the holes at a number of distances from the weld centreline. At least 3 points represent each distance in the Y direction.

3.1.5.2 Synchrotron X-ray diffraction technique

The specimen geometry used for residual stress measurements by the synchrotron X-ray diffraction was equal to that shown in Figure 3.3(b). The incident beam was calibrated to impinge on the welded samples in a transmission mode. The X-ray diffraction pattern by Debye-Scherrer cones was captured by a perpendicular to the beam Perkin Elmer XRD1621 detector with an active area of $400 \text{ mm} \times 400 \text{ mm}$. The specimens were covered with a thin layer of copper paste to calibrate the distance between the specimen and the detector. The photon energy was 87.5 keV. A line scan was performed across the weld seam with a beam cross section of $0.1 \times 0.1 \text{ mm}^2$ in the weld area and $1.0 \times 1.0 \text{ mm}^2$ outside of the weld. Thus, the beam cross section was tuned for either high spatial resolution or good time resolution. α -Ti (102) and (103) reflections were used to determine the strain magnitude. The entire diffraction pattern was fitted to calculate the strain and deduce the residual stress. The plane stress condition was assumed to derive the stresses from the calculated strains. A detailed procedure for calculating the stresses based on the given diffraction pattern can be found in [115, 116].

3.1.6 Mechanical properties

3.1.6.1 Tensile testing

Tensile tests of the base metal and the welds were carried out according to the DIN ISO 6892 [117] procedure using an electro-mechanical Zwick Roell testing machine equipped with a 100-kN load cell. The specimen elongation was measured by an optoelectronic laser extensometer (Fiedler WS-180) with an initial length of 50 mm. The load-bearing cross section of the tensile specimen was $10.0 \text{ mm} \times 2.0 \text{ mm}$ and the total specimen length was 186 mm. A constant crosshead displacement rate of 0.5 mm/min was applied during the tensile testing. Five specimens were tested for each of the different weld conditions in order to account for scatter and to get reliable results. The values of load as a function of displacement were recorded and then a dedicated *Python*-written code was used to plot an engineering stress-strain curve and estimate the main mechanical properties: the Young's modulus E , the yield strength $\sigma_{0.2}$, ultimate tensile strength (UTS), and fracture strain ε .

3.1.6.2 Fatigue testing

Load-controlled uniaxial fatigue tests were conducted at room temperature using a Testronic 100-kN RUMUL resonant testing machine. The experiments were performed in accordance with ASTM E466-07 [118] at a resonant frequency of around 80 Hz and an applied load ratio $R = 0.1$. The specimens with a uniform test section of $8 \text{ mm} \times 20 \text{ mm}$ were used, as shown in Figure 3.4. All the edges were rounded to 0.5 mm in order to prevent a premature edge crack formation. The welding seam was located at the centre of the gage length, and fatigue loading was applied transverse to the weld direction. The fatigue tests were carried out up to 10^7 load cycles (≈ 34 hours of operation). In the following, the term 'fatigue limit' corresponds to fatigue strength at this number of cycles.

After fatigue testing, the specimens were selected for further fracture surface examinations. The fracture surface topography is a useful method for understanding the relationship between the fracture behaviour and microstructural characteristics. Important clues to the underlying causes of fatigue fracture may be revealed by the microfractographic analysis at appropriate magnification. Fracture surfaces of the fatigue specimens were examined using both OM and SEM. The SEM fractographic observations were performed in the secondary electron contrast with acceleration voltage of 25 kV, using a 30- μm spot size and a working distance of 15 mm.

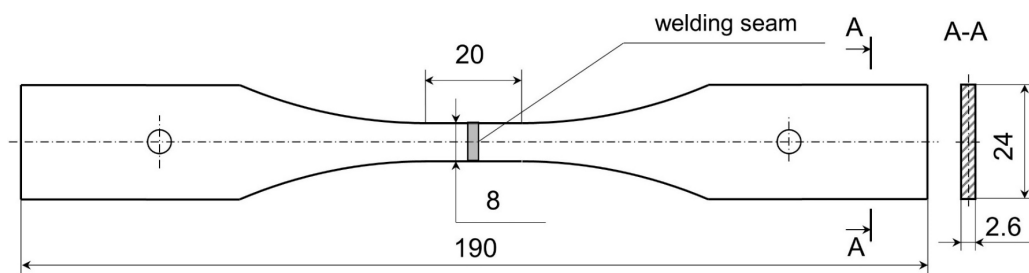


Figure 3.4. Geometry of a fatigue specimen.

3.1.6.3 Fatigue crack propagation (FCP) testing

Fatigue crack propagation (FCP) tests were conducted using a 25-kN servo-hydraulic testing machine. The measurement procedure was based on recommendations specified in the ASTM E647-11 standard [119]. Conventional compact tension C(T) specimens with a width of 50 mm were used. An initial crack with a length of 12.5 mm was introduced by an electro-discharge machining. The tests were carried out at a room temperature, with a load ratio of $R = 0.1$ and a constant frequency of 10 Hz. All specimens were polished in the area of expected crack extension. Crack length measurements were accomplished by both optical and compliance techniques. A travelling microscope was used to obtain accurate visual measurements of crack lengths on the surface. Simultaneously, the measurement of the crack opening displacement (COD) was done by the clip gage attached to the mouth of the crack. For both methods, the crack growth was curved using the crack length data as a function of the number of load cycles. For the crack growth rates greater than 10^{-8} m/cycle, constant load amplitude tests in which the stress intensity factor (SIF) range ΔK increases were employed. In accordance with ASTM E647, the K -decreasing procedure was used for the near-threshold region with crack growth rates up to 10^{-10} m/cycle.

3.1.7 Radiographic inspection

X-ray inspection has been applied to characterize the porosity distribution in the laser-welded seams. For the X-ray analysis, additional plates with a sufficient length given by the standards [120, 121] were welded with the optimal parameter set. Traditional radiographic inspection is conventionally performed from the top side of the welded sheet. As a result, the obtained image is a projection of all the pores onto the inspection plane. Consequently, the position of a pore relative to the surface cannot be detected by this method. Since the in-depth location of a pore is of great importance for fatigue performance, transverse X-ray analysis of the extracted welding seam was conducted in this work. The fusion zone of the weldment was precisely cut and subjected to lateral radiographic inspection, as shown in Figure 3.5. Width of the FZ after cutting was around 2.5–3.0 mm. A total length of 75 mm was inspected for each weld condition. The X-ray analysis was carried out using a microfocus X-ray inspection system (Y.Cougar Basic, YXLON) operating at a tube voltage of 90 keV and a current of approximately 30 μA , depending on the specimen thickness. The pixel size at the most appropriate magnification was about 4 μm .

A special *Python*-written code was developed to interpret the radiography images, porosity localization and the size evaluation. The obtained images were characterized by a low contrast between defects and the background. Moreover, non-uniform illumination was usually observed as a result of the inevitable flatness deviations upon cutting. To overcome these challenges, several image-processing techniques from the open-access *openCV* library, such as noise reduction and

adaptive thresholding, were used. Finally, the processed images were used for statistical analysis of the two porosity distributions, namely the spatial and size distributions.

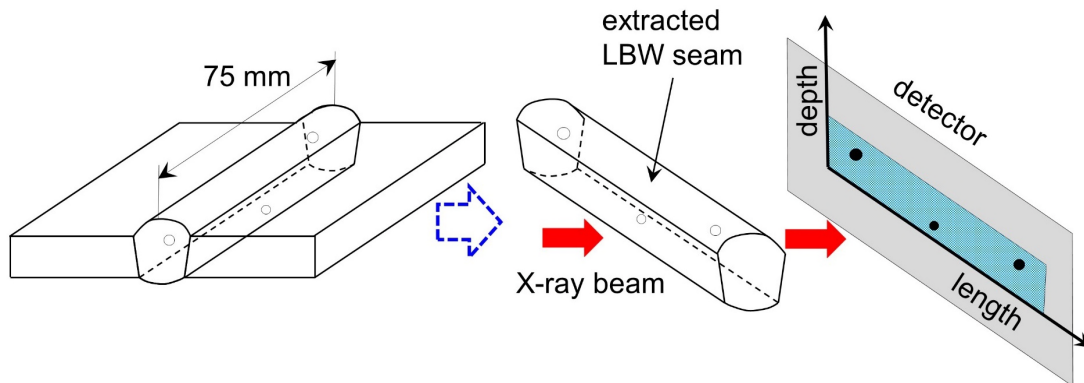


Figure 3.5. Schematic illustration of the lateral X-ray analysis of the weld FZ.

3.1.8 Heat treatment

Since titanium alloys are chemically active and prone to pick up atmospheric gases at elevated temperatures, inert gas or a vacuum atmosphere should be ensured during their thermal treatment. The heat treatment of welded specimens was conducted using a vacuum furnace (Centorr Vacuum Industries) at a vacuum degree of 10^{-1} Pa. The parameters of different types of PWHT with the corresponding abbreviations are listed in Table 3.2. Annealing temperatures did not exceed the β transus temperature of nearly 1000°C for the Ti-6Al-4V alloy [28]. During the heat treatment, the welded plates were hung in the oven using a molybdenum wire to prevent any contact between the specimens and the furnace wall. No significant distortion was observed after the heat treatment. Cooling down to room temperature was performed in argon atmosphere (AC).

Table 3.2. Parameters of the post-weld heat treatment types.

Heat treatment	T / time / cooling
Stress relief annealing, SRA1	540°C / 4 h / AC
Stress relief annealing, SRA2	650°C / 2 h / AC
Full annealing, FA1	750°C / 2 h / AC
Full annealing, FA2	850°C / 1 h / AC
Recrystallization annealing, RA	920°C / 45 min / AC
Duplex annealing, DA	RA+SRA1

In some cases, the heat treatment was performed to generate a fully martensitic microstructure. For this purpose, the water quenching (WQ) was used to activate the required high cooling rates. Conventional atmospheric oven was used if the heat treatment was followed by quenching. As discussed in Section 4.3.5, the holding time and the heat treatment temperature were varied in order to achieve the desired microstructure. The specimens were subjected to WQ immediately after the heating step. In this case, the specimens were subsequently machined in order to remove an oxygen-enriched brittle α case layer. Based on the microstructural analysis, circa 0.2-mm-deep surface layer had to be removed for a good surface quality.

3.2 Adopted fracture mechanics concepts

3.2.1 Stages of fatigue life

Generally, the fatigue life of a component subjected to cyclic loading can be divided into three stages: fatigue crack initiation, fatigue crack propagation, and the final failure. The flowchart of the lifetime stages with the corresponding length scales is shown in Figure 3.6. The definition of the crack initiation phase has undergone major modifications and revisions over the past several decades. It is a well-established fact that initiation covers a major part of the total fatigue life in the HCF regime. However, there are different viewpoints on the methodology for its assessment. The early investigations in the field were based on the ‘engineering’ approach, in which the initiation period is considered as a number of cycles required to form a crack of detectable size that is usually around 1.0 mm. Strictly speaking, this definition is arbitrary because the reference detectable crack size depends on the experimental techniques used. Furthermore, this methodology allows one to assess the initiation phase by purely empirical models. Over the last several decades, with the help of modern procedures enabling the accurate crack growth detection, an increasing number of studies have shown, that fatigue crack initiation, in a narrower sense – i.e. the formation of a microstructurally short crack – occurs at a very early stage of fatigue life [122, 123]. From this perspective, the period over which a detectable crack is formed, can be estimated based on physically based models relying on the propagation of short cracks [124].

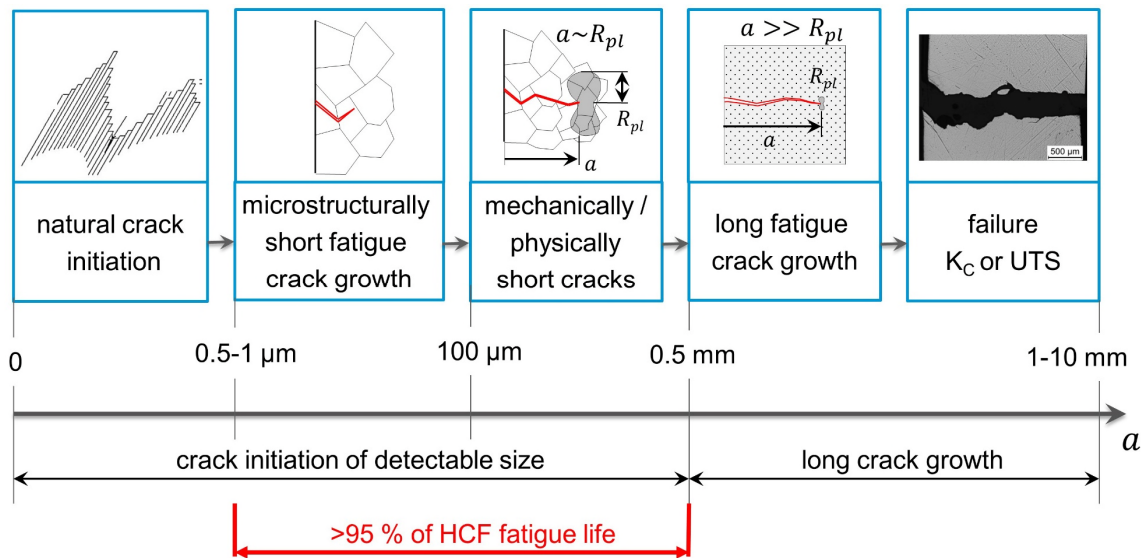


Figure 3.6. Stages of fatigue life with an approximate length scale corresponding to the fine-grained martensitic microstructure of Ti-6Al-4V.

Numerous researchers have emphasized the importance of short crack behaviour during the initiation phase [71, 124]. According to the published literature, a traditionally used engineering crack initiation phase can be further subdivided into three foregoing phases [14]:

Natural crack initiation phase within which a fatigue crack is formed due to irreversible plastic deformation leading to extrusions and intrusions at the free surface. This process is accelerated at pre-existing defects and notches such as pores, non-metallic inclusions etc. It is worth mentioning that there is no established definition for the end of this stage because it is difficult to determine the moment at which a defect becomes a crack.

Microstructurally short fatigue crack growth is characterized by a crack length comparable to the characteristic microstructural dimension, e.g. the average grain size (see Figure 3.6). Its propagation is discontinuous and is affected by various microstructural barriers that can lead even to the crack arrest. The arrest of the largest microstructurally short crack formed in a component corresponds to the current definition of fatigue limit [68].

Mechanically/physically short crack growth begins when the crack length is sufficient to enclose a number of grains and to be described by continuum mechanics. The influence of local microstructure gradually decreases, and the crack propagation becomes more stable. However, the crack at this stage is designated as being mechanically short because its dimensions are comparable to mechanical discontinuities such as the plastic zone size at the crack tip R_{pl} . Simultaneously, a gradual built-up of the crack closure effect is promoted with an increasing crack length. If the crack is so small that the crack closure at its tip is not fully developed, this crack is designated as a physically short crack. Depending on the material and its microstructure, the stages of mechanically and physically short cracks may prevail and suppress each other; however, for most metallic materials, these stages are overlapped and the crack propagation is characterized by simultaneous effect of the above-mentioned phenomena [71].

The last stages of the lifetime, as demonstrated in Figure 3.6, encompass the growth of the so-called long cracks. The crack front of these cracks is by several orders of magnitudes larger than any relevant microstructural or mechanical dimensions, thus fulfilling the hypothesis of small scale yielding, the basis of LEFM. In the region of high cycles (HCF) and very high cycles (VHCF), this stage is normally negligibly short compared to the preceding stages and, therefore, is not relevant within this work.

3.2.2 Stress intensity factor (SIF)

A central role in any fracture mechanics model plays a correlation between the cyclic crack propagation rate and the magnitude of local stress fields at the crack tip. Therefore, an initial crack, which propagates under applied load, has to be known or at least assumed. LEFM is based on the application of the theory of elasticity to bodies containing cracks or defects in order to correlate the crack growth rates with local stress fields. In other words, the linearity between stresses and displacements is assumed. In the mid 1950's, Irwin made a significant contribution to the field of LEFM by showing that the local stresses near a crack tip have the general form given by

$$\sigma_{ij} = \frac{K}{\sqrt{2\pi r}} f_{ij}(\varphi) + \dots, \quad (3.4)$$

where r and φ are cylindrical coordinates of a point near the crack tip (see Figure 3.7(a)) and K is the stress intensity factor (SIF) [14]. He also showed that the energy-based approach developed by Griffith [125] is equivalent to the stress intensity approach and the unstable crack propagation occurs if a stress intensity achieves the critical value K_c , known as fracture toughness. It can be seen from Equation (3.4) that a stress singularity exists at the crack tip. Since metallic materials plastically deforms as the yield strength is exceeded, a plastic zone will be inevitably formed at the crack tip. Nevertheless, LEFM remains valid if the plastic zone size remains small in relation to the crack length (small scale yielding hypothesis).

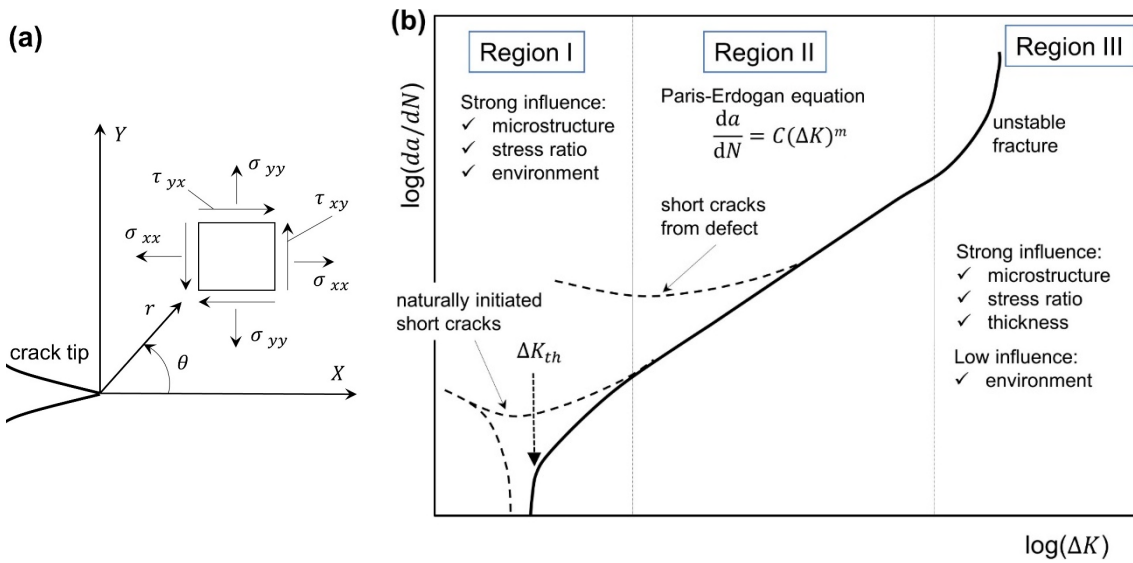


Figure 3.7. (a) Local stresses at the crack tip in polar coordinates; (b) representation of the propagation rate of a crack da/dN as a function of the stress intensity factor ΔK (FCP curve).

Thus, the stress intensity factor K introduced by Equation (3.4) defines the magnitude of the local stress distribution at the crack tip. This factor depends on numerous aspects including loading, crack size, its shape, and geometric features. It is generally given by:

$$K = Y\sigma\sqrt{\pi a}, \quad (3.5)$$

where Y is the crack geometry factor, σ is the remotely applied stress, and a is the crack length. Stress intensity factor solutions have been obtained for a wide range of crack geometries and can be found in handbooks and compendia [126]. In recent years, numerical methods including finite elements analysis have been widely used for determining the SIF values of parts with complicated geometries.

The use of fracture mechanics makes it possible to predict the number of cycles required for a crack to grow to some specified critical size. Thus, a reliable service life of a cracked component can be estimated by knowing the material-specific crack growth rates. Typical constant-amplitude crack propagation data are shown schematically in Figure 3.7(b). The crack growth rate da/dN is plotted against the applied SIF range ΔK . A plot of $\log(da/dN)$ versus $\log(\Delta K)$ has a sigmoidal form and can be subdivided into three regions: threshold region, stable crack growth (Paris region), and unstable crack growth (close to fracture toughness). Most of the current applications of LEFM are associated with the region of stable crack growth, where the FCP curve is almost linear. Numerous curve fits have been suggested for this purpose [14]. One the simplest and most widely used relationship is the Paris-Erdogan equation [127]. If the applied stress intensity is below the threshold value ΔK_{th} , fatigue cracks cease to propagate. The magnitude of the FCP threshold depends on the microstructure, environment, and, in some cases, on the crack length.

The FCP threshold ΔK_{th} plays a key role in fatigue design and structural integrity assessment. Designing a component or an engineering structure such that the anticipated ΔK values for service conditions are below ΔK_{th} , would be highly desirable. However, this is often impractical due to the low level of operating stresses required and corresponding weight increase. Therefore, a damage-tolerance approach is currently used in the aerospace industry, where weight savings are of great importance. Within this approach, the stresses can be higher than the threshold value; however,

the crack growth rates have to be controlled such that the crack does not reach a critical length until the next inspection. Another problem concerning the application of ΔK_{th} is related to the propagation of short cracks. As shown in Figure 3.7(b), a conventional definition of the FCP threshold is not applicable to the short-crack regime. Therefore, a traditional LEFM-based approach must be modified in order to apply the fracture mechanics concepts for the lifetime prediction.

3.2.3 Short cracks

As previously discussed, a major part of the entire fatigue life is attributed to the crack initiation phase that can be considered as a propagation of short cracks [128]. This section presents a common framework of dealing with short cracks based on the cyclic R-curve and Kitagawa-Takahashi (KT) diagram that are two widely used forms of analysis. The major challenge related to dealing with short cracks is that the extrapolation of LEFM in this region can yield over-conservative estimates because short cracks can grow considerably faster than long cracks at the same SIF range (Figure 3.7(b)). The primary reason for this phenomenon is the violation of the similitude principle and the small-scale yielding state, which is the foundation of LEFM. To overcome these difficulties, several models of anomalous short-crack growth behaviour have been proposed [14, 129, 130]. Majority of the short-crack models rely on the dependence of the short-crack propagation threshold on the crack size. In principle, this dependence can be expressed either in terms of stresses $\Delta\sigma_{th}(a)$ (KT diagram) [131] or in terms of the SIF threshold $\Delta K_{th}(a)$ (the cyclic R-curve) [132].

The KT diagram describes the crack growth threshold stress $\Delta\sigma_{th}(a)$ as a function of crack length a and empirically combines both the endurance limit for short cracks and the long crack propagation threshold in a single diagram. From a practical viewpoint, it is an effective engineering tool because the analysis is based solely on stresses, without the calculation of SIF values. A schematic illustration of the KT diagram is shown in Figure 3.8(a). It is worth mentioning that a horizontal asymptote at the endurance limit of the KT diagram reflects the assumption of an infinite number of cycles below the $\Delta\sigma_{th}$ level. It was discussed in Section 2.3.1 that, in the light of recent findings in the field of VHCF, this assumption is not always valid. The cyclic R-curve in turn operates with stress intensities and shows the material resistance to the onset of crack propagation, thus reflecting a gradual growth of the FCP threshold with an increasing crack length [132], as shown in Figure 3.8(b). The growth of ΔK_{th} is related to the gradual built up of crack closure with increasing crack length. When a crack is sufficiently long, its FCP threshold approaches the horizontal asymptote $\Delta K_{th,LC}$ for long cracks.

There is a direct relation between these two concepts, and it is possible to calculate the KT diagram from the cyclic R-curve and vice versa. As shown in Figure 3.8(a, b), the information provided by the cyclic R-curve is also found in the KT diagram. Both diagrams can be subdivided into three ranges: A, B, and C [71]. In the range A, the microstructurally short crack growth is indicated by the dashed curve representing the crack acceleration and arrest at microstructural barriers. This range is followed by the mechanically/physically short crack regime, in which plasticity and crack closure effects play a key role. Finally, the long crack propagates in range C. From a practical viewpoint, the most contradictory and complex problem is to characterize the shape of the cyclic R-curve or KT diagram in the region B. The slope in this region reflects the sensitivity of a material to short cracks and is, therefore, decisive for fatigue life evaluation. Various approaches have been suggested to describe the smooth transition from the endurance region, A, to the region of long cracks, C [71, 132, 133]. The majority of the models offer an empirical equation validated by experiments, but do not explain the physical mechanisms of the short-crack phenomenon.

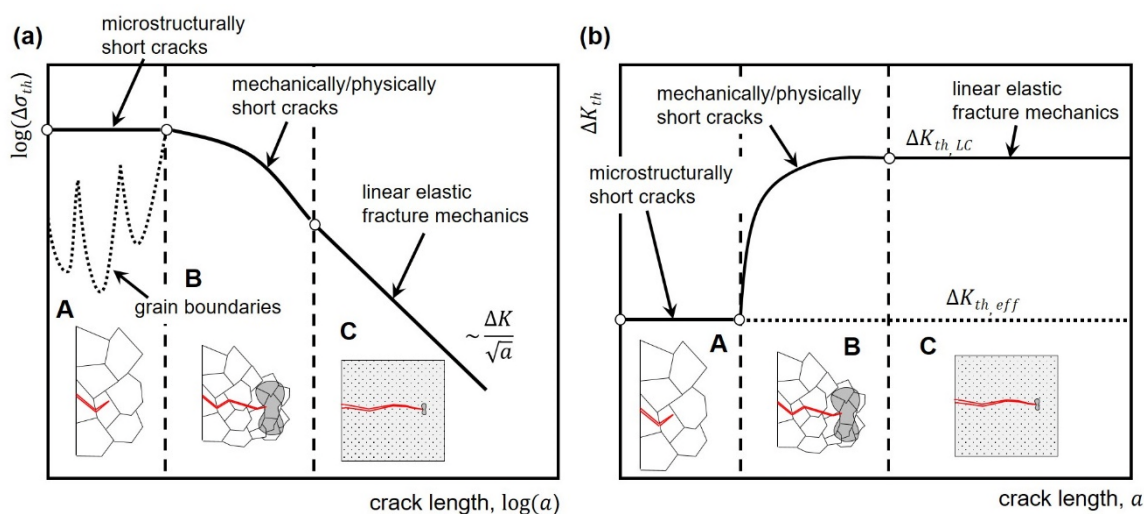


Figure 3.8. Schematic comparison of the (a) Kitagawa-Takahashi diagram and (b) the cyclic R-curve.

Since the cyclic R-curve operates with the crack growth threshold in terms of stress intensity, it is more beneficial to use this concept within a fracture mechanics framework for fatigue life assessment. The experimental procedure for determining the cyclic R-curve is rather complicated [134], and several analytical models for its construction are available [130, 135]. In the present study, the features of the material and internal crack growth have hindered the application of existing concepts for the cyclic R-curve construction. Therefore, several modified and adopted approaches have been proposed and implemented.

3.3 Statistical tools

3.3.1 Basic concepts of fatigue statistics

Scatter is an inherent stochastic feature associated with the fatigue-failure phenomenon. Fatigue lives of similar specimens subjected to equal cyclic loads under the same conditions can vary significantly. Scatter of the fatigue limit is one of the major engineering problems related to fatigue design, because high intensity factors are needed to outweigh the large deviations. Sources of scatter are different for the crack initiation period and the crack growth period; however, it is generally recognized that the crack nucleation and micro-crack growth are much more sensitive to various uncertainties. It is of great importance to characterize and quantify all potential sources of scatter in order to predict the lifetime variability.

Large scatter of the fatigue test series and a typical shape of the S-N curve are depicted in Figure 3.9. It can be seen that the scatter band is narrower at higher stresses and wider at low stresses [14]. A large scatter band of the fatigue limit is attributed to specimens that do not fail after the assigned for fatigue limit number of cycles (run-outs). This scatter behaviour can be interpreted as following. At a high stress value, surface conditions and the influence of defects are less important because microcracks emerge early in the fatigue life. Therefore, a major part of the life is covered by the stable growth of long cracks characterized by relatively low scatter. At low stresses close to the fatigue limit, crack nucleation and the behaviour of short cracks can depend on the local inhomogeneities, micro-notches and microstructural irregularities. These can vary from specimen to specimen and have a significant effect on the duration of the initiation period. As a result, the scatter band in the region of high cycles is significantly larger than in the LCF region.

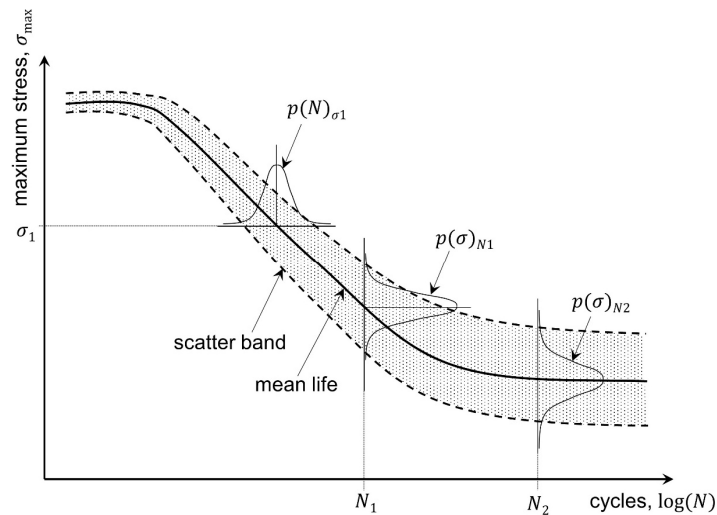


Figure 3.9. Probabilistic S-N curve with a corresponding scatter band.

Information on the distribution function of the fatigue life should be obtained by carrying out a large number of similar experiments at the same stress level. The probability density function (PD-function), $p(N)_{\sigma_1}$ or $p(\log(N))_{\sigma_1}$ in Figure 3.9 represents the distribution of the lifetime for the given stress magnitude σ_1 . Similarly, $p(\sigma)_{N_1}$ is the PD-function of the fatigue strength for a selected fatigue life N_1 . A special function of the latter type is the PD-function of the fatigue limit because, from the engineering perspective, the load spectrum of a structure has to be kept below the fatigue limit. Generally, the lifetime distribution function is assumed and fitted to experimental data of a large test series. The two most popular distributions are the normal distribution (Gaussian distribution of $\log(N)$) and the Weibull distribution [136]. The well-known normal distribution has a cumulative distribution function (CD-function) given by

$$P(x) = \frac{1}{s\sqrt{2\pi}} \int_{-\infty}^x \exp\left(-\frac{1}{2}\left[\frac{x-\mu}{s}\right]^2\right) dx, \quad (3.6)$$

with μ as the mean value and s as the standard deviation of the variable x . Considering the lifetime scatter, it is normally assumed that the variable of interest is the logarithm of fatigue life, $x = \log(N)$. The resulting distribution is, therefore, called log-normal. For a given test series, the values of μ and s can be approximately determined by their statistical estimates [136]. A detailed description of the Weibull distribution is given in the following section. Verification of the validity of the two above-mentioned distributions requires a very large number of similar fatigue tests. In order to measure how close the experimental data are to the fitted line, the coefficient of determination or the r^2 parameter is normally used. It can be determined as follows:

$$r^2 = 1 - \frac{SS_{res}}{SS_{tot}}, \quad (3.7)$$

where SS_{res} is the residual sum of squares in relation to the fitted line and SS_{tot} is the total sum of squares [136]. In general, the higher the r^2 parameter, the better a selected distribution function describes the experimental data.

It is important to note that regardless of the selected distribution function, low failure probabilities are of great practical concern. The lower limits are associated with safety factors and therefore happen

to be more significant for engineering problems. The characteristic lives corresponding to the specific values of failure probability $P(\log(N))$ are normally used for analysis. Typical values are $P(\log(N)) = 0.01, 0.05$ or 0.10 , which represent the failure probability of 1, 5 and 10% respectively; or the probabilities of survival of 99, 95 and 90% respectively. If this procedure is repeated at several stress levels, S-N curves for certain probabilities or the so-called P-S-N curves can be plotted. The average curve is associated with a failure probability of $P = 50\%$. The prediction of fatigue life is usually done for the mean S-N curve; however, it is of great practical interest to be able to account for the most essential sources of fatigue scatter and to incorporate them into the predictive schemes. This helps to reduce the required safety factors on the fatigue limit and the design stress. Thus, the accurate statistical assessment of fatigue life, based on predictive models, is an indispensable step towards arriving at more reasonable and less conservative safety factors enabling the weight reduction of a structure.

3.3.2 Weibull plot

The Weibull distribution is one of the most widely used distributions in reliability analysis [137]. The most common form of the Weibull CD-function of fatigue life N is as follows [138]:

$$F(N) = 1 - \exp\left(-\left(\frac{N - N_0}{N_\alpha}\right)^\beta\right), N \geq N_0, \quad (3.8)$$

where N_α is a scale parameter (characteristic life), β is the shape parameter that determines the appearance or shape of the distribution and N_0 is the location parameter. Characteristic life corresponds to a number of cycles at which 63.2% of the specimens is expected to fail [139]. For $N_0 = 0$, Equation (3.8) becomes the two-parameter Weibull distribution or standard Weibull model with a distribution function

$$F(N) = 1 - \exp\left(-\left(\frac{N}{N_\alpha}\right)^\beta\right). \quad (3.9)$$

A principal objective of the lifetime statistical analysis is to use the available experimental data in order to verify the validity of the chosen Weibull probability model, estimate the model characteristics, and to make a statement about the effect of any fatigue improvement techniques on the lifetime distribution. To assess the fit of an assumed model, a graphical method, based on probability plots, was used in this work. The Weibull probability plot (WPP) is a common graphical method for informally checking the assumption of the Weibull distribution model and for estimating the two Weibull parameters [136]. This method is very popular due to its simplicity, graphical appeal, and effectiveness. In the early 1970's, a special paper was developed for plotting the data in this format [140]. Nowadays, most numerical software packages for reliability assessment contain programmes to produce these plots. The WPP can be constructed taking logarithms twice of both sides of Equation (3.9):

$$\log(-\log(1 - F(N))) = \beta \log(N) - \beta \log(N_\alpha). \quad (3.10)$$

Plotting $y = \log(-\log(1 - F(N)))$ against $x = \log(N)$, as is usually done in a Weibull plot, one should see the following linear relationship:

$$y = \beta (x - \log(N_\alpha)). \quad (3.11)$$

If the Weibull distribution is a reasonable fit for the experimental data, they should follow a straight-line pattern when plotted by the WPP methodology. To plot the experimental data on the WPP, the empirical distribution function has to be found. The latter can be estimated as follows. First, for a given test data series, N_1, \dots, N_k , that was experimentally determined, the lifetimes are ordered from the smallest to largest to get $N_{(1)} \leq \dots \leq N_{(k)}$. Then, the found values are associated with empirical estimates of their CD-function p_i (or the so-called p_i -quantile estimates), which can be calculated by the Bernard's median rank formula [138]:

$$p_i = \frac{i - 0.3}{k + 0.4}, \quad (3.12)$$

where i is the number of failed specimens with $N < N_{(i)}$, k is the sample size (total number of specimens). Finally, a probability plot is created by plotting the ordered experimental data $N_{(i)}$ against the $\log(\log(1 - p_i))$ values in a special Weibull probability format. The vertical axis of this plot is then scaled to obtain the Weibull distribution as a linear relationship. After comparing the two different types of welding or post-weld treatments, all the test series are plotted in one WPP and the conclusion is made by contrasting the characteristic lives and shape parameters. The described procedure was applied to quantify the effect of LSP on the fatigue behaviour of welded joints and is presented in Section 5.4.

3.3.3 Multivariate random variables

To correlate the fatigue life scatter with the variations of internal defects, a probabilistic fatigue assessment model has to be developed. Within this model, an internal defect is characterized by two stochastic parameters: the size and position, which can be combined into one two-dimensional random variable. Multivariate random variable is an effective tool to characterize the behaviour of several uncertain numerical quantities correlated to each other within the same probabilistic model. This section briefly describes some mathematical instruments and terminology used in this work to deal with them.

Let (X, Y) be a set of two continuous random variables designated as a random vector or two-dimensional (bi-variate) random variable. Analogous to univariate random variables, the joint cumulative distribution function (joint CD-function) of a bi-variate random variable is defined as

$$F_{X,Y}(x, y) = P(X < x, Y < y). \quad (3.13)$$

In other words, the joint CD-function is equal to the probability of X and Y being smaller than x and y , respectively. According to the fundamental statistical properties of CD-functions, it is non-negative, non-decreasing, and tends to 1, when $x, y \rightarrow \infty$ (normalization condition).

The joint probability density function (joint PD-function) is then defined as the second partial derivative from a CD-function over its components

$$p_{X,Y}(x, y) = \frac{\partial^2 P_{X,Y}(x, y)}{\partial x \partial y}. \quad (3.14)$$

For a known joint PD-function, it is relatively easy to visualize the behaviour of a bi-variate random variable by plotting the contour lines of $p_{X,Y}(x, y)$. An example of this plot is shown in Figure 7.6(a) for the joint PD-function of a pore size and depth in a weld.

The joint PD-function enables to compute the probability that a bi-variate random variable belongs to an area S in the probability space. This can be done by integrating the joint density over this area:

$$P((X, Y) \in S) = \int_S p_{X,Y}(x, y) dx dy. \quad (3.15)$$

The distribution of individual components of a multivariate random variable can be deduced from the joint distribution function. For a given bi-variate joint PD-function, the marginal distribution of an individual random variable X can be obtained by integrating the joint PD-function over another component:

$$p_X(x) = \int_{y=-\infty}^{\infty} p_{X,Y}(x, y) dy. \quad (3.16)$$

If the two individual random variables X and Y are interdependent, i.e. there is a correlation between them, a conditional PD-function of X given Y can be defined as

$$p_{X|Y}(x|y) = \frac{p_{X,Y}(x, y)}{p_Y(y)}. \quad (3.17)$$

On the other hand, the two random variables are mutually independent if, and only if, their joint PD-function factors into the individual marginal density functions

$$p_{X,Y}(x, y) = p_X(x) \cdot p_Y(y). \quad (3.18)$$

The presented mathematical operations with two-dimensional random variables provide a necessary theoretical background for the development of a probabilistic model accounting for the stochastic nature of the internal defects that initiate fatigue cracks. A detailed description of the mathematical tools used in the multivariate statistical analysis can be found elsewhere [138].

4 Weld characterization

The aim of this chapter is to provide a comprehensive analysis of the weld characteristics including the weld quality, microstructure, and mechanical properties. First, optimization of the principle LBW process parameters is briefly presented. Then, the microstructure and microtexture of the weld zones are characterized in detail with a particular emphasis on the influence of the heat treatment on the weld microstructure. Finally, the tensile and fatigue properties of the welded butt joints are described on the basis of extensive experimental data. The link between the microstructural features and the resulting mechanical properties is discussed. The results presented in this chapter are very important because they act as a starting point for further fatigue strength improvement and modelling of the fatigue performance. The content of this chapter has been partially published in [141].

4.1 Laser beam welding (LBW)

The final weld characteristics are attributed to a combination of the welding parameters that define the interaction of the laser beam with a specimen surface. The definition of the process parameters is of great significance to achieve a sufficient weld quality. In practice, there are two different approaches to the determination of the optimal parameter set, namely design of experiments (DoE) and simple trial and error method. DoE is a powerful tool for determination of the optimum set of process parameters that helps to minimise the number of experiments and material needed [142]. In spite of the numerous benefits of DoE, identification of the process parameters in this study was accomplished based on conventional empirical analysis. There are two principal reasons that should be mentioned in this regard. First, the results of optimization rely on a set of the weld quality criteria comprising quite a long list of requirements in accordance with the aerospace standards [120, 121]. Very often, only a few of them are taken as objective functions for DoE analysis, e.g. the porosity level and the weld width. As a result, other factors are not accounted for and the ‘optimum’ parameter set found by this strategy does not fully comply with the given quality regulations. On the other hand, accounting for all the relevant weld quality characteristics accompanied by careful statistical analysis is a time-consuming task that does not fully conform to the main objectives of this work. The majority of the weld properties can be usually described implicitly by the simple functions of laser power or welding speed. Therefore, it is significantly more effective to find these relationships empirically in the desired parameter window without wasting material for redundant experiments.

Although it may seem inappropriate to conduct a further analysis without a careful and detailed optimization of the welding parameters based on DoE, the chosen methodology fully corresponds to the basic philosophy of this work. In practice, the process parameters are not completely transferable from one welding facility to another due to differences in laser sources, experimental set-up, or clamping. Moreover, as will be shown further, the results of optimization are very sensitive and depend not only on the specimen thickness but also on the specimen size. Hence, the resulting optimum parameter set cannot be used when some of these influential factors slightly deviate from the given value. Instead of choosing the best weld obtained in a particular laboratory and dealing with it, an alternative methodology to deal with any weld, even with insufficient quality, should be developed. Instead of looking for an ideal weld, the focus of this work is on the post-processing techniques that will increase the mechanical properties even if the process parameters are not carefully adjusted. In other words, the subsequent weld treatment will tolerate the weld imperfections caused by inappropriate welding parameters.

In the early stages of the work, the LBW process parameters were consistently varied in a systematic way to identify the weld with sufficient quality characteristics. As an initial point, the results of the previous study on LBW of Ti-6Al-4V [11] were used and further improved. For this purpose, the following assessment criteria for a good weld were employed: full penetration, minimum laser power, maximum welding speed, minimum underfill depth and reinforcement height. At this stage, the porosity level was not considered for the sake of simplicity and to save time. The problem of internal defects will be studied in detail in Section 4.9, where the LBW parameters will be optimized, exclusively based on the number of pores.

The LBW process parameters used in the present work are listed in Table 4.1. Parameter sets leading to insufficiently penetrated joints are not included in the table. Initially, the small coupons with dimensions $40 \times 80 \text{ mm}^2$ were used for experiments. However, the optimum parameter set identified using the small coupons was not completely transferable to large specimens. Regions of incomplete penetration are typical weld defects when the specimen size is relatively large. Plausible reasons for this size effect can be attributed to higher heat transfer to the base metal and instabilities in laser power over the weld length. A slight increase in laser power by around 10% has a positive effect and normally eliminates this problem. Although the overall efficiency is slightly lowered by this action, a stable weld quality over the entire length of the joint is achieved. Parameter set #4754 was finally employed for the welding of large $110 \times 190 \text{ mm}^2$ coupons, from which the fatigue specimens were then extracted.

Table 4.1. LBW process parameters investigated in the optimization process.

Specimen number	Laser power, kW	Welding speed, m/min	Focus position, mm	Filler wire feed rate, m/min	Argon flow, l/min
#2986	4.5	2.5	0	3.0	15
#2988	4.5	4.0	0	3.0	15
#2992	4.5	4.0	-3	0	15
#2993	4.5	4.0	-3	2.0	15
#2994	5.0	4.0	-3	2.5	15
#2995	5.5	4.0	-3	3.0	15
#2996	5.5	4.0	-3	3.5	15
#2997	5.5	4.0	-3	2.5	15
#3001	5.5	4.0	0	3.0	15
#4754	5.5	4.0	0	4.0	15
#4920	3.5	3.0	0	0	15
#4921	7.0	4.0	0	0	15

Cross sections of some of the most representative parameter sets from the previous table are demonstrated in Figure 4.1(a–f). The upper row of images contains the welds without filler material, and the lower row presents the welds performed with an addition of Ti-6Al-4V filler material. Without filler metal, underfills are always present and their depth increases with an increasing laser power. The addition of filler wire partially or totally eliminates the weld underfills; however, additional material in the weld zone leads to the formation of reinforcements that are more pronounced with increasing heat input. Despite some beneficial effect, the use of filler material

increases the complexity and sensitivity of the welding set-up due to an additional wire-feeding device. The parameter set corresponding to the optimal combination of weld characteristics is shown in Figure 4.1(e). An additional 500 W in the total laser power in total 5.5 kW is needed to prevent the previously mentioned lack of penetration for large specimens.

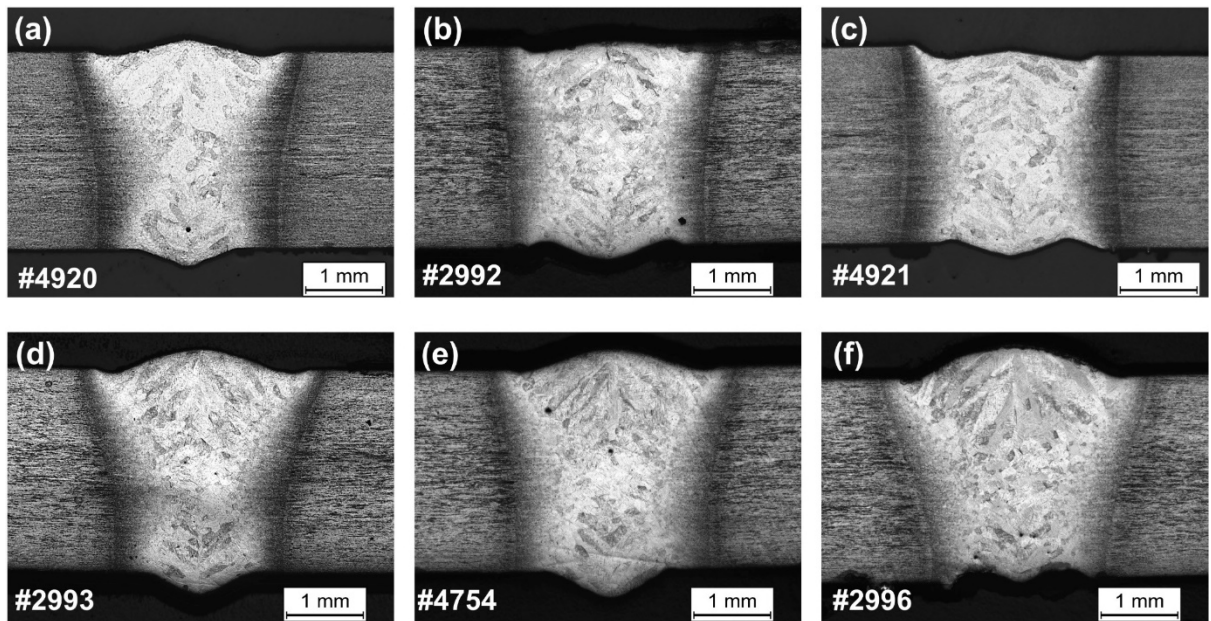


Figure 4.1. Typical cross sections of welded seams produced with different process parameter sets. Specimen configurations correspond to those listed in Table 4.1.

The optimum parameter set defined in this section should not be considered as a single possible parameter set resulting in a high-quality weldment. As shown in Figure 4.1(a–f), fully penetrated joints can be produced in a relatively wide window of process parameters. Therefore, the chosen parameter set acts more as a recommendation and will be used for further characterization. Following the above-mentioned philosophy of this work, LBW is only an instrument to produce the specimens containing defects for subsequent fatigue analysis. Optimization of the LBW parameters itself is not in the focus of this study. The weld defects produced by inappropriate welding parameters are in some cases even desirable in this work in the sense that their effect on fatigue properties is studied.

4.2 Macroscopic appearance of the weld

In this section, the main macro-characteristics of the Ti-6Al-4V butt joint welded with the optimum process parameters (#4754) will be analysed by means of optical microscopy. Hereinafter, the results of the analysis refer to this particular parameter set. A visual inspection of the laser weldments showed bright silver metallic surfaces from the top and root sides, indicating stable argon shielding gas atmosphere during the LBW process. All the welds were fully penetrated and showed an hourglass seam shape. A typical transverse cross section of the laser-beam-welded joint is shown in Figure 4.2(a, b). Three distinct regions of the weld are visible: the fusion zone (FZ), heat-affected zone (HAZ) and unaffected base material (BM). The FZ was distinguished by its columnar prior β grains, which grew from the fusion line to the weld centre (see Figure 4.2(a, b)). This distinctive coarse-grained morphology is clearly visible even with low magnification. The fusion line that is a boundary between the FZ and the HAZ has a smooth contour and can be distinguished by the first layer of epitaxially grown β grains. It should be noted that no significant differences in the weld

geometry and shape were found between the as-welded and heat-treated conditions. Heat treatment temperatures were not sufficiently high to affect the weld macro-characteristics.

Note that Figure 4.2(a, b) contains two cross sections of the same weld, although their shape and appearance may look different. The underlying reason for this effect is the inherent unsteadiness of the weld characteristics over the length of the joint. A comparison of the cross sections presented in Figure 4.2(a) and (b) indicates significant differences in the weld shape, reinforcement height and the underfill depth. For instance, the macrograph presented in Figure 4.2(a) reveals almost no underfills, whereas relatively deep underfills of 110 μm are observed in another weld cross section demonstrated in Figure 4.2(b). Thus, a single weld cross section cannot guarantee the uniformity of the weld profile over the whole length of the seam. This problem can usually be solved by extracting more than one specimen for metallurgical examination. Instability of the weld properties over its length is of great practical importance and leads to the conclusion that the weld characteristics should be considered as random variables and require corresponding statistical tools for their assessment. This problem should be carefully addressed if the experiments are designed and evaluated by the DoE or other statistical tools. Very often, the above-mentioned phenomenon is totally neglected and the analysis is based exclusively on a ‘typical’ weld cross section that does not fully reflect the real situation. The basic problem of treating the weld characteristics as stochastic variables is related to the increased time and costs of the work needed to prepare multiple cross sections. In this work, the welding seam was subjected to statistical analysis on the basis of five measurements in different cross sections.

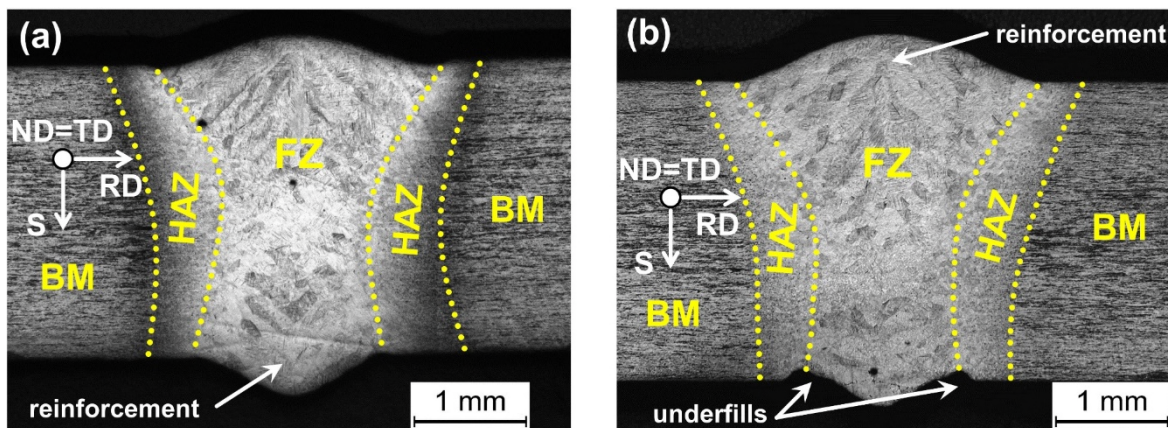


Figure 4.2. Two different cross sections of the same laser-beam-welded Ti-6Al-4V butt joint: (a) cross section with almost no underfills; (b) cross section with excessive filler material from the top side and 110- μm -deep underfills at the root side.

The most frequently observed defects in laser weldments of titanium alloys are underfills and FZ porosity [13, 55]. These imperfections are particularly undesirable for structures subjected to cyclic loading because they lead to stress concentration and, consequently, premature crack formation. The evaporation and/or expulsion of the molten material from the weld pool and liquid metal flow around the keyhole are dominant processes affecting the formation of underfills [13, 65], which are always present in cases of autogenous laser welding. The use of an additional filler wire enables overfilling to be produced and geometrical weld imperfections such as underfills to be partially eliminated. Note that Figure 4.2(b) illustrates that the underfill depth varies along the weld length. Additionally, the use of filler wire resulted in weld reinforcements from the top and root sides. An abrupt change in thickness due to weld reinforcement leads to stress concentration at the weld toes and reduces the fatigue strength of the joints as well. In the present work, the maximum measured underfill depth was

approximately 125 μm , which is less than 5% of the specimen thickness. The maximum observed reinforcement was approximately 350 μm , which is 14% of the plate thickness.

The quality of laser weldments used in the aerospace industry is strictly regulated by several standards, for example, the American AWS D17.1 [121] and European EN 4678 [120]. In terms of underfills and weld reinforcements, EN 4678 is more stringent; the maximum allowed underfill depth for butt joints is limited to 5% of the total thickness and maximum reinforcement to the value of $(0.15 \cdot t + 0.1)$ mm, where t is the specimen thickness. For the 2.6-mm-thick plates, this leads to the maximum allowed values of 130 μm and 490 μm for underfills and reinforcements, respectively. In comparison, the AWS D17.1 standard restricts the underfill depth to 7% and the reinforcement height to 33% of the plate thickness. Hence, the optimum weld produced in this work confidently passed the acceptance criteria in terms of the weld profile imperfections for the aerospace industry.

Numerous pores typically encountered in the cross sections of the weld indicate that the welding-induced internal defects are always present in the weld zone. However, the number of pores in a single cross section does not suffice for their statistical processing as it is normally done for non-metallic inclusions in steel [68]. A radiographic inspection is needed for this purpose. The spherical shape of most pores observed in the present study indicates a gas-type porosity. The investigation into the influence of welding parameters on the amount of porosity in the laser-beam-welded Ti-6Al-4V butt joints will be described in Section 4.9.

4.3 Microstructural analysis

Three distinct regions of the welding seam, as shown in Figure 4.2(a, b), were carefully studied by means of OM and SEM. OM is a fast and simple way for microstructural characterization; however, it has a limited magnification (up to $\times 1000$) and the results obtained are usually more qualitative in nature. Thus, the general appearance and the weld zones were primarily investigated by OM and the regions of interest were then observed with higher magnification using SEM. EBSD measurements with the special *OIM Analysis*TM software enabled the measurement of the average grain size, β -phase content and the quantitative texture analysis. In the following sections, the microstructure of each weld region is described in detail.

4.3.1 Base material (BM)

The as-received BM microstructure of the 2.6-mm-thick Ti-6Al-4V sheet consists of globular α grains with the average grain size of 3.1 ± 0.6 μm and an intergranular retained β phase, as shown in Figure 4.3(a, b). The bright regions in Figure 4.3(a) are the equiaxed or lamellar α grains and the dark regions are the intergranular β phase distributed at the α grain boundaries. The volume fraction of the β phase was estimated to be around 10%, which is typical for the Ti-6Al-4V alloy [22]. Figure 4.3(a) shows an OM image of the BM microstructure in the middle section of the sheet. It corresponds to what is known as the mill-annealed microstructure for a hot-worked plate that is not fully recrystallized [22, 28]. Mill-annealing is a very common processing route in which the recrystallization step is completely omitted and the cooling rate after hot deformation determines the

resulting microstructure. As a result, non-recrystallized regions with deformed lamellar appearance are partially retained and spread in the equiaxed microstructure, as shown in Figure 4.3(a, b).

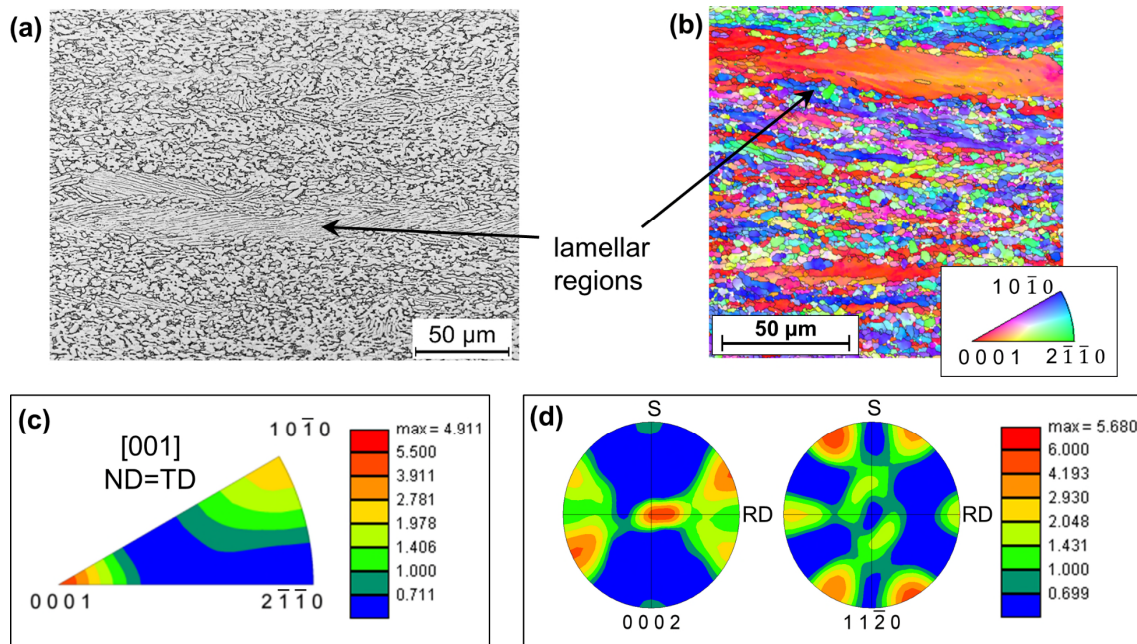


Figure 4.3. Microstructure of the BM in the as-received mill-annealed condition. (a) OM image; (b) crystal orientation map; (c) inverse pole figure; (d) (0001) and $(11\bar{2}0)$ pole figures.

As mentioned in Section 2.1.3, crystallographic texture of the α phase can influence the mechanical properties of the final product [73, 143]. For the as-received Ti-6Al-4V sheet material, the crystal orientation primarily develops through the deformation process involved in the hot rolling. The microtexture analysis, as represented by the orientation map and pole figures in the cross-section plane, is shown in Figure 4.3(b–d). The regions of analysis shown in Figure 4.3(c, d) are taken from the middle section of the plate. It should be kept in mind, that the normal to the cross section (ND) coincides with the transverse direction of the sheet ($ND=TD$), and S stands for the thickness direction (see Figure 4.2). The colour in the crystal orientation map (Figure 4.3(b)) is based on a colour-coded inverse pole figure, where different colours refer to different crystallographic orientations. The laminated morphology of material in the rolling direction, which is clearly visible in Figure 4.3(a, b), apparently originates from the plastic deformation of lamellar structure during the rolling process and subsequent recrystallization. The large, red regions in the orientation map in Figure 4.3(b) correspond to not fully recrystallized lamellar regions. They have the same colour due to an almost equal crystallographic orientation and were not considered for the calculation of the average grain size. It may be noted that the large lamellar zones can be regarded as coarse single grains surrounded by a fine-grained matrix. As will be shown further, these regions have a big negative impact on the fatigue behaviour and should be considered with a great deal of caution.

The base material texture is characterized by preferred crystal directions such as $\langle 0001 \rangle // ND$ (4.87 mrd (multiple of a random density)) with spread angles between 10° and 20° as well as less pronounced $\langle 10\bar{1}0 \rangle // ND$ (2.52 mrd) with spread angles between 15° and 25° , as shown by the inverse pole figure in Figure 4.3(c). The grains with a $\langle 10\bar{1}0 \rangle // ND$ crystal direction are in blue coloured in Figure 4.3(b) and grains with $\langle 0001 \rangle // ND$ crystal direction are in red, respectively. The (0002) pole figure shows that basal planes are aligned both in the rolling direction (RD) and transverse direction

(TD) (see Figure 4.3(d)). According to an investigation by Salem [143], this type of texture indicates that the Ti-6Al-4V sheet was cross-rolled. Based on the analysis of the orientation distribution function (ODF), which is not presented here for the sake of brevity, the main texture components were identified: $\{0001\}\langle 11-20 \rangle$ ($11.6 \text{ mrd} < f_{OD} < 13.5 \text{ mrd}$) and $\{01-10\}\langle 2-1-10 \rangle$ ($4.3 \text{ mrd} < f_{OD} < 9.6 \text{ mrd}$), where f_{OD} is the ODF probability density function. The designation $\{hkil\}\langle uv tw \rangle$ means that the $\{hkil\}$ planes of the grains are oriented parallel to the sheet plane, whereas the $\langle uv tw \rangle$ directions are parallel to the rolling direction.

4.3.2 Fusion zone (FZ)

High peak temperatures, severe temperature gradients, and rapid thermal fluctuations occur as the laser beam passes through a material. The boundary of the FZ – the so-called fusion line – corresponds to the position of a solidus temperature ($T_s = 1604^\circ\text{C}$ for titanium). During the welding process, the material of the FZ is melted and subsequently resolidified. Microstructural transformations taking place upon solidification of the molten pool lead to the resulting morphology that is quite different from the original prior to melting. As a result, the position of the fusion line can be clearly distinguished by the coarse-grained morphology, as opposed to the fine globular BM microstructure (see Figure 4.2).

A basic understanding of the welding metallurgy and the main mechanisms of transformation kinetics are needed to explain this morphology of the weld region. The fusion welds solidify from the edge of the fusion zone and the solid-liquid interface moves in towards the weld centreline. Once the solidification is complete, the local temperature of the material starts decreasing gradually. Solid-state transformations during the cooling period alter the local microstructure and depend on the alloy composition. As discussed in Section 2.1.3, the Ti-6Al-4V titanium alloy undergoes an allotropic change from a high-temperature BCC β phase to a low-temperature HCP α phase upon cooling [22]. Hence, the $\beta \rightarrow \alpha$ transformation occurs on the trailing edge of the weld zone, as a single-phase β region transforms into the α phase. The resulting products and morphology, therefore, can be related to the cooling rates during solidification.

The FZ microstructure is characterized by columnar prior β grains that grow from the HAZ in the direction opposite to that of the heat flow and impinge at the weld centre line after solidification, as shown by OM image in Figure 4.2(a). The average size of prior β grains depends primarily on the heat input during LBW, with a higher heat input promoting a larger grain size [13, 65, 144]. In the present study, the average prior β grain size in the as-welded condition was approximately 200–300 μm . Figure 4.4(a) demonstrates that within the prior β grains, the FZ predominantly consists of an acicular α' martensite, resulting from a diffusionless $\beta \rightarrow \alpha'$ transformation upon high cooling rates encountered in the LBW process. The martensitic microstructure is characterized by long, orthogonally oriented thin plates having an acicular morphology similar to one reported by Ahmed and Rack [35]. Since no secondary α phase was observed along the prior β grain boundaries, it can be concluded that the cooling rate in the welding zone was high enough to provide the $\beta \rightarrow \alpha'$ diffusionless transformation during the laser welding, i.e. more than 410 K/s. The microstructure observed in the FZ is a typical type of microstructure for FZ of laser-welded joints [11, 13] as well as electron-beam-welded joints [53, 145]. As shown in Section 4.3.5, the microstructure of the FZ is very close to that obtained after water quenching from the β -phase field. Consequently, the cooling rates during the LBW process are comparable to rapid cooling in water.

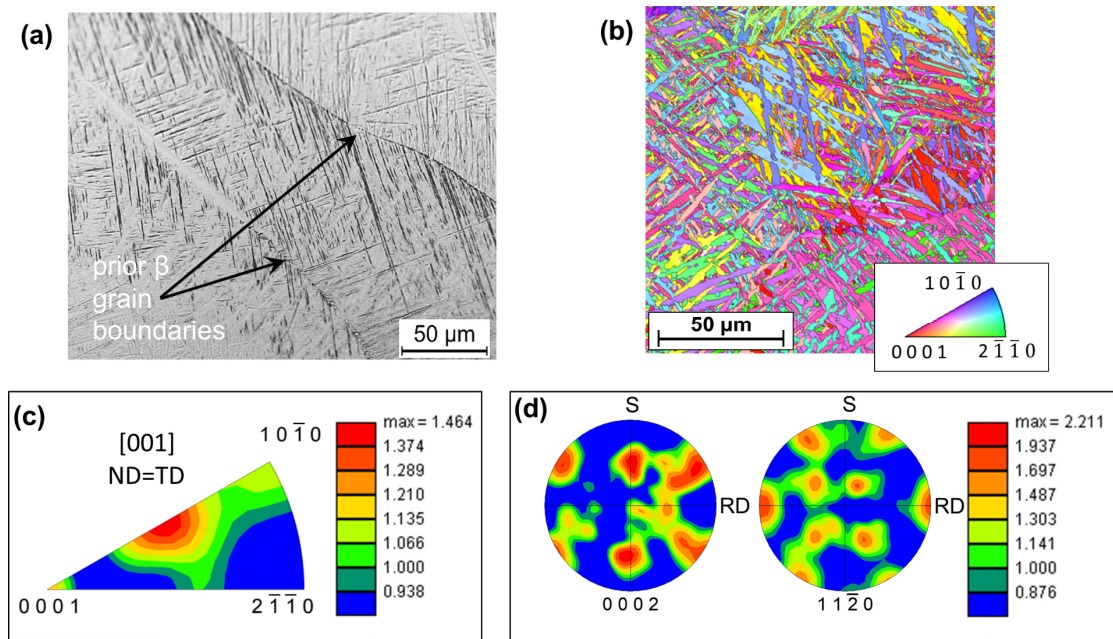


Figure 4.4. Microstructure of the FZ. (a) OM image of the microstructure; (b) orientation map in the cross section; (c) inverse pole figure; (d) (0001) and (11-20) pole figures in the cross-section plane.

It is of great importance to understand and characterize the changes in crystal orientation that took place in the weld region due to melting and subsequent solidification. Owing to the coarse-grained morphology in the FZ, the main microtexture components were examined at a lower magnification ($\times 100$) in order to obtain higher statistical weight. It can be seen in Figure 4.4(c, d) that the FZ is characterized by considerably weaker texture components than those of the BM. Strictly speaking, pole figures of the FZ reveal almost a random texture without any preferred orientation. This is related to the fact that this zone was completely melted during the LBW process. However, the FZ texture has some interesting features that are worth mentioning. First, it can be concluded that the $\{0001\}\{11-20\}$ and $\{01-10\}\{2-1-10\}$ texture components, which are the strongest in the BM, are comparatively less pronounced in the FZ. Additionally, based on a microtexture analysis, the main direction of crystal growth during solidification of the molten pool can be determined. Comparing the (11-20) pole figures shown in Figure 4.3(d) and Figure 4.4(d), it can be inferred that the preferred direction of crystal growth was the $\langle 11-20 \rangle // \text{RD}$ crystal direction.

4.3.3 Heat-affected zone (HAZ)

HAZ is a transition region between the acicular morphology of the FZ and the globular microstructure in the BM. It is usually subdivided into two sub-regions based on the β transus temperature: near-HAZ and far-HAZ. In the HAZ adjacent to the FZ (near-HAZ), the temperatures during the LBW process exceed the β transus. Consequently, this region consists predominantly of the transformed acicular microstructure. Since the temperatures in the HAZ adjacent to the BM (far-HAZ) are lower than the β transus, its microstructure is very similar to that of the BM. Microstructure analysis of both the near-HAZ and far-HAZ is shown in Figure 4.5(a–f).

As illustrated in Figure 4.5(a), the microstructure of the HAZ zone adjacent to the BM (1.4 mm from the weld centre) remained nearly equal after the thermal cycles imposed by the neighbouring FZ. However, it was characterized by finer globular grains having an average size of $2.1 \pm 0.7 \mu\text{m}$ and a wider distribution of crystal directions between $\langle 0001 \rangle // \text{ND}$ and $\langle 10-10 \rangle // \text{ND}$ compared to that of the

base material (see Figure 4.3(c)). A textural analysis has shown that the strongest texture components are still $\{0001\}\langle 11\text{-}20\rangle$ ($11.8 \text{ mrd} < f_{OD} < 14.0 \text{ mrd}$) and $\{01\text{-}10\}\langle 2\text{-}1\text{-}10\rangle$ ($4.7 \text{ mrd} < f_{OD} < 8.6 \text{ mrd}$) but they are superimposed with other weaker components, leading to a slight misorientation of around 5° . Some of the BM components have been dissolved and new components have emerged within the orientation band after welding. The misorientations between the base material and the heat-affected zone indicate microstructural distortion of laser-beam-welded Ti-6Al-4V butt joint due to the heat input and the subsequent rapid cooling during the joining process.

A significant change of microstructure was observed for the near-HAZ at a distance of 1.06 mm from the FZ centre line, as shown in Figure 4.5(d-f). The equiaxed initial microstructure of the BM was transformed into the acicular morphology with a small amount of embedded globular grains. The transformation was accompanied by grain refinement and a further weakening of the $\{0001\}\langle 11\text{-}20\rangle$ component dominating in the BM and far-HAZ adjacent to the BM. The $\langle 11\text{-}20\rangle$ pole figure shows a tendency towards the formation of $\langle 11\text{-}20\rangle//\text{RD}$ fibre texture present in the FZ (Figure 4.5(f)). This fact confirms that $\langle 11\text{-}20\rangle//\text{RD}$ is the preferred direction of crystal growth during the solidification.

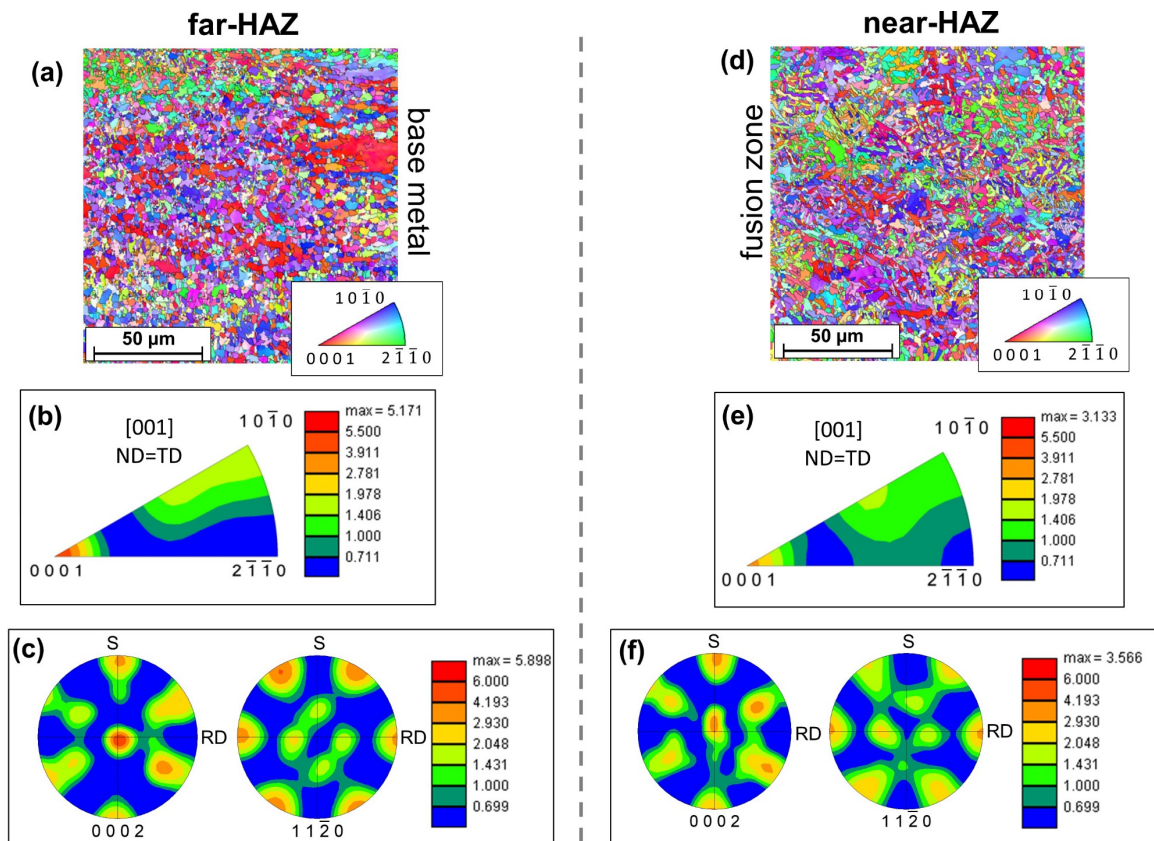


Figure 4.5. Microstructure of the HAZ in the as-welded condition: (a–c) orientation map, inverse pole figure and pole figures of the far-HAZ; (d–f) orientation map, inverse pole figure and pole figures of the near-HAZ.

4.3.4 Effect of heat treatment on the weld microstructure

A crystallographic analysis of the heat-treated welds revealed no significant texture transformations after the application of PWHT. The previously identified dominant texture components were not affected in spite of slight deviations in numerical values of peaks. Orientation maps and pole figures of the heat-treated specimens did not show any significant deviations from the as-welded condition.

Apparently, heat treatment at temperatures lower than the β transus without any deformation is not sufficient for texture variations. Therefore, our further analysis will focus mainly on microstructural characteristics such as the average grain size, which can be determined by conventional OM.

Figure 4.6 shows the influence of various types of PWHT on the average grain size in the BM as well as the average lamella thickness in the weld zone. The graph shows a steady increase in the grain size with increasing PWHT temperatures. In general, all the investigated types of PWHT can be categorized into two groups, according to their influence on the grain size. Heat treatments at temperatures less than 750°C (SRA1 and SRA2) did not change the grain size significantly neither in the BM nor in the FZ. The recrystallization processes, leading to coarsening of the microstructure, were activated at higher temperatures starting from 800°C (FA2 and RA). The maximum average grain size in the BM is reached after recrystallization annealing at 920°C and is equal to $4.9 \pm 1.5 \mu\text{m}$.

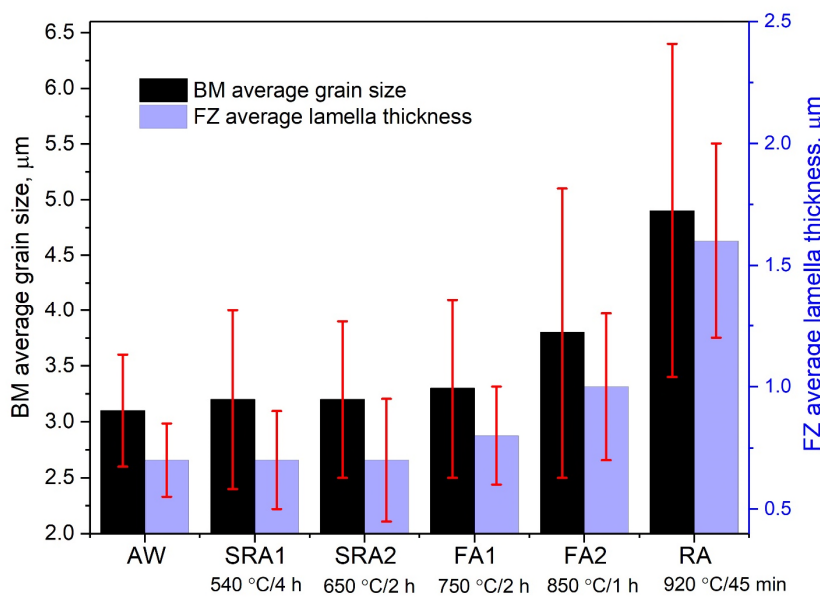


Figure 4.6. The influence of PWHT on the grain size in the BM and the lamella thickness in the FZ.

OM images of the BM microstructure after PWHT at temperatures higher than 750°C are shown in Figure 4.7. The results of stress-relief annealing at lower temperatures are not shown because the OM detected no significant microstructural changes after their application. It can be seen that the application of the heat treatment in the range of 750–900°C leads to grain coarsening of the BM, and this effect is more pronounced at higher temperatures. The α phase is fully recrystallized after RA and almost all the lamellar regions are transformed into equiaxed grains. The latter effect of a gradual decomposition of α lamellae into globular grains at high temperature annealing should be emphasized because it is of great practical relevance. As will be shown in Section 6.2, large lamellar regions of the mill-annealed microstructure affect the BM fatigue performance. Therefore, high-temperature annealing is one of the potential methods aimed at the improvement of fatigue properties.

The response of the martensitic FZ microstructure to the application of PWHT has certain features that need to be mentioned. Light microscopic and SEM observations have shown that heat treatments with temperatures up to 650°C (SRA1 and SRA2) do not significantly affect the microstructure of the FZ. Apparently, such low temperatures are not sufficient for complete martensite decomposition

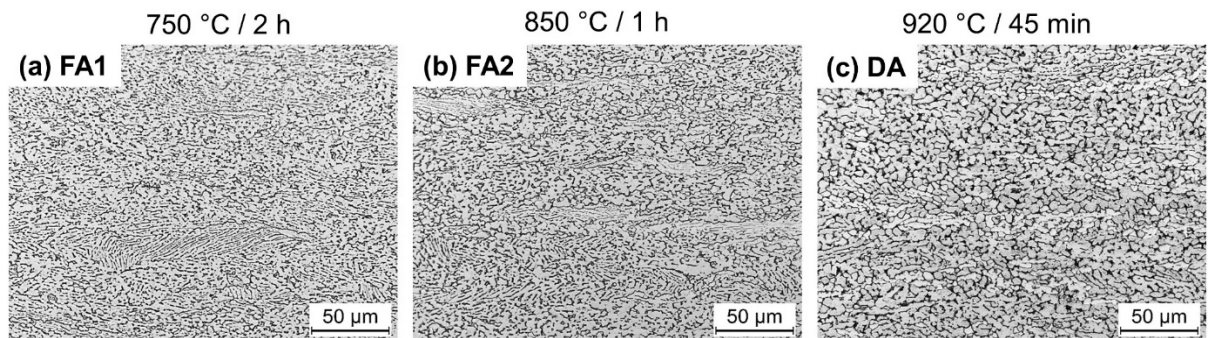


Figure 4.7. The influence of PWHT on the microstructure of the BM. (a) FA1: 750°C for 2 h; (b) FA2: 850°C for 1 h; (c) RA: 920°C for 45 min.

into an equilibrium $\alpha+\beta$ structure. Sallica-Leva et al. studied the effects of the heat treatment on the mechanical properties of an acicular α' martensite obtained by selective laser melting [146]. In their work, the microstructure of the test samples heat-treated at 650°C was very similar to that of the starting condition, whereas significant grain coarsening was observed after heat treatment at 800°C. Their results are in a good agreement with our findings. It is well established that the martensite decomposition occurs by the β phase precipitation and the gradual transformation of the supersaturated α' phase into the α phase by the diffusion of excessive vanadium from the α' to β phase. In this process, β phase is normally precipitated at the α' grain boundaries, i.e. between the martensitic plates.

Figure 4.6 shows the influence of PWHT on the average thickness of α' (α) laths in the FZ. Significant grain coarsening of the microstructure was observed after PWHT at temperatures higher than 800°C. This result is a consequence of transformation of the fine martensitic morphology into an equilibrium lamellar $\alpha+\beta$ structure and the diffusion-controlled growth of obtained platelets at high temperatures, as illustrated in Figure 4.8(a–c). Starting from the temperature of 750°C (FA1), a secondary α phase at prior β grain boundaries, designated as grain boundary α , begins to appear. Furthermore, the thickness of the grain boundary α gradually increases with increasing PWHT temperature. After the DA heat treatment, the colonies of parallel α plates are formed during the recrystallization processes. In contrast, the fine α' needles are nearly orthogonal and the α colonies are not so pronounced in case of a fully martensitic structure (see Figure 4.4(a)). As can be seen from Figure 4.8(c), the α colony size in the DA condition is clearly visible and is approximately 20–30 μm . These α colonies should not be confused with prior β grains. The prior β grain size was not altered after the application of PWHT. Moreover, it is an order of magnitude larger than the α colony size and cannot be seen in Figure 4.8(c) due to high magnification.

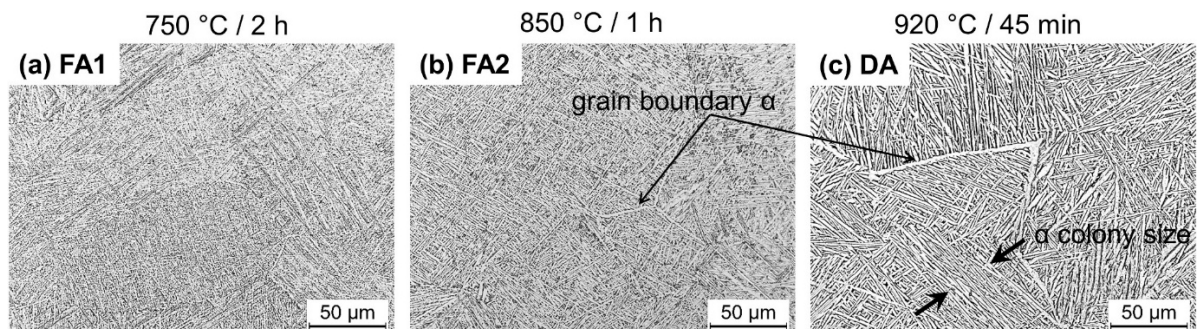


Figure 4.8. Influence of PWHT on the microstructure of the FZ. (a) FA1: 750°C for 2 h; (b) FA2: 850°C for 1 h; (c) DA: 920°C for 45 min.

Since the HAZ has a bimodal microstructure and consists of equiaxed primary α grains in the transformed β matrix, the effect of PWHT on the HAZ microstructure is, somehow, the combination of the above-mentioned effects on the BM and FZ, that is, the coarsening of primary α grains and the transformation of a fine martensitic structure into a coarse lamellar. Both of them have already been described in detail earlier in this Section.

4.3.5 Thermally simulated material of the weld zone

As stated above, a dramatic difference in microstructure and texture between the FZ and BM has been found on comparing the microstructure of the weld zones. This leads to strong gradients of local mechanical properties in the weld region. The variations of local strength over the weld zone is of great scientific and practical importance because it forms the basis of any structural design and assessment. In this work, the development of a fatigue prediction model relies on a careful consideration of the strength mismatch. Therefore, one of the objectives of the work was to experimentally determine the local static and fatigue strength of the material within the FZ. For this, the FZ microstructure was thermally simulated in order to achieve the highest similarity to the FZ in terms of the most important microstructural parameters. A similar approach to the thermomechanical simulation of different weld regions for steel was reported by Madia et al. [147].

Based on the findings discussed in Section 4.3.2, water quenching was employed in order to simulate the rapid cooling accompanying the laser-welding process. The specimens were hung in an atmospheric oven for a short period of time to achieve the β transus temperature and then quenched in the cold water. As a result, a fully martensitic microstructure is formed in the specimen. The most influential parameter in this case is the holding time at high temperature and the temperature itself because these parameters control the β grain growth. Therefore, these two parameters were consistently varied in order to achieve the β grain size equal to that of the FZ and, in addition, the same microhardness.

Based on our findings, to simulate the FZ microstructure, the specimens should be kept in the oven at 1100°C for three minutes and, then, immediately subjected to water quenching. Increased temperature or the holding time may cause an undesired β grain growth. Figure 4.9(a–d) presents the martensitic microstructure simulated by this methodology compared to the weld morphology. It can be seen that there is a satisfactory match between the real and simulated microstructure in terms of the most important microstructural characteristics. Additionally, Figure 4.9(b, d) demonstrates that the simulated martensitic microstructure has equivalent response to the application of the recrystallization annealing. By this, simulated microstructure of the weld after PWHT could be successfully produced. The deviations in microhardness values of the simulated microstructure from the as-welded condition was less than 3%.

The successful accomplishment of the thermal simulation for the FZ microstructure had a significant positive impact on further analysis and characterization, as it enabled the manufacture of the macro-specimens that were used for measuring the mechanical properties of Ti-6Al-4V with three basic types of microstructure: equiaxed, lamellar, and martensitic. As a result, all the microstructural types encountered in the welds have been fully characterized. Based on this method, the specimens for tensile, fatigue, and crack growth testing were produced with fully martensitic and lamellar morphologies, thus simulating the mechanical properties of the weld zone. The latter helped obtain all the fundamental material properties required for the development of a fatigue-assessment model.

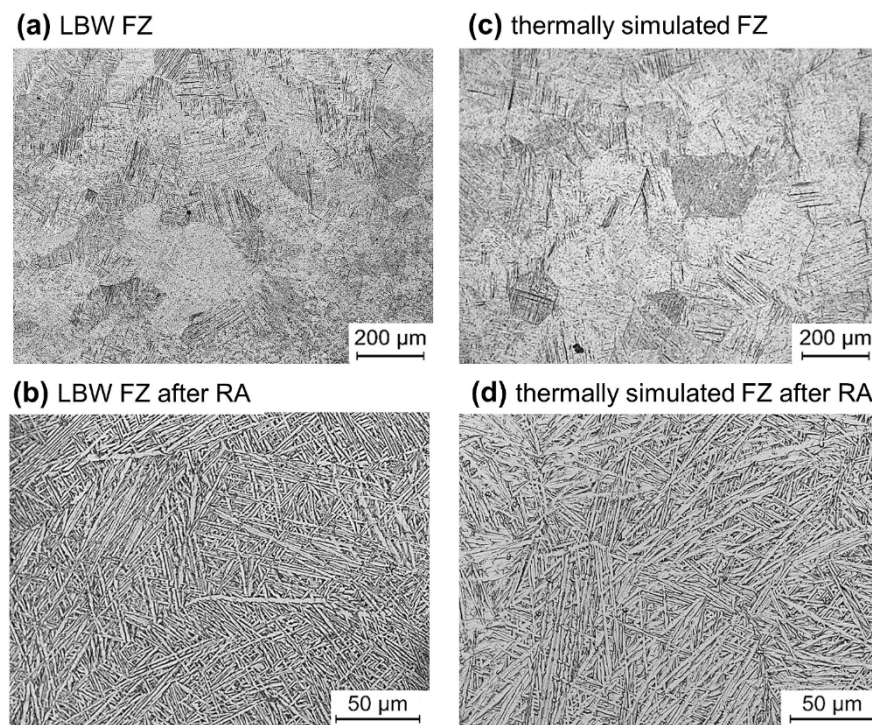


Figure 4.9. Thermal simulation of the FZ microstructure: (a) FZ microstructure in the as-welded condition; (b) thermally simulated material of the as-welded FZ; (c) FZ microstructure after application of RA (920°C, 45 min); (d) thermally simulated material of the FZ after RA.

4.4 Hardness

4.4.1 Microhardness in the as-welded condition

The spatial distribution of microhardness across the laser-welded Ti-6Al-4V butt joint in the as-welded condition is presented in Figure 4.10(a). The microhardness profiles were measured at the top (radiation exposure side), middle, and root sections of the weld, as demonstrated by the corresponding weld cross section in Figure 4.10(a). No statistically significant difference was found among the three testing positions; that is, no thickness gradient was observed in the present study. The average microhardness value of the base material was found to be $336 \pm 8 \text{ HV}_{0.5}$ (mean value with standard error). The FZ exhibits the highest average microhardness of approximately $396 \pm 10 \text{ HV}_{0.5}$, which is, roughly, 18 % more than that in the BM. Owing to a pronounced microhardness difference in a limited volume, it decreases abruptly as the distance from the FZ line increases. The microhardness profile within the FZ is relatively uniform without considerable fluctuations from the average value. Slight deviations in the range of circa $\pm 5\%$ can be related to the fact that a typical hardness measurement spot has a size of about $40 \mu\text{m}$ that is significantly smaller than the average prior β grain size (200–300 μm). As a result, neighbouring points are located in different β grains with a different crystallographic orientation. The latter acts as an additional source of the measurement scatter. Figure 4.10(b) illustrates the above-mentioned observation by an OM image of the microhardness measurement line in the FZ region.

The microhardness map of the weld obtained in this work presents a typical distribution characteristic for laser processed $\alpha+\beta$ titanium alloys. Similar results have been previously reported by several researchers for laser-welded [13, 67] and electron-beam-welded Ti-6Al-4V alloy [50, 51]. An almost

uniform microhardness plateau within the FZ is related to the use of Grade 5 as a filler wire material. In the case of LBW with Grade 2 (commercially pure titanium) filler material, a significant drop of microhardness in the centre of the FZ was observed [11]. Thus, the chemical composition of the filler wire determines the alloying content of the FZ and the resulting microhardness value. The width of the microhardness plateau fully corresponds to the width of the FZ with the near-HAZ, as presented in Figure 4.10(a).

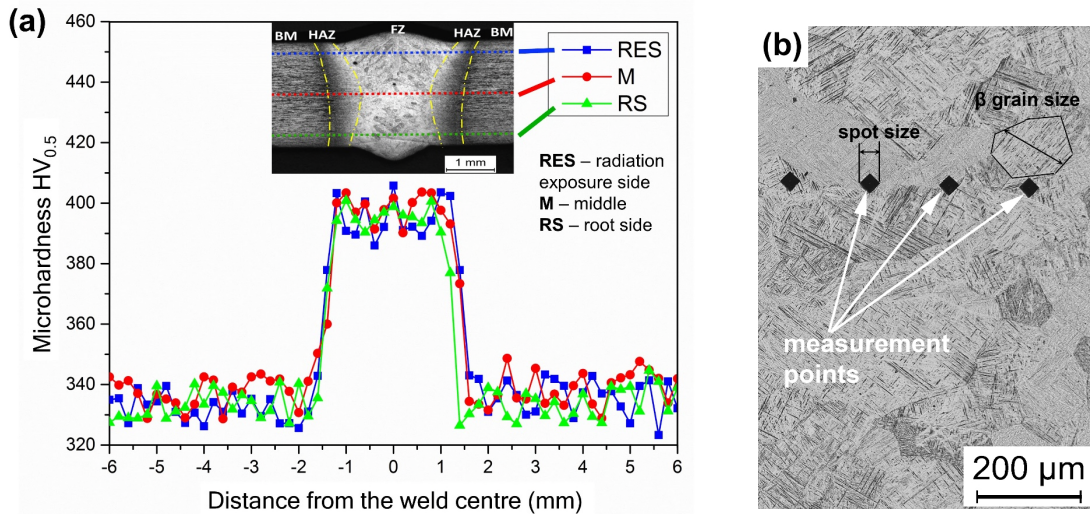


Figure 4.10. (a) Microhardness profile of the laser-welded Ti-6Al-4V butt joint measured in the as-welded condition; (b) OM image of the microhardness measurement line in the FZ.

The steep rise of microhardness from the BM to the FZ through the HAZ is correlated with local changes in microstructure, which were activated during the LBW and subsequent cooling. The occurrence of a maximum hardness value in the FZ is attributed to the formation of a strong martensitic microstructure due to the high cooling rates during solidification. In other words, local self-quenching of the FZ promotes a diffusionless $\beta \rightarrow \alpha'$ transformation accompanied by a considerable hardening effect. An acicular α' phase produced by the martensitic mechanism from the high-temperature β phase field exhibits higher strength and lower ductility, which is attributed to the fine size of the martensitic plates and high defect density [22]. Apparently, the influence of local microtexture plays a minor role in comparison to the hardening effect from $\beta \rightarrow \alpha'$ phase transformation. As clearly is visible in Figure 4.10(a), the HAZ is characterized by strong inhomogeneity and plays a role of a transition zone from an acicular martensitic morphology within the FZ to an equiaxed microstructure in the BM. The strong spatial variation of the microstructure, namely, the decrease in the martensite content, leads to a high gradient of microhardness inside the HAZ. It is worth mentioning that Squilace et al. reported that the hardness gradient in the HAZ is inversely proportional to the heat input during the LBW [13]. However, the parametric optimization conducted in this work demonstrated that welding process parameters have a weak influence on the resulting microhardness profile.

4.4.2 Effect of heat treatment

Hardness mapping provides an additional insight into the spatial distribution of local material properties in the weld region. Being proportional to the material's yield strength, it mirrors the weld strength mismatch. Therefore, microhardness measurements were carried out also for the heat-treated

welds in order to link the microstructural transformations activated by PWHT with the final local mechanical properties. The variations of the average microhardness values in the as-welded condition and after the PWHT under different conditions are shown in Figure 4.11. In this graph, the bar heights represent the mean values from 20 points measured in the corresponding weld area. For simplicity, standard errors of the mean values that are typically in the range of 10–20 HV_{0.5} are not shown. It can be seen that the hardness in the FZ is commonly higher than that in the BM, but their difference depends strongly on the annealing temperature. The changes in microhardness after conducting the PWHT are strictly related to the microstructural alterations that occurred during PWHT. Since the effect of heat treatment depends, in particular, on the initial microstructure, the BM and FZ undergo different transformations, and will be discussed separately in the following sections.

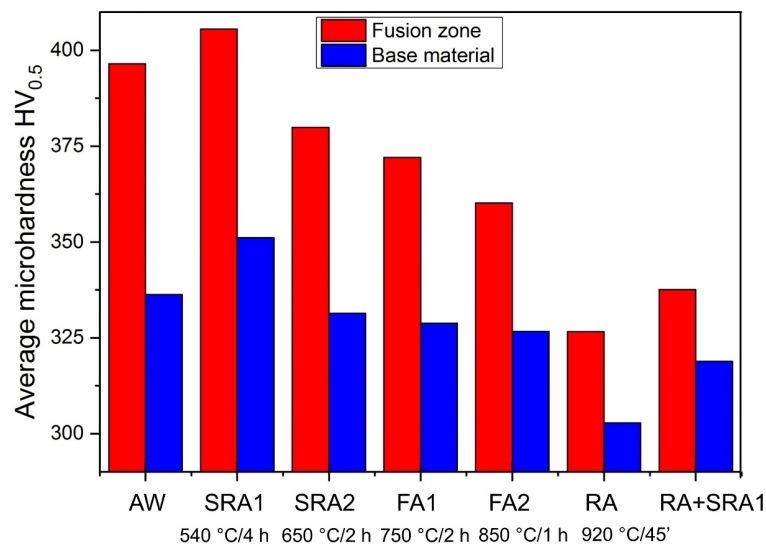


Figure 4.11. Influence of heat treatment on the average microhardness in the FZ and BM.

4.4.2.1 Base metal

As shown in Figure 4.11, annealing at 540°C for 4 h slightly increased the average microhardness of the BM from 336 ± 8 HV_{0.5} in the as-welded condition up to 351 ± 10 HV_{0.5} after annealing. This unexpected hardening effect accompanying the low-temperature annealing was not evident from the OM and SEM observations and can be attributed to precipitation hardening of the α phase by coherent Ti₃Al particles (α_2 phase) [22, 28, 148]. This phenomenon can be explained as follows. During the annealing at 540°C, a significant alloy element partitioning takes place; i.e. the α phase is enriched with α -stabilizing elements (Al), and the β phase is enriched with β -stabilizing elements (V, Fe). The partitioning effect is caused by the diffusion processes activated at this temperature [149]. Coherent α_2 particles can then be precipitated in the α phase by an aging mechanism owing to increased Al content. The age-hardening effect of the α phase in Ti-6Al-4V by the Ti₃Al particles was well documented by Lutjering et al. [22]. In the Ti-6Al-4V alloy, the Ti₃Al solvus temperature is approximately 550°C. Annealing at temperatures lower than 550°C will precipitate α_2 particles, whereas a heat treatment at 600°C will be only a stress-relieving treatment [26]. The latter is in a good agreement with our findings. Heat treatment at 650°C for 1 h led to average microhardness of 331 ± 10 HV_{0.5}, which is slightly lower than that in the starting condition. Evidence for the aging effect at 540°C was not apparent from the OM images or EBSD results because a typical size of the α_2 particles is approximately several dozen nanometres [22].

The fact of element partitioning between the two phases of Ti-6Al-4V during the SRA1 treatment was indirectly proven by the measurements of chemical composition. For this purpose, the alloying element content was experimentally determined by the EDX point analysis of α and β grains. For each phase, 10 measurement points in different grains were used for statistical processing of results. Figure 4.12 shows the average content of alloying elements in the α and β phases after various types of PWHT. As shown in Figure 4.12, Al content in the α phase and V and Fe content in the β phase increase, starting from the lowest annealing temperature (SRA1). Moreover, this partitioning effect is more pronounced at the lowest temperature corresponding to the SRA1 treatment. With increasing temperature, in spite of further partitioning processes, α_2 precipitates are dissolved and do not have any strengthening effect. Thus, it can be inferred that the alloying element diffusion activated at elevated temperatures is responsible for a slight hardening effect by promoting the α_2 precipitation in the α phase.

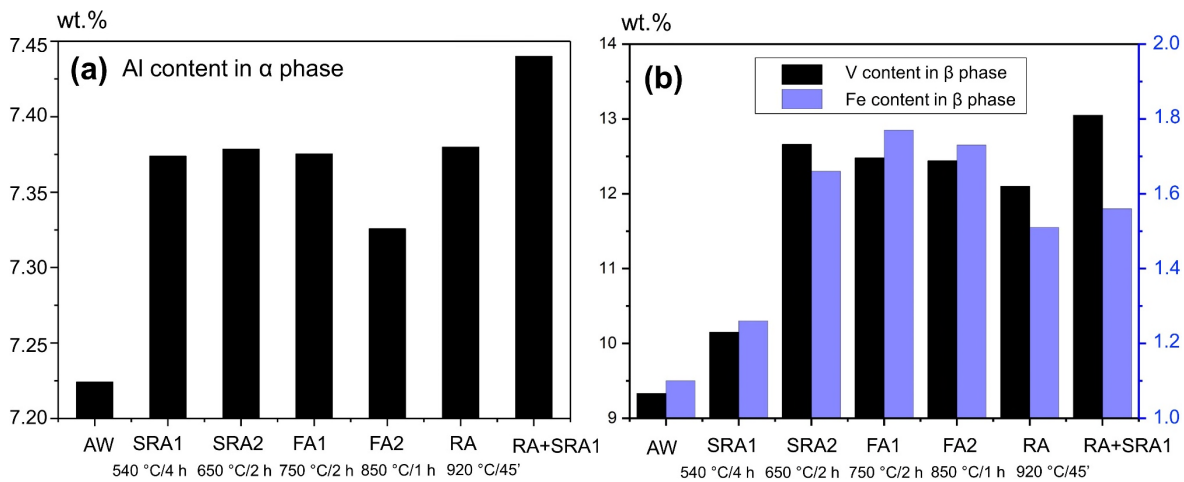


Figure 4.12. Alloying elements partitioning in the BM due to application of the PWHT: (a) Al content in the α phase; b) V and Fe contents in the β phase.

As presented in Figure 4.11, post-weld annealing in the temperature range of 650–850°C does not affect the average microhardness in the BM significantly, and it slightly decreases with increasing temperature. An appreciable drop in microhardness was observed after recrystallization annealing at 920°C for 45 min. These results are related to grain coarsening in accordance with the Hall-Petch mechanism [150, 151]; they are consistent with the microstructural observations discussed in the previous section. However, it should be mentioned that, according to our results, the Hall-Petch relationship is relatively weak for the Ti-6Al-4V alloy. Although the average grain size has almost doubled, the hardness values decreased by only about 10%. As shown in Figure 4.11, the second step of the DA treatment has a similar hardening effect on the BM microhardness. The application of the stress-relief annealing at 540°C leads to the hardening of the coarsened structure obtained after RA due to the precipitation of the α_2 phase by the same mechanism as previously discussed for the SRA1 treatment.

4.4.2.2 Fusion zone

Figure 4.11 shows that, generally, the effect of PWHT on the average microhardness in the FZ has a similar trend, as discussed for the BM. However, the mechanisms leading to the final products are different. Note that the FZ had a completely different initial microstructure prior to PWHT; therefore, the microstructural changes differ from those in the BM. First, no α_2 precipitates can be formed in the

supersaturated martensitic α' phase. The hardening effect observed in the FZ after the SRA1 annealing can be attributed to the tempering of the as-welded martensitic structure. A number of researchers [62, 67, 152] have already observed this effect at relatively low heat treatment temperatures. The metastable α' martensitic phase is supersaturated in β stabilizers as a result of the diffusionless $\beta \rightarrow \alpha'$ transformation. Upon annealing, it decomposes into equilibrium $\alpha + \beta$ phases by the precipitation of incoherent β particles at dislocations or β phase layers at plate boundaries [22]. Chesnutt et al. [153] investigated the aging of β -quenched Ti-6Al-4V and used transmission microscopy to show the micro-precipitation of the β phase particles in tempered martensite at similar temperatures. According to our results, the precipitation hardening of the FZ takes place only after the SRA1 annealing, whereas heat treatment at 650°C for 2 h leads to partial decomposition of martensite with attendant reduction of microhardness. Starting from the temperature of 750°C, grain coarsening of a fine-lamellar microstructure in the FZ is responsible for the gradual reduction of microhardness with increasing temperatures (see Figure 4.11). After the RA treatment at 920°C, the martensitic FZ was completely transformed into equilibrium coarse lamellar $\alpha + \beta$ morphology with the lowest hardness values nearly equal to that of the BM in the as-received condition, as shown in Figure 4.11. After the recrystallization, both the BM and FZ consisted of equilibrium $\alpha + \beta$ phases. The hardening mechanism of the FZ that took place during the aging step in duplex annealing (DA treatment) was, apparently, the same as described above for the BM, that is, precipitation of coherent α_2 particles.

4.5 Residual stresses

4.5.1 As-welded condition

Residual stresses generated close to the weld zone have been measured by two methods: X-ray diffraction by synchrotron radiation and the incremental HDM. The residual stress profiles for the as-welded condition obtained by these two techniques are presented in Figure 4.13(a). The residual stress state is represented by the two stress components: σ_{xx} in the longitudinal weld direction and σ_{yy} in the transverse direction. Longitudinal stresses are, therefore, parallel to the welding seam, as previously shown in Figure 3.3(b).

As presented in Figure 4.13(a), the X-ray diffraction gives a detailed profile of residual stresses in the weld area, enabling the detection of the stress variations across the FZ and HAZ. Both stress components exhibit a similar three-peak morphology with the tensile residual stress maxima located symmetrically to the weld centre line. Liu et al. reported a similar form of residual stress profile for laser-welded TiAl-alloys [154]. Longitudinal residual stresses parallel to the weld line are almost by a factor of five higher than a transverse component. This relation between the stress components is typical for the welds and is related to a significantly higher restriction for the expansion of the molten material in the longitudinal weld direction [155, 156, 157]. The maximum tensile residual stress of 540 MPa is located in the far-HAZ and this is ca. 110 MPa higher than the value in the FZ centre. Interestingly, the peaks of tensile residual stresses are located in the far-HAZ outside the weld zone. The stresses steeply decrease with increasing distance from the HAZ, and compressive residual stresses are formed in the BM surrounding the weld. The maximum compressive stresses are around -80 MPa and located outside the weld area at a distance of approximately 12–15 mm. The residual stress profile gradually approaches zero in the far field near the free edge of the specimen (this region is not shown in Figure 4.13(a, b)). The profile of transverse stresses has a similar form with the peaks not exceeding 120 MPa and located outside the weld. In contrast to the longitudinal stress component,

compressive transverse residual stresses of roughly -80 MPa were found at the centre of the FZ. Several researchers have reported similar residual stress profiles for the welded Ti-6Al-4V [158].

The HDM method gives the average stresses in the area, where the material was removed (drilled), i.e. in the blind hole with a diameter of 0.6 mm and depth of 0.3 mm. As no depth-dependent gradient of residual stresses was observed by the HDM in the present study, the depth profiles were averaged, and each measurement position was characterized by the mean value of residual stresses at the depth of 0.3 mm. Thus, each point in Figure 4.13 contains 30 statistically processed experimental values (three holes with 10 steps each). The distribution of residual stresses obtained by this methodology is shown in Figure 4.13(a). The central point highlights the high tensile longitudinal stresses up to 650 MPa, which is considerably higher than the results of X-ray diffraction. These high tensile residual stresses near the weld are balanced by compressive longitudinal stresses further away from the weld line. The magnitude of compressive residual stresses of ca. -105 MPa is also slightly overestimated in comparison to the X-ray results. Transverse residual stresses have a similar profile but are an order of magnitude lower than the longitudinal component, with a maximum value not exceeding 50 MPa.

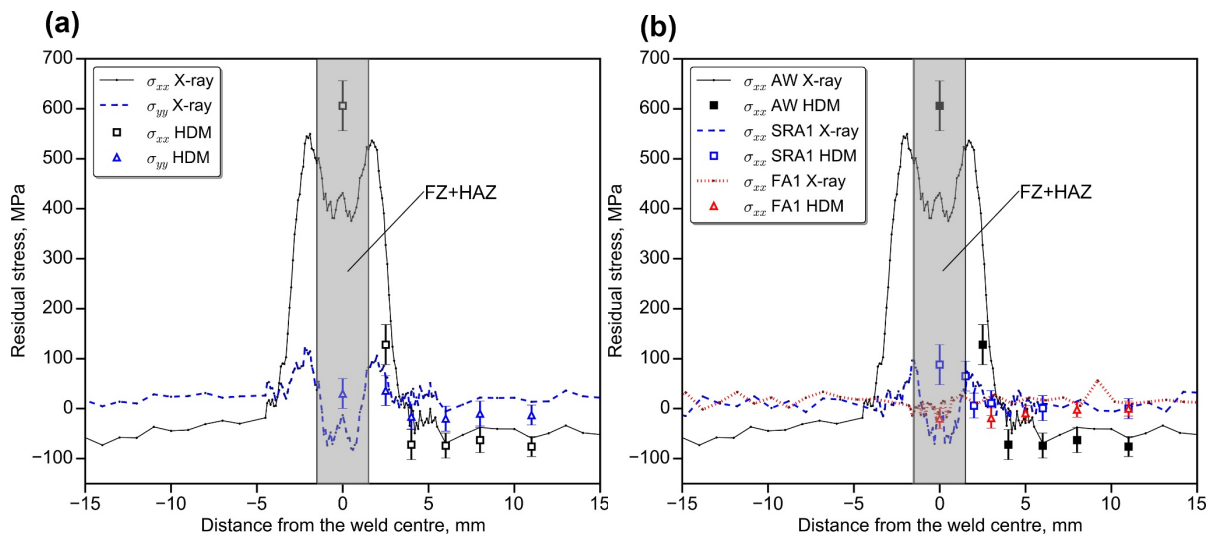


Figure 4.13. Residual stress distribution in the vicinity of the laser-beam welded Ti-6Al-4V butt joint: (a) residual stresses in the as-welded condition measured by the X-ray diffraction and HDM; (b) effect of PWHT on the longitudinal residual stress profile.

The presented results allow a comparison of the two methods regarding their suitability for the measurement of weld residual stresses. Figure 4.13 illustrates that, in spite of significantly different numerical values, both residual stress measurement techniques have several important common outcomes. First, both methods combine the fact that high longitudinal residual stresses are produced in the weld itself and the immediately adjacent parent material during solidification. Furthermore, longitudinal stresses prevail and are by an order of magnitude higher than the transverse component. Second, the width of the weld region with tensile residual stresses was estimated to be almost equal by these two techniques. The distance between the two points, where the stresses change their sign, can be used as an effective size of this area. As shown in Figure 4.13(a), a narrow zone of approximately 8mm width (4 mm from each side) was detected by the HDM almost as precisely as by the synchrotron measurements. Thus, HDM is a fast and effective alternative to conventional, time-consuming X-ray diffraction. Although it does not provide a detailed residual stress profile, the

most important characteristics of the stress field around the weld can be determined within a short time and with a fewer costs that are required for synchrotron measurements.

4.5.2 Effect of heat-treatment

The stress-relieving effect of heat treatment at elevated temperatures is presented in Figure 4.13(b). Two types of PWHT were chosen for this purpose: SRA1 and FA1. Since the longitudinal residual stresses significantly prevail over transverse stresses, Figure 4.13(b) presents only the evolution of a longitudinal component. A good agreement was found between the experimental data provided by the two stress measurement techniques. As presented in Figure 4.13(b), annealing at 540°C (SRA1) yields the stress relief at the centre of the FZ to approximately 90 MPa, according to the HDM. The X-ray diffraction gives a comparable remaining peak stress of 114 MPa. However, in contrast to the HDM results, its position corresponds to the far-HAZ. Surprisingly, according to the X-ray diffraction measurements, compressive residual stresses are formed in the weld zone after this type of heat treatment. These compressive residual stresses were not detected by the HDM, apparently, because the HDM gives the average stresses integrated over the entire drilled region, whereas the X-ray diffraction gives the results in local values averaged through the thickness.

After PWHT at 750°C (FA1), the residual stress was almost entirely relieved, and the remaining peak stress was lower than 50 MPa, as measured by both methods. Apparently, PWHT at higher temperatures completely removes the welding-induced residual stresses in the welding seam. The results suggest that the SRA1 treatment has a sufficient positive impact in terms of stress relief with an effectiveness is around 90%. As stated in Section 4.3.4, this type of heat treatment does not lead to any microstructural changes either in the BM nor in the FZ because the temperature of 540°C does not activate the martensite decomposition or the grain growth in the BM. Moreover, it has a slight hardening effect, as demonstrated by the microhardness measurements. These results are of great importance for further weld characterization because they provide an effective procedure enabling the crack growth measurements directly in the FZ, as discussed in Section 4.8.

Note that presented results correspond to a specimen geometry different from the one used in fatigue testing. The specimen size should be considered an influential factor when evaluating the effect of residual stresses on fatigue properties of welded joints [155]. After the extraction of S-N specimens from the welded plate, residual stresses are almost fully relieved due to relatively short width of the gauge length (8 mm). Sufficient length of the joint is needed to retain high longitudinal residual stresses after cutting. The latter was confirmed by the HDM technique in the extracted fatigue specimens and does not allow us to draw any conclusions about the influence of residual stresses on the fatigue properties of laser-welded Ti-6Al-4V butt joints. However, in the case of larger specimens and real components, welding residual stresses may affect the final fatigue properties. Large-scale specimens must be tested to separately investigate the influence of residual stresses on the fatigue behaviour of laser-welded joints.

4.6 Tensile tests

The weld static strength is of great practical concern in the light of strict requirements imposed on the joint structural integrity. For this reason, tensile strength of the laser-welded joints was measured and compared with that of the BM with various types of microstructure. The results of the tensile tests for the Ti-6Al-4V BM and the laser-welded butt joint are shown in Figure 4.14 and are summarized in Table 4.2. In this table, the specimens designated as LT are loaded in the rolling

direction and TL specimens in the transverse sheet direction. Experimental results suggest that the microstructure has a remarkable impact on the mechanical properties. As illustrated in Figure 4.14, the as-received BM has the highest ductility, reaching up to 16% in terms of fracture strain. Additionally, the Ti-6Al-4V sheet exhibits anisotropy because of the rolling process. UTS in the rolling direction (LT specimens) is slightly higher with a commensurate decrease in fracture strain. There are no significant differences between the as-received BM and the laser-welded joint with regard to the yield strength and ultimate tensile strength. The underlying reason for these results is that all the welded joints fractured in the BM. It was reported that this type of fracture is also typical for laser-welded Ti-6Al-4V T-joints in a hoop-stress test [11]. In other words, it can be concluded that the joint efficiency in terms of tensile strength is 100%. Intact FZ and the BM failures in the tensile test are related to the inherent strength mismatch of laser-beam-welded Ti-6Al-4V. As indicated by the microhardness map, the weld zone is overmatched and, therefore, the main plastic deformation of the butt joint occurs in the BM. Since the fracture strain was determined over the entire gauge length, it included the non-plastically deformed weld region. As a result, the specimens with welds in the middle part have a slightly reduced elongation compared to that of the BM, as shown in Figure 4.14. Thus, martensitic transformation and the following increase in the local strength of the weld zone provides a shielding effect that protects the weld from mechanical damage in tensile testing. Kashaev et al. reported that the position of fracture could be predicted, based on a finite elements analysis supported by a careful analysis of the local mechanical properties [159].

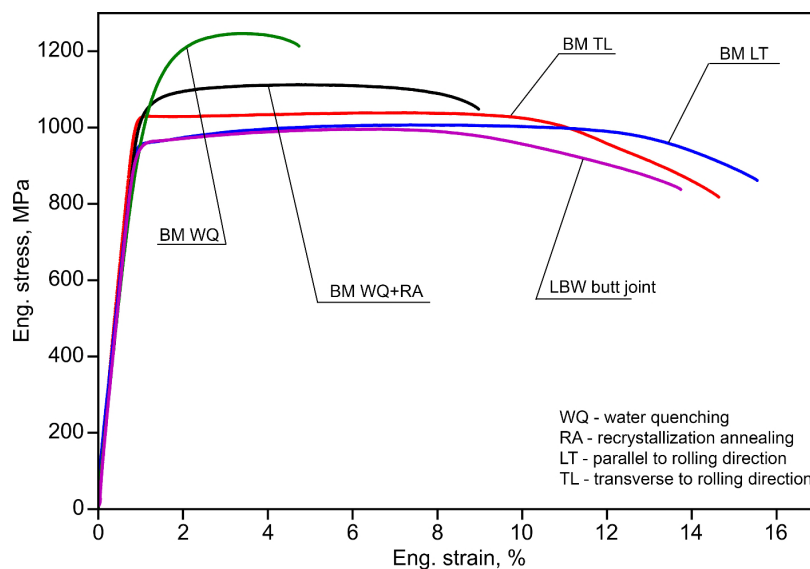


Figure 4.14. Engineering stress-strain curves for the BM with different microstructures compared to that of the laser-welded Ti-6Al-4V butt joint.

Table 4.2. Tensile properties of the Ti-6Al-4V BM and the laser-welded joint (mean values with standard errors from five measurements).

	BM LT	BM TL	BM water quenched	BM water quenched + RA	LBW butt joint
E , GPa	107.0 ± 2.1	119.9 ± 3.3	104.4 ± 2.7	109.8 ± 7.2	110.7 ± 3.5
$\sigma_{0.2}$, MPa	957.0 ± 4.8	1028 ± 14.6	1076 ± 5.8	1049 ± 6.1	962.3 ± 9.5
UTS, MPa	1004 ± 2.9	1038 ± 11.3	1258 ± 12.1	1112 ± 3.4	1007 ± 11.4
ϵ , %	15.8 ± 0.3	14.6 ± 2.0	4.7 ± 2.1	8.9 ± 2.5	13.8 ± 0.7

Figure 4.14 also presents the engineering stress-strain curves of the BM subjected to different types of heat treatment. The water-quenched condition, with fully martensitic morphology, has a UTS equal to 1258 ± 12.1 MPa, which is the highest value from all the tested specimens in this work. High tensile strength of this microstructure is compensated by a very low ductility. The stress-strain curve has almost no plastic region, indicating a brittle type of fracture with an elongation of 4.7%. The stress-strain curve of the quenched BM represents the behaviour of the FZ under static loading, and clearly demonstrates the concept of the overmatched laser-welded joint. Martensitic morphology (green curve in Figure 4.14) is stronger than the BM and, at the same time, it is more brittle and has a lower fracture strain. Therefore, plastic deformation is concentrated primarily in the weaker and more ductile BM. As a result, the weld stress-strain curve is almost equal to that of the BM with a slight decrease in fracture strain. It is important to note that the described overmatching effect expressed by the stress-strain curves cannot be affected by the LBW process parameters. Numerous researchers reported that the weld tensile strength could not be altered by the parametric optimization because the martensitic phase is inevitably formed during the LBW process [13, 160].

The black curve in Figure 4.14 corresponds to the recrystallized lamellar microstructure that is typical for the weld zone after recrystallization annealing RA or duplex annealing DA. It can be seen that lamellar microstructure has a UTS of 1112.1 MPa, which is higher than that of the BM but lower than that of the martensitic state. In addition, lamellar microstructure exhibits a higher ductility than that of the fully martensitic microstructure. Owing to the activation of the recrystallization processes during RA, the local mechanical properties of the martensitic microstructure gradually approach the as-received BM properties. The experimental results are consistent with the microhardness measurements, i.e. the FZ microhardness after RA was similar to that of the as-received BM. Hence, RA and DA types of heat treatment reduce the strength mismatch between the BM and FZ and improve the local ductility of the FZ. The latter is of great importance for the fatigue behaviour because a higher ductility is related to a lower notch sensitivity, as will be shown in the following section. Kabir et al. demonstrated that, after recrystallization annealing, the fracture position of laser-welded Ti-6Al-4V shifts from the BM to the weld HAZ [67].

The results of tensile testing suggest that the load-carrying capacity of the joint is directly linked to the distribution of local mechanical properties in the weld area. In contrast to aluminium alloys, the laser processing of $\alpha+\beta$ titanium alloys leads to their hardening and, thereby, to strength overmatch. Although this may seem to have a big positive impact on the overall strength of the weld, this tendency is valid only for static strength. Overmatching and the increased brittleness of the weld zone are negative factors when the joint is subjected to cyclic loading. From this perspective, high temperature annealing, leading to the martensite decomposition, homogenizes the weld microstructure, decreases the strength mismatch and makes the FZ more ductile, which is of paramount practical interest.

4.7 Fatigue tests

Fatigue properties were characterized by conventional S-N curves showing the magnitude of a maximum cyclic stress (peak stress) σ_{max} as a function of the number to cycles to failure N . A semi-logarithmic scale is used for the representation of S-N curves because the linear scale on the stress axis allows a more uniform presentation of data over a wider stress range. Figure 4.15(a) shows the experimentally determined S-N curves of the BM with various microstructures and the S-N curve for the laser-welded Ti-6Al-4V butt joint without any post-processing treatment, i.e. in the as-welded

condition. Arrows indicate the specimens that had not failed after 10^7 load cycles (run-outs). The corresponding fatigue limits are summarized in Table 4.3.

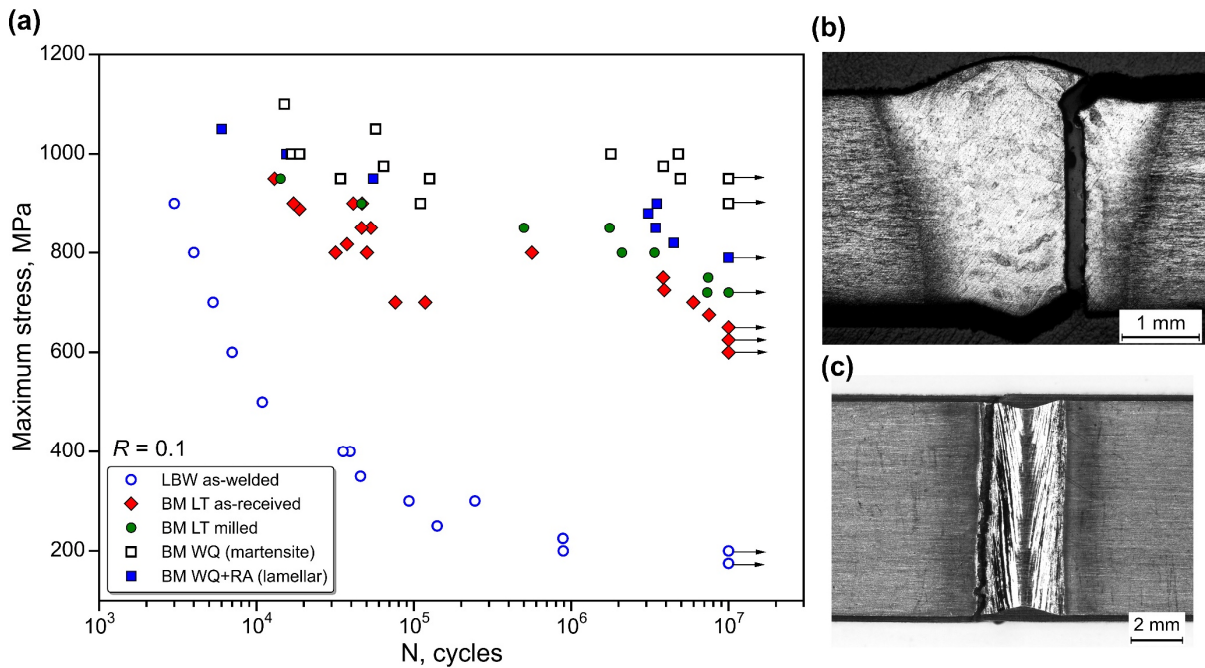


Figure 4.15. (a) S-N curves of the BM in comparison to those of the as-welded joint; (b) transverse cross section of the weld seam after fatigue fracture ($\sigma_{max} = 300$ MPa; $N = 244,300$ cycles); (c) view from the top on the specimen after fatigue fracture ($\sigma_{max} = 200$ MPa; $N = 889,700$ cycles).

Table 4.3. Fatigue limits of the weld and BM with various types of microstructure.

Condition	Fatigue limit at 10^7 cycles, MPa
BM LT as-received	600–650
BM LT milled	720–750
BM water quenched (martensite)	900–950
BM water quenched + RA (lamellar)	790–820
LBW butt joint (as-welded)	180–200

It can be seen that the fatigue behaviour of the as-welded joints without any post-processing technique is relatively poor. Surface defects such as underfills and reinforcements play the role of stress concentrators and have a strong deteriorative effect on fatigue life. The use of filler wire partly prevented the formation of deep underfills. However, the combined effect of the weld reinforcements and underfills at the weld toes has a big negative impact on the joint load-carrying capacity. As a result, the as-welded condition is characterized by a fatigue limit in the range of 180–200 MPa. The failure always occurs in the welding seam, initiating at the face or root underfill. Figure 4.15(b) demonstrates a typical cross section of the specimen after fatigue failure. The crack started from the bottom weld toe and then propagated through the FZ perpendicular to applied external stress. Note that the fatigue crack grew solely in the martensitic FZ without deflecting into the BM or HAZ. A top view of the S-N specimen in Figure 4.15(c) illustrates the position of the fatigue crack in relation to the weld seam. In the specimen shown in Figure 4.15(c), the crack started at the top underfill. The crack line almost completely corresponds to the weld toe or the underfill/reinforcement transition. It

can be, therefore, inferred that these crack-initiation zones are the most critical weld imperfections with regard to the cyclic loading. Notch effect introduced by the weld underfills, which is additionally exacerbated by the FZ brittleness, has a strong deleterious effect on the fatigue performance and should be considered with caution.

Figure 4.15(a) also reveals that the fatigue limit of the as-received BM without any subsequent processing is higher by a factor of three than that of the weld and reaches 600–650 MPa or nearly 65% of the BM yield strength. In this case, fatigue cracks also always initiate from the surface. Crack nucleation in the as-received material commonly occurs at the surface roughness that is about $R_z \approx 3.0 \mu\text{m}$. One of the simplest procedures aiming at fatigue properties improvement and lifetime prolongation is conventional machining (grinding or milling). In this work, several as-received titanium sheets were milled from both sides down to a thickness of 2 mm in order to study the effect of surface roughness on the BM fatigue behaviour. Machining both reduces the surface roughness to $R_z \approx 1\text{--}1.5 \mu\text{m}$ and results in the generation of compressive residual stresses in the 0.2-mm-thick surface layer, as measured by the HDM [141]. Improved surface quality and the introduction of favourable compressive stresses in the near-surface region have a beneficial effect on the HCF resistance of the Ti-6Al-4V BM. Figure 4.15(a) shows that the milling of the specimen surfaces increases the fatigue limit up to 720–750 MPa (approximately 15% improvement).

Considering the fatigue behaviour of a component in the presence of notches, it is always necessary to have the fatigue properties of a smooth unnotched material for reference. Since the failures of the laser-welded joints always occur in the FZ (regardless of the surface state, as will be shown further) fatigue cracks initiate and grow exclusively in the martensitic microstructure obtained after the laser processing (see Figure 4.15(b)). Thus, the S-N curve of the as-received BM cannot act as a reference because it represents a globular microstructure of the sheet prior to welding (Figure 4.3(a)). Strictly speaking, S-N specimens with fully martensitic microstructure of the FZ should be produced and tested in order to have a reference curve for the weld. The S-N curve obtained by this methodology would represent the highest possible fatigue strength for this type of microstructure. Since it is unfeasible to produce those specimens by a local laser-processing technique, heat treatment followed by water quenching was employed to simulate the FZ microstructure, as reported above in Section 4.3.5. It must be noted that the oxygen-enriched α case surface layer was removed by milling; therefore, the specimens had a milled surface quality. Fully martensitic microstructure of these specimens obtained by thermal simulation is shown in Figure 4.9.

As shown in Figure 4.15(a), a martensitic morphology has a fatigue limit of around 900–950 MPa, which is significantly higher than that of the globular microstructure of the BM. It implies that the fatigue limit of the acicular morphology is about 73–75% of its yield strength (≈ 1258 MPa); it is appreciably higher than this ratio for globular microstructure (65%). Additionally, the result obtained suggests that the HCF properties follow the same tendency as microhardness and the tensile strength, i.e. the water quenching leads to a substantial increase in the unnotched HCF properties of the Ti-6Al-4V alloy. A 30% increase in fatigue strength of the martensitic microstructure is the result of the strengthening effect upon high cooling rates, which was discussed above. Thus, martensitic transformation, which always accompanies the LBW process of Ti-6Al-4V, triggers a simultaneous strengthening of the static and unnotched fatigue properties of the material. In other words, the laser-welded joint is overmatched in terms of both tensile and unnotched fatigue properties. This effect is additionally reflected by the growth of microhardness within the FZ. In this context, poor fatigue performance of the weld may seem to contradict to the excellent fatigue properties of the martensitic

FZ. The underlying reason for this discrepancy is attributed to the welding-induced defects that are inevitably present in a weld seam. The weld defects and discontinuities do not allow the stronger martensitic FZ to shield the joint from the applied cyclic loading, as it is normally fulfilled during the static test. The notch effect and a premature fatigue crack initiation weaken the FZ from the early stages of the fatigue life. As a result, although the FZ microstructure is considerably stronger, welding defects cause a drop in the fatigue limit and worsen the overall fatigue behaviour even lower than the BM level. It can be concluded from our results that in the absence of any welding-induced defects, the FZ would have higher fatigue properties than those of the BM.

A few additional comments should be made on the results obtained in order to avoid some ambiguity. Fatigue properties of a material should not be confused with the crack growth resistance or fracture toughness. Very often, microstructural transformations in the material have opposite effects on the tensile strength, fatigue properties, and fracture toughness. Moreover, the increase in static strength is usually compensated by a commensurate decrease in fracture toughness due to increased brittleness. Our results suggest that there is a positive correlation between the tensile strength and the unnotched HCF properties of Ti-6Al-4V, as demonstrated by testing of the quenched specimens with fully martensitic microstructure. However, the results do not allow any conclusions to be drawn about the changes in the material toughness. It will be shown later that, in spite of a pronounced hardening effect, the martensitic transformation does not have any beneficial effect of the crack propagation resistance.

Finally, it is important to note that the obtained S-N curve of the unnotched martensitic microstructure acts as a reference, but these properties are not achievable for the laser-welded joints. From the point of view of structural integrity, the fatigue behaviour of overmatched welded joints would be always limited by the properties of a weaker BM.

4.8 Fatigue crack propagation (FCP) tests

The resistance of the FZ microstructure to the macro-crack growth was studied by the FCP testing of C(T) specimens with the welding seam in the middle part, as schematically shown in Figure 4.16(a). However, a challenging problem that prevented the experiments in the standard set-up was the crack deflection from the FZ into the BM, as illustrated in Figure 4.16(b). The crack always initiated at an angle of around 30° to the notch and, then, after passing the HAZ, was growing in the BM at the same angle. Since the crack did not propagate perpendicularly in the direction of the external load, its propagation rate gradually decreased until it totally stopped in the BM. At this point, the second crack was initiated at the same angle but in an opposite part of the specimen (see Figure 4.16(b)).

At the early stages of the present work, two central hypotheses were postulated for this phenomenon: either this is an effect of overmatching or an effect of longitudinal residual stresses. To verify these hypotheses, two additional tests were undertaken. First, a C(T) specimen was machined in the weld zone in order to produce a 0.25-mm-deep groove from both sides of the FZ. By this action, the cross section in the middle part of the FZ was reduced by 25% in thickness. Surprisingly, this measure did not have any essential influence and the crack growth was still deflected. Second, the stress relief annealing prior to the FCP testing was carried out in order to reduce the longitudinal residual stresses. To avoid martensite decomposition and significant microstructural changes, the heat treatment parameters were based on the results reported in Section 4.3.4. This approach had a positive effect and the crack finally propagated perpendicularly to the applied load, thus remaining in the martensitic

FZ. Note that the applied stress relief treatment (SRA1: 540°C, 4h) does not affect the FZ microstructure and microhardness. Therefore, strength overmatch was still present in the tested specimens after the stress relief. It can be concluded that the core reason for the crack deflection is attributed to the weld residual stresses, and the strength mismatch does not have any influence on the crack path. This can additionally explain the angle of crack deflection, i.e. additional tensile stress component (roughly 600 MPa) is added to external stress at the notch tip (roughly equal to UTS). By this, the maximum principal stress is rotated by about 30°, as shown in Figure 4.16(b). As a result, the crack grows perpendicularly to the maximum principal stress.

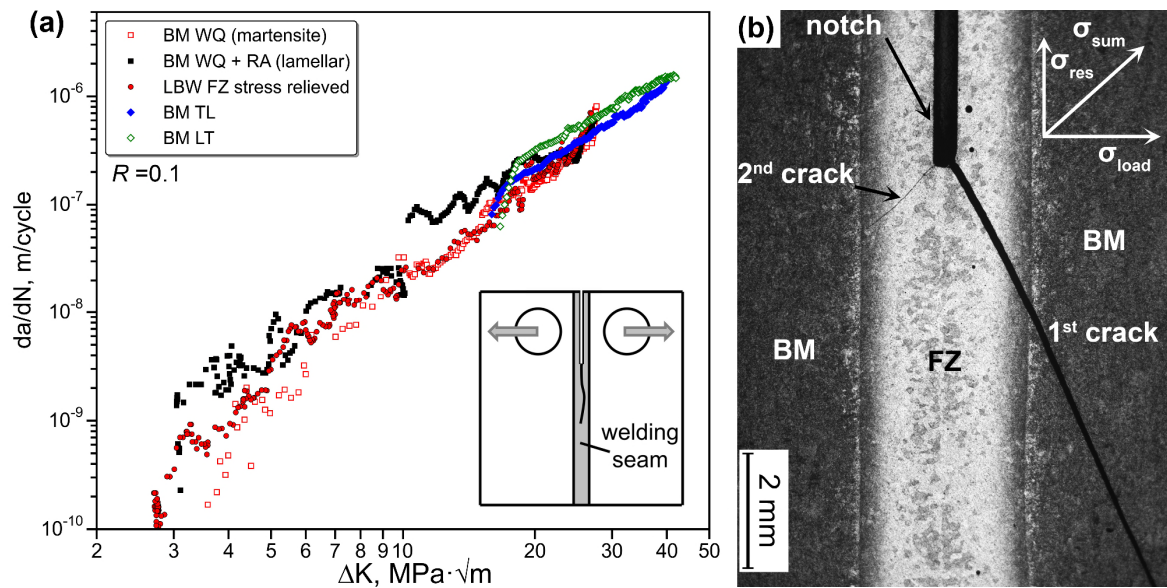


Figure 4.16. (a) Results of the FCP testing using the C(T)50 specimens; (b) crack deflection from the FZ to the BM because of welding-induced longitudinal residual stresses.

The resulting FCP data obtained by the above-mentioned method are shown in Figure 4.16(a). As a reference, the crack growth resistance of the as-received Ti-6Al-4V base metal is also presented in two principal sheet directions. We can see that in the Paris region, which is within the SIF range of 10–40 $\text{MPa}\cdot\sqrt{\text{m}}$, the crack growth rates in the FZ are comparable to those in the BM. Thus, in spite of a considerably higher tensile strength, hardness, and fatigue limit, the martensitic microstructure of the weld exhibits almost the same crack growth resistance as that of the globular microstructure in the BM. Hence, the term ‘overmatch’ does not apply to the FCP properties of the laser-welded joints. This finding suggests that a special attention should be paid to the damage tolerance characteristics of the Ti-6Al-4V butt joints. Although it may seem that the weld has excellent crack growth resistance, it is normally attributed to the welding-induced residual stresses. Once these stresses are relieved by any type of heat treatment or by elevated operation temperatures, the weld exhibits significantly higher FCP rates. This important issue should be carefully considered in the damage tolerance assessment of the laser-welded titanium joints.

Additionally, Figure 4.16(a) shows the FCP curves of the BM with thermally simulated microstructure. It can be seen that, in the Paris region, all the types of microstructure have similar crack growth rates. A big scatter that can be attributed to various sources, including some unrelieved residual stresses, characterizes the experimental data in the threshold region. The results obtained for fully martensitic morphology after water quenching and lamellar microstructure are very close to the FZ curve, although a slightly higher threshold was observed. Generally, it can be seen that lamellar

microstructure demonstrates slightly higher crack growth rates. Threshold SIF range of the martensitic FZ was detected to be $2.7 \text{ MPa}\cdot\sqrt{\text{m}}$. A relatively low threshold magnitude can be related to the fine-grained martensitic morphology. This value is important and will be later used as an input parameter for the fatigue assessment model. The thermally simulated microstructures exhibit slightly higher thresholds within the range of $3.0\text{--}3.2 \text{ MPa}\cdot\sqrt{\text{m}}$.

4.9 Porosity characterization

4.9.1 Spatial and size distributions

The porosity distribution of the laser-welded Ti-6Al-4V butt joints was quantitatively characterized by the transverse X-ray analysis of the extracted FZ. An experimental set-up and description of the inspection procedure have been previously discussed in Section 3.1.7. In this section, a detailed statistical processing of the X-ray results will be done only for the one LBW parameter set, and then the described procedure will be applied to find a correlation between the LBW process parameters and the porosity distribution. A typical image obtained by the lateral X-ray inspection of the weld is shown in Figure 4.17(a). It should be noted that the magnified view shown in this figure represents roughly 5 mm of the weld length, taken from the stable middle region. For statistical analysis and evaluation, the total weld length of 75 mm was considered. The regions at the beginning and at the end of the weld – the so-called run-ins and run-outs – were not considered. Note that the horizontal axis in Figure 4.17(a, b) corresponds to the longitudinal welding direction, while the vertical axis represents the thickness direction.

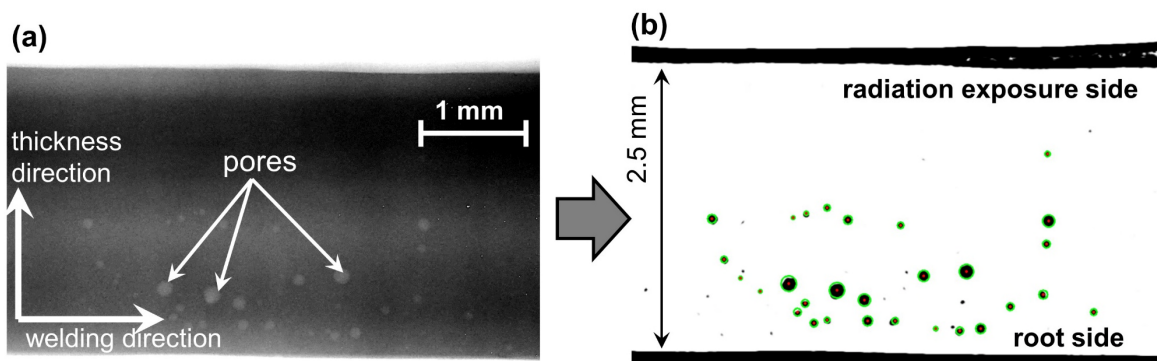


Figure 4.17. (a) A typical image from the lateral X-ray inspection of the laser-welded Ti-6Al-4V butt joint (welded with $P = 3.5 \text{ kW}$, $v = 2 \text{ m/min}$); (b) the result of automatic image processing and pore detection.

As shown in Figure 4.17(a), the welding-induced porosity can be distinguished by the intensity distribution in the X-ray image – i.e. the pores are brighter than the weld area. The result of image processing and automatic pore detection by a dedicated *Python* script is presented in Figure 4.17(b). The majority of the pores have been detected, thus demonstrating a high efficiency of the developed procedure. All the pores have rounded contours, implying that this is a gas-type porosity. A remarkable result to emerge from the image analysis is that majority of the pores is concentrated in the bottom part of the FZ. This trend is clearly visible even in Figure 4.17(a), in which the number of pores is not sufficiently high for statistical processing. Conventional X-ray inspection from the top side showed that these pores are concentrated in the middle region of the FZ, i.e. on the line of keyhole movement.

The described spatial distribution of internal welding-induced pores can give some important insights into the mechanism of porosity formation. Apparently, the keyhole instability and collapse are the primary reasons for the entrapment of some portions of the shielding gas within the welding seam. During the welding process, the bottom tip of the keyhole fluctuates, thus causing the vapour channel to collapse. Owing to a high solidification rate and insufficient time to escape, the bubbles filled with shielding gas produce randomly distributed porosity in the FZ. The distance of a pore to the nearest free surface is of great concern for fatigue analysis. Hereinafter, the distance from the pore to the weld root side is denoted by the term ‘distance to the surface’.

A total of 1,018 pores have been detected over the inspection length of 75 mm for the given welding parameter set shown in Figure 4.17(a, b). The minimum size of a pore that could be detected under the experiment and software limitations was around 15 μm . Taking this into account, the real number of pores present in the welding seam is even higher. All the pores were measured, and their size and location were statistically analysed. Histograms of the pore diameter and the pore depth are shown in Figure 4.18(a) and (b), respectively. The average pore diameter found by the X-ray inspection is 64 μm , while the average distance from the weld root side is 650 μm . Statistical data assessment revealed that the pore-diameter distribution and the distance from the surface could be relatively well described by the log-normal distribution with a PD-function given by:

$$p_D(d) = \frac{1}{s\sqrt{2\pi}} \exp\left(-\frac{(\ln d - \mu)^2}{2s^2}\right) \quad (4.1)$$

where μ and s are the mean and standard deviation of logarithm $\ln(d)$, which is, by hypothesis, normally distributed. The same distribution has already been introduced in Section 3.3.1 for description of fatigue scatter. The resulting fitted histograms and the corresponding fit parameters with r^2 -coefficients are shown in Figure 4.18(a, b). The values of r^2 close to 1.0 support the validity of the assumed distribution function. Finally, the described methodology with statistical analysis was applied consistently for welds with various parameter sets in order to find the correlation between the welding parameters and the porosity level. It has been found that the process parameters do not have a significant impact on the position of the maxima in the pore distributions. The major influence is related to the number of pores and is described in the following section.

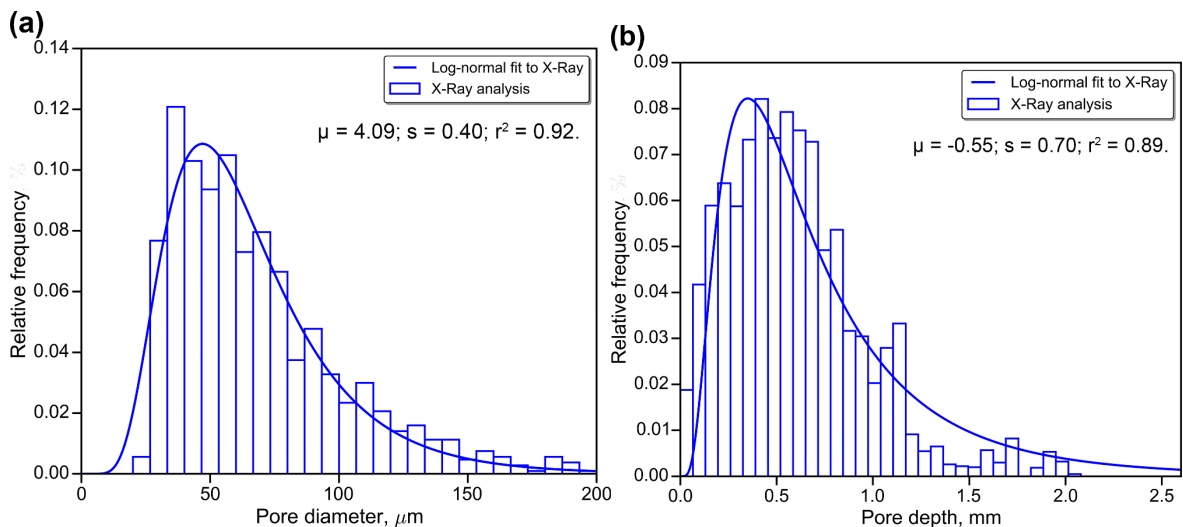


Figure 4.18. The results of transverse X-ray analysis of the FZ: (a) histogram of the pore diameter distribution; (b) histogram of the pore depth distribution.

4.9.2 Effect of process parameters

The porosity level in the laser-beam-welded seams is directly linked to the keyhole behaviour and the weld solidification mechanisms. It implies that the number of pores is primarily affected by the LBW process parameters. From this perspective, a correlation between the LBW parameters and the pore distribution in the welds can provide a method to minimize the porosity level. In order to study and quantitatively characterize this effect, laser power and welding speed were consistently varied, and the obtained welding seams were subjected to the lateral X-ray inspection, as discussed earlier in this chapter.

In accordance with AWS D17.1 standard [121], the accumulated length of pores in a 75-mm-long weld joint was used to evaluate the porosity level. For simplicity, the total length of pores was normalized by the inspection length. The porosity level as a function of laser power for different welding speeds is shown in Figure 4.19(a). The joints with incomplete penetration or insufficient quality due to excessive laser power were not considered in the assessment. As can be seen, for each welding speed, the accumulated length of pores tends to increase steeply with higher laser powers. A remarkable growth of the porosity level occurs typically when the laser power reaches the values of 4.5–5.0 kW, depending on the welding speed. In the region of 5.0–8.0 kW, the number of pores is the highest and is almost equal for different welding speeds. For lower laser powers up to 4.5 kW, total length of pores decreases slightly with an increasing welding speed; however, this effect is far less pronounced than that of a change in the laser power.

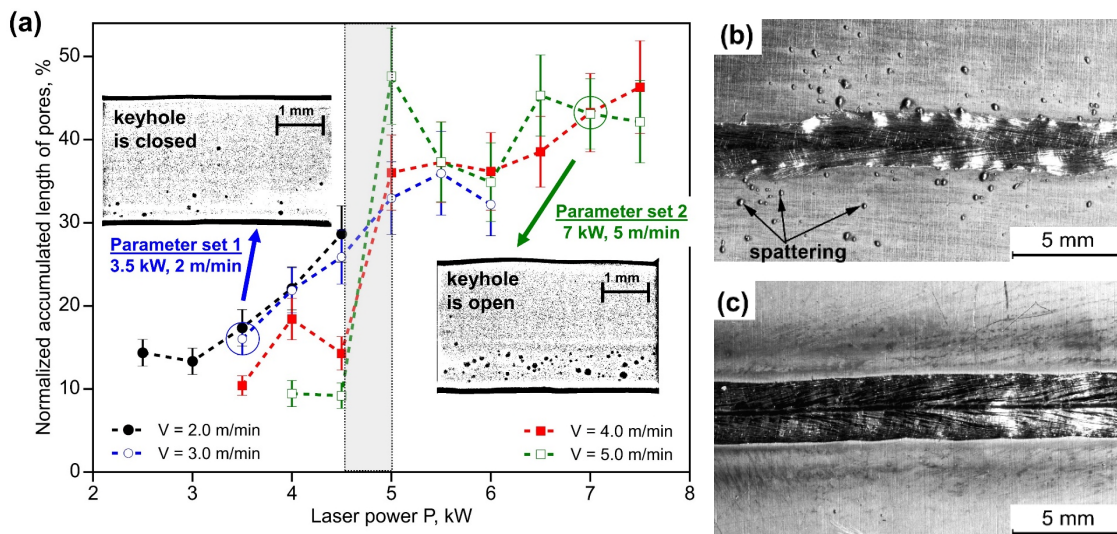


Figure 4.19. (a) Effect of LBW parameters on the porosity level; (b) spatter on the root side due to open keyhole (Parameter set 2); (c) bottom side of the joint after LBW with closed keyhole (Parameter set 1).

Visual inspection of the welds revealed that there is a strong correlation between the porosity level and the spattering of the FZ. Drastic increase in porosity level almost completely corresponds to the beginning of spattering at the bottom weld surface. To demonstrate this effect, Figure 4.19(b, c) show the bottom appearance of the weldments produced with two different welding parameter sets. Parameter Set 1 (3.5 kW, 2 m/min) corresponds to a low porosity level and Parameter Set 2 (7 kW, 4 m/min), in opposite, has the highest porosity level. It was observed that for each welding speed, the increase in the number of pores is always accompanied by an enhanced spatter on the bottom surface. Apparently, the main reason for spattering is the penetration of the laser beam through the whole thickness of the welding zone. This occurs when the laser power is sufficiently high and the keyhole

tip reaches the rear side of the plate. As a result, the keyhole becomes open and a plasma plume is formed not only above the weld but also under the bottom surface. Figure 4.19(a) also shows that the spatial distribution of pores is also affected by the keyhole dynamics. After welding with an open keyhole, the majority of pores is concentrated near the bottom surface of the FZ. In contrast, the LBW with a closed keyhole yields a more uniform distribution of pores over the weld thickness and the pore concentration in the root side is less pronounced, as shown in Figure 4.19(a).

These results indicate that, depending on the keyhole behaviour, the pores are formed via different mechanisms. In the region of low laser powers, keyhole instability and collapse have the strongest influence on the formation of pores [161, 162]. This leads to the formation of bubbles predominantly in the root surface layer, and increases the overall porosity level. At high laser powers, the keyhole is open and the inert gas can additionally enter the keyhole from the bottom surface. Moreover, for the pores in the lower part of the weld, it is significantly more difficult to escape by an upward flow within a short time, when the material is melted. This additionally increases the overall porosity level when welding with an open keyhole. Similar findings regarding the enhanced porosity formation during the laser welding with an open keyhole have been reported in [163].

Conventional X-ray inspection of the welded joints from the top revealed that the two pore formation mechanisms result in entirely different pore distribution with regard to the central keyhole position. As shown in Figure 4.20(a, b), a closed keyhole leaves the bubbles exactly in the middle part of the FZ. This location clearly indicates that the pores are formed by the keyhole tip fluctuations. In contrast, after the LBW with an open keyhole, the pores are located at the remote distance from the FZ centre line and close to the fusion line. Furthermore, the position of pore clusters constantly changes from one side to another over the weld length. Figure 4.20(b) also depicts the big impact of an open keyhole on the number of pores. These findings confirm the existence of two dominant pore formation mechanisms that lead to essentially different porosity levels and their spatial distribution.

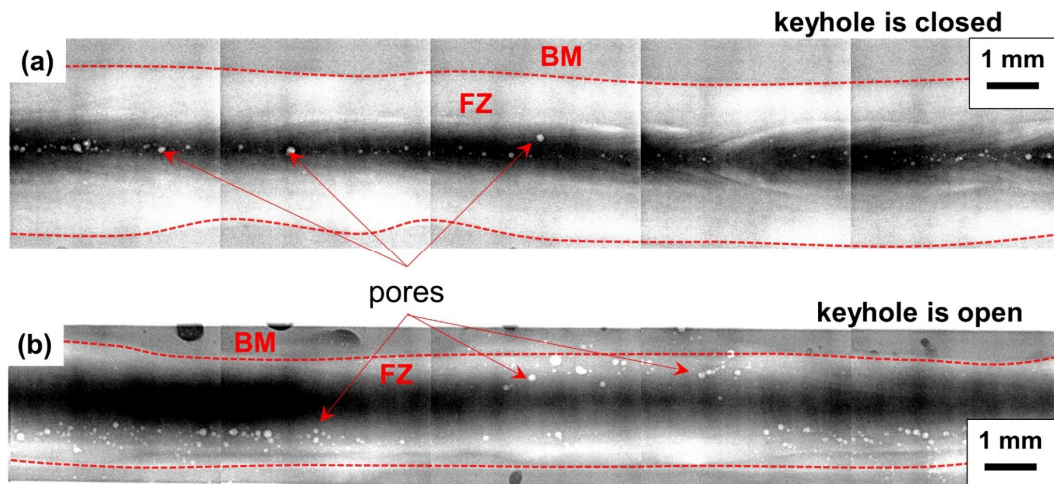


Figure 4.20. Effect of the keyhole behaviour on spatial porosity distribution: (a) X-ray image of the weld with closed keyhole (Parameter Set 1); (b) X-ray image of the weld with open keyhole (Parameter Set 2).

Summarizing the results of this section, it can be concluded that the optimum parameter set for minimizing the weld porosity should have a high welding speed of 4.0–5.0 m/min and a laser power lower than 4.5 kW. The process parameters in this range enable the reduction of the spattering at the root side as well. Moreover, laser power is the most influential factor that determines the porosity level through the keyhole stability and should be treated with some special caution.

5 Methods for improvement of fatigue properties

One of the important conclusions from the previous chapter is that fatigue strength of laser-welded Ti-6Al-4V joints is considerably reduced by the inherent weld defects generated within a weld FZ. Relatively poor fatigue performance is one of the major problems in the context of industrial applications. In this section, five different methods aiming at the fatigue lifetime prolongation of the laser-welded Ti-6Al-4V butt joints will be considered and discussed in detail. Three of them, namely machining, laser remelting, and laser peening treatments can be referred to as local surface modification methods applied as post-processing techniques. The ability to be potentially applied exclusively on a limited area in the proximity to the weld is a valuable attribute from the practical viewpoint. The fourth method is based on the heat treatment in a vacuum atmosphere. Various types of PWHT were investigated and the effect of heat treatment is linked to the microstructural transformations discussed in Section 4.3.4. The drawback of PWHT is that a full welded component or a structure have to be heat-treated, which is very often undesirable due to microstructural transformations within the BM around the weld. Finally, optimization of the LBW process parameters supported by the X-ray results is proposed as a possible way to raise the fatigue strength of the weld. The results presented in this chapter has been partially published in [164].

5.1 Machining

Conventional machining of the weld is one of the simplest and most effective methods for improving the fatigue performance. In this study, the welds were milled flush with the sheet surface on both sides to the final thickness of 2.2 mm. As a result, the weld underfills were completely removed along the entire length of the joint, providing a smooth transition from the weld to the BM. The resulting roughness after milling was about $R_z = 1.5 \mu\text{m}$. The S-N curve for machined laser-welded joints is given in Figure 5.1(a). The number of tested specimens for the machined condition was appreciably higher than that for other S-N curves due to the significance of this curve for further analysis. As will be shown in Chapter 7, the developed fatigue assessment model is validated by these experimental data. Therefore, an increased number of specimens is required for statistical processing of the results and model validation.

Figure 5.1(a) shows that milling of the surface weld imperfections such as underfills and weld toes provides a significant increase in fatigue strength. Fatigue limit approaches the range of 500–520 MPa that is by a factor of 2.5 higher than in the as-welded condition. In the LCF region, the S-N curve for the milled condition approaches the static strength of a weld, which is equal to the strength of the BM, as reported in Section 4.6. Interestingly, fatigue failure of the specimens tested at maximum stresses higher than ca. 900 MPa ($N < 10^4$ cycles) often occurs in the base metal. It implies that the LCF strength of the weld is close to that of the BM. This result is consistent with the higher tensile strength of the martensitic microstructure as compared to the equiaxed BM. Hence, the term ‘overmatching’ is also applicable to the LCF properties of the weldments. In contrast, the specimens tested in the HCF regime ($N > 10^5$ cycles) were characterized by the fatigue failure located exclusively in the FZ and the S-N curve of the machined condition is considerably lower compared to that of the BM. The fatigue limit of the machined welds is by roughly 30% lower than the BM fatigue limit with milled surface quality. It is important to note that, strictly speaking, this result cannot be considered as a reduction of 30% because the two above-mentioned S-N curves represent different microstructures and cannot be directly compared. The term ‘efficiency’ is more suitable in

this case, i.e. the welded joint after machining has a 70% efficiency in terms of load bearing capacity in the HCF regime. The maximum cyclic load that the weld can transfer up to 10^7 cycles is around 70% of that parameter for the unwelded BM.

The location of fatigue failure in the FZ even in case of machined joints is attributed to internal microstructural features or defects undermining the fatigue strength of the joint. This fact is supported by our previous findings showing that the formation of internal defects is an inevitable process, regardless of the LBW parameters. As a result, fatigue crack nucleation commonly occurs at internal welding-induced defects within the FZ. In experiments with butt welds in the as-welded condition, the stress concentration at the weld toes or underfills is much more severe than that due to minor defects existing in the welding zone; therefore, these defects are less important. By removing the stress concentrators from the weld surface, internal defects become the most critical notches in the joint and exhibit their full deleterious effect. Thus, surface features and imperfections can overshadow the internal defects in their influence on fatigue behaviour.

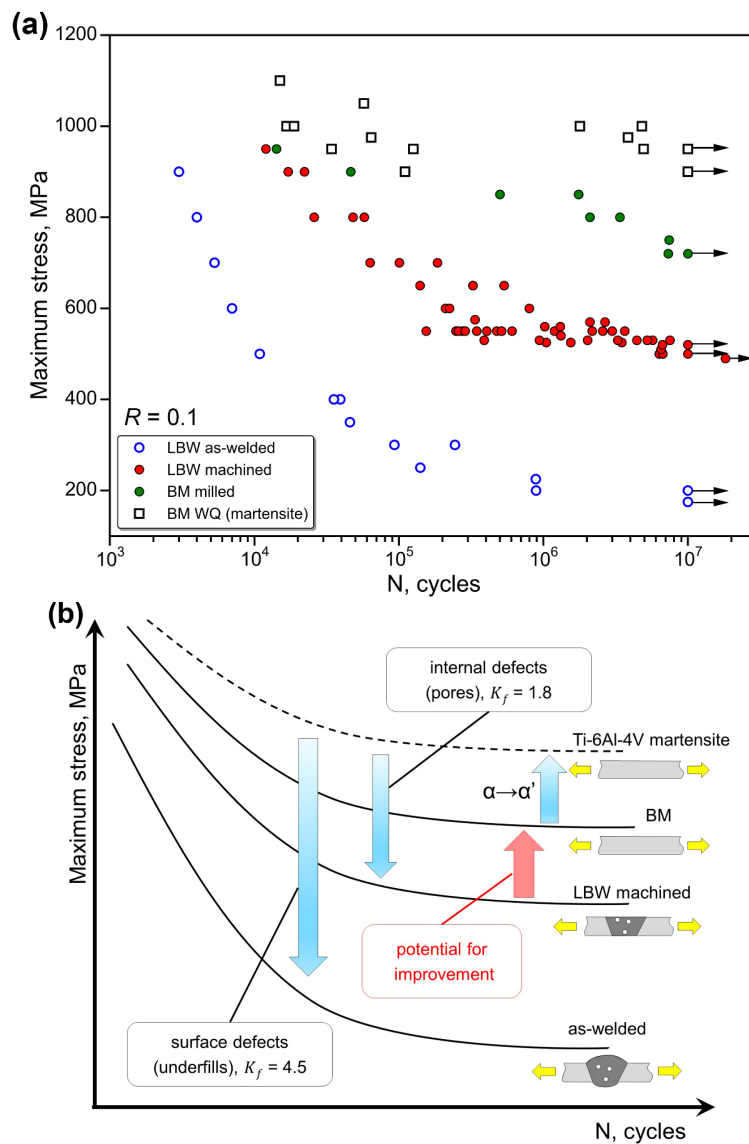


Figure 5.1. (a) S-N curves of laser-welded Ti-6Al-4V butt joints and the effect of machining; (b) schematic illustration of the effect of defects on the S-N curves and the region of potential improvement.

Fracture surfaces of the milled joints were examined by OM in order to identify the weld defects responsible for fatigue failure. Fractographic observations revealed that internal porosity is a typical type of defect at the crack initiation site of machined welds. A typical fracture surface of the machined joint after fatigue failure in the HCF region is illustrated in Figure 5.2. Three distinctive areas can be distinguished: crack initiation size, the region of stable crack growth, and the final fracture. Owing to subsurface crack initiation, a bright circular area, called ‘fish-eye’, is normally observed around the crack nucleation site. As discussed in Section 2.3.4, this circular pattern is a common attribute of fatigue fracture originating from internal defects [68]. A comprehensive analysis of the fish-eye mark and its detailed description will be given in Chapter 6, but, for now, a crucial role of internal porosity in the HCF failure of machined Ti-6Al-4V welds has to be emphasized.

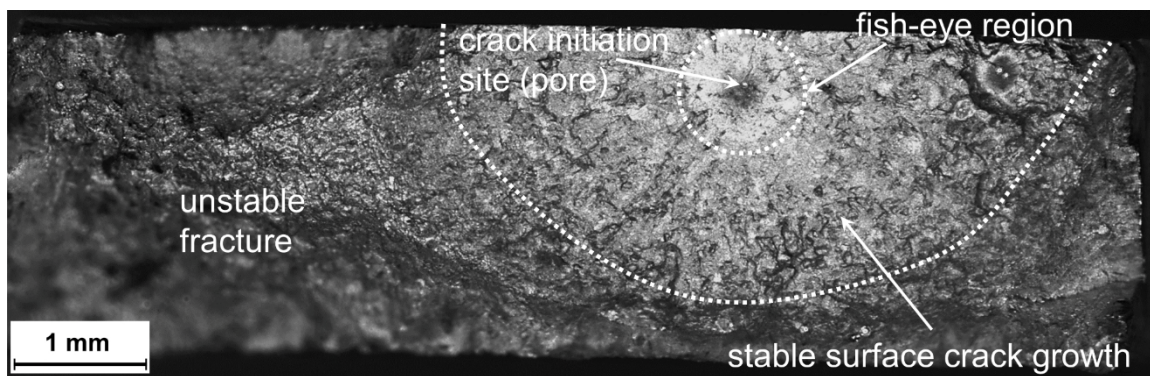


Figure 5.2. Fracture surface of the machined weld after failure in the HCF regime due to internal crack initiation ($\sigma_{max} = 600$ MPa; $N = 7.9 \cdot 10^5$ cycles).

As far as the main reason for fatigue failure in the FZ is elucidated, a more reasonable and sound interpretation of the experimental results shown Figure 5.1(a) can be given. In this context, the fish-eye mechanism of fatigue failure plays a central role. For the sake of clarity, S-N curves are demonstrated schematically in Figure 5.1(b). The S-N curve of the unnotched martensitic Ti-6Al-4V with a fatigue limit of 900 MPa acts as a reference curve. It shows the highest achievable fatigue strength and lies higher than any other curve. The as-received BM has a lower fatigue limit, and this difference stems from the pronounced hardening effect during the $\alpha \rightarrow \alpha'$ transformation. The as-welded condition is characterized by the lowest fatigue strength that is caused by the notch effect of surface defects such as underfills. Machining removes the surface stress concentrators, thereby activating the internal fatigue failure from the pores. The crack origin transition moves the S-N curve in the region of higher stresses.

The effect of crack-like defects on fatigue limit is usually expressed by the fatigue notch factor K_f , which is the ratio of the unnotched fatigue limit of the material to fatigue limit in the presence of a defect. The results of fatigue testing enable to estimate the fatigue notch factors for various types of weld stress concentrators. In the as-welded condition, a notch effect introduced by the weld underfills is characterized by a relatively high value of fatigue notch factor around 4.5 (see Figure 5.1(b)). The effect of internal defects (porosity) is less detrimental and is characterized by the fatigue notch factor of 1.8. These values may be then used for estimation of the material notch sensitivity.

Regardless of the pore diameter, the value of the elastic stress concentration factor for an internal spherical pore in titanium is approximately $K_t = 2.1$ [165]. The notch sensitivity factor is defined as the ratio of the fatigue notch factor K_f to the elastic stress concentration factor K_t :

$$q = \frac{K_f - 1}{K_t - 1}. \quad (5.1)$$

The values of q for various materials and defect shapes are normally below 1.0, i.e. the drop of fatigue limit due to the notch effect is less severe than the elastic stress concentration at the notch. According to Equation (5.1), the notch sensitivity factor of the martensitic FZ in terms of porosity influence is approximately 0.86. This value shows that the fatigue limit reduction does not fully reflect the stress concentration level around a pore. Apparently, plastic deformation at the notch root mitigate the stress concentration to some degree, and the fatigue limit is slightly higher than the value predicted by the theory of elasticity. Nevertheless, relatively high notch sensitivity close to 1.0 is consistent with material brittleness and the small average pore radius [14].

The results obtained suggest that the shift of the crack initiation site to the interior of the specimen has a strong beneficial effect on the fatigue performance. On the other hand, the S-N curve of the machined joints is still located slightly lower than the curve of the milled BM. It implies that, in the presence of notches, the stronger martensitic phase exhibits a fatigue limit lower than that of the unnotched equiaxed microstructure. First, it explains the position of the fatigue fracture in the FZ. After machining, the notched FZ acts as the weakest spot in the joint in spite of its higher unnotched fatigue strength. Second, it opens a region for potential fatigue property improvement up to the S-N curve of the BM. Obviously, the latter is the highest fatigue strength that can be achieved for the welded joint, unless additional measures to increase the BM fatigue properties are undertaken.

5.2 Post-weld heat treatment (PWHT)

As stated earlier, the machined laser-welded Ti-6Al-4V butt joints exhibit fatigue properties that are around 30% lower compared to those of the BM. In order to reduce this gap and to move the S-N curve closer to the BM level, several additional measures have been proposed. Generally, there are two ways to realize the desired improvement. First, the number of defects can be minimized at the stage of LBW. Second, the resistance of the microstructure to fatigue crack initiation and growth can be maximized. This section will present the second option based on the application of PWHT. For this purpose, various types of PWHT described in Section 3.1.8 have been employed.

The influence of different PWHT types on the fatigue performance of the laser-beam-welded Ti-6Al-4V butt joints is shown in Figure 5.3. It is worth mentioning that all the data in Figure 5.3 represent the flush-milled condition because the welds were machined after the heat treatment. Therefore, the curve for machined welds should be regarded as a reference while assessing the effect of PWHT. As shown in Figure 5.3, if the annealing temperature is lower than 750°C (SRA1 and SRA2), the results of the tests lie in the scatter range of the S-N curve for machined condition. Considering the inherent scatter of fatigue experiments, no statistically significant influence of low-temperature annealing ($T < 750^\circ\text{C}$) on the fatigue performance was found. Application of SRA1 or SRA2 heat treatments resulted in the fatigue limit of 500–520 MPa, which is equal to the corresponding reference fatigue limit. However, annealing at temperatures above 750°C (FA2, DA) leads to a slight improvement of fatigue properties, as shown in Figure 5.3. The specimens annealed at 850°C (FA2) and subjected to duplex annealing (DA) show the highest value of fatigue limit in the range of 540–550 MPa. For comparison, the as-welded or specimens heat-treated at lower temperatures endure, on average, less than 500,000 cycles at this level of stress. Thus, it can be

concluded that annealing at temperatures above 750°C increases the fatigue strength of the joint and shifts the S-N curve towards higher values of stress.

Fatigue failures of the heat-treated welds in the HCF region are always observed in the FZ, similar to the as-welded and machined states. This result is in agreement with the fact that the PWHT does not affect the internal defects, and numerous pores remain within the weld zone. Since the specimens subjected to PWHT were milled thereafter, we can assume that equality of surface roughness was provided, and we can exclude this factor from further consideration. This allows us to consider microstructural changes as the dominant factor affecting the fatigue properties of the laser-welded joints. The link between the results of microstructural analysis and fatigue behaviour can be provided, based on our previous findings. This correlation relies on the analysis of microstructural parameters that determine the crack growth resistance of the material.

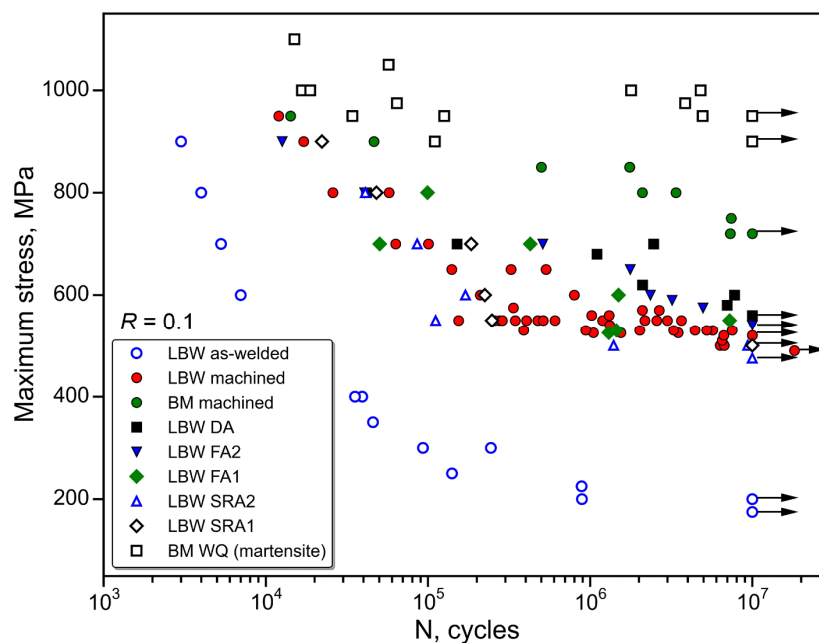


Figure 5.3. Effect of PWHT on fatigue properties of laser-welded Ti-6Al-4V butt joints.

As briefly reported in Section 2.3.2, the most influential microstructural parameter on the crack growth resistance of lamellar microstructure is the α colony size, as it determines the effective slip length [22, 166]. This parameter should be considered as an effective microstructural size for lamellar morphology within the FZ. In this context, a martensitic structure can be regarded as an extreme case of very fine lamellar morphology. The yield strength and the unnotched fatigue strength decrease with an increase in the α colony size. However, if macrocracks or sharp notches already exist in the material, a coarse lamellar microstructure is more beneficial for fatigue performance because the increased effective slip length retards fatigue crack propagation due to an increased level of crack front roughness [26]. The trade-off between decreased strength and increased toughness makes the coarse lamellar microstructure less sensitive to notches and more advantageous for usage in applications where the notched fatigue strength is of great concern.

Annealing of the laser-welded Ti-6Al-4V butt joints at temperatures up to 750°C is insufficient for complete martensite decomposition of the fine-grained FZ into the equilibrium lamellar $\alpha+\beta$ structure. The width of the individual α' lamellae and the average α' colony size remained almost the same after heat treatments at such low temperatures, and no significant microstructural changes were

observed. In spite of a slight increase in microhardness, mechanical properties also remained approximately the same. We can infer that the low-temperature annealing does not affect the HCF performance of the laser-beam-welded Ti-6Al-4V butt joints.

As described above, starting from the temperature of 750°C, a metastable martensitic structure in the FZ transforms into an equilibrium lamellar $\alpha+\beta$ morphology, as shown in Figure 4.8(a–c). With increasing temperature, the width of individual lamellae and the α colony size increase with a commensurate increase of the effective slip length and a corresponding decrease in the yield strength. A coarse lamellar structure with lower density of defects after annealing at high temperatures has a lower strength and higher ductility than martensitic morphology, as demonstrated by tensile testing. This was further indirectly confirmed by decreased microhardness in the FZ after PWHT at high temperatures. Although the static strength of the joint decreased to some extent, more ductile and softer material in the FZ was more beneficial for the HCF properties than a hard martensitic structure. High-temperature annealing reduced the notch sensitivity of the FZ, and internal defects have become less detrimental for fatigue properties than in the martensitic structure. Considering the fatigue limit of ca. 550 MPa, notch sensitivity of the annealed microstructure is equal to $q = 0.77$ that is lower than the value for the as-welded microstructure ($q = 0.86$). Increased α colony size and, consequently, larger effective slip length leads to a more bifurcated crack growth profile and increased crack propagation resistance of the material. Thus, the coarse-grained lamellar microstructure is more ductile, less brittle, and, therefore, more defect-tolerant than the fine-grained martensitic microstructure. These results and conclusions are consistent with the works of Yoder et al. [166, 167] and Lütjering et al. [22, 26].

Transverse cross sections of the fractured heat-treated specimens have been made to ascertain these findings. This task involved a big challenge of manually grinding the specimen with multiple steps until a pore is found. To compare the crack front roughness in different FZ conditions, grinding and polishing was performed precisely up to the plane containing the pore with a crack. The required tolerance of grinding for this purpose is approximately $\pm 10 \mu\text{m}$. As shown in Figure 5.4(a, b), the coarser lamellar microstructure displayed a more tortuous and deflected crack path in the region adjacent to the pore than the finer-scale martensitic microstructure. The effective slip length in case of annealed material is the α colony size of ca. 30–50 μm , but it is the width of individual α plates (around 1 μm) in case of martensitic morphology. The increased crack path tortuosity leads to enhanced crack deflection that increases the material FCP resistance and the overall fatigue performance.

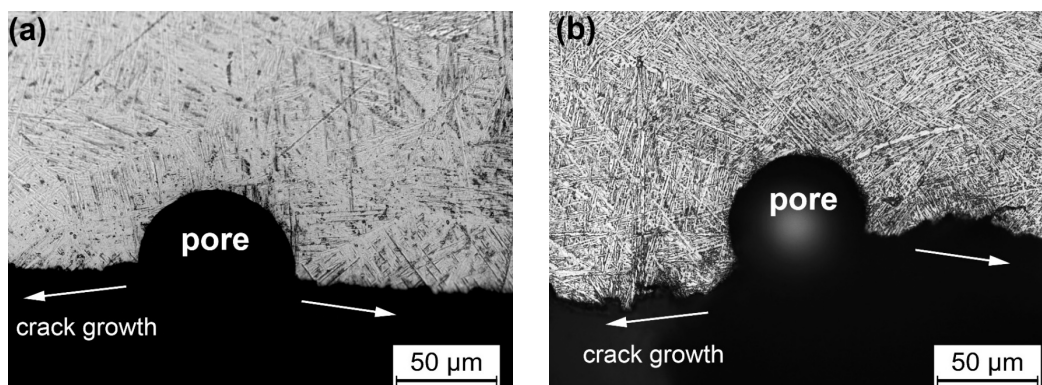


Figure 5.4. Comparison of the crack front roughness profiles in the zone adjacent to the crack-initiating pore. (a) As-welded condition; (b) annealed at 850°C for 1 h (FA2).

5.3 Laser surface remelting (LSR)

Despite its beneficial effects, machining as a post-processing technique has several major drawbacks. It is well known that titanium alloys exhibit relatively low machinability [22, 28]. As a result, the introduction of a milling step into the manufacturing process would inevitably lead to higher costs and lower productivity. In this context, the concept of non-contact LSR treatment by the defocused laser beam eliminates the inherent problems of machining. It provides high processing speeds, flexibility of the process, and allows the use of the same laser equipment as for welding. Without readjusting the welding set-up, the weld seam can be directly processed after the LBW process. A major drawback of the method is, however, a high heat input during the LSR processing.

A typical cross section of the weld subjected to the LSR post-weld treatment is shown in Figure 5.5(b) in comparison to the as-welded seam in Figure 5.5(a). Since the focal spot size of the defocused laser was larger than the weld width, LSR processing has a pronounced smoothing effect, thus, reducing the notch effect from the weld underfills. Although some insignificant residual curvature is usually present after the post-processing, the surface stress concentration is negligibly low compared to that induced by subsurface porosity. Therefore, fatigue cracks most likely nucleate at internal defects as observed for machined joints. All the welds subjected to the LSR treatment exhibited the fish-eye type of fracture indicating the occurrence of internal crack initiation. As shown in Figure 5.5(c), fatigue properties of the LSR-treated joints are slightly higher in comparison to the machined condition. The latter is, presumably, related to the final depth of pores after the application of post-processing. The removal of the surface layer of the material by milling leads to a decrease in the average pore depth. This is negatively reflected by the fatigue properties. On the contrary, LSR-treatment keeps the material thickness constant and, consequently, the pore position relative to the surface does not change. The fatigue limit in the range of 540–560 MPa for the LSR-treated joints was the highest among the investigated post-processing techniques.

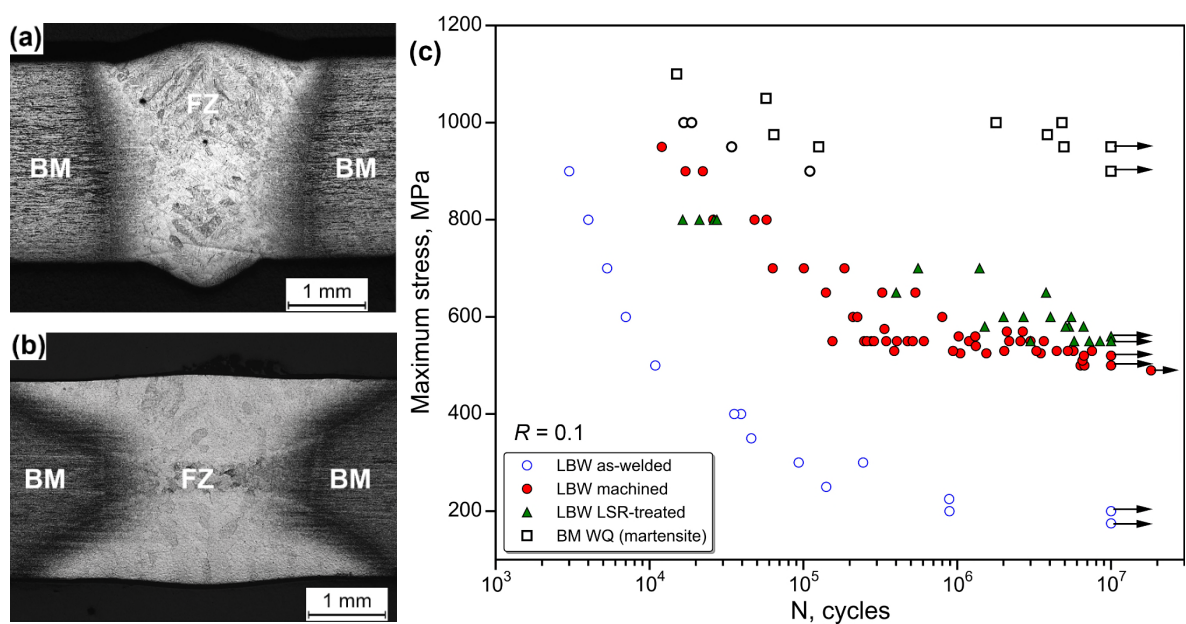


Figure 5.5. (a) Cross section of the weld in the as-welded condition; (b) effect of the LSR treatment on the weld shape; (c) S-N curves of the LSR-treated welds in comparison to those of the BM and machined condition.

In order to verify if the LSR treatment affects the porosity level or its distribution, additional radiographic inspection tests were undertaken. Interestingly, the porosity level within the FZ did not significantly change following the application of the LSR technique. Moreover, no differences in the pore positions were observed. This result indicates that the time when the material is in the molten state during the LSR process is not sufficient for emersion of the pores. Hence, the LSR treatment has, essentially, the same improvement mechanism as conventional machining, i.e. it removes the surface notches retaining the internal defects.

Based on the results of this section, it might be, by mistake, concluded that the LBW process can be completely omitted and the welding can be performed by the defocused laser beam. This situation corresponds to the so-called conduction mode welding without the formation of a keyhole, as presented in Section 2.2.1. Indeed, it will result in almost pore-free welds, but the material thickness that can be welded by this technique is limited up to about 1.5 mm for the current set-up used in this work. Figure 5.5(b) clearly illustrates the molten zone depth during the LSR processing. It can be observed that a 2.6-mm-thick titanium sheet would not have been completely penetrated by the LSR treatment from both sides, although these parameters were close to the maximum achievable for the current set-up. High back reflection and increased heat input into the specimen impose restrictions on the laser power used in the LSR process. From this perspective, keyhole welding is more promising because it has a significantly larger range of weldable thicknesses (up to 50 mm [6, 168]). Hence, a double-step technique including both LBW and LSR has the biggest potential to be used in practical applications.

5.4 Laser shock peening (LSP)

LSP is an effective local modification technique for generating compressive residual stresses in the near-surface layer up to several millimetres in depth. The induced residual stress field might have a strong beneficial effect on the fatigue performance because it considerably suppresses the fatigue crack growth in the treated area. By this, a significant improvement and lifetime prolongation can be achieved for surface cracks [93] and through-thickness cracks [169]. This section describes the effect of LSP as a post-processing mechanical treatment for both the as-welded joints and machined joints. As discussed in the previous sections, in order to stimulate any remarkable effect, the residual stress field should restrain the growth of nucleated surface cracks for the as-welded joints and the propagation of internal cracks for machined welds respectively.

Prior to studying the effect of LSP on the fatigue strength of laser-welded Ti-6Al-4V joints, the generated residual stress field and depth profiles were measured by the HDM. It should be noted that the measurements were performed using the water-quenched BM titanium specimens with a fully martensitic microstructure. The basic argument for this approach is related to the fact that fatigue cracks initiate and grow solely in the FZ of the weld. Therefore, the effect of LSP on the welded martensitic microstructure is of primary interest. Direct residual stress measurement in the weld after LSP is unfeasible due to limitations imposed by the HDM facility. The results shown in Figure 5.6(a) suggest that compressive residual stresses after the LSP processing are formed in the surface layer of 0.9 mm in depth. Owing to the use of steel foil as an ablative layer, the thermal relieving effect of the LSP plasma [170] was prevented and compressive residual stresses of about -200 MPa were formed at the specimen surface. Figure 5.6(a) demonstrates that the two estimated stress components σ_{xx} and σ_{yy} are close to each other and approach the yield strength of the material at the peak point. Error bars represent the 95% confidence intervals from five measurements. The maximum compressive

stress is achieved at the depth of 0.2–0.3 mm, and then its intensity gradually reduces with increasing depth. At the depth of 0.9 mm, the sign of residual stresses changes to positive. This graph indicates that tensile residual stresses dominate in the middle section of the 2.6-mm-thick specimens used in the present work. Note that the measured data correspond to the fully martensitic structure, whereas the weld shape and irregularities might have some effect on the real LSP stress profile in the welding seam. Therefore, the results presented should be interpreted as qualitative.

As shown in Figure 5.6(b), the LSP treatment of the as-welded joints has a pronounced positive impact on the fatigue behaviour, leading to a fatigue limit of approximately 380–400 MPa, which is close to the fatigue limit of the machined joints. Thus, residual stresses around the weld help to mitigate the severity of the notch effect induced by the weld underfills. Apparently, the crack growth rates are significantly lower when the crack grows in the 0.9-mm-deep compressive residual stress field. This yields a significant fatigue life prolongation, as shown in Figure 5.6(b). In spite of high compressive residual stresses induced by LSP, surface crack initiation was still observed for all the LSP-treated specimens. Fatigue cracks always initiated from the weld underfills similar to the as-welded state. It implies that compressive residual stresses mitigate the severity of the underfill notch effect to some extent, but it is not sufficient to shift the crack nucleation to the subsurface region. Surface weld defects still overshadow the internal porosity after the LSP treatment.

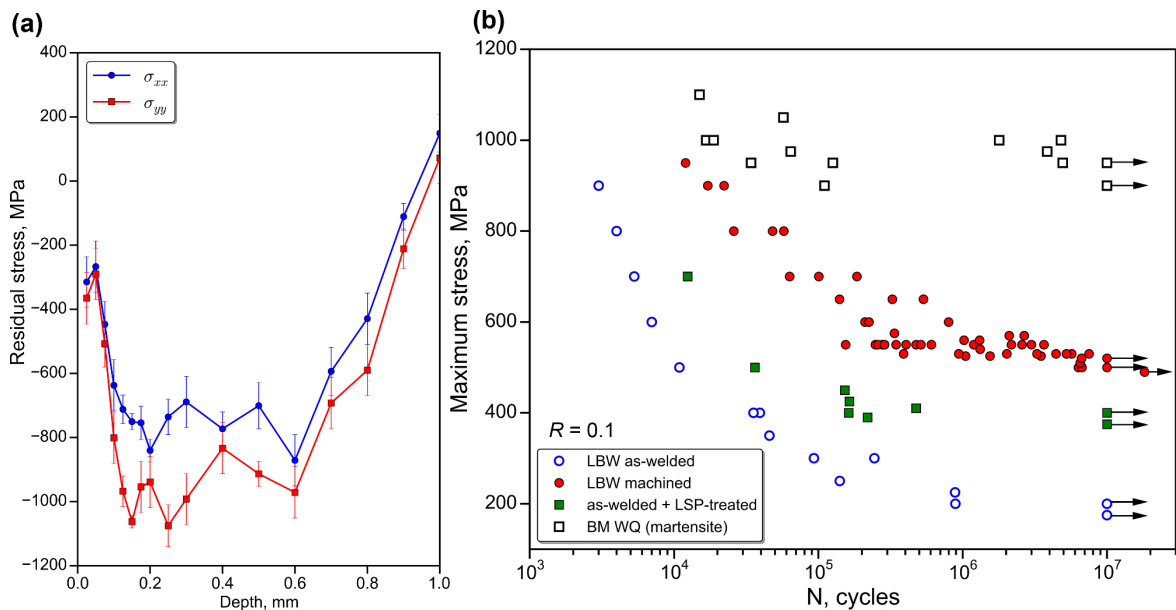


Figure 5.6. (a) In-depth profile of LSP-induced residual stresses; (b) effect of the LSP treatment on fatigue properties of the as-welded joints.

The concept of applying LSP on the machined or LSR-treated joints has some important features to be accounted for. Considering the mechanism of internal crack initiation, the depth of compressive residual stresses is of great importance. To achieve a retardation of the crack nucleation and growth, the residual stress field should cover the potential crack initiation site. Since the typical depth of the pores on the fracture surface is around 0.4–0.5 mm (see Figure 4.18(b)), one should expect a positive effect of the LSP treatment on the fatigue behaviour because the compressive residual stresses are formed up to a depth of 0.9 mm. Nevertheless, a big scatter in the pore distribution and the residual stress profiles might play a negative role. The first fatigue trials with the LSP-treated machined specimens indicated that the effect of the LSP treatment was comparable to fatigue scatter, i.e. a big

scatter in fatigue life overweighs the effect of LSP. The conventional Wöhler concept, based on the S-N curves, requires a large number of specimens to quantitatively distinguish a positive shift of the S-N curve from the large fatigue scatter. Therefore, an alternative approach, based on the fatigue testing of numerous specimens at one stress level, was selected. In this case, a limited number of specimens is sufficient for statistical processing of experimental results.

To study the effect of LSP on the internal crack initiation and growth, 16 machined and 16 LSP-treated specimens were tested at one equal stress level of 550 MPa. This stress level is representative for the HCF region, which is in the focus of our study. Statistical analysis showed that the Weibull probability distribution can adequately describe a high degree of lifetime variability. Moreover, there is a particular interest in regression reliability models based on the Weibull distribution [137, 171]. Basic properties of the Weibull distribution and the procedure for the construction of the Weibull plot are presented in Section 3.3.2. The results of fatigue tests for both sets of specimens (machined and LSP-treated) are presented by the Weibull probability plotting in Figure 5.7(a). Plotting and the accompanying calculations have been performed using *Python*. The fitting of experimental data to Weibull distribution was done by the ordinary least squares technique. This yielded the estimates for the Weibull model parameters, which are shown in Figure 5.7(a) for each curve.

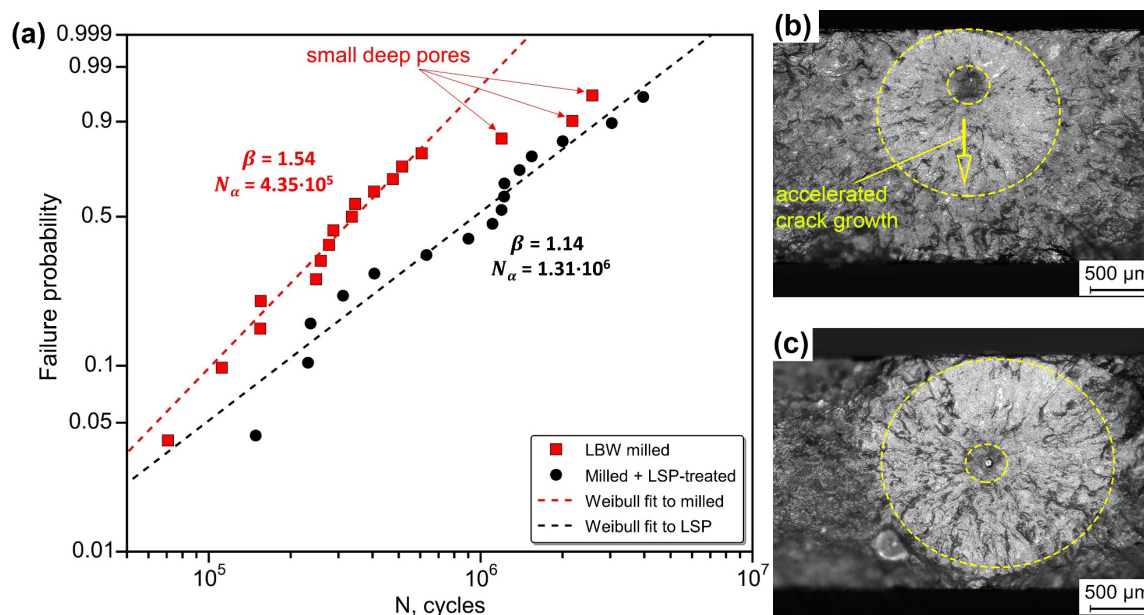


Figure 5.7. (a) Weibull plot showing the effect of LSP on the fatigue life distribution of machined joints; (b) the eccentric fish-eye appearance due to residual stresses; (c) the fish-eye appearance when the crack origin is in the middle part of the specimen where tensile residual stresses prevail.

As can be seen, the experimental points fall onto a straight line, implying that the Weibull model describes the experimentally determined lifetime distribution fairly well, and it is a reasonable fit for the experimental data. It can be seen that some points in the right tail of the curve for machined condition do not follow the line. This relates to a slightly different crack initiation mechanism. Small deep pores were found on the fracture surface of these specimens, whereas larger subsurface pores were observed in most cases. These specimens might have been extracted from the region of the welded sheet with a relatively low porosity level. As shown in Figure 5.7(a), application of the LSP treatment increases the Weibull scale parameter N_α almost by a factor of three. The Weibull shape parameter β (slope) decreased from 1.54 to 1.14 after the LSP treatment, indicating that the spread

of fatigue life was slightly higher. It is evident from the results that compressive residual stresses have, on average, a positive impact on the fatigue life; however, the increased fatigue scatter band should be taken into consideration. The decreased Weibull shape parameter is associated with a higher dispersion of results. These findings indicate that the application of LSP treatment for the suppression of the internal crack growth has less improvement potential than in the case of surface cracks. Moreover, increased fatigue scatter should be dealt with extreme caution.

Careful fractographic inspection of the LSP-treated specimens after fatigue failure revealed some characteristic features that were not observed beforehand. Typical fractographic images are presented in Figure 5.7(b, c). Generally, the LSP-treated specimens could be divided into two groups, according to the form of the fish-eye mark. In the first group, the fish-eye circle was not symmetrical to the crack nucleation site (Figure 5.7(b)). The observed eccentricity and wide lower fish-eye region imply that the internal crack was propagating in this area noticeably faster. These observations have a good correlation with the profile of compressive residual stresses that are declining to the centre of the specimen. The specimens from the second group exhibit the largest fish-eye circles with the pore located approximately in the middle of a specimen. This appearance also matches with the residual stress profile because the middle section corresponds to the region with tensile residual stresses. These findings further support and confirm the positive role of compressive residual stresses on the fatigue failure that started from internal defects.

5.5 Process parameter variation

The last method investigated in this work aims to minimize the porosity level and, thereby, to increase the fatigue limit of the surface-treated welds (machined or LSR-treated). In order to study the effect of porosity distribution on the fatigue strength, S-N specimens were welded with different porosity levels. For this purpose, Parameter Sets 1 and 2, as shown in Figure 4.19(a), were used. Parameter Set 1 was characterized by a low laser power, closed keyhole, and consequently, a relatively lower number of pores. Parameter Set 2, on the contrary, has a high laser power, therefore an open keyhole, and a high level of porosity. The LSR treatment was applied after welding to prevent the surface crack initiation. This step is required to stimulate the internal crack initiation from the weld pores. A traditional Wöhler approach, based on the S-N curves, was used for comparing the fatigue properties.

The results of fatigue testing are shown in Figure 5.8. Surprisingly, no statistically significant difference was found in the fatigue properties between the welds with low and high porosity levels. In other words, no remarkable correlation between the fatigue limit and the distribution of defects was observed. These tests showed that the influence of the LBW process parameters on the fatigue strength of subsequently surface-treated welds is relatively low. These unexpected results can be interpreted as following. The results of the X-ray analysis demonstrated that the two selected parameter sets had extremely different porosity levels. Note that in spite of the impact on porosity level, the process parameters have no effect on the pore size distributions. The increased number of pores can have an impact on the fatigue life primarily through the increased probability to have a more detrimental defect in the extracted fatigue specimen. Indeed, the larger the number of pores in the weld seam, the higher the probability of having a larger pore close to the surface and, as a result, a shorter fatigue life. The pore populations in fatigue specimens welded with these two different process parameters comprised approximately 30 and 50 pores for the Parameter Set 1 and Parameter Set 2, respectively. Apparently, this number of pores was not enough to yield any statistically significant difference that could be observed during fatigue testing. This inference can be additionally

supported by the statistics of extreme values (SEV) normally used for the characterization of steel cleanliness [68, 172]. As reported in Section 2.3.4, non-metallic inclusions or other types of defects in steel initiate the subsurface cracks in the HCF and VHCF regions. In the SEV methods, the maximum size of defect in a given steel volume is proportional to the logarithm of the steel weight [99, 172]. Thus, the variation in the defect population size of several orders of magnitude is required in order to detect a statistically significant difference in the maximum defect size. Hence, the increase only by a factor of two observed in the present work was not significant from the statistical point of view. Fatigue testing of large laser-welded fatigue specimens is required to estimate the effect of the defect population size on the fatigue strength.

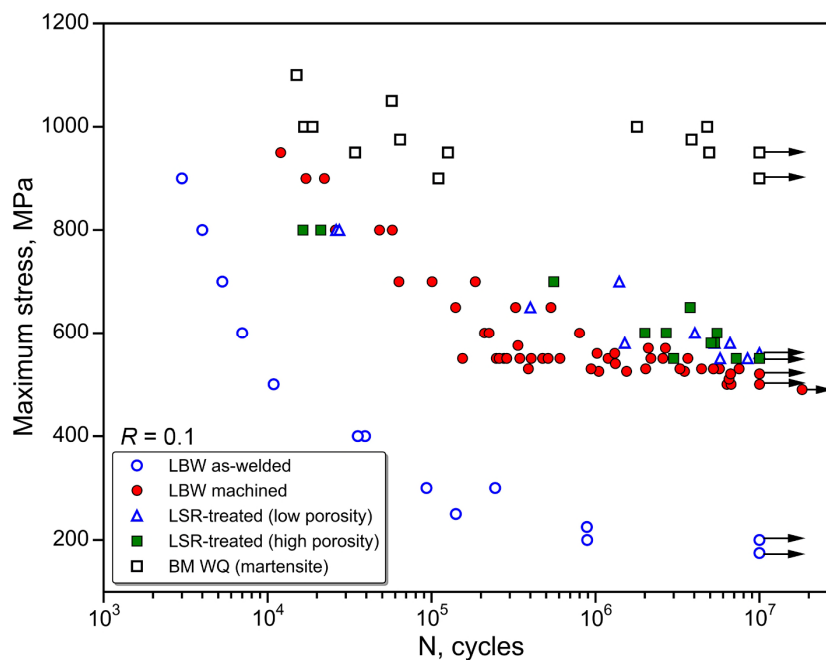


Figure 5.8. Effect of porosity level of the fatigue behaviour of the LBW Ti-6Al-4V butt joints.

The main conclusion that can be drawn from these results is that fatigue performance of the laser-welded Ti-6Al-4V butt joints after the LSR processing or machining cannot be altered significantly by the welding parameters unless a relatively large component is welded. Variations in the process parameters can reduce the number of pores, but it is impossible to avoid them completely. As a result, the fatigue properties stay almost equal regardless of the welding parameters. Note that this conclusion is valid only for the surface-treated joints. In case of the as-welded condition, where the cracks start from the weld underfills, the LBW parameters determine the underfill depth and radius, thus playing an important role.

5.6 Conclusions

Comparison of the investigated methods for improvement of the HCF performance suggests that they can be categorized into two groups in accordance with the mechanism responsible for the lifetime extension (see Figure 5.9). The first group, including machining and laser remelting (LSR), aims at the prolongation of the fatigue life by the shift of the crack origin to the subsurface. The methods of the second group deal with the internal crack growth and aim to suppress the growth of internal cracks. This can be accomplished by varying the microstructure (PWHT), generating the residual

stresses (LSP) or changing the number of pores. LSP, as an instrument for generating the near-surface residual stresses, can be applied both to the as-welded condition and to the surface-treated welds.

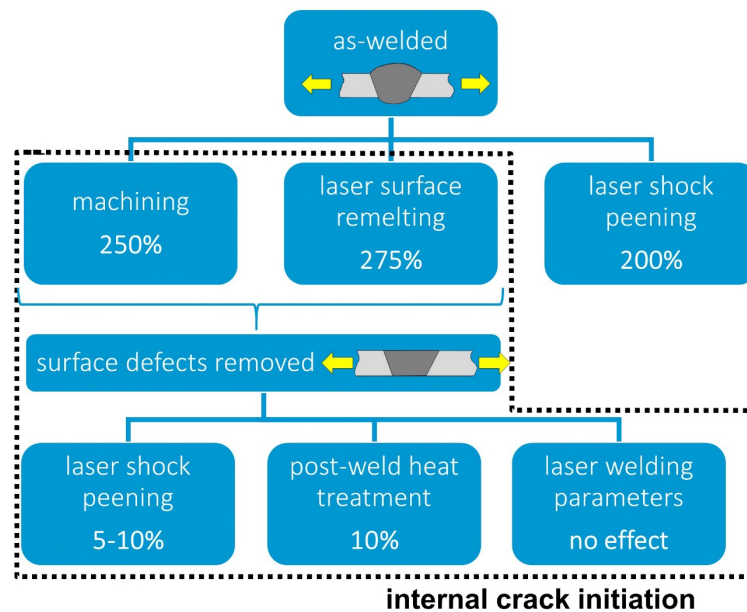


Figure 5.9. Comparison of different improvement methods in terms of their influence on fatigue limit.

Based on the results of this section, it can be concluded that the most powerful tools aimed at lifetime prolongation are surface modification methods leading to internal crack nucleation. A slight additional increase of around 10% can be provided by the subsequent heat treatment or LSP. The LBW process parameters have a relatively weak effect on the resulting weld fatigue properties of the surface-treated welds. Therefore, future investigations in this area as well as industrial practice should concentrate on the surface modification techniques leading to an appreciable improvement of more than 250% in terms of fatigue limit. The results highlight that internal welding induced porosity plays a key role in the fatigue failure of the laser-welded butt joints. Internal defects are unavoidable and have the most harmful effect that does not allow the weld fatigue limit to approach the BM level. For a reasonable quantitative assessment, the porosity distribution has to be carefully analysed and modelled by statistical tools including statistics of extremes. It is noteworthy that all the considered methods, besides PWHT, are not material-specific. Hence, the results and conclusions are transferable to other processing or manufacturing technologies that result in material degradation and pore formation, e.g. various forms of additive manufacturing [82], powder metallurgy [86] and also for parts operating in very-high-cycle fatigue regime [81, 85, 173].

6 Mechanism of internal fatigue failure

The results presented in the previous chapters reveal the paramount significance of internal welding-induced defects for the HCF properties of laser-welded titanium joints. The highlighted practical guidelines for the lifetime prolongation suggest that any type of surface smoothing technique has a big impact on the resulting load bearing capacity of a component in terms of the HCF behaviour. The weld porosity governs the fatigue failure of the welded joint, if a sufficient surface quality and low roughness are provided. These findings underline the need for a deeper understanding of the fatigue failure mechanisms for the particular case of fatigue fracture originating from internal pores. The purpose of this section is to provide a necessary experimental background and to gain a deeper insight into the mechanics of internal fatigue crack initiation and growth. Further progress and incorporation of the found improvement methods into industrial practice depends on a careful consideration and quantitative assessment of the fatigue failure characteristics.

Important clues to the underlying reasons and mechanisms of fatigue fracture may be revealed by the fractographic analysis at an appropriate magnification. Therefore, fracture surfaces of the specimens after fatigue testing were subjected to a detailed fractographic examination using both OM and SEM. The principal objective at this stage is to relate the fracture surface appearance to the weld characteristics including microstructure, residual stress, and inherent inhomogeneities. Quantitative fractographic assessment yields numerous fundamental material properties that are prerequisites for further development of a fatigue life prediction model.

6.1 Fish-eye fracture of welds

A fractographic analysis revealed that all fractures of the machined and LSR-treated laser-welded specimens occur from internal pores or clusters of pores induced by welding. In contrast, the joints with the as-welded surface condition always exhibit surface crack initiation at the top or root underfills. In the following, only the surface-treated welds are considered for assessment. It was briefly described in Section 5.1 that an internal crack that originates from a pore forms a clear fish-eye ring-like pattern on the fracture surface. The low-magnification image of the typical fish-eye fracture surface comprising several zones is presented in Figure 5.2. Hereinafter, only the circular fish-eye region of the fracture surface will be in the focus of the characterization because this particular region plays a key role in the HCF fracture.

Figure 6.1(a–d) shows an example of fatigue fracture surface for the LSR-treated specimen that endured $N = 5.7 \cdot 10^6$ cycles at a maximum stress of $\sigma_{max} = 550$ MPa. The OM image of the fish-eye region is demonstrated in Figure 6.1(a). The SEM view of the same fish-eye pattern with a slightly higher magnification is presented in Figure 6.1(b). The crack nucleation sites can be easily distinguished by the characteristic appearance of the fracture surface. The fish-eye region is clearly visible as a bright circular area surrounding the crack nucleation site. In the optical microscope, the crack origin appears as a dark region around a pore, whereas it is a white zone in the SEM image. Figure 6.1(b) reveals that a cluster of two small pores actually caused the fatigue failure of this specimen. The fish-eye mark presented in Figure 6.1(a) is a unique feature attributed to fatigue failure originating from internal defects. As discussed in Section 2.3.4, a remarkably similar fish-eye type of fracture caused by subsurface crack initiation is also normally observed in the VHCF regime of high-

strength steels [68, 100] and titanium alloys [21] as well as in additively manufactured parts [82]. Hence, the results presented in this work are also relevant in the frames of the above-mentioned topics.

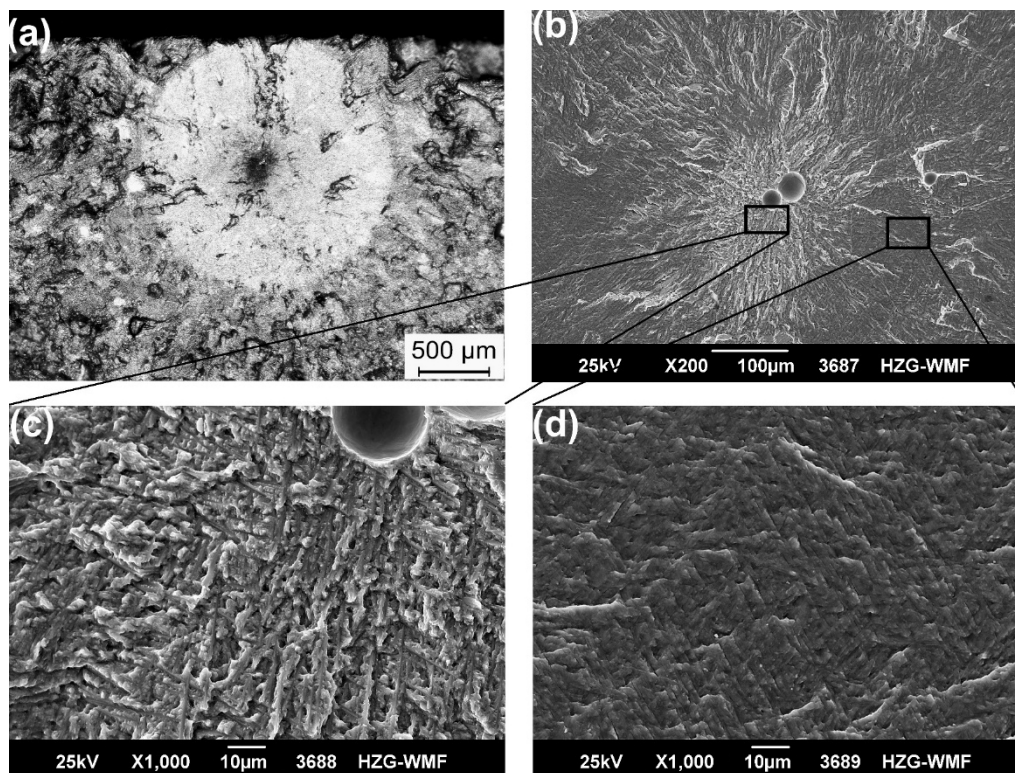


Figure 6.1. Fish-eye fracture surface of the laser-beam-welded Ti-6Al-4V butt joint after LSR treatment ($\sigma_{max} = 550$ MPa, $N = 5.7 \cdot 10^6$ cycles): (a) overview OM image; (b) SEM image of the ODA area; (c) magnified view of the ODA region; (d) magnified view of the smooth area.

Fish-eye marks are typically symmetrical with a pore precisely at the centre of the white circle unless the LSP treatment is applied (Section 5.4). The radius of the fish-eye circle is typically equal to the distance from the specimen surface to the pore. Apparently, the bright appearance of the fish-eye area in the OM image is related to the smooth fracture surface, which reflects more light. The author believes that the most plausible explanation for this effect is the one given by Murakami et al. for steels in [68]. It is based on cyclic contact of fracture surfaces in the absence of atmospheric effects within the smooth area and by cyclic contact in the atmosphere outside of the fish-eye. Presumably, the contact of the two crack flanks is considerably enhanced in a vacuum-like environment. As a result, the roughness of a fracture surface is reduced due to a smoothing effect during the crack propagation. It is noteworthy that no fatigue striations were observed in the ODA in contrast to the area of stable surface-crack growth.

A dark area in the close proximity to the pore can be observed in the optical micrograph of the fracture surface, as shown in Figure 6.1(a). Owing to its unique topography, this particular area is darker in the OM and brighter in the SEM, operating in the secondary electrons contrast (see Figure 6.1(b)). More detailed SEM image of the above-mentioned zone in the proximity to the crack origin site is shown in Figure 6.1(c) with higher magnification. It was found that a characteristic zone exhibiting a fine granular morphology with numerous facets and cleavages was produced in this region. The region near the internal crack initiation site was called an optically dark area (ODA) by Murakami [68], a granular bright facet by Shiozawa et al. [70], and a fine granular area by Sakai et al. [97]. In the

following, the term ODA is used for this particular region of the fish-eye. According to the SEM observations, ODA zone has a fracture surface that is distinctly different from that of the surrounding smooth area of the fish-eye. A very rough fibrous morphology composed of a large number of facets was observed within the ODA. On the contrary, smooth area outside of the ODA was characterized by a relatively flat surface without any morphological features, as shown in Figure 6.1(d). The transition from the ODA to the smooth area displays a steep gradient with regard to the micromorphology and roughness. It has been shown by Tanaka et al. [101] for steels and by Cao et al. [86] for Ti-6Al-4V that ODA plays a crucial role in the VHCF and HCF regimes; however, a uniform understanding of the mechanisms leading to its formation has not been achieved yet.

At present, there are at least five independent theoretical models attempting to explain the ODA formation. A detailed review and description of the existing ODA models can be found elsewhere [100]. In addition to the existing theoretical models, some important experimental results on the ODA formation can be found in the literature. Nakamura et al. gives three necessary conditions to be fulfilled for the ODA generation: vacuum, repeating contact of fracture surfaces, and fatigue life over 10^7 cycles [174]. In contrast to earlier findings, the present work demonstrates that the fish-eye fractures of Ti-6Al-4V can occur in the range of 10^5 – 10^7 load cycles. Moreover, it was observed that a high number of cycles does not guarantee the clarity of the fish-eye pattern. Very often the fish-eye marks formed after around $3 \cdot 10^5$ cycles have more pronounced ODA zones than those tested up to 10^7 cycles. Our findings suggest that instead of the fatigue life, the applied stress is decisive for the ODA formation. In this context, clear fish-eye patterns were observed only in the HCF region at stresses close to the fatigue limit (500–700 MPa). No ODA regions were found for stresses higher than 700 MPa.

Several researchers indicated that ODA in steel tends to be observed only at low stress ratios ($R = -1$) due to the crack-closure effect [175]. However, the results of this work indicate that the fish-eye failure in Ti-6Al-4V occur under high load ratios above zero ($R > 0$) as well. The lack of any agreement on the mechanism of ODA formation is related to significant difficulties related to the experimental determination of internal crack growth rates. This opens a wide field for superficial and, sometimes, speculative deductions based on indirect measurements and wrong assumptions. As a result, a large variety of existing published models that are sometimes contradictory can be found in the literature.

In this study, the results of quantitative fractographic analysis have been statistically processed in order to find some tendencies and deeper insights into the ODA zone formation. According to the well-known Murakami methodology, the effective ODA size is usually characterized by the \sqrt{area} parameter, where *area* is the projected area of the dark region on the load direction [68]. Following this strategy, in this work, an effective ODA radius was estimated as $\sqrt{area}/\sqrt{\pi}$. Figure 6.2(a) shows the relationship between the effective ODA radius obtained by the fractographic analysis and the applied maximum stress. It can be seen that the ODA typically has a radius of 150 μm and is characterized by a big scatter. Additionally, it has a slight tendency to decrease with increasing stress levels. Further analysis of the experimental data was based on the calculation of stress intensity at the ODA periphery, i.e. at the transition from the ODA zone to the smooth area. The SIF range for internal circular cracks can be estimated according to [176] as

$$\Delta K = \left(\frac{2}{\pi}\right) \Delta\sigma\sqrt{\pi a}, \quad (6.1)$$

where $\Delta\sigma = \sigma_{max} - \sigma_{min}$ is the stress range and a is the crack radius that is equal to the ODA radius in this case. The results are presented in Figure 6.2(b) in the form of the SIF range at the edge of the ODA zone ΔK_{ODA} plotted against the applied maximum stress. It can be seen that the ΔK_{ODA} values are in the range of 5.5–8.5 $\text{MPa}\cdot\sqrt{\text{m}}$ and increase slightly with increasing maximum cyclic stress. This tendency is more pronounced than that for the ODA radius. Our results are consistent with the findings of Liu et al. [85] for the VHCF of Ti-6Al-4V ($\Delta K_{ODA} = 6\text{--}8 \text{ MPa}\cdot\sqrt{\text{m}}$) and those of Cao et al. [86] for HCF of Ti-6Al-4V produced by powder metallurgy ($\Delta K_{ODA} = 7\text{--}9 \text{ MPa}\cdot\sqrt{\text{m}}$). For comparison, the threshold SIF range of long cracks $\Delta K_{th,LC}$ for Ti-6Al-4V in vacuum environment, as reported by Oguma [81], is also shown in Figure 6.2(b). It is clear that ΔK_{ODA} values at the periphery of the ODA zone are quite close to the threshold values, albeit slightly higher.

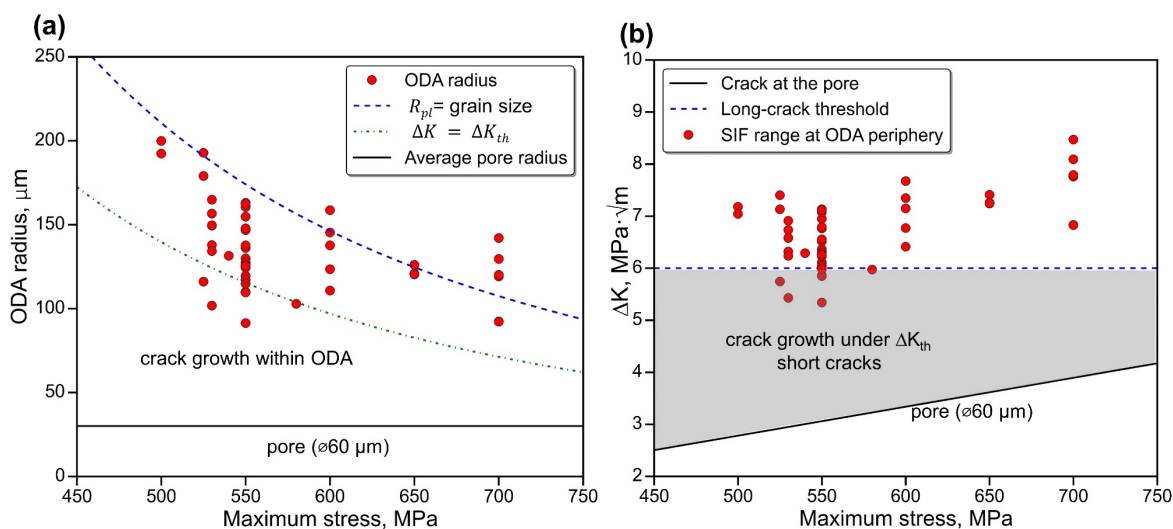


Figure 6.2. Relationship between the ODA characteristics and applied maximum stress: (a) ODA size; (b) the SIF range at the ODA periphery.

Figure 6.2(b) pinpoints that, in spite of stress intensities being lower than the threshold value, the internal crack is able to propagate within the ODA zone. Since the specimens were fractured, fatigue cracks inevitably grew in the grey area marked in Figure 6.2(b). One of the most striking characteristics of the ODA region is that the crack growth is not governed by the traditional fracture mechanics concepts. In the entire ODA area, the crack propagates under stress intensities not exceeding the required minimum level for long cracks. This conclusion will be further used in the development of fatigue life assessment model described in the following chapter.

The results of quantitative fractographic assessment are in good agreement with previous findings for Ti-6Al-4V [21, 174] and support two important concepts of ODA formation. First, since the ODA is not observed at higher stresses, it can be concluded that the ODA formation is linked to the early-stage crack growth in the near-threshold region close to the fatigue limit. It is well known that, when the crack length approaches the threshold magnitude, material microstructure gradually becomes more and more influential. Hence, microstructural characteristics should have a big role and affect the ODA properties. In addition, our experimental results suggest that a theoretical model based on the plastic zone at the crack tip, as reported by Zhao et al. [177], is in accordance with the quantitative fractographic analysis (see Figure 6.2(a)). In the above-mentioned model, it is assumed that the formation of ODA is completed when the size of the plastic zone at the crack tip R_{pl} is equal to the characteristic grain size of the material. The described model may also explain a much rougher

morphology of the ODA area. When the crack is growing in the ODA zone, the crack propagation step per cycle is smaller than the effective microstructural size; the crack, searching for the most favourable path, is significantly deflected. As a result, the fracture surface comprises many facets and is characterized by a relatively rough topography. In the smooth area, the crack propagation step per cycle is larger than the grain size, the crack is less deviated, and the fracture surface is smoother. As shown in Figure 6.2(a), the model of Zhao gives a reasonable prediction of the ODA radius.

Second, the results indicate that the SIF range at the ODA edge is close to the threshold values for long cracks measured in vacuum. Figure 6.2(a) shows that the ODA size prediction based on the known threshold gives a satisfactory result as well. Thus, the ODA size might be approximately considered as a region where $\Delta K < \Delta K_{th,LC}$. The reason for the unavoidable crack growth even when the applied SIF range is lower than the threshold can be attributed to the not fully developed crack closure for short cracks, as mentioned in Section 3.2.1. From this perspective, the ODA formation is attributed to the growth of short cracks in the proximity to the pore. This concept also can reasonably explain the typical fish-eye morphology. When the crack is short, not fully developed crack closure leads to very rough fracture surface in the ODA region. Outside of the ODA, the enhanced crack closure results in the smooth area due to the contact of fracture surfaces.

Summarizing the above-mentioned ideas, one can conclude that different theoretical concepts can result in similar interpretations of the results. It is not feasible to distinguish and to characterize all the effects involved in the ODA formation separately. The author believes that the ODA zone is the result of a combined effect from short cracks, crack closure and microstructurally sensitive crack growth in the early stages. The data obtained from the quantitative fractographic analysis were additionally used for characterization of the porosity distribution. The pore size and position at the crack initiation site were measured; the resulting histogram is shown in Figure 6.3. A total of 62 fractured specimens after fatigue-testing were considered for analysis. Statistical assessment showed that the pore-diameter distribution could be described by a log-normal distribution similar to the X-ray results. The arithmetic mean of the pore diameter found by fractographic observations is 93 μm and the average distance from the surface is 411 μm .

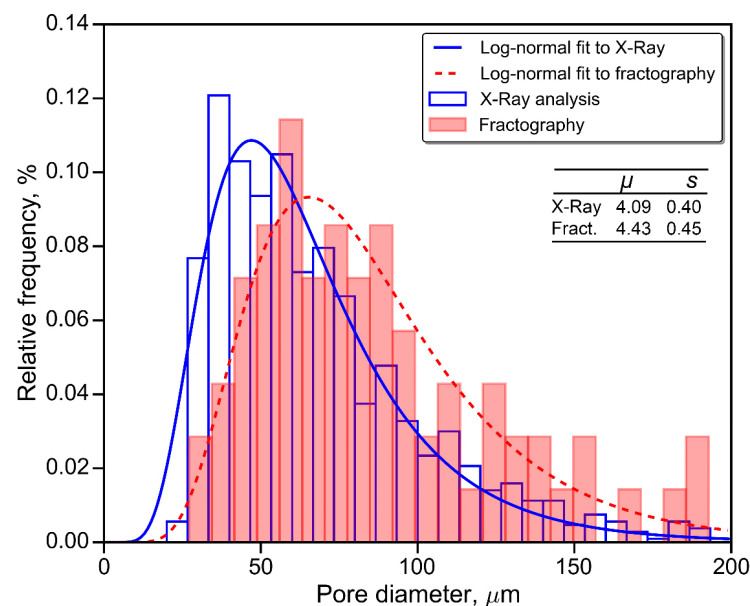


Figure 6.3. Histogram of the pore diameter from fractographic observations compared to the X-ray results.

On comparing the resulting pore-size distributions determined by the X-ray and fractographic measurements, a shift of approximately 30 μm in terms of average values was found. As shown in Figure 6.3, the crack-initiating pores at the fracture surface are, on average, larger than the pores detected and analysed by the X-ray analysis. Thus, larger pores are more detrimental and nucleate the fatigue cracks more often. Similar findings are reported by Ting et al. for porosity in the cast A319 aluminium alloy [178]. The shift between the pore-size distributions determined by the radiographic and fractographic methods, demonstrated in Figure 6.3, is very important because it can give some insights into the crack initiation mechanism. An adequate interpretation of this effect is given in the following chapter. A fatigue-life assessment model developed in this work can correlate these two distributions quantitatively.

6.2 Fish-eye fracture of base material

The titanium base metal generally does not contain inclusions or pores, which are typically the cause of internal cracks in laser weldments. For this reason, Ti-6Al-4V in the as-received condition exhibits surface crack initiation even in the HCF regime up to 10^7 cycles. The surface roughness acts as a crack origin regardless of the stress level and the number of cycles. As discussed in Section 4.7, machining the surface of fatigue specimens reduces the roughness and has a positive impact on the fatigue performance of the BM, similar to the laser-welded joints. Closer fractographic inspection and analysis of the fracture surfaces of the machined BM specimens with different types of microstructure revealed the interior crack initiation similar to that of the welds. In the region of high cycles that is roughly shown in Figure 6.4(a) cracks were found to originate not only from surface but also in the interior of the specimen. It is clear that the region of potential fish-eye failure of the BM lies higher than that of the welds. Crack nucleation sites could not be detected with standard OM; therefore, fracture surfaces were studied using SEM with high magnification. The fish-eye fracture surface of the mill-annealed machined specimen is presented in Figure 6.4(b). A clear ring-like pattern containing the bright ODA zone with a smooth darker area can be observed around the crack origin. Similar fracture surface appearance was observed for the heat-treated specimens with lamellar and martensitic microstructures. Thus, interior-initiated fatigue fracture of Ti-6Al-4V occurs even in the absence of metallurgical flaws such as welding porosity.

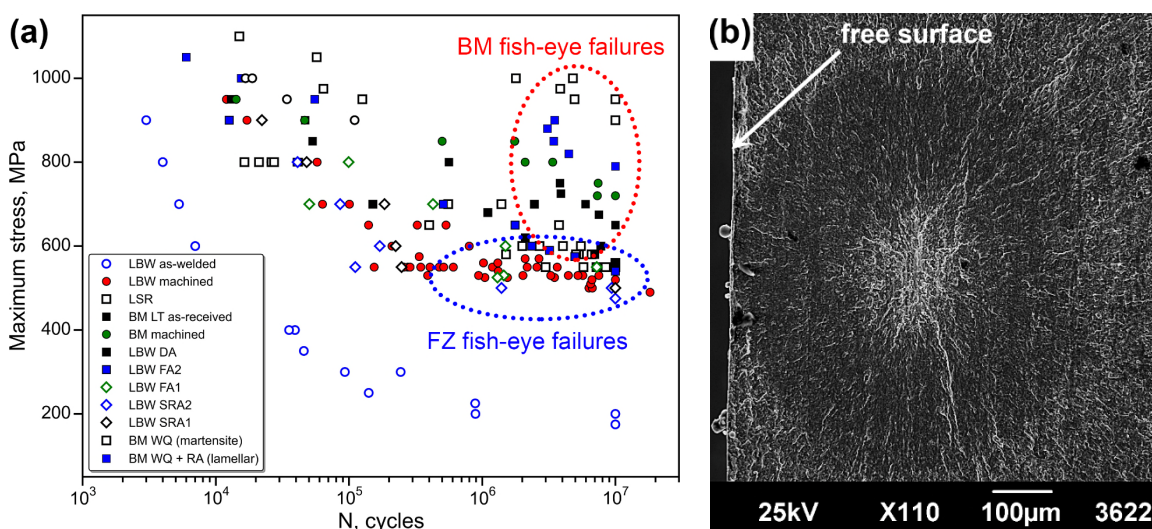


Figure 6.4. (a) Regions of internal fish-eye fractures for the FZ and BM; (b) fish-eye fracture surface of the machined Ti-6Al-4V with mill-annealed microstructure ($\sigma_{max} = 800$ MPa, $N = 2.1 \cdot 10^6$ cycles).

Initiation areas and the ODA regions were further subjected to the SEM fractographic analysis in order to correlate the occurrence of internal crack initiation with microstructural characteristics. In all cases, the crack initiation area of the fracture surface revealed faceted features having a cleavage-like appearance. No inclusions or defects were found at the crack origins. The form and shape of the facets at the crack initiation sites were found to have a good correlation with the microstructure. Hence, the microstructure itself has some internal ‘weak spots’ leading to the crack nucleation underneath the surface. The link between the mentioned material weak spots and its microstructure is of great importance from the practical and scientific point of view. Figure 6.5(a–f) shows the crack initiation sites identified at the ODA centres and the corresponding types of microstructure considered in this work, namely globular in the as-received condition (Figure 6.5(a, d)), lamellar in the recrystallization annealed state (Figure 6.5(b, e)) and the martensitic after water quenching (Figure 6.5(c, f)). A thorough analysis and comparison of the micrographs and the SEM images suggest that there is a compelling correlation between the crack origins and the microstructural types.

Fracture surface of the fatigue specimen with equiaxed morphology after mill-annealing shown in Figure 6.5(a) exhibits elongated oval facets parallel to the specimen surface. The shape and direction of these internal features almost completely reproduce the form of not fully recrystallized lamellar zones retained after the mill annealing. This match is clearly visible by comparing the microstructure cross section in Figure 6.5(d) and the fractographic image in Figure 6.5(a). Hence, the coarse lamellar zones surrounded by the fine-grained structure in the mill-annealed material act as hard α grains and have a detrimental effect on the overall fatigue properties. Interestingly, this serious drawback of the mill-annealing heat treatment is never mentioned when the properties of the mill-annealed microstructure are compared with those of the fully equiaxed [28]. Our findings indicate that the recrystallization annealing is needed in order to improve the resistance of this type of microstructure against the internal crack initiation.

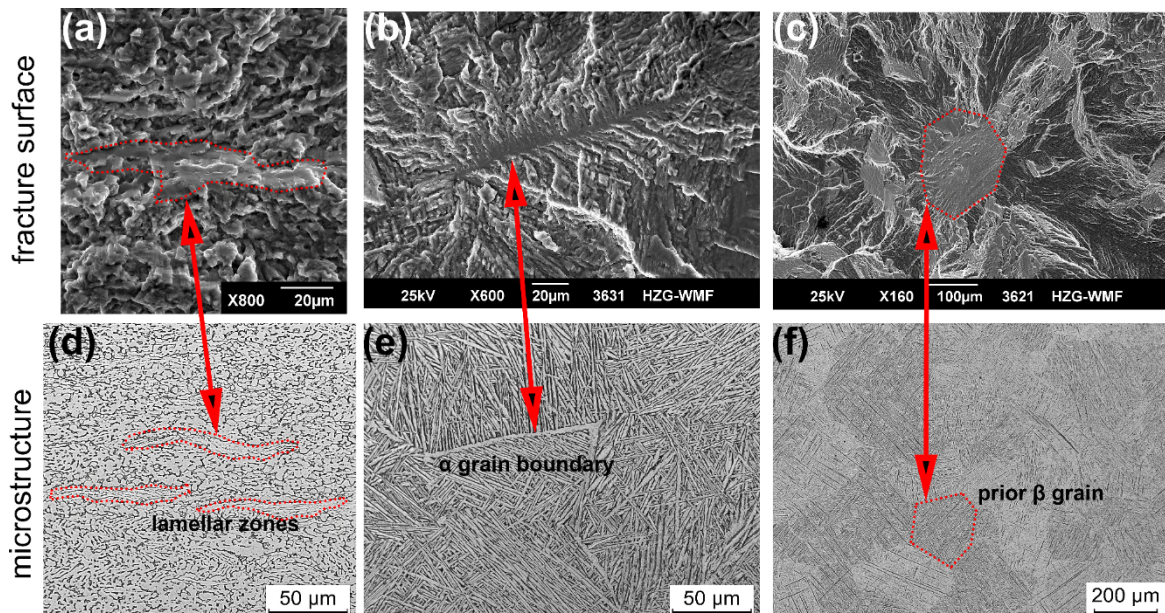


Figure 6.5. Crack initiation sites in Ti-6Al-4V with different types of microstructure: (a) crack origin in the mill-annealed microstructure ($\sigma_{max} = 800$ MPa, $N = 2.1 \cdot 10^6$ cycles); (b) crack origin in the lamellar microstructure ($\sigma_{max} = 880$ MPa, $N = 3.1 \cdot 10^6$ cycles); (c) crack origin in the martensitic microstructure ($\sigma_{max} = 1000$ MPa, $N = 4.8 \cdot 10^6$ cycles); (d) mill-annealed microstructure; (e) lamellar microstructure after WQ+RA; (f) martensitic microstructure after WQ.

Figure 6.5(b) demonstrates the internal crack origin of the coarse lamellar morphology obtained after high temperature annealing of the martensitic structure at 920°C (RA). A long and narrow cleavage perpendicular to the neighbouring platelets was found in the middle of the ODA zone. Figure 6.5(e) shows a good correspondence between the crack origin shape and the grain boundary α phase that is inevitably formed upon recrystallization annealing. Thus, similar to the globular structure discussed above, coarse grains of the α phase, squeezed between the prior β grains, are prone to cleavage during the cyclic loading. Therefore, these features should be considered with some special caution prior to heat treatment. Wherever possible, the heat treatment temperature should be minimized in order to prevent an excessive formation and growth of grain boundary α phase.

Large internal cleavage-like features were observed at the crack initiation sites for the martensitic specimens, as shown in Figure 6.5(c). These specimens exhibited the highest fatigue limit in the range of 900–950 MPa achieved in this work. The size and form of a large facet at the crack origin resembles a prior β grain shown in Figure 6.5(f). Apparently, this facet is a result of cleavage along the preferred crystal direction favourable to slip band formation. The mechanism of this type of fracture was studied by several researchers [84, 179] and is based on the inherent anisotropic nature of the hexagonal α phase, which leads to increased local internal stresses, depending on the local misorientation of neighbouring grains.

The results presented in this section indicate that internal crack initiation is a unique attribute of fatigue failure in the HCF regime for Ti-6Al-4V, in spite of its purity in terms of non-metallic inclusions. Good surface quality is a prerequisite for the crack origin shift. Cleavage of single α grains or prior β grains is typically observed at the crack initiation sites. Our findings suggest that each type of material microstructure has its own hard brittle grains that break first in a planar way either by a slip-based mechanism [180] or a cleavage-based mechanism [179]. An anisotropic nature of the α phase enhances this process due to local misorientation of neighbouring grains. Additionally, a grain size correlates fairly well with the occurrence of internal crack initiation and facet formation. The presented results further support the significance of the internal fatigue crack origin in the Ti-6Al-4V alloy. As reported by numerous researchers [86, 181], most of the fatigue life is spent on the formation of a characteristic ODA zone. Therefore, internal cracks should be taken into account in the lifetime assessment models not only for welded components, as demonstrated in the following chapter, but also for defect-free parts. Until now, all the design guidelines and standards rely only on the surface crack initiation. Introduction of the fish-eye failure modes into the design rules is essential, especially for components with a high surface quality.

6.3 Generalized scheme of the fish-eye fracture

The analysis of HCF failures of the surface-treated specimens, either laser-welded or without welding, suggests that fatigue cracks very often initiate from pores or microstructural inhomogeneities underneath the surface. The detailed fractographic analysis provides an important insight into the mechanism of internal fatigue failure. Based on these findings, a simplified concept of the fish-eye fracture can be constructed. Figure 6.6 illustrates a schematic view of the fish-eye fracture surface after internal crack nucleation in the HCF regime.

The fatigue crack originates from some type of internal defects such as welding pores or non-metallic inclusions. Additionally, microstructural features of the defect-free material leading to cleavage of hard α grains should be considered as potential crack origins. The fish-eye region is subdivided into

two regions, according to the surface roughness and its appearance: the ODA region surrounding the crack initiation site and the remaining smooth area. The fish-eye radius equals the depth of the crack origin. The shape of the fish-eye is circular, unless near-surface compressive residual stresses are present. These can be generated by the LSP treatment, as shown in Section 5.4. In case of subsurface residual stresses, the fish-eye mark exhibits an eccentric shape due to decelerated crack growth in the treated region. The ODA size is typically in the range of 150–250 μm and tends to slightly decrease with increasing stress levels. At the ODA edge, the SIF range of a fatigue crack approaches the threshold value for long cracks in a vacuum. The growth of short cracks within the ODA is characterized by an anomalous behaviour due to a reduced crack closure effect, microstructural influence, and the effect of the environment at the crack tip. In the HCF regime, in a major part of the fatigue life, the crack propagates in the ODA [86, 100].

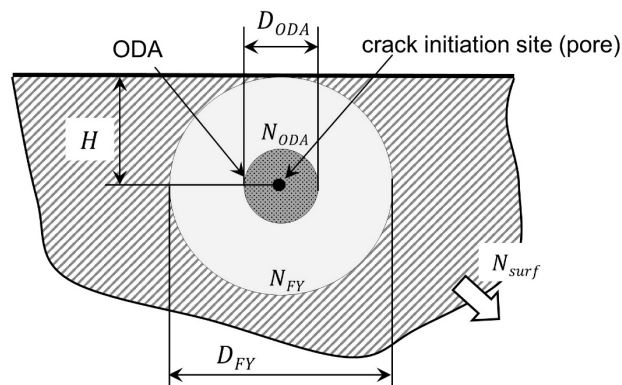


Figure 6.6. Schematic illustration of the fish-eye fracture surface caused by internal crack initiation.

Based on the given schematic view in Figure 6.6, the overall fatigue life N can be, therefore, presented as a sum of the initiation phase N_i , short crack growth within the ODA (N_{ODA}), crack propagation in the smooth area (N_{FY}) and, finally, outside of the fish-eye (N_{surf}):

$$N = N_i + N_{ODA} + N_{FY} + N_{surf}. \quad (6.2)$$

The most ambiguous part of the fatigue life is the initiation phase N_i . Under some circumstances, e.g. when sharp crack-like defects are present in a component, the initiation stage can be neglected [71, 122]. As shown in Section 6.1, the ODA stage of fatigue life N_{ODA} has a unique feature that the crack growth in this zone is characterized by the SIF range values below the conventional threshold value for long cracks. Some alternative approaches rather than conventional LEFM should be employed to describe the crack growth in this stage. The quantitative relationship between the different stages of fatigue life in Equation (6.2) is of paramount significance and will be analysed in the following chapter. The mechanism of the fish-eye formation presented above summarizes the experimental evidence obtained within this work and plays a key role in the development of a fatigue assessment model.

"All models are wrong, but some are useful"

George E.P. Box

7 Lifetime prediction

As shown in the previous chapter, internal welding-induced porosity is a crucial factor that controls the fatigue performance of machined laser-welded Ti-6Al-4V butt joints. Once a high surface quality with low roughness is ensured, fatigue cracks are disposed to emanate from underneath the surface. Therefore, it is one of the major problems for practical applications to account for interior-initiated fatigue failure. In order to achieve a sufficiently high reliability of a component with respect to cyclic loading, a quantitative characterization of the effect of internal defects on fatigue strength is required. In the following section, a developed analytical model for fatigue life assessment is presented in detail. The main purpose of this model is to predict the fatigue behaviour of welded joints in the presence of randomly distributed subsurface porosity. The model should be able to predict both the finite fatigue life for a given applied stress magnitude and the fatigue limit. The results presented in this chapter has been partially published in [182].

7.1 Model development

7.1.1 Model assumptions

Any attempt to model the HCF behaviour of a structure relies on careful consideration of the assumptions employed. In this study, based on metallographic observations and the X-ray inspection, internal pores are considered as spherical cavities. As shown in Section 5.1, inherent brittleness of the martensitic FZ leads to a high notch sensitivity of the FZ in terms of porosity influence. Stress concentration in the proximity of a pore leads to premature crack nucleation in the early stages of the fatigue life. It has been demonstrated by numerous researchers that, in the presence of sharp defects or inclusions, the crack initiation period is negligible and the crack growth covers a large portion of the entire fatigue life [96, 122, 183]. Therefore, in this study, we ignored the crack initiation time and assumed that the first crack is formed at a pore after the first loading cycle. It is important to note that ‘crack initiation’ means the development of a crack in one grain due to the accumulation of irreversible plastic deformation. This term should not be confused with the engineering crack-initiation period for a crack of detectable size (~ 1 mm), as mentioned in Section 3.2.1. In this work, the total fatigue life is approximated to be the number of cycles for a crack to grow from a pore to the critical crack size needed for unstable crack growth. Thus, the approach based on the concept of fracture mechanics that considers the gradual degradation of the load-bearing capacity due to continuous crack growth is used for fatigue life evaluation.

Multiple crack initiation and interaction between neighbouring cracks were not considered; only one pore with a diameter d at a known distance from the surface h is considered as a crack-initiating defect. In other words, only one single dominating crack is considered at a time. The rationale behind this assumption is based on the fractographic observations of specimens tested in the region of high cycles close to the fatigue limit. In this regime, the fracture surface always exhibits only one dominant crack growing from a pore to the final failure. Even if the crack front encounters other pores, the

crack coalescence does not have any significant effect on further propagation. This situation is demonstrated in Figure 5.2, where two crack nucleation sites are visible. Nevertheless, multiple crack initiation did not affect the lifetime because the crack coalescence occurred in the final stages of fatigue life. This is not the case for low-cycle fatigue (LCF) regions ($N < 10^4$ cycles), where several crack nucleation sites and crack interaction are typically observed. Hence, special attention should be paid to the interpretation of the modelling results in the LCF region because the model can give over-conservative estimates. In this regard, Madia et al. recently reported a modelling procedure accounting for multiple fatigue crack propagation in weldments operating in the LCF regime [184].

Pore position (depth) and diameter h and d , as input data, were taken from the X-ray analysis. First, average values determined in Section 4.9 were used for the development and validation of a deterministic assessment model. Then, pore position and size were considered as random variables and a probabilistic approach was used for their incorporation into the model. Owing to internal crack nucleation, surface conditions and roughness do not play any significant role and are not considered as an influential factor for internal crack growth. A schematic drawing of the simplified model is shown in Figure 7.1.

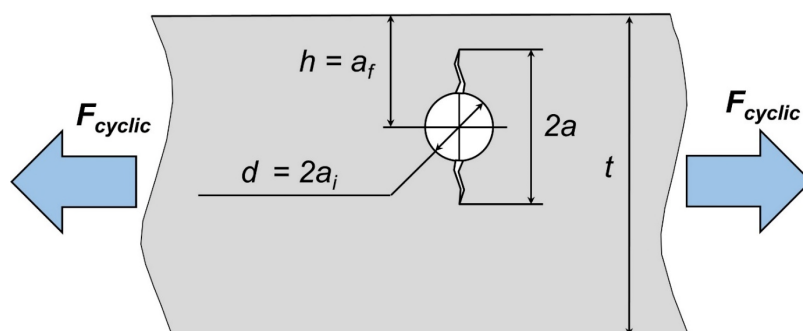


Figure 7.1. Schematic 2D-representation of a fatigue crack initiated from an internal pore.

It is important to note that a pore is considered as a three-dimensional defect with a stress concentration factor of 2.1, as calculated previously in Section 5.1. In case of two-dimensional open holes, the stress distribution around a notch root is different and is characterized by an elastic stress concentration factor of 3.0 [165]. Fatigue crack growth was also modelled considering the three-dimensional local constraint at the crack tip. For this purpose, the SIF range was calculated, based on the formula for internal penny-shaped cracks given by Equation (6.1). Since the pore depth is, normally, larger by an order of magnitude than the pore diameter, the influence of a free surface on the stress state at the crack tip was ignored. This assumption is not valid for pores very close to the surface; however, as demonstrated by fractographic observations, the percentage of these failures is relatively low.

7.1.2 Modified fracture-mechanics framework

Owing to internal crack initiation and subsequent crack growth in vacuum, the numerical procedures used in the common practise for surface cracks have been adopted with modification in the present study. Any fracture-mechanics-based analysis requires an initial crack, which grows under cyclic loading up to a critical size. In the present study, an initial crack size a_i is assumed to be equal to the average pore radius found by the X-ray inspection, namely $32 \mu\text{m}$. Hence, the resulting S-N curve represents the mean life of a specimen (see Figure 3.9). Fatigue scatter will be introduced further in

Section 7.2.1. After the crack initiation at a spherical cavity, the internal crack propagates within the specimen in a vacuum environment. At this stage, the crack forms a fish-eye mark comprising the ODA zone and the smooth area. When the crack reaches the surface, it transforms into a surface crack and propagates in the atmosphere much faster compared to internal cracks. Unstable crack growth and the final failure occurs if the remaining cross section can no longer carry the maximum load of the loading cycle. Considering the typical depth of the crack nucleation site, we can conclude that internal cracks are no more than 500–700 μm long.

It is well known that the size of the notch strongly affects the approach applicable to the fatigue life assessment [176]. If the size of a crack is comparable to the average grain size or any characteristic microstructural dimension, its behaviour is strongly affected by these micro-obstacles. In this case, the crack propagation cannot be considered in the light of continuum fracture mechanics, and the local micro-mechanical damage models should be developed. Fracture surface observations revealed that crack nucleation usually occurs at either relatively large pores or clusters of very small pores. A typical size of the crack origin site varied in the range of 50–100 μm . Since these values are almost two orders of magnitude larger than the average thickness of the martensitic plate in the FZ (around $0.7 \pm 0.3 \mu\text{m}$), the behaviour of such cracks can be described, in principle, by a continuum fracture mechanics framework, but with special attention paid to the crack driving force parameter.

A general scheme of the fracture-mechanics approach is illustrated in Figure 7.2. A quantitative analysis is based on the constitutive relationship between the fatigue crack growth rate da/dN and some function of the applied stress intensity factor range ΔK . This function can be regarded as a crack driving force because it determines the crack propagation behaviour. Long crack propagation rate can be described accurately by the Paris law [127], where only two material constants are required, to be deduced by fitting to experimental data. Several generalizations of the Paris' law are available in the literature [185, 186]. Most of them are derived to take into account the R -ratio, smooth transition at the near threshold condition, and fracture toughness. The fatigue crack growth equation selected in this work, as originally proposed by Forman and Mettu [187] and subsequently used in the NASGRO software [188], is as follows:

$$\frac{da}{dN} = C(U \cdot \Delta K)^n \left(1 - \frac{\Delta K_{th}}{\Delta K}\right)^p, \quad (7.1)$$

where C , n , and p are material constants that depend on the environment and the applied conditions, U is the crack-closure ratio, and ΔK_{th} is the threshold stress intensity factor range. C and n parameters control the position and slope of the FCP curve in the Paris regime (Figure 3.7(b)). Parameter p determines the curvature in the near-threshold region. It should be noted that, in its original form, Equation (7.1) has a part containing the fracture toughness of the material. In this work, the part accounting for unstable crack growth is not relevant and has been neglected. For the specimen geometry investigated in the present study, this assumption does not result in a significant error in the HCF regime. However, this factor should be accounted for in the LCF region.

The number of cycles needed for growth of a crack from the initial crack length a_i to the final crack length a_f is then calculated by integrating the two sides of Equation (7.1) for a given stress level. The SIF range for internal circular crack is determined by Equation (6.1) using the current crack length. Owing to the power law in this equation, the estimated fatigue life is not strongly dependent on the final crack length, whereas it is quite sensitive to the initial crack size. It implies that the pore size and the ODA zone dimensions have a big impact on the modelling results.

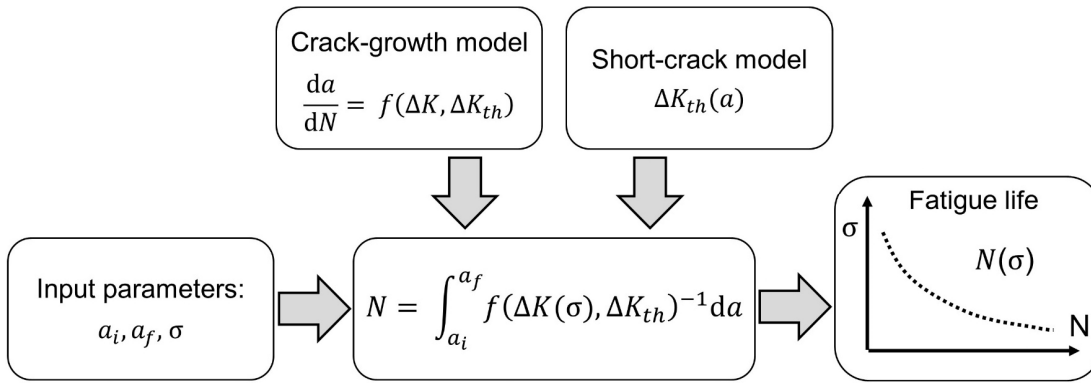


Figure 7.2. Fracture mechanics approach for fatigue analysis.

The long crack closure ratio U is defined as the ratio of effective SIF range ΔK_{eff} to applied SIF range ΔK . It was obtained according to the crack opening stress equation developed by Newman [189] based on the results of the modified strip yield model [190]:

$$U = \frac{\Delta K_{eff}}{\Delta K} = \frac{1-f}{1-R}, \quad (7.2)$$

with f being the crack closure function. For calculating the f function, plane strain conditions for internal crack growth are assumed. Newman reported the detailed procedure for the f function determination using the constraint factor and the stress ratio [189]. For $R = 0.1$, the crack closure ratio obtained by the described procedure was in the range of 0.80 – 0.85, depending on the applied stress.

Once the crack reaches the specimen surface, it transforms into a surface crack and propagates much faster compared to the internal growth stage. The primary reasons for this phenomenon are environmental effect and the sudden rise of stress intensity at the crack tip. The SIF range for surface semi-elliptical crack can be approximately estimated using the Murakami approach [68] or taken from the compendium on linear SIF solutions [126]. The surface crack part of the fatigue life can be easily calculated using the experimentally determined FCP properties of martensitic Ti-6Al-4V shown in Figure 4.16(a). The estimations showed that the number of cycles spent for surface crack propagation was negligible compared to the total number of cycles. Typically, specimen with a surface crack endures less than 10^3 cycles before failure. These estimations were additionally supported by the observations of the specimen surface during fatigue tests using OM. After the crack becomes visible in OM, the specimen endures normally less than five seconds of cyclic loading at a frequency of 80 Hz. According to these findings, the total lifetime N in the HCF regime was approximated as the number of cycles for internal crack growth, i.e. the final crack length was equal to the pore depth under the surface $a_f = h$. The aforementioned assumption is valid only in the HCF regime and in case of a thin-walled component. Otherwise, the surface crack period can be comparable to the entire fatigue life and should be accounted for.

Fundamental material properties represented by the parameters C, n, p in Equation (7.1) play a crucial role in the model development. As a first approximation, the experimentally determined FCP curve of the martensitic Ti-6Al-4V microstructure shown in Figure 4.16(a) was fitted by Equation (7.1). To reduce the number of fitting variables by the least squares, the slope parameter n was kept the same as in the Paris region ($n = 3.15$). The corresponding material parameters after fitting the experimental data to the NASGRO equation are as follows: $C = 2.74 \cdot 10^{-11}$ m/cycle, $n = 3.15$, $p = 0.11$. The

experimental data and the fitted lines corresponding to Paris equation and NASGRO equation are presented in Figure 7.3(a). As the next step, the S-N curve of the weld was predicted as a number of cycles for a crack to reach the specimen surface. However, tremendous discrepancy was found between the predicted fatigue properties and the experimental results, as shown in Figure 7.3(b). In the HCF region, the resulting fatigue life after the integration of Equation (7.1) was underestimated by about two orders of magnitude. Based on these findings, it was concluded that internal cracks in the FZ of the laser-welded joint grow with considerably slower rates than expressed by Figure 7.3(a). The most plausible reason for this effect is the influence of a crack tip environment, i.e. the absence of atmospheric gases at the crack tip of the internal crack. Although some portion of the shielding gas (argon) could be entrapped in a pore, a vacuum-like environment apparently has a strong retarding effect on the FCP rate. The effect of the environment should be carefully considered to ensure adequate fatigue life predictions in case of internal crack initiation.

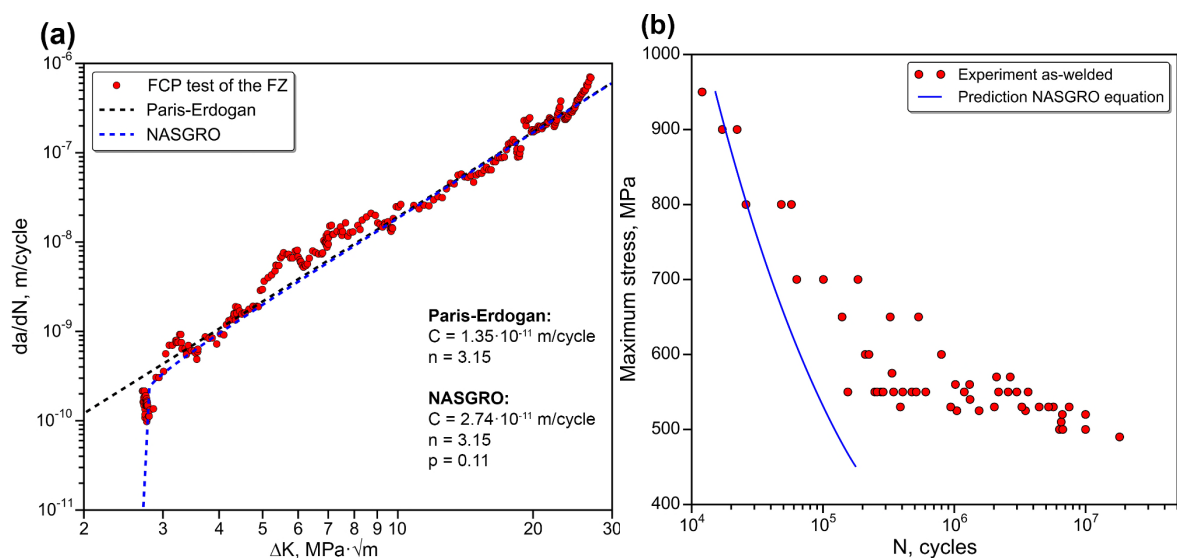


Figure 7.3. (a) Fitting of the experimental data to the Paris and NASGRO equations; (b) prediction of the S-N curve using the experimentally found material parameters C , n , p .

The effect of vacuum on the crack growth in the Ti-6Al-4V alloy has been studied by several researchers [191, 192, 193, 194]. It is generally accepted that the decrease in surface energy owing to oxides and adsorbates is the primary reason for a faster growth of cracks in the air than in a vacuum [193, 194]. Surface energy in a vacuum is higher than that in air and the plastic deformation at a crack tip occurs much more easily. The enhanced plasticity causes a blunting of the crack tip and, as a result, severe crack closure. In addition, high reversibility of slip in vacuum enhances the plasticity effects and increases the material resistance against the crack growth [194]. The latter was indirectly confirmed in this study by the absence of a striations pattern in the smooth area of the fish-eye. It has to be mentioned that the vacuum level was found to have a strong impact on the crack growth [81]. It was observed that the threshold SIF range in a vacuum is significantly higher than that found in the atmosphere. The values of ΔK_{th} at 10^{-10} m/cycle in the literature vary in the range of 6–8 MPa·√m [191, 193, 195], which is more than by a factor of two higher compared to the value found experimentally for the FZ in the present study (see Figure 7.3(a)).

Several problems are associated with the incorporation of the environmental effect into the fracture mechanics model. First, internal cracks in the laser-welded Ti-6Al-4V butt joints propagate at stress intensities that are much lower than the typical threshold magnitudes of Ti-6Al-4V alloy in a vacuum.

This is illustrated in Figure 6.2(b), where the SIF range at the pore just after the crack initiation and in the major part of the ODA is in the range of 3–5 MPa·√m. In contrast, based on the published data, thresholds for long cracks in vacuum are at least 6.0 MPa·√m [192, 193]. These high threshold values are in contradiction with our results of fatigue testing. The specimen fracture clearly demonstrates that, in spite of very low SIF values in the ODA zone, internal cracks are able to grow even at stress intensities below ΔK_{th} . This effect can be explained by the propagation of the so-called short cracks. The concept was briefly introduced in Section 3.2.3 (Methodology). Many researchers have shown that short fatigue cracks propagate faster than long cracks at the same applied SIF range; moreover, they can grow at stress intensities lower than the fatigue threshold [124, 176]. It implies that the short crack behaviour should be considered in the assessment model.

The second problem stems from the environmental effect and is related to the FCP resistance of the FZ in a vacuum. Unfortunately, the data obtained by the FCP testing of the FZ cannot be used as input data because they do not represent the crack growth behaviour of internal cracks. Moreover, since the vacuum level, which has a strong impact on the FCP behaviour, is unknown, it is very difficult to simulate the internal crack growth by conventional FCP testing techniques. Some alternative approaches should be elaborated to find the FCP properties of internal fatigue cracks. In the following two sections, the developed modifications of the model aiming to overcome these two problems are presented in detail.

7.1.3 Short cracks model

As stated in Section 3.2.3, short cracks can be categorized into microstructurally, mechanically, physically, and chemically short cracks, depending on the dominant mechanism leading to their faster growth [124]. In the light of the aforementioned assumptions, the approach used in the present work focuses on the model of physically short cracks that are significantly larger than an effective microstructural dimension, but their growth rate is still higher due to reduced crack closure effect. The basic idea behind this approach is that the crack closure phenomenon shows a transient behaviour and gradually builds up. The crack growth threshold reflects this tendency and increases with the growing crack length until it reaches a constant value for long cracks $\Delta K_{th,LC}$ [71]. The evolution of crack closure as a function of crack length is reflected in the reduced threshold values for short cracks, and is usually expressed by the cyclic R-curve, schematically shown in Figure 7.4.

Generally, the overall threshold $\Delta K_{th}(a)$ can be subdivided into an intrinsic part $\Delta K_{th,eff}$ which is material-specific and a crack-length-dependent extrinsic part $\Delta K_{th,op}$ reflecting the gradual build-up of crack closure:

$$\Delta K_{th}(a) = \Delta K_{th,eff} + \Delta K_{th,op}(a). \quad (7.3)$$

If the cyclic R-curve is known, the short-crack effect can be considered in the crack growth model by introducing the relationship $\Delta K_{th}(a)$ in Equation (7.1). In this case, the FCP rate of a short crack depends on the position of the applied SIF range curve $\Delta K_{ap}(\sigma)$ relative to the cyclic R-curve (see Figure 7.4). If the cyclic R-curve is lower than the applied external stress intensity, the crack is growing with acceleration. If the applied load is sufficiently low, the curve of the applied SIF range is tangential to the cyclic R-curve, and the crack can become arrested owing to the build-up of crack closure at the crack tip. This condition corresponds to the fatigue limit and implies the existence of the so-called non-propagating cracks even in the intact specimens after testing up to 10^7 cycles.

Numerous researchers observed the existence of these cracks in the case of steels [68, 135]. In the present work, arrested cracks at the fatigue limit of stress have been found by metallographic inspection of the specimens that endured 10^7 load cycles, and one of these cracks is presented in Figure 7.4(b). The existence of these cracks in machined laser-welded titanium butt joints can be regarded as an additional evidence of the short-crack effect. There are two experimental procedures for determining the cyclic R-curve [132, 135], but the characteristics of experimental facilities used in this work were not sufficient for the detection and precise measurements of the short crack length. Therefore, further analysis and modelling are based on the simplified construction of the cyclic R-curve.

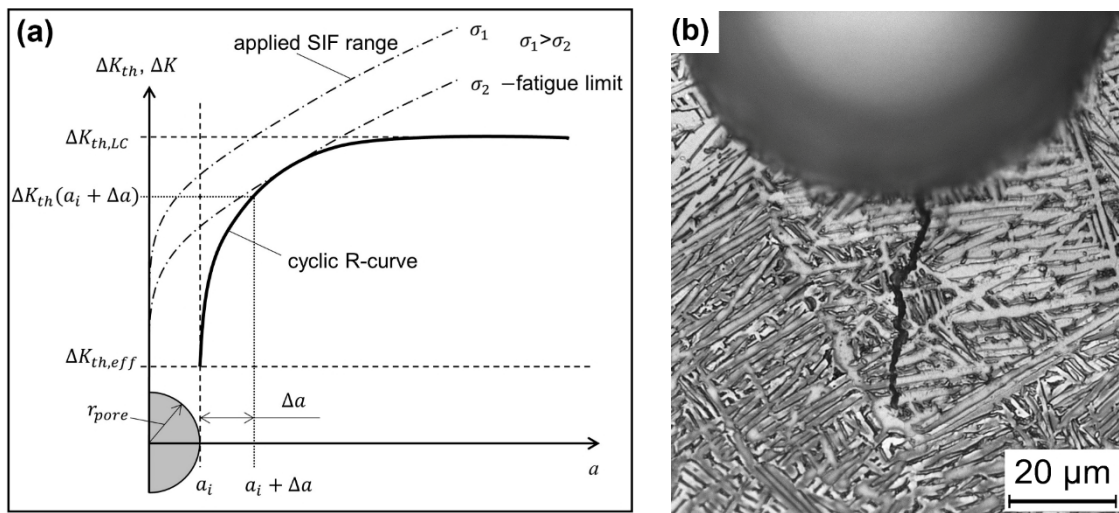


Figure 7.4. (a) Schematic view of the cyclic R-curve approach. (b) Arrested crack nucleated at a pore in the weld FZ of Ti-6Al-4V tested at the fatigue limit ($\sigma_{max} = 550$ MPa, $N = 10^7$ cycles).

Zerbst and Madia proposed a method for a simple estimation of the cyclic R-curve, based on a modified El Haddad description of the Kitagawa-Takahashi diagram [135]. In their approach, the cyclic R-curve is approximated by the following equation:

$$\Delta K_{th}(\Delta a) = \Delta K_{th,LC} \sqrt{\frac{\Delta a + a^*}{\Delta a + a^* + a_0}}, \quad (7.4)$$

where $\Delta a = a - a_i$ is a crack extension, a_0 is the El Haddad fit parameter, and the additional parameter a^* has to be determined from the condition $\Delta K_{th}(0) = \Delta K_{th,eff}$. Thus, a short crack threshold is assumed to be approximated by the square root function shifted by the fit parameter a^* . A major drawback of this method is that the material properties affecting the slope of the cyclic R-curve are not accounted for. As a first approximation, it provides a conservative estimate based on the data that can be easily determined using conventional macro-specimens. However, this method requires a calculation of the El Haddad parameter a_0 [133]:

$$a_0 = \frac{1}{\pi} \left(\frac{\Delta K_{th,LC}}{Y \cdot \Delta \sigma_e} \right)^2, \quad (7.5)$$

where Y is a boundary correction function and $\Delta \sigma_e$ is the unnotched fatigue limit. The dependence of a_0 parameter on both Y and fatigue limit of the material makes it geometrically and environmentally

dependent. Hence, for reasonable estimations, representative conditions at the crack tip for internal cracks should be accounted for. Without any experimental data on $\Delta\sigma_e$ in vacuum, this method cannot be used for internal cracks growing in a vacuum-like environment. Note that, in its original form, it was used only for surface cracks.

An alternative simplified method is proposed, which does not require the El Haddad parameter for construction of the cyclic R-curve. The cyclic R-curve is approximated by the following extended El Haddad's equation:

$$\Delta K_{th}(\Delta a) = \Delta K_{th,LC} \sqrt{\frac{\Delta a + a_1}{\Delta a + a_2}}, \quad (7.6)$$

where a_1 and a_2 are fit parameters. The fit parameters have to be chosen such that two conditions are fulfilled. First, the short crack threshold $\Delta K_{th}(\Delta a)$ should approach the intrinsic value $\Delta K_{th,eff}$ with the decreasing crack length $\Delta a \rightarrow 0$. From this condition, which is analogous to that introduced by Zerbst and Madia, the position of the cyclic R-curve on the Δa -axis is determined. Second, the cyclic R-curve should be tangential to the applied SIF range curve when the stress is equal to the notched fatigue limit. In case of weldments, it corresponds to the fatigue limit of machined joints containing cracks. Upon the fulfilment of this condition, the shape of the cyclic R-curve is deduced. The rationale behind the latter condition is that we consider the pores as crack-like defects and the fatigue limit corresponds to the arrest of these cracks emanating from the pores. The arrested crack in the run-out specimen shown in Figure 7.4(b) supports this interpretation of the fatigue limit for martensitic Ti-6Al-4V. Note that the two parameters a_1 and a_2 , responsible for the slope and position of the curve fitted by the described procedure, are independent of each other.

Thus, three experimentally determined parameters for the construction of the simplified cyclic R-curve are needed, namely intrinsic threshold $\Delta K_{th,eff}$ in vacuum, long crack threshold $\Delta K_{th,LC}$ in vacuum, and the notched fatigue limit $\Delta\sigma_e$ in the presence of pores. By this methodology, there is no need to determine the unnotched fatigue limit in a vacuum, something that is not feasible within this work. Assuming that the intrinsic part $\Delta K_{th,eff}$ is a material property and is not dependent on the crack length, it can be derived as the long-crack threshold obtained at a high R -ratio ($R > 0.7$), where no crack closure is expected [135]. From the literature review, this parameter is microstructure- and environmentally insensitive; for Ti-6Al-4V, it is approximately $1.5\text{--}2.0 \text{ MPa}\cdot\sqrt{\text{m}}$ [196]. The long crack threshold $\Delta K_{th,LC}$ for the stress ratio of $R = 0.1$ in a vacuum is taken as the lowest value found in the literature: $\Delta K_{th,LC} = 6.0 \text{ MPa}\cdot\sqrt{\text{m}}$ [191]. The derived by the described methodology values of a_1 and a_2 fit parameters are $5.3 \text{ }\mu\text{m}$ and $52.8 \text{ }\mu\text{m}$, respectively.

Besides the lower threshold values, the short cracks do not have a fully developed crack closure effect. In order to account for faster growth of short cracks, the evolution of crack closure during the crack propagation should be taken into account. Therefore, it is assumed that the development of a crack closure effect is mirrored by the gradual growth of the short-crack fatigue threshold. The increased crack closure ratio $U_{SC}(a)$ for physically short cracks is then calculated as to the ratio of fatigue thresholds [147]:

$$\frac{U_{SC}(a) - 1}{U_{LC} - 1} = \frac{\Delta K_{th}(a) - \Delta K_{th,eff}}{\Delta K_{th,LC} - \Delta K_{th,eff}}. \quad (7.7)$$

Finally, the dependence of crack-closure ratio on the crack length $U_{SC}(a)$ and that of the threshold $\Delta K_{th}(\Delta a)$ are incorporated into Equation (7.1). The integration of the modified NASGRO equation enables to account for anomalous short crack growth due to reduced threshold and crack closure effects. Based on this simplified phenomenological approach for considering short cracks, only three experimentally determined parameters define the cyclic R-curve. The fatigue limit in the presence of pores, being one of them, was determined considering a big scatter of fatigue life. Note, that only one experimental value $\Delta\sigma_e$ is required for this purpose. In this context, the shape of the entire S-N curve is not relevant for the short crack model.

7.1.4 FCP properties derived from the S-N data

To date, no clear mechanism of internal crack growth in any material have been fully elucidated. One of the underlying reasons for this is the extreme complexity of experiments for measurement of internal crack growth rates. On the other hand, the experimentally determined FCP rates of internal cracks are critical for developing any predictive model. There are some published data on the FCP rates for Ti-6Al-4V in a vacuum [81, 192, 195]. However, since the microstructure has a big impact on the FCP rates of the Ti-6Al-4V alloy, it is not appropriate to take the experimental data from the literature, as these data are typically provided for equiaxed or lamellar microstructures. Another factor to consider is the vacuum level, which is unknown for internal crack growth. Hence, it is not completely clear if the data measured in the ultra-high vacuum are applicable to the current model of internal fatigue cracks. Apparently, the pores are filled with some portion of the shielding gas that determines the crack tip atmosphere. All these aspects make the experimental determination of the crack growth rates in the representative conditions of internal cracks unrealistic.

In the present study, the FCP properties of small fatigue cracks have been derived from the experimental S-N data in the HCF regime. A similar approach was used by Tanaka et al. for an indirect estimation of the FCP curves of internal cracks growing from inclusions in a bearing steel [101]. This approach is based on the assumption that the crack propagation law is expressed by Equation (7.1). Yoshinaka et al. reported that the retardation effect of a vacuum environment on the FCP rates is most pronounced for short cracks and is negligible in the Paris region ($\Delta K > 20 \text{ MPa}\cdot\sqrt{\text{m}}$) [194]. Therefore, we assume that the material constants C and n in a vacuum are equal to those determined in the atmosphere, namely $C = 2.74 \cdot 10^{-11} \text{ m/cycle}$, $n = 3.15$. By using the least-square technique, the parameter p is then determined to minimize the difference between the calculated and experimental S-N data in the HCF regime, as shown in Figure 7.5(a). The value of p obtained by this procedure was found to be 1.65. Note that the resulting value of p depends primarily on the shape and slope of the S-N curve, whereas the fitting of a_1 and a_2 parameters was done exclusively on the basis of the fatigue limit $\Delta\sigma_e$. Hence, the three model fitting parameters a_1 , a_2 and p are independent and do not affect each other. It should be noted that experimental S-N data only in the range of 500–700 MPa were considered, i.e. the LCF region was not included.

Figure 7.5(b) shows the effective FCP curve of internal cracks growing in a vacuum-like environment calculated by the described methodology. As expected, the internal cracks propagate at a rate that is several orders of magnitude slower than that of surface cracks under normal conditions. For reference, the FCP data for long cracks growing in a vacuum environment reported by Oguma [81] are shown in Figure 7.5(b). The curve obtained for interior-initiated cracks in the present study is relatively close to the published experimental data, though slightly higher. Apparently, one of the main reasons for this difference is another type of microstructure studied by Oguma [81]. In addition, the developed

procedure allows estimating the growth rates of short cracks with not fully developed crack closure effect. The behaviour of internal short cracks is shown in Figure 7.5(b) by dashed lines for four applied stress levels. Short cracks in vacuum grow considerably faster than long cracks in the same environment but are still much slower than long cracks in the atmosphere. The effective FCP curve of internal short cracks is an essential result of the model validation. Using these data, the growth of internal cracks can be predicted in a component with a given stress distribution and defect population. Thus, a simplified construction of the cyclic R-curve under reasonable assumptions provides the necessary crack growth characteristics without complex and time-consuming experiments on FCP testing of short cracks.

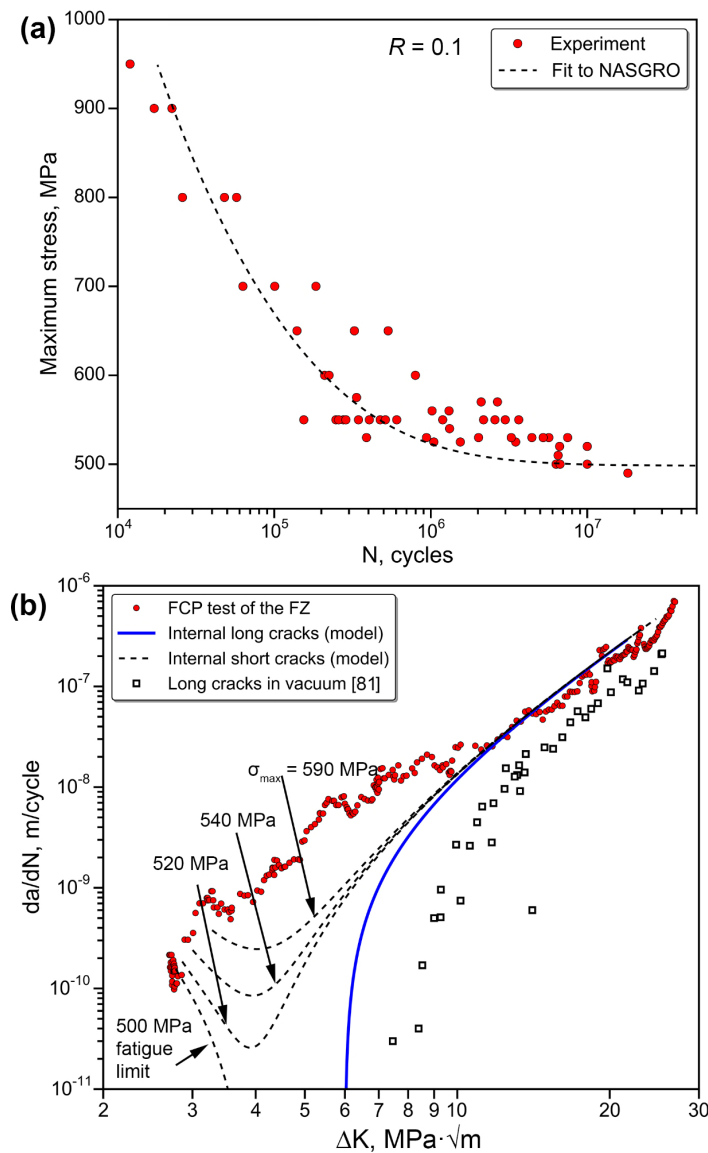


Figure 7.5. Validation of the fatigue-life assessment model: (a) fitting of the experimental S-N curve to the NASGRO equation; (b) resulting effective FCP curve for internal cracks in comparison to experimentally determined FCP curve of long cracks in vacuum [81].

The effective FCP curve found by the methodology described above represents the relationship between the crack growth rate da/dN and the applied stress for internal cracks, i.e. the dependence $da/dN=f(\Delta K, \Delta K_{th})$. If determined experimentally, this relationship is a material property. The

curve derived in this work is however an estimation of the $da/dN=f(\Delta K, \Delta K_{th})$ dependence for short cracks. The position and shape of the calculated curve depend on the model assumptions. In order to apply this FCP curve to other prediction models, one should use similar approaches based on the NASGRO equation (Equation (7.1)) and the cyclic R-curve (Equation (7.6)) for adequate results.

7.2 Application of the model

The fit parameters of the fatigue crack growth law found in the previous section enable the use of the developed model to predict the fatigue behaviour of a component with a subsurface pore of a given diameter at a given distance from the surface. The presented deterministic framework for fatigue assessment is based on the assumption that there is only one dominant crack in a component. In reality, as a result of casting, welding, or any type of processing, a population of defects is always present in a structure. This significantly complicates the application of the model to prediction because the input parameters, e.g. the initial crack length, become random variables. To account for a known population of defects under the surface, the probabilistic part of the model, dealing with uncertainties of the input parameters, should be developed. In this regard, one of the major challenges is the criterion to account for which pore from a population is the critical one that is likely to initiate a dominant crack. In the following section, the fatigue scatter of the laser-welded Ti-6Al-4V machined butt joints is predicted on the basis of measurements of porosity distribution. These results are further used to predict the shift between the two pore size distributions obtained by an X-ray inspection and fractographic measurements, as presented in Section 6.1.

7.2.1 Prediction of fatigue scatter

Scatter is an inherent characteristic of any fatigue damage process. The fatigue life of similar specimens under the same fatigue load can vary significantly, as shown in Figure 7.5(a). A lifetime prediction model should adequately address this issue and deal with the statistical aspects of the fatigue phenomenon. For this purpose, various sources for scatter in fatigue should be recognized, the most influential of which should be distinguished and incorporated into the model.

In order to assess the effect of porosity population on the fatigue life scatter of the machined joints quantitatively, the following assumptions are made. As mentioned in Section 7.1.2, an initial crack size has a strong influence on the results of integration. Therefore, the large scatter range of fatigue life reflects a big variance in the pore size. In the present study, both the diameter and position of a pore are assumed to be the most influential factors affecting the fatigue life; the fatigue scatter band was found to be correlated with the distribution of the pore size and location. Other potential sources for fatigue scatter, e.g. uncertainties in material properties, residual stresses etc., have not been considered in the present model. Note that in contrast to the standard procedure for evaluation of steel cleanliness [68], the current model accounts not only for a pore size but also for a pore position.

Within a probabilistic framework for fatigue assessment, fatigue life N for a given stress level is considered as a random variable and is characterized by its PD-function $p_N(N)$ and distribution function (or CD-function) $P_N(N)$. The resulting fatigue life is controlled by variations of two stochastic input parameters – the diameter D and the position of the initial defect H – which are equal to double the initial crack size $2a_i$ and the final crack size a_f , respectively. In order to build a probabilistic model, we need to define the probability distribution functions of the random input parameters. These distributions were measured by the X-ray analysis and then fitted by the lognormal

distribution functions, as shown in Figure 4.18. Let (D, H) be a two-dimensional random variable with its own joint distribution function $p_{D,H}(d, h)$ showing the probability of finding a pore with a known diameter d at a distance h from the surface. More details about dealing with bi-variate random variables can be found in Section 3.3.3. Assuming that random variables D and H are independent, the joint PD-function equals

$$p_{D,H}(d, h) = p_D(d) \cdot p_H(h), \quad (7.8)$$

where $p_D(d)$ and $p_H(h)$ are marginal PD-functions of the pore diameter and pore position respectively. Figure 7.6(a) shows a contour plot of the joint PD-function constructed in this manner. According to the X-ray analysis, the graph demonstrates that majority of the pores have a diameter of 50–60 μm and a depth of 400–500 μm . It is important to note that Figure 7.6(a) is just a more suitable form of the experimental data representation and acts as input data for further probabilistic analysis.

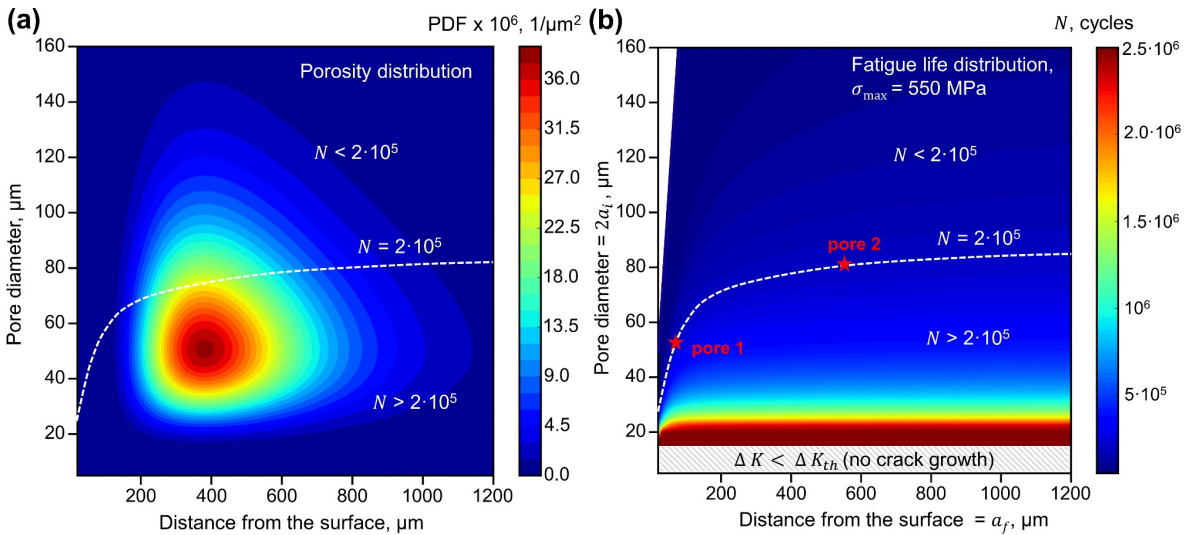


Figure 7.6. Probabilistic framework for fatigue-life assessment: (a) joint (D, H) probability density function of the pore distribution; (b) fatigue life as a function of a pore diameter and position ($\sigma_{max} = 550$ MPa).

Applying the described in Section 7.1 deterministic fatigue life prediction model for each point (d, h) in Figure 7.6(a), the distribution of fatigue life $N(d, h)$ can be obtained. The resulting contour plot for one stress level $\sigma_{max} = 550$ MPa in the HCF regime is shown in Figure 7.6(b). The plot illustrates the fatigue life as a function of two variables – pore diameter and pore depth. Note that the two plots shown in Figure 7.6(a) and (b) have the same axes and ranges, i.e. they could be combined in one plot. The colour in the left plot shows the probability of finding a given pore in a given position, whereas the colour in the right plot is proportional to the corresponding fatigue life of this pore. One specific value of fatigue life $N = 2 \cdot 10^5$ cycles is shown in Figure 7.6(b) by a corresponding contour line. All the pores identified by a contour line lead to equal fatigue life.

Some further comments should be made on the shape of the contour lines representing the lines of constant fatigue life in Figure 7.6(b). In the region of deep pores ($h > 400$ μm), the lines are almost constant, meaning that fatigue life is not affected by the pore position. This is a consequence of the power law in the crack growth model. In this case, a major part of the total fatigue life, the crack propagates within the ODA zone, which has a typical radius of around 150–200 μm . Therefore, a pore depth that is much larger than the ODA radius does not affect the fatigue life significantly. When

the crack initiation site is deeper, the number of cycles spent for the propagation of the long crack outside the ODA is negligibly small compared to the short crack period. In contrast, the in-depth position affects the total fatigue life for the pores that are located in the subsurface layer of about 200 μm . In this region, the total fatigue life decreases with decreasing distance from the surface. In order to have the same fatigue life for a pore closer to the surface, it must be smaller than that located in the interior of the specimen. For example, the same fatigue life of $2 \cdot 10^5$ cycles will be caused by a pore with a diameter of 78 μm at a distance of 600 μm from the surface (pore 2) and by a pore of 55 μm at 100 μm underneath the surface (pore 1), as shown in Figure 7.6(b).

The obtained distribution $N(d, h)$ enables to develop a criterion for identifying a life-controlling pore in a structure, i.e. a pore that initiates a dominant crack. Indeed, since we assume that the crack initiation period is negligibly short, all the pores from a given population will nucleate cracks in the early stages of fatigue life. Under this assumption, without considering the possibility of crack coalescence, a dominant crack that leads to fracture will be the crack with the shortest life. Additional evidence supporting the adequacy of this criterion can be found in the fractographic observations. As shown in Figure 5.2, if the dominant crack occasionally passes some other pores, we always observe that these pores also initiate cracks, but the growth of these cracks is slower and less detrimental than that of the dominant crack. Thus, in order to find the worst pore from a given population, all the pores should be shown as points (d_i, h_i) in Figure 7.6(b). Then, a critical pore is determined as a pore located beyond the contour line with the shortest fatigue life. Note that according to conventional standard procedures to assess a population of internal defects, the largest defect is regarded as a critical one, regardless of its depth. In this case, contour lines in Figure 7.6(b) would be straight and parallel to the horizontal axis. In this work, accounting also for the pore depth leads to a different curves shape with a gradual decrease near the surface, as shown for the contour line of $2 \cdot 10^5$ cycles in Figure 7.6(b).

It is important to emphasize that the criterion of a critical pore in the described modelling strategy is not based solely on the pore diameter. It is a trade-off between the pore size and its position, which determines the most detrimental defect in a component. Moreover, this trade-off depends on the FCP properties of the material. In other words, the largest pore in a component is not always the most detrimental one. This conclusion, which might be contradictory to existing quality standards of welded structures, has been facilitated by the fractographic observations in the present study. Very often, the largest pore in the specimen does not initiate the dominant crack because it is relatively deep under the surface. Similar findings have been reported for additively manufactured Ti-6Al-4V components produced by electron beam melting [197].

Finally, the distribution function of the fatigue life for a given stress level can be determined by combining the modelling results in Figure 7.6(b) and experimental data on the porosity distribution in Figure 7.6(a). Let us consider the fatigue life of $N = 2 \cdot 10^5$ cycles expressed by the dashed lines in Figure 7.6(a, b). The probability of reaching the given lifetime is equal to the probability that all the pores in a component have fatigue lives longer than $2 \cdot 10^5$ cycles. The pores meeting this requirement are located under the line of $N = 2 \cdot 10^5$, as shown in Figure 7.6(a). Consequently, the desired probability to have a fatigue life of at least $2 \cdot 10^5$ cycles can be calculated by integrating the joint PD-function of the pore distribution in the region under the contour line for a selected fatigue life $N = 2 \cdot 10^5$. The fatigue life distribution function for a given stress magnitude is obtained by applying the aforementioned strategy to different N levels.

The results are shown in Figure 7.7 for two typical stress levels in the HCF region: 550 MPa and 525 MPa. For the model validation, 15 fatigue specimens have been tested at each stress level. The empirical estimate for the distribution function was determined by Equation (3.12) according to the Bernard's median rank formula [138]. The procedure for constructing the empirical distribution function is given in Section 3.3.2. Note that the fatigue scatter range is larger for lower stress magnitude of 525 MPa, which is consistent with the general scatter characteristics of the fatigue failure phenomenon, given in Section 2.3.1.

Owing to the curvature of the contour line, the two-dimensional integral is taken over the irregular shape under the curve in Figure 7.6(a). Therefore, the resulting lifetime distribution function shown in Figure 7.7 slightly differs from the log-normal distribution function that describes the porosity size and depth. If only the size of the pore would have been accounted for, the resulting lifetime distribution would repeat the pore size distribution and could be determined by scaling the initial distribution of the pore size.

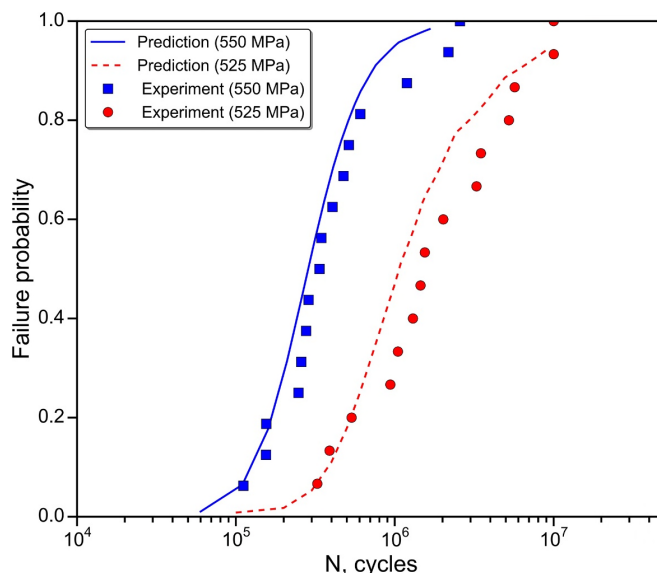


Figure 7.7. Prediction of the fatigue scatter range for two stress levels: 550 MPa and 525 MPa.

A satisfactory agreement between the modelling and experiments for both applied stresses can be seen in Figure 7.7. Nevertheless, the model gives slightly conservative estimates in the region of longer fatigue lives. Predicted fatigue lives corresponding to 10% probability of failure for two investigated stress levels are $1.2 \cdot 10^5$ and $3.5 \cdot 10^5$ cycles, respectively. Applying the described methodology for different stress levels, probabilistic S-N curves (P-S-N) can be constructed. The mean values μ and standard deviations s of the logarithmic fatigue life are listed in Table 7.1. A good match between the predicted and experimental standard deviations proves the assumption that the pore size and position are the main sources of fatigue scatter. Further analysis of other fatigue scatter sources such as uncertainties in crack growth characteristics and microstructure should improve the model predictions.

Table 7.1. Statistical characteristics of the scatter range predicted in comparison to experimental results

Stress, MPa	$\mu_{\log N}$ (exp.)	$\mu_{\log N}$ (model)	$s_{\log N}$ (exp.)	$s_{\log N}$ (model)
525	6.27	6.05	0.46	0.51
550	5.61	5.47	0.38	0.31

7.2.2 Probabilistic modelling of the initiating pore size distribution

As shown in Section 6.1, the pore diameter distribution function from the X-ray analysis differs from that found by fractographic observations. It has been demonstrated that the crack-initiating pores are, on average, larger than the pores detected by the X-ray inspection. The developed probabilistic model has the ability to predict this shift and quantitatively correlate these two distribution functions. In this regard, a criterion of the shortest fatigue life plays a key role. By applying this criterion to the pore population in a structure, only the pores are selected, which leads to the initiation of a dominant crack. Consequently, the distribution of these pores can be estimated. The following section demonstrates this procedure for the particular case of machined laser-welded Ti-6Al-4V butt joints.

Figure 7.6(a) shows the graphical representation of the joint PDF function for two random variables – pore diameter D and pore position H – present in a material volume prior to fatigue testing. By definition of the joint PD-function [138] given in Section 3.3.3, it is equal to:

$$p_{D,H}(d, h) = p_D(d) \cdot p_{H|D}(h|d), \quad (7.9)$$

where $p_D(d)$ is the marginal distribution function of D and $p_{H|D}(h|d)$ is the conditional distribution function of H given D . Since we have assumed that D and H are independent, the conditional distribution function $p_{H|D}(h|d)$ is equal to the marginal distribution $p_H(h)$ found by the X-ray analysis. In other words, we assumed that the pore depth does not affect its size distribution. As a result, the joint PD-function was obtained by a simple multiplication of two marginal PD-functions, in accordance with Equation (7.8). On the other hand, if the joint PD-function is known, the marginal density function associated with a pore diameter alone can be deduced from the joint PD-function $p_{D,H}(d, h)$ by integrating Equation (7.8) on all values of the pore position h . From the normalization condition for $p_H(h)$, the corresponding integral of Equation (7.8) is equal to initial $p_D(d)$ for any d value. However, this is valid only for the initial pore distribution existing in the specimen prior to fatigue testing and cannot be applied to the pores at the fracture surface.

For the lifetime-controlling pores that initiate dominant fatigue cracks, Equation (7.8) becomes invalid because the condition of independency is no longer fulfilled. In this case, the position of a pore at the fracture surface is influenced by its diameter. The probability of a dominant crack initiation from a pore (d, h) is proportional to the probability of fatigue failure from this pore $p_N(N(d, h))$, as determined in the previous section. In other words, for a pore with a given size d , the probability to be found at the fracture surface at the distance h is linked to the probability of failure from this pore. Consequently, the conditional distribution function $p_{H|D}^{in}(h|d)$ and the joint PD-function of the crack-initiating pores $p_{D,H}^{in}(d, h)$ can be determined by the following equations:

$$p_{H|D}^{in}(h|d) = A \cdot p_H(h) \cdot p_N(N(d, h)), \quad (7.10)$$

$$p_{D,H}^{in}(d, h) = p_D(d) \cdot p_{H|D}^{in}(h|d) = A \cdot p_D(d) \cdot p_H(h) \cdot p_N(N(d, h)), \quad (7.11)$$

where $p_N(N)$ is the PD-function of the fatigue life distribution. The coefficient A is deduced from the normalization condition. Equation (7.11) represents the joint PD-function of the initiating pores. The marginal PD-function for the initiating pores $p_D^{in}(d)$ can be derived by integrating Equation (7.11) over all h values, i.e. through the entire specimen thickness. Determined by this procedure, the distribution $p_D^{in}(d)$ represents the predicted pore-size distribution for the crack-initiating pores.

The resulting distribution of the life-controlling pores predicted by the described methodology is shown in Figure 7.8. Fractographic results compared to the estimated size distribution of the life-controlling pores. For reference, the initial PD-function of the welding-induced pores found by the X-ray inspection is also provided. A good agreement between the experimental fractographic results and the model prediction can be seen. A good match between the modelling and experiment proves the validity of the employed assumptions, thus providing a deeper insight into the underlying mechanism of the shift between two distributions. In the intact specimen, prior to fatigue testing, the pore size distribution has its initial $p_D(d)$ density function. After fatigue testing and fracture, the size of a pore at the crack nucleation site is revealed. The critical pore that initiated a dominant crack was selected from a population by the criterion of the shortest fatigue life, as expressed by Figure 7.6. In this procedure, the largest pore is not necessarily the critical one. However, on average, the application of this criterion to a large number of pores leads to a slight shift of the pore size distribution $p_D^{in}(d)$ in the direction of larger pores compared to initial $p_D(d)$.

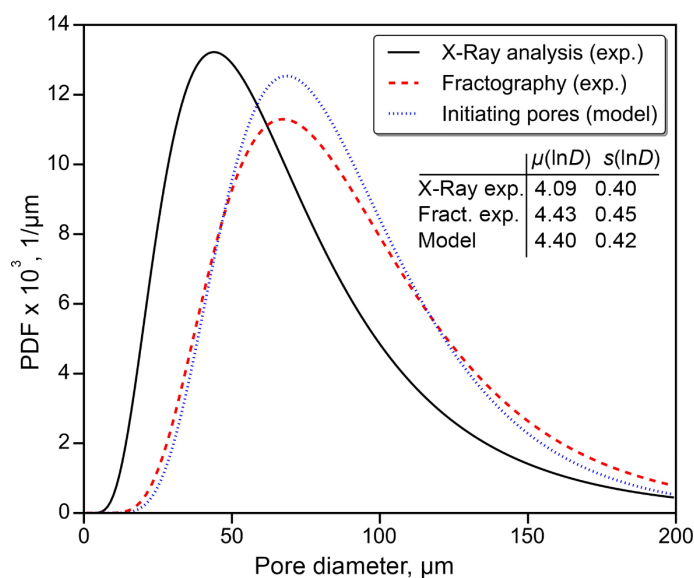


Figure 7.8. Fractographic results compared to the estimated size distribution of the life-controlling pores.

It is important to note that the shift between the welding-induced pores and the crack-initiating pores is indirectly linked to the FCP properties of the material because they determine the fatigue life. Based on our assumptions, the pore that nucleates a dominant crack has the shortest fatigue life in a pore population. The lifetime that is a number of cycles for internal crack growth depends primarily on the material properties including the crack growth resistance. Consequently, for a given welding-induced porosity distribution, the shape of the pore size distribution at the fracture surface is affected by the material and its FCP behaviour.

7.3 Conclusions

Fatigue testing of laser-welded Ti-6Al-4V butt joints revealed the extreme importance of internal defects and the need for incorporating them into predictive schemes. Based on extensive experimental research, a model for fatigue-life assessment accounting for the growth of short cracks in a vacuum-like environment has been elaborated. It is demonstrated that the fracture mechanics-based framework can be successfully applied to develop the fatigue life estimation model. In order to generate accurate

predictions, the model should account for internal crack initiation, environmental effect and the short crack growth. Owing to a significant complexity associated with experimental determination of the internal crack growth rates, the crack propagation law in a vacuum environment have been derived from the experimental S-N data. Most of the existing short crack models have been developed for surface cracks without accounting for vacuum. A simple and practical method for a simplified construction of the cyclic R-curve has been proposed and successfully introduced into the model.

Deviation of the pore size and position is the primary source of scattering in the fatigue life of the surface-treated welds. A probabilistic scheme that considers randomly distributed internal defects has been presented. Based on the X-ray measurements of porosity distribution, the fatigue scatter range of the laser-welded joints can be predicted. A satisfactory agreement between the model and experimental data has been demonstrated. A criterion of a critical pore, i.e. a pore that initiates a dominant crack, plays a key role in the probabilistic modelling. An assumption based on the shortest fatigue life supported by the fractographic observations gives a reasonable agreement with experiments. The developed probabilistic strategy can quantitatively correlate the pore size distributions obtained by the X-ray inspection and fractography. Moreover, the shift between the two distributions can be successfully predicted. Among others, this shift depends on the FCP properties of the material. The developed assessment tool might be potentially used for the lifetime prediction of components with complex geometry, which contain a population of internal material flaws or defects.

8 Summary and outlook

8.1 Summary and conclusions

The present PhD work addresses the HCF properties of laser-welded Ti-6Al-4V butt joints and the role of the weld microstructure, surface and internal defects, residual stresses, and local mechanical properties. Extensive experimental program has been carried out to quantify the effects of different factors on the resulting HCF strength. Experimental results provided a basis for deeper understanding of fatigue crack initiation leading to a final failure. Fundamental material-specific properties have been determined and successfully used to develop a HCF prediction model.

As stated in the Introduction, three global research objectives were initially identified and pursued throughout this work. First, the fatigue failure mechanism was studied by comprehensive weld characterization and mechanical testing. Then, the effectiveness of five different fatigue life extension techniques were quantitatively analysed. Finally, a model for HCF life prediction was developed and validated by the experimental data. The following conclusions corresponding to the above-mentioned research objectives can be drawn:

1. Weld characterization. LBW parameters have been consistently varied in order to obtain the optimum combination of weld macro-characteristics meeting the acceptance criteria for the aerospace industry. The weld profile parameters were statistically processed and the variation of the weld shape over the joint length was addressed. The microstructural analysis of the weld zones suggests that thermal cycles during laser welding results in strong microstructural gradients from the BM to FZ. High cooling rates encountered during solidification promote a diffusionless $\beta \rightarrow \alpha'$ martensitic transformation in the FZ. As a result, the FZ microstructure is characterized by the fine martensitic morphology within large columnar prior β grains. HAZ displays a transition region between the acicular FZ and the globular microstructure in the BM. The steep rise of microhardness from the BM to the FZ is correlated with local microstructural transformations and reflects a pronounced hardening effect associated with the martensitic reaction. Thus, LBW creates a strength mismatch between the weld zone and the base metal, which, in turn, provides a shielding effect protecting the weld from mechanical damage in tensile testing. In order to determine the local mechanical properties of the martensitic FZ, heat treatment followed by water quenching was employed to simulate the weld microstructure. It was demonstrated that the UTS of martensitic Ti-6Al-4V reaches around 1260 MPa, whereas ductility is very poor with elongation at fracture lower than 5%. In spite of considerably higher tensile strength, the weld martensitic microstructure exhibits almost the same crack growth resistance as that of the globular microstructure in the BM.

The effect of PWHT in the temperature range of 540–920°C on the weld microstructure, hardness, and residual stresses was studied. Annealing at 540°C leads to slight hardening of both the FZ and the BM due to the α_2 precipitation and martensite tempering, respectively. Recrystallization processes are activated at higher heat treatment temperatures of 750–920°C. PWHT in this temperature range modifies the FZ microstructure, improves the weld ductility, but this is accompanied by a slight decrease in tensile strength. These results are attributed to grain coarsening in the BM and martensite decomposition into the equilibrium $\alpha + \beta$ phases within the FZ. Grain growth of lamellar microstructure in the FZ is responsible for a gradual reduction of microhardness with increasing PWHT temperatures. Recrystallization annealing at 920°C helps to minimize the microhardness

mismatch between the FZ and BM from 18% in the as-welded condition to 6% in the annealed condition. In addition, it was shown that annealing at 540°C for 4 h relieves high welding-induced residual stresses by around 90%.

HCF performance of laser-welded Ti-6Al-4V butt joints without any post-processing technique is relatively poor due to the notch effect introduced by the weld underfills and increased FZ brittleness. Surface defects such as underfills and weld toes play a role of stress concentrators and have a strong deteriorative effect on the fatigue life. The as-welded condition is characterized by a fatigue limit of about 180–200 MPa. In contrast, a fatigue limit of the as-received BM is by a factor of three higher than that of the weld and reaches 600–650 MPa. In the absence of any defects, martensitic microstructure has a fatigue limit of around 900–950 MPa that is considerably higher than that of globular microstructure. These results suggest that the unnotched HCF properties of the martensitic microstructure follow the same tendency as microhardness and the tensile strength. However, inherent weld defects do not permit the realization of these theoretically achievable FZ properties.

Porosity distribution in the laser-welded Ti-6Al-4V butt joints was quantitatively characterized by the transverse X-ray analysis and correlated with the LBW process parameters. A remarkable growth of the porosity level occurs typically when the laser power reaches the values of 4.5–5.0 kW, depending on the welding speed. Drastic increase in porosity level almost completely corresponds to beginning of spattering at the bottom weld surface. This leads to the conclusion that the keyhole stability and its openness determine the porosity level. The optimum parameter set for minimizing the weld porosity should have a high welding speed of 4.0–5.0 m/min and a laser power lower than 4.5 kW. Moreover, laser power is the most influential factor that governs the porosity level through the keyhole behaviour.

2. Methods for improvement of fatigue properties. Five different methods aiming to extend the fatigue lifetime of laser-welded Ti-6Al-4V butt joints have been compared and discussed. Conventional machining of the weld is one of the simplest and most effective methods for improving the fatigue performance. The fatigue limit of machined joints approaches the range of 500–520 MPa, which is 250% higher than in the as-welded condition. PWHT at temperatures above 750°C can further increase the fatigue limit of machined joints by approximately 10% up to 540–550 MPa. LSR is a more simple and cost-effective technology that enables the improvement of the fatigue limit by approximately 275%. Fractographic observations revealed that internal welding-induced porosity determines the fatigue life of the joints after any surface smoothing technique. Owing to subsurface crack initiation, a bright circular area, called ‘fish-eye’, is normally observed around the crack nucleation site. The shift of the crack initiation site to the interior of the specimen has a strong beneficial effect on the fatigue performance.

It was demonstrated that the effectiveness of LSP for fatigue life extension is more pronounced for surface defects than for internal defects such as porosity. LSP treatment of the as-welded joints has a pronounced positive impact on the fatigue behaviour, leading to a fatigue limit of in the range of 380–400 MPa, which is close to the fatigue limit of the machined joints. Effect of compressive residual stresses on internal fatigue crack initiation and growth was statistically analysed by the Weibull distribution. Although the characteristic life increased by a factor of three, special attention should be paid to a larger fatigue scatter band after LSP. These findings indicate that the application of LSP treatment to suppress the internal crack growth has less improvement potential, just as for surface cracks.

Fatigue performance of the laser-welded Ti-6Al-4V butt joints after the LSR processing or machining cannot be altered significantly by the adjustment of welding parameters. Variations in the process parameters can reduce the number of pores, but it is impossible to completely avoid them. As a result, the fatigue properties stay almost equal regardless of the welding parameters.

3. Lifetime assessment. Fatigue testing of laser-welded and surface-treated Ti-6Al-4V butt joints revealed the crucial role of internal defects such as porosity in the HCF failure. These findings underline the need to incorporate the internal defects into the HCF prediction models. A detailed fractographic analysis provided important insights into the mechanism of internal fatigue failure and enabled the construction of a generalized scheme of the fish-eye failure. An analytical fracture mechanics model for fatigue life assessment accounting for interior-initiated fatigue cracks has been developed. For reasonable estimations, the model should account for internal crack initiation, environmental effects at the crack tip, and the short crack growth behaviour. The model was validated using the S-N data of machined joints. By this, the crack growth characteristics of internal short cracks were derived. A simplified method for the construction of the cyclic R-curve has been proposed and successfully used in the model.

The constructed methodology gives the opportunity to estimate the fatigue scatter range, which is extremely important for reliability analysis. For this purpose, the pore distribution was statistically processed and correlated with the fatigue scatter range. A probabilistic methodology that considers randomly distributed internal defects in a component has been elaborated. The results are in a good agreement with the experimental findings. Surprisingly, it was shown that the life-controlling defect is not necessarily the largest defect from a given population. In fact, several random variables such as defect size and its position determine the crack initiation potential. The developed probabilistic strategy can also predict the distribution of crack-initiating pores found by fractographic measurements. Finally, the developed and validated model can be further used to predict the failure probability of a component with a complex geometry and a population of defects.

In addition to the main results summarized above, the present work generated some other interesting findings with regard to internal fatigue fracture of the Ti-6Al-4V base metal. It was demonstrated that internal crack initiation causes the HCF failure of Ti-6Al-4V base metal, despite its purity in terms of non-metallic inclusions. Each type of microstructure has its own hard brittle α grains that break by a cleavage-based mechanism in the region of high cycles. Therefore, interior-initiated cracks might be potentially formed in a defect-free component and should be accounted by probabilistic lifetime evaluation models.

8.2 Recommendations for future work

The present work has raised many challenging questions with regard to mechanisms and mechanics of internal fatigue failure in the region of high cycles. There is still some ambiguity on the conditions responsible for the crack origin shift to the subsurface. Further fatigue testing should provide a quantitative surface quality criterion that will determine the transition from surface-initiated to internally-initiated fatigue failure. Future work needs to be carried out to enhance the understanding of the fish-eye formation. There is still no general agreement on the crack growth behaviour within the ODA zone. In this regard, in-situ crack growth measurements of internal cracks using a synchrotron radiation would help to verify the existing theoretical models and to determine precisely the crack initiation period.

Future studies should concentrate on the application of the laser-based surface smoothing techniques for extension of fatigue life. In this PhD work, the welding procedure enabling the joint fatigue strength comparable to that of the BM was developed. The author believes that a combination of improvement techniques presented in this work, such as laser remelting combined with PWHT and subsequent LSP, has the biggest potential for industrial applications. The results of this work suggest that under these circumstances, fatigue cracks will inevitably initiate underneath the surface. This serves as an additional stimulus to develop probabilistic assessment models accounting for internal crack initiation in the HCF and VHCF regimes.

To improve the model predictions, it is recommended that further research should focus on the application of advanced statistical tools such as statistics of extremes for the description of the defect population. The short crack model should be broadened in order to account for mechanically short cracks. 3D tomography investigations of fatigue specimens prior to testing should correct the current criterion for the life-controlling defect in a given population. Finally, the model developed and validated in this work can be applied to predict the fatigue behaviour of additively manufactured Ti-6Al-4V parts, where internal defects also play a key role.

Bibliography

- [1] “Strategic Research & Innovation Agenda. Update, Volume 1.,” ACARE, 2017. [Online]. Available: www.acare4europe.org. [Accessed 08.11.2018].
- [2] “Flightpath 2050. Europe's Vision for aviation. Report on the high level group on aviation research,” Publications Office of the European Union, Luxembourg, 2011.
- [3] CleanSky, “Joint Technical programme,” Clean Sky 2, Brussels, 2015.
- [4] L. Albugues and P. Rodrigo, “Fatigue behaviour of fuselage panels with welded stiffeners,” in *22nd ICAF Symposium of the International Committee on Aeronautical Fatigue*, Sheffield, 2004.
- [5] J. Williams and E. Starke, “Progress in structural materials for aerospace systems,” *Acta Materialia*, vol. 51, p. 5775–5799, 2003.
- [6] W. Duley, *Laser Welding*, Hoboken: Wiley-Interscience, 1998.
- [7] R. Boyer, “An overview on the use of titanium in the aerospace industry,” *Materials Science and Engineering A*, vol. 213, p. 103–114, 1996.
- [8] E. Benini, Ed., “Titanium in the gas turbine engine,” in *Advances in Gas Turbine Technology*, London, IntechOpen, 2011, p. 315–336.
- [9] N. Kashaev, V. Ventzke, M. Horstmann, S. Riekehr, G. Yashin, L. Stutz and W. Beck, “Microstructure and mechanical properties of laser beam welded joints between fine-grained and standard Ti-6Al-4V sheets subjected to superplastic forming,” *Advanced Engineering Materials*, vol. 17, p. 374–382, 2015.
- [10] J. Ahn, L. Chen, C. Davies and J. Dear, “Parametric optimisation and microstructural analysis on high power Yb-fibre laser welding of Ti-6Al-4V,” *Optics and Lasers in Engineering*, vol. 86, p. 156–171, 2016.
- [11] N. Kashaev, V. Ventzke, V. Fomichev, F. Fomin and S. Riekehr, “Effect of Nd:YAG laser beam welding on weld morphology and mechanical properties of Ti-6Al-4V butt joints and T-joints,” *Optics and Lasers in Engineering*, vol. 86, p. 172–180, 2016.
- [12] H. Wirdelius, E. Lindgren and P. Henrikson, “System for lifetime assessment of laser welded titanium components based on automated defect detection,” in *The 4th CEAS Conference. Book of Abstracts*, Linköping, 2013.
- [13] A. Squillace, U. Prisco, S. Ciliberto and A. Astarita, “Effect of welding parameters on morphology and mechanical properties of Ti-6Al-4V laser beam welded butt joints,” *Journal of Materials Processing Technology*, vol. 212, no. 2, p. 427–436, 2012.
- [14] J. Schijve, *Fatigue of structures and materials*, Delft: Springer, 2009.
- [15] B. Cowles, “High cycle fatigue in aircraft gas turbines - an industry perspective,” *International Journal of Fatigue*, vol. 80, p. 147–163, 1996.
- [16] B. Cowles, “Application and life prediction of titanium alloys in military gas turbine engines,” in *International Symposium sponsored by the TMS Titanium Committee*, Chicago, 1998.
- [17] T. Bartsch, “High Cycle Fatigue Science and Technology Program,” USAF, Dayton, 2002.

- [18] T. Nicholas, "Material allowables for high cycle fatigue in gas turbine engines," in *RTO AVT Specialists' meeting on Application of Damage Tolerance Principles for Improved Airworthiness of Rotorcraft*, Corfu, 1999.
- [19] L. Wagner, "Effect of mechanical surface treatment on fatigue performance of titanium alloys," in *International Symposium sponsored by the TMS Titanium Committee*, Chicago, 1998.
- [20] X. Liu, C. Sun and Y. Hong, "Faceted crack initiation characteristics for high-cycle and very-high-cycle fatigue of a titanium alloy under different stress ratios," *International Journal of Fatigue*, vol. 92, p. 434–441, 2016.
- [21] J. McEvily, T. Nakamura, H. Oguma, K. Yamashita, H. Matsunaga and M. Endo, "On the mechanism of very high cycle fatigue in Ti–6Al–4V," *Scripta Materialia*, vol. 59, no. 11, p. 1207–1209, 2008.
- [22] G. Lütjering and J. Williams, *Titanium*, 1st ed., Berlin, Heidelberg: Springer-Verlag, 2003.
- [23] C. Elrod, "Review of titanium application in gas turbine engines," in *ASME Turbo Expo 2003*, Atlanta, 2003.
- [24] S. Audion, G. Khelifati, J. Delfosse, P. Oillic and R. Peraldi, "Extending the use of titanium alloys on A350XWB," in *12th World Conference on Titanium*, Beijing, 2011.
- [25] M. Donachie, *Titanium. A Technical Guide*, Materials Park: ASM International, 2000.
- [26] G. Lütjering, "Influence of processing on microstructure and mechanical properties of (α + β) titanium alloys," *Materials Science and Engineering A*, vol. 243, no. 1–2, p. 32–45, 1998.
- [27] A. Zarkades and F. Larson, *The Science, Technology and Application of Titanium*, R. Jaffee and N. Promisel, Eds., Oxford: Pergamon Press, 1970.
- [28] R. Boyer, G. Welsch and E. Collings, Eds., *Materials Properties Handbook: Titanium Alloys*, Materials Park: ASM International, 1994, p. 483–633.
- [29] S. Banerjee and P. Mukhopadhya, *Phase Transformations, Examples from Titanium and Zirconium Alloys*, Oxford: Elsevier, 2007.
- [30] H. Aaronson, M. Enomoto and J. Lee, *Mechanisms of Diffusional Phase Transformations in Metals and Alloys*, Boca Raton: CRC Press, 2010.
- [31] W. Zhang, W. S. Zhao, D. X. Li and M. L. Sui, "Martensitic transformation from α -Ti to β -Ti on rapid heating," *Applied Physics Letters*, vol. 84, p. 4872–4874, 2004.
- [32] T. Massalski, "Massive transformations revisited," *Metall and Materials Transactions A*, vol. 33, p. 2277–2283, 2002.
- [33] J. Peters and R. Ritchie, "Foreign-object damage and high-cycle fatigue: role of microstructure in Ti-6Al-4V," *International Journal of Fatigue*, vol. 23, p. 413–421, 2001.
- [34] F. Fomin, M. Froend, V. Ventzke, P. Alvarez, S. Bauer and N. Kashaev, "Metallurgical aspects of joining commercially pure titanium to Ti-6Al-4V alloy in a T-joint configuration by laser beam welding," *The International Journal of Advanced Manufacturing Technology*, vol. 97, p. 2019–2031, 2018.
- [35] T. Ahmed and H. Rack, "Phase transformations during cooling in α + β titanium alloys," *Materials Science and Engineering A*, vol. 243, no. 1–2, p. 206–211, 1998.
- [36] L. Smith, P. Threadgill and M. Gittos, *Welding titanium. A designers and users handbook*, Cambridge: TWI, 1999.

-
- [37] X. Gao, L. Zhang, J. Liu and J. Zhang, "A comparative study of pulsed Nd:YAG laser welding and TIG welding of thin Ti6Al4V titanium alloy plate," *Materials Science and Engineering A*, vol. 559, p. 14–21, 2013.
- [38] B. Mehdi, R. Radji, V. Ji, B. Alili, D. Bradai, F. Deschaux-Beaume and F. Soulie, "Microstructure and residual stresses in Ti6Al4V alloy pulsed and unpulsed TIG welds," *Journal of Materials Processing Technology*, vol. 231, p. 441–448, 2016.
- [39] N. Babu, S. Raman, R. Muthili and S. Saroja, "Correlation of microstructure with mechanical properties of TIG weldments of Ti-6Al-4V made with and without current pulsing," *Materials Characterization*, vol. 58, p. 581–587, 2007.
- [40] A. Short, "Gas tungsten arc welding of $\alpha+\beta$ titanium alloys: a review," *Materials Science and Technology*, vol. 25, p. 309–324, 2009.
- [41] R. Kumar and S. Bharathi, "A review study on A-TIG welding of 316(L) austenitic stainless steel," *International Journal of Emerging Trends in Science and Technology*, vol. 2, no. 3, p. 2066–2072, 2015.
- [42] J. Norrish, *Advanced welding processes. Technology and process control*, Cambridge: Woodhead Publishing, 2006.
- [43] X. Yang, S. Li and H. Qi, "Ti-6Al-4V welded joints via electron beam welding: microstructure, fatigue properties, and fracture behavior," *Materials Science and Engineering A*, vol. 597, p. 225–231, 2014.
- [44] G. Thomas, V. Ramachandra, K. Nagarajan, B. Pant, B. Sarkar and R. Vasudevan, "Electron beam welding studies of 25-mm-thick Ti-6Al-4V sections," *Welding Research Supplement*, p. 336–341, 1989.
- [45] N. Suresh, M. Pillai and J. Mathew, "Investigations into the effects of electron beam welding on thick Ti-6Al-4V titanium alloy," *Journal of Materials Processing Technology*, vol. 192–193, p. 83–88, 2007.
- [46] N. Gouret, E. Oliver, G. Dour, R. Fortunier and B. Miguet, "Assessment of the origin of porosity in electron-beam-welded TA6V plates," *Metallurgical and Materials Transactions A*, vol. 35, p. 879–889, 2004.
- [47] T. Mohandas, D. Banerjee and V. Rao, "Fusion zone microstructure and porosity in electron beam welds of an alpha + beta titanium alloy.," *Metallurgical and Materials Transactions A*, vol. 30, p. 789–798, 1999.
- [48] F. Pengfei, M. Zhiyong, Z. Congjin, W. Yajun and W. Chunming, "Microstructures and fatigue properties of electron beam welds with beam oscillation for heavy section TC4-DT alloy," *Chinese Journal of Aeronautics*, vol. 27, no. 4, p. 1015–1021, 2014.
- [49] W. Lu, Y. Lei, X. Li and Y. Shi, "Effect of electron beam welding on fracture behaviour of thick TC4-DT alloy," *Science and Technology of Welding and Joining*, vol. 17, no. 4, p. 277–281, 2012.
- [50] S. Wang and X. Wu, "Investigation on the microstructure and mechanical properties of Ti-6Al-4V alloy joints with electron beam welding," *Materials and Design*, vol. 36, p. 663–670, 2012.
- [51] X. Yang, S. Li and H. Qi, "Tensile properties and failure analysis of Ti-6Al-4V joints by electron beam welding," *Rare Metals*, vol. 35, no. 6, p. 450–455, 2014.

- [52] N. Babu, S. Raman, S. Murthy and G. Reddy, "Effect of beam oscillation on fatigue life of Ti-6Al-4V electron beam weldments," *Materials Science and Engineering A*, vol. 471, no. 1-2, p. 113-119, 2007.
- [53] C. Tsai and L. Wang, "Improved mechanical properties of Ti-6Al-4V alloy by electron beam welding process plus annealing treatments and its microstructural evolution.," *Materials and Design*, vol. 60, p. 587-598, 2014.
- [54] R. Collins, S. Kimmins, D. Campassens and P. Rodrigo, "Advanced materials and manufacturing techniques on future airbus aircraft and the implications for fatigue and damage tolerance," in *22nd ICAF Symposium of the International Committee on Aeronautical Fatigue*, Sheffield, 2004.
- [55] A. Kabir, X. Cao, M. Medraj, P. Wanjara, J. Cuddy and A. Birur, "Effect of Welding Speed and Defocusing Distance on the Quality of Laser Welded Ti-6Al-4V," in *Materials Science and Technology*, Houston, 2010.
- [56] Comunity Research and Development Information Service, European Comission, [Online]. Available: https://cordis.europa.eu/project/rcn/199337_en.html. [Accessed 06.11.2018].
- [57] T. Balasubramanian, M. Balakrishnan, V. Balasubramanian and M. Muthu Manickam, "Effect of welding process on joint characteristics of Ti-6Al-4V alloy," *Science and Technology of Welding and Joining*, vol. 16, p. 702-708, 2011.
- [58] A. Kabir, X. Cao, P. Wanjara, J. Cuddy, A. Birur and M. Medraj, "Use of filler wire for laser welding of Ti-6Al-4V," *Canadian Metallurgical Quarterly*, vol. 51, p. 320-327, 2012.
- [59] J. Blackburn, C. Allen, P. Hilton and L. Li, "Nd:YAG laser welding of titanium alloys using a directed gas jet," *Journal of Laser Applications*, vol. 22, p. 71-78, 2010.
- [60] E. Akman, A. Demir, T. Canel and T. Smazcelok, "Laser welding of Ti6Al4V titanium alloys," *Journal of Materials Processing Technology*, vol. 209, p. 3705-3713, 2009.
- [61] F. Caiazzo, F. Curcio, G. Daurelio and F. Minutolo, "Ti6Al4V sheets lap and butt joints carried out by CO₂ laser: mechanical and morphological characterization," *Journal of Materials Processing Technology*, vol. 149, no. 1, p. 546-552, 2004.
- [62] S. Wang, J. Liu and D. Chen, "Effect of post-weld heat treatment on the fatigue properties of dissimilar titanium alloy joints," in *13th International Conference on Fracture*, Beijing, 2013.
- [63] A. Costa, R. Miranda, L. Quintino and D. Yapp, "Analysis of beam material interaction in welding of titanium with fiber lasers," *Materials and Manufacturing Processes*, vol. 22, no. 7-8, p. 798-803, 2007.
- [64] J. Blackburn, C. Allen, A. Khan, P. Hilton and L. Li, "Dual focus Nd:YAG laser welding of titanium alloys: effect on porosity formation," *Lasers in Engineering*, vol. 22, no. 5-6, p. 319-336, 2012.
- [65] X. Cao, A. Kabir, P. Wanjara, J. Gholipour, A. Birur, J. Cuddy and M. Medraj, "Global and local mechanical properties of autogenously laser welded Ti-6Al-4V," *Metallurgical and Materials Transactions A*, vol. 45, p. 1258-1272, 2014.
- [66] F. Cao, G. Debaecker, M. Jahazi, S. Marya, J. Cuddy and A. Birur, "Effect of post treatment on Nd:YAG laser welded Ti-6Al-4V alloy quality," *Materials Science Forum*, vol. 638-642, p. 3655-3660, 2010.
- [67] A. Kabir, X. Cao, J. Gholipour, P. Wanjara, J. Cuddy, A. Birur and M. Medraj, "Effect of postweld heat treatment on microstructure, hardness, and tensile properties of laser welded

- Ti-6Al-4V,” *Metallurgical and Materials Transactions A*, vol. 43, no. 11, p. 4171–4184, 2012.
- [68] Y. Murakami, *Metal Fatigue: Effects of Small Defects and Nonmetallic Inclusions*, 1st ed., Oxford: Elsevier, 2002.
- [69] C. Bathias, “There is no infinite fatigue life in metallic materials,” *Fatigue and Fracture of Engineering Materials and Structures*, vol. 22, p. 559–565, 1999.
- [70] K. Shiozawa, “S–N curve characteristics and subsurface crack initiation behaviour in ultra-long life fatigue of a high carbon-chromium bearing steel,” *Fatigue and Fracture of Engineering Materials and Structures*, vol. 24, no. 12, p. 781–790, 2002.
- [71] U. Zerbst, M. Vormwald, R. Pippan, H. Gaenser, C. Sarrazin-Baudoux and M. Madia, “About the fatigue crack propagation threshold of metals as a design criterion - A review,” *Engineering Fracture Mechanics*, vol. 153, p. 190–243, 2016.
- [72] G. Wu, C. Shi, W. Sha, A. Sha and H. Jiang, “Effect of microstructure on the fatigue properties of Ti–6Al–4V titanium alloys,” *Materials and Design*, vol. 46, p. 668–674, 2013.
- [73] M. Peters, A. Gysler and G. Lütjering, “Influence of texture on fatigue properties of Ti-6Al-4V,” *Metallurgical Transactions A*, vol. 15, p. 1597–1605, 1984.
- [74] R. Mirrisey, D. McDowell and T. Nicholas, “Frequency and stress ratio effects in high cycle fatigue of Ti-6Al-4V,” *International Journal of Fatigue*, vol. 21, p. 679–685, 1999.
- [75] K. Moussaoui, M. Mousseigne, J. Senatore, R. Chieragatti and P. Lamesle, “Influence of milling on the fatigue lifetime of a Ti6Al4V titanium alloy,” *Metals*, vol. 5, p. 1148–1162, 2015.
- [76] S. Maddox, *Fatigue Strength of Welded Structures*, Cambridge: Abington Publishing, 1991.
- [77] T. Balasubramanian, V. Balasubramanian and M. Muthumanikkam, “Fatigue performance of gas tungsten arc, electron beam, and laser beam welded Ti-6Al-4V alloy joints,” *Journal of Materials Engineering and Performance*, vol. 20, p. 1620–1630, 2011.
- [78] Y. Fan, “Mechanical properties of laser beam welded Ti-6Al-4V. PhD Thesis,” The University of Nottingham, Nottingham, 2010.
- [79] C. Casavola, C. Pappalettere and F. Tattoli, “Experimental and numerical study of static and fatigue properties of titanium alloy welded joints,” *Mechanics of Materials*, vol. 41, no. 3, p. 231–243, 2009.
- [80] D. Neal and P. Belnkinsop, “Internal fatigue origins in $\alpha+\beta$ titanium alloys,” *Acta Metallurgica*, vol. 24, p. 59–63, 1976.
- [81] H. Oguma, “Very high cycle fatigue properties of Ti-6Al-4V alloy. PhD thesis,” Hokkaido University, Hokkaido, 2006.
- [82] H. Gong, K. Rafi, H. Gu, G. Janaki Ram, T. Starr and B. Stucker, “Influence of defects on mechanical properties of Ti–6Al–4V components produced by selective laser melting and electron beam melting,” *Materials and Design*, vol. 86, p. 545–554, 2015.
- [83] A. Pilchak, A. Bhattacharjee, A. Rosenberger and J. Williams, “Low ΔK faceted crack growth in titanium alloys,” *International Journal of Fatigue*, vol. 31, no. 5, p. 989–994, 2009.
- [84] J. Everaets, B. Verlinden and M. Wevers, “The influence of the alpha grain size on internal fatigue crack initiation in drawn Ti-6Al-4V wires,” *Procedia Structural Integrity*, vol. 2, p. 1055–1062, 2016.

- [85] X. Liu, C. Sun and Y. Hong, "Effects of stress ratio on high-cycle and very-high-cycle fatigue behavior of a Ti-6Al-4V alloy," *Materials Science and Engineering A*, vol. 622, p. 228–235, 2015.
- [86] F. Cao and K. Chandran, "The role of crack origin size and early stage crack growth on high cycle fatigue of powder metallurgy Ti-6Al-4V alloy," *International Journal of Fatigue*, vol. 102, p. 48–58, 2017.
- [87] K. Masaki, Y. Yonakuni, N. Hisamori, Y. Suga, Y. Kobayashi and D. Gowa, "Influence of zirconia shot peening treatment on high cycle fatigue properties of Ti-6Al-4V," *Journal of the Society of Materials Science, Japan*, vol. 65, no. 9, p. 679–686, 2016.
- [88] G. Leverant, B. Langer, A. Yuen and S. Hopkins, "Surface residual stresses, surface topography and the fatigue behavior of Ti-6Al-4V," *Metallurgical Transactions A*, vol. 10, no. 2, p. 251–257, 1979.
- [89] S. Berge, "Fatigue of titanium fusion welds - models for assessment of defect sensitivity," in *International Symposium sponsored by TMS Titanium Committee*, Chicago, 1998 .
- [90] S. Laine, K. Knowles, P. Doorbar, R. Cutts and D. Rugg, "Microstructural characterisation of metallic shot peened and laser shock peened Ti-6Al-4V," *Acta Materialia*, vol. 123, p. 350–361, 2017.
- [91] A. Gujba and M. Medraj, "Laser peening process and its impact on materials properties in comparison with shot peening and ultrasonic impact peening," *Materials*, vol. 7, p. 7925–7974, 2014.
- [92] R. Nalla, I. Altenberger, U. Noster, G. Liu, B. Scholte and R. Ritchie, "On the influence of mechanical surface treatments deep rolling and laser shock peening on the fatigue behavior of Ti-6Al-4V at ambient and elevated temperatures," *Materials Science and Engineering A*, vol. 355, no. 1–2, p. 216–230, 2003.
- [93] X. Zhang, Y. Zhang, J. Lu, F. Xuan, Z. Wang and S. Tu, "Improvement of fatigue life of Ti-6Al-4V alloy by laser shock peening," *Materials Science and Engineering A*, vol. 527, p. 3411–3415, 2010.
- [94] Z. Cao, Z. Che and S. Zou, "The residual stress distribution and fatigue property of TC4 laser-welded joint treated by laser shock peening," in *5th International Conference on Information Engineering for Mechanics and Materials*, Huhhot, 2015.
- [95] T. Gurney, *Fatigue of Welded Structures*, Cambridge: University press, 1979.
- [96] Y. Li, W. Guo, N. Xu, X. Wu, J. Shi and H. Ma, "Crack growth process in GBF are of SUJ2 steel in very high cycle fatigue regime," *Materials Science and Technology*, vol. 29, no. 12, p. 1463–1469, 2013.
- [97] T. Sakai, Y. Sato and O. N., "Characteristic S–N properties of high-carbon chromium bearing steel under axial loading in long-life fatigue," *Fatigue and Fracture of Engineering Materials and Structures*, vol. 25, no. 8-9, p. 765–773, 2002.
- [98] A. Fjeldstad, A. Wormsen and G. Haerkegard, "Simulation of fatigue crack growth in components with random defects," *Engineering Fracture Mechanics*, vol. 75, no. 5, p. 1184–1203, 2007.
- [99] S. Beretta and Y. Murakami, "Statistical analysis of defects for fatigue strength prediction and quality control of materials," *Fatigue and Fracture of Engineering Materials and Structures*, vol. 21, no. 9, p. 1049–1065, 1998.

-
- [100] Y. Li, L. Zhang, Y. Fei, X. Liu and M. Li, "On the formation mechanisms of fine granular area (FGA) on the fracture surface for high strength steels in the VHCF regime," *International Journal of Fatigue*, vol. 82, p. 402–410, 2016.
- [101] K. Tanaka and Y. Akiniwa, "Fatigue crack propagation behavior derived from S-N data in very high cycle regime," *Fatigue and Fracture of Engineering Materials and Structures*, vol. 25, p. 775–784, 2002.
- [102] M. Chapetti, "A simple model to predict the very high cycle fatigue resistance of steels," *International Journal of Fatigue*, vol. 33, p. 833–841, 2011.
- [103] Q. Wang, J. Berard, A. Dubarre, G. Baudry, S. Rathery and C. Bathias, "Gigacycle fatigue of ferrous alloys," *Fatigue and Fracture of Engineering Materials and Structures*, vol. 22, p. 667–672, 1999.
- [104] M. Nakajima, N. Kamiya, H. Itoga and H. Ko, "Experimental estimation of crack initiation lives and fatigue limit in subsurface fracture of a high carbon chromium steel," *International Journal of Fatigue*, vol. 28, p. 1540–1546, 2006.
- [105] Y. Jang, Y. Jeong, C. Yoon and S. Kim, "Fatigue life prediction for porosity-containing cast 319-T7 aluminum alloy," *Metallurgical and Materials Transactions A*, vol. 40, p. 1090–1099, 2009.
- [106] S. Beretta and S. Romano, "Comparison of fatigue strength sensitivity to defects for materials manufactured by AM or traditional processes," *International Journal of Fatigue*, vol. 94, p. 178–191, 2017.
- [107] AMS 4911N: Titanium alloy, sheet, strip and plate, 6Al-4V annealed, SAE International, Warrendale, 2013.
- [108] N. Paton and M. Mahoney, "Creep of titanium-silicon alloys," *Metallurgical Transactions A*, vol. 7, p. 1685–1694, 1976.
- [109] ISO 11146-1:2005, Lasers and laser-related equipment – Test methods for laser beam widths, divergence angles and beam propagation ratios, ISO, Santa Clara, 2005.
- [110] H.-J. Bunge, Texture analysis in materials science. Mathematical methods (in German), Berlin: Akademie-Verlag, 1969.
- [111] B. Agarwal, X-Ray Spectroscopy, Berlin: Springer-Verlag, 1991.
- [112] ASTM E384-11, Standard Test Method for Knoop and Vickers Hardness of Materials," ASTM International, West Conshohocken, 2011.
- [113] ASTM E837-11, Standard test method for determining residual stresses by the hole-drilling strain gage method, ASTM International, West Conshohocken, 2011.
- [114] M. Steinzig and E. Ponslet, "Residual stress measurement using the hole drilling method and laser speckle interferometry, Parts I–IV," *Experimental Techniques*, vol. 27, no. 2,3,4,5, 2003.
- [115] K.-D. Liss, A. Bartels, A. Schreyer and H. Clemens, "High energy X-rays: a tool for advanced bulk investigations in materials science and physics," *Textures and Microstructures*, vol. 35, p. 219–252, 2003.
- [116] G. Dovzhenko, S. Hanke, P. Staron, E. Maawad, A. Schreyer and M. Horstmann, "Residual stresses and fatigue crack growth in friction surfacing coated Ti-6Al-4V sheets," *Journal of Materials Processing Technology*, vol. 262, p. 104–110, 2018.

- [117] DIN EN ISO 6892-1:2009-12. Metallische Werkstoffe - Zugversuch - Teil 1: Prüfverfahren bei Raumtemperatur (ISO 6892-1:2009); Deutsche Fassung.
- [118] ASTM E466-07, Standard Practice for Conducting Force Controlled Constant Amplitude Axial Fatigue Tests of Metallic Materials, ASTM International, West Conshohocken, 2007.
- [119] ASTM E647-11, Standard Test Method for Measurement of Fatigue Crack Growth Rates, ASTM International, West Conshohocken, 2011.
- [120] EN 4678:2011, Aerospace series – Weldments and brazements for aerospace structures, European Committee for Standardization, Brussels, 2011.
- [121] AWS D17.1 Specification for fusion welding for aerospace applications, American Welding Society, Miami, 2001.
- [122] J. Polak, “Cyclic deformation, crack initiation, and low-cycle fatigue,,” in *Comprehensive Structural Integrity. Cyclic Loading and Fracture*, R. Ritchie and Y. Murakami, Eds., Pergamon, 2003, p. 1–39.
- [123] U. Zerbst, M. Madia and D. Hellmann, “An analytical fracture mechanics model for estimation of S-N curves of metallic alloys containing large second phase particles,,” *Engineering Fracture Mechanics*, vol. 82, pp. 1115-134, 2012.
- [124] S. Suresh and R. Ritchie, “Propagation of short fatigue cracks,,” *International Metal Reviews*, vol. 29, p. 445–475, 1984.
- [125] A. Griffith and M. Eng, “The phenomena of rupture and flow in solids,,” *Philosophical Transactions of the Royal Society A*, vol. 221, p. 163–198, 1921.
- [126] Y. Murakami, Stress Intensity Factors Handbook, Oxford: Pergamon Press, 1987.
- [127] P. Paris and F. Erdogan, “A critical analysis of crack propagation laws,,” *Journal of Basic Engineering*, vol. 85, p. 528–533, 1963.
- [128] K. Tanaka and Y. Nakai, “Fatigue growth threshold of small cracks,,” *International Journal of Fatigue*, vol. 17, no. 5, p. 519–533, 1981.
- [129] A. McEvily and K. Minakawa, “Crack closure and the growth of short and long fatigue cracks,,” *Scripta Metallurgica*, vol. 18, no. 1, p. 71–76, 1984.
- [130] M. Chapetti, “Fatigue propagation threshold of short cracks under constant amplitude loading,,” *International Journal of Fatigue*, vol. 25, p. 1319–1326, 2003.
- [131] H. Kitagawa and S. Takahashi, “Applicability of fracture mechanics to very small cracks or the cracks in the early stage,,” in *2nd International Conference on Mechanical Behaviour of Materials*, Cleveland (OH), 1976.
- [132] K. Tanaka and Y. Akiniwa, “Resistance curve method for predicting propagation threshold of the short fatigue cracks at notches,,” *Engineering Fracture Mechanics*, vol. 30, no. 6, p. 863–876, 1988.
- [133] M. El Haddad, T. Topper and K. Smith, “Prediction of non propagating cracks,,” *Engineering Fracture Mechanics*, vol. 11, no. 3, p. 573–584, 1979.
- [134] B. Taberning and R. Pippin, “Determination of the length dependence of the threshold for fatigue crack propagation,,” *Engineering Fracture Mechanics*, vol. 69, p. 899–907, 2002.
- [135] U. Zerbst and M. Madia, “Fracture mechanics based assessment of the fatigue strength: approach for the determination of the initial crack size,,” *Fatigue and Fracture of Engineering Materials and Structures*, vol. 38, no. 9, p. 1066–1075, 2015.

-
- [136] M. J. Crowder, A. Kimber, R. Smith and T. Sweeting, *Statistical Analysis of Reliability Data*, London: Chapman & Hall, 1991.
- [137] J. Xiong and R. Sheno, "Reliability and confidence levels of fatigue life," in *Fatigue and Fracture Reliability Engineering*, London, Springer-Verlag, 2011, p. 27–61.
- [138] L. Sachs and J. Hedderich, *Angewandte statistik. Methodensammlung mit R (in German)*, Berlin-Heidelberg: Springer, 2006.
- [139] C. Lai, D. Murthy and M. Xie, "Weibull distributions and their applications," in *Springer Handbook of Engineering Statistics*, H. Pham, Ed., London, Springer, 2005, p. 63–78.
- [140] D. Murthy, M. Xie and R. Jiang, *Weibull Modells*, New Jersey: Wiley-Interscience, 2004.
- [141] F. Fomin, V. Ventzke, F. Dorn, N. Levichev and N. Kashaev, "Effect of microstructure transformations on fatigue properties of laser beam welded Ti-6Al-4V butt joints subjected to postweld heat treatment," in *Study of Grain Boundary Character*, T. Tanski, Ed., Rijeka, InTechOpen, 2017, p. 111–141.
- [142] S. Karl, B. David and T. Hochkirchen, *Statistische Versuchsplanung: Design of Experiments (DoE)*, Heidelberg: Springer, 2010.
- [143] A. Salem, "Texture separation for α/β titanium alloys," in *Electron Back-Scatter Diffraction in Materials Science*, 2 ed., New York, Springer Publishers, 2009.
- [144] M. Peters and J. Williams, "Microstructure and mechanical properties of a welded $\alpha+\beta$ Ti Alloy," *Metallurgical Transactions A*, vol. 15, p. 1589–1596, 1984.
- [145] N. Babu, S. Raman, C. Srinivasa Murthy and G. Reddy, "Effect of beam oscillation on fatigue life of Ti-6Al-4V electron beam weldments," *Materials Science and Engineering A*, vol. 471, p. 113–119, 2007.
- [146] E. Sallica-Leva, R. Caram, A. Jardini and J. Fogagnolo, "Ductility improvement due to martensite α' decomposition in porous Ti-6Al-4V parts produced by selective laser melting for orthopedic implants," *Journal of the Mechanical Behaviour of Biomedical Materials*, vol. 54, p. 149–158, 2016.
- [147] M. Madia, U. Zerbst, H. Beier and B. Schork, "The IBESS model – elements, realization and validation," *Engineering Fracture Mechanics*, vol. 198, p. 171–208, 2017.
- [148] M. Song, J. Lei, Y. Ma and L. Y.Y., "Effect of aging treatment on microstructure and mechanical properties of a two-phase titanium alloy," *Materials Science Forum*, vol. 654–656, p. 851–854, 2010.
- [149] L. Wang, H. Lin and C. Tsai, "Characterization and mechanism of α_2 -Ti₃Al and γ -TiAl precipitation in Ti-6Al-4V alloy following tungsten arc welding," *Key Engineering Materials*, vol. 520, p. 320–329, 2012.
- [150] E. Hall, "The deformation and ageing of mild steel: III discussion of results.," *Proceedings of the Physical Society. Section B*, vol. 64, p. 747–753, 1951.
- [151] N. Petch, "The cleavage strength of polycrystals," *Journal of the Iron and Steel Institute*, vol. 174, p. 25–28, 1953.
- [152] G. Tomas, V. Ramachandra, R. Ganeshan and R. Vasudevan, "Effect of pre- and post-weld heat treatments on the mechanical properties of electron beam welded Ti-6Al-4V alloy," *Journal of Materials Science*, vol. 28, p. 4892–4899, 1993.

- [153] J. Chesnutt, C. Rhodes and J. Williams, "Relationship between mechanical properties, microstructure, and fracture topography in $\alpha+\beta$ titanium alloys," in *Fractography – Microscopic Cracking Processes*, Materials Park, ASTM, 1976, p. 99–138.
- [154] J. Liu, "Phase transformations and stress evolution during laser beam welding and post heat treatment of TiAl-alloys. PhD thesis," Helmholtz-Zentrum Geesthacht, Geesthacht, 2015.
- [155] K. Masubuchi, *Analysis of Welded Structures*, Oxford: Pergamon Press, 1980.
- [156] S. Majumkar and R.P.V. Tayade, "A Review on Stresses Induced During Welding," *International Journal of Engineering Development and Research*, vol. 2, p. 1817–1825, 2014.
- [157] R. Singh, "Chapter 5 - Stresses, Shrinkage, and Distortion in Weldments," in *Applied Welding Engineering*, 2nd ed., New York, Elsevier, 2016, p. 201–238.
- [158] Liu, C, Zhang, J. and J. Niu, "Numerical and experimental analysis of residual stresses in full-penetration laser beam welding of Ti6Al4V alloy," *Rare Metal Materials and Engineering*, vol. 38, no. 8, p. 1317–1320, 2009.
- [159] N. Kashaev, D. Pugachev, V. Ventzke, F. Fomin, I. Burkhardt, J. Enz and S. Riekehr, "Microstructure and mechanical performance of autogenously fibre laser beam welded Ti-6242 butt joints," *Materials Science and Engineering A*, vol. 694, p. 110–120, 2017.
- [160] J. Mazumder and W. Steen, "Microstructure and mechanical properties of laser welded titanium 6Al-4V," *Metallurgical Transactions A*, vol. 13, p. 865–871, 1982.
- [161] J. Xu, Y. Rong, Y. Huang, P. Wang and C. Wang, "Keyhole-induced porosity formation during laser welding," *Journal of Materials Processing Technology*, vol. 252, p. 720–727, 2018.
- [162] J. Vollp, "Dynamik und Stabilität der Dampfkapillare beim Laserstrahlschweißen. PhD thesis" (in German), Bremen: BIAS Verlag, 2017.
- [163] S. Tsukamoto, "Developments in CO₂ laser welding," in *Handbook of Laser Welding Technologies*, Woodhead Publishing, 2013, p. 17–46.
- [164] F. Fomin, B. Klusemann and N. Kashaev, "Surface modification methods for fatigue properties improvement of laser-beam-welded Ti-6Al-4V butt joints," *Procedia Structural Integrity*, vol. 13, p. 273–278, 2018.
- [165] S. Timoshenko and J. Goodier, *Theory of Elasticity*, New York: McGraw-Hill, 1982.
- [166] G. Yoder, L. Cooley and T. Crooker, "Quantitative analysis of microstructural effects on fatigue crack growth in Widmanstätten Ti-6Al-4V and Ti-8Al-1Mo-1V," *Engineering Fracture Mechanics*, vol. 11, p. 805–816, 1979.
- [167] G. Yoder, L. Cooley and T. Crooker, "Fatigue crack propagation resistance of beta-annealed Ti-6Al-4V alloys of differing interstitial oxygen contents," *Metallurgical Transactions A*, vol. 9, p. 1413–1420, 1978.
- [168] C. Dawes, *Laser Welding: A Practical Guide*, Cambridge: Woodhead Publishing, 1992.
- [169] N. Kashaev, V. Ventzke, M. Horstmann, S. Chupakhin, S. Riekehr, R. Falck, E. Maawad, P. Staron, N. Schell and N. Huber, "Effects of laser shock peening on the microstructure and fatigue crack propagation behaviour of thin AA2024 specimens," *International Journal of Fatigue*, vol. 98, p. 223–233, 2017.
- [170] K. Ding and L. Ye, *Laser Shock Peening*, Boca Raton: CRC Press, 2006.

-
- [171] A. Hallinan, "A review of the Weibull distribution," *Journal of Quality Technology*, vol. 25, no. 2, p. 85–93, 1993.
- [172] H. Atkinson and G. Shi, "Characterization of inclusions in clean steels: a review including the statistics of extremes methods," *Progress in Materials Science*, vol. 48, p. 457–520, 2003.
- [173] F. Yoshinaka, T. Nakamura, S. Nakayama, D. Shiozawa, Y. Nakai and K. Uesugi, "Non-destructive observation of internal fatigue crack growth in Ti–6Al–4V by using synchrotron radiation μ CT imaging," *International Journal of Fatigue*, vol. 93, no. 2, p. 397–405, 2016.
- [174] T. Nakamura, H. Oguma and Y. Shinohara, "The effect of vacuum-like environment inside sub-surface fatigue crack on the formation of ODA fracture surface in high-strength steel," *Procedia Engineering*, vol. 2, p. 2121–2129, 2010.
- [175] S. Kovacs, T. Beck and L. Singheiser, "Influence of mean stresses on fatigue life and damage of a turbine blade steel in the VHCF-regime," *International Journal of Fatigue*, vol. 49, p. 90–99, 2013.
- [176] T. Anderson, *Fracture Mechanics: Fundamentals and Applications*, 3 ed., Boca Raton: CRC Press, 2005.
- [177] A. Zhao, J. Xie, C. Sun, Z. Lei and Y. Hong, "Prediction of threshold value for FGA formation," *Materials Science and Engineering A*, vol. 528, no. 22-23, p. 6872–6877, 2011.
- [178] J. Ting, V. Frederick and F. Lawrence, "Modelling the long-life fatigue behaviour of a cast aluminium alloy," *Fatigue and Fracture of Engineering Materials and Structures*, vol. 16, p. 631–647, 1993.
- [179] S. G. Ivanova, R. R. Biederman and R. D. Sisson, "Investigation of fatigue crack initiation in Ti-6Al-4V during tensile-tensile fatigue," *Journal of Materials Engineering and Performance*, vol. 11, no. 2, p. 226–231, 2002.
- [180] S. Jha, C. Szczepanski, P. Golden, W. Porter and R. John, "Characterization of fatigue crack-initiation facets in relation to lifetime variability in Ti–6Al–4V," *International Journal of Fatigue*, vol. 42, p. 248–257, 2012.
- [181] V. Kazymyrovich, "Very high cycle fatigue of engineering materials: A literature review," *Karlstad University Studies 22*, Karlstad, 2009.
- [182] F. Fomin, M. Horstmann, N. Huber and N. Kashaev, "Probabilistic fatigue-life assessment model for laser-welded Ti-6Al-4V butt joints in the high-cycle fatigue regime," *International Journal of Fatigue*, vol. 116, p. 22–35, 2018.
- [183] Y. Kuroshima, T. Ikeda, M. Harada and S. Harada, "Subsurface crack growth behavior on high cycle fatigue of high strength steel," *Transactions of the Japan Society of Mechanical Engineers A*, vol. 64, no. 626, p. 2536–2541, 1998.
- [184] M. Madia, B. Schork, J. Bernhard and M. Kaffenberger, "Multiple crack initiation and propagation in weldments under fatigue loading," *Procedia Structural Integrity*, vol. 7, p. 423–430, 2017.
- [185] X. Zheng and M. Hirt, "Fatigue crack propagation in steels," *Engineering Fracture Mechanics*, vol. 18, no. 5, p. 965–973, 1983.
- [186] F. Ellyin, *Fatigue Damage, Crack Growth and Life Prediction*, London: Chapman & Hall, 1997.
- [187] R. Forman and S. Mettu, "Behavior of surface and corner cracks subjected to tensile and bending loads in Ti-6Al-4V alloy. NASA Technical Report," NASA, Philadelphia, 1992.

- [188] NASA, "Fatigue crack growth computer program 'NASGRO', Version 3.0 - reference manual," NASA, 2000.
- [189] J. Newman, "A crack opening stress equation for fatigue crack growth," *International Journal of Fatigue*, vol. 24, no. 4, p. R131–R135, 1984.
- [190] J. Newman, "A crack-closure model for predicting fatigue-crack growth under aircraft spectrum loading," NASA, TM-81941, 1981.
- [191] H. Oguma and T. Nakamura, "Fatigue crack propagation properties of Ti–6Al–4V in vacuum environments," *International Journal of Fatigue*, vol. 50, p. 89–93, 2013.
- [192] A. McEvily and G. Velasquez, "Fatigue crack tip deformation processes as influenced by the environment," *Metallurgical Transactions A*, vol. 23, p. 2211–2221, 1992.
- [193] D. Duquette and M. Gell, "The effect of environment on the mechanism of Stage I fatigue fracture," *Metallurgical Transactions*, vol. 2, no. 5, p. 1325–1331, 1971.
- [194] F. Yoshinaka, T. Nakamura and K. Takaku, "Effects of vacuum environment on small fatigue crack propagation in Ti–6Al–4V," *International Journal of Fatigue*, vol. 91, p. 29–38, 2016.
- [195] P. Irving and C. Beevers, "The effect of air and vacuum environments on fatigue crack growth rates in Ti-6Al-4V," *Metallurgical Transactions*, vol. 5, no. 2, p. 391–398, 1974.
- [196] R. Ritchie, D. Davidson, B. Boyce, J. Campbell and O. Roder, "High cycle fatigue of Ti6Al4V," *Fatigue and Fracture of Engineering Materials and Structures*, vol. 22, p. 621–631, 1999.
- [197] S. Tammis-Williams, P. Withers, I. Todd and P. Prangnell, "The influence of porosity on fatigue crack initiation in additively manufactured titanium components," *Scientific Reports*, vol. 7, no. 1, p. Article number: 7308, 2017.